Physik - Department

Studies of Proton Recoils in Organic Liquid Scintillators Used in Present and Future Neutrino Experiments

Dissertation

von

Vincenz Felix Maria Zimmer

Technische Universität München

Technische Universität München

Physik - Department

Lehrstuhl für Experimentalphysik und Astroteilchenphysik

Studies of Proton Recoils in Organic Liquid Scintillators Used in Present and Future Neutrino Experiments

Vincenz Felix Maria Zimmer

Vollständiger Abdruck der von der Fakultät für Physik der Technischen Universität München zur Erlangung des akademischen Grades eines

Doktors der Naturwissenschaften (Dr. rer. nat.)

genehmigten Dissertation.

Vorsitzender:	Univ.-Prof. Dr. Norbert Kaiser
Prüfer der Dissertation:	
1.	Univ.-Prof. Dr. Lothar Oberauer
2.	Priv.-Doz. Dr. Andreas Ulrich

Die Dissertation wurde am 02.09.2015 bei der Technischen Universität München eingereicht und durch die Fakultät für Physik am 29.09.2015 angenommen.

Abstract

For next-generation liquid scintillator based neutrino detectors, like the proposed LENA (50 kt) and planned JUNO (20 kt) detectors, elastic neutrino-proton scattering is one of the major detection channels for neutrinos from a galactic core collapse supernova. For a proper interpretation of the obtained data, the light output of the liquid scintillator, which is a nonlinear function of the initial proton energy, needs to be known. This thesis describes a quantitative study of this nonlinearity, the so-called quenching effect. Proton recoils in the scintillator were induced using a pulsed beam of monoenergetic neutrons. The neutron beam was produced at the neutron scattering facility at the Maier-Leibnitz-Laboratorium (MLL) in Garching, using the nuclear reaction $p(^{11}B, n)^{11}C$.

Various organic liquid scintillators were studied at different incident neutron energies ranging from $\sim 4.7\,\mathrm{MeV}$ to $\sim 11.2\,\mathrm{MeV}$. The measurements included all scintillators from the running Double Chooz and Borexino experiments as well as the favored scintillators for the LENA and JUNO detectors. Furthermore, an unprecedented variety of scintillator mixtures based on linear alkylbenzene (LAB) has been investigated, featuring different concentrations of the primary wavelength shifter 2,5-diphenyloxazole (PPO), of the secondary wavelength shifter 1,4-bis(2-methylstyryl)benzene (bisMSB) and of nonscintillating n-paraffine.

The application of a pulsed beam allows the determination of the neutron energy by a time of flight (ToF) measurement. Using this information, the light output for protons was extracted from the obtained proton recoil spectra, measured at different incident neutron energies. The energy dependent behavior of the light output for protons could successfully be described by the semi-empiric Birks model. Birks-factors kB between $(0.0095 \pm 0.0005)\,\mathrm{cm/MeV}$ and $(0.0149 \pm 0.0007)\,\mathrm{cm/MeV}$ were obtained for the different scintillators. An increasing quenching effect for LAB-based scintillators with decreasing concentrations of PPO below $\sim 3\,\mathrm{g/l}$ was found. For PPO concentrations above $\sim 3\,\mathrm{g/l}$ no significant change of the energy dependent light output was observed. Furthermore, the results show no significant impact of the bisMSB concentration on the quenching effect. The dilution of LAB with nonscintillating n-paraffine was found to increase the quenching effect. The behavior of the quenching characteristics for protons, obtained for the various LAB-based scintillators, is in good agreement with our common knowledge of the scintillation processes in multicomponent liquid scintillators.

Fast neutron induced proton recoils are a major background in liquid scintillator based neutrino experiments. They can principally be discriminated from γ-ray and electron interactions by using the difference in the characteristic scintillation pulse shape for different particle types. Using the ToF information from the measurements performed at the MLL, background reduced datasets of events due to γ-ray induced electrons and neutron induced protons were obtained. Therefore, this setup provides an excellent opportunity to investigate the pulse shape discrimination (PSD) capabilities of organic liquid scintillators.

The so-called tail-to-total method was used to parameterize the difference in the scintillation pulse shape for γ-ray and neutron induced events. The PSD performance as a function of the visible energy between $0.25 - 4.00\,\mathrm{MeV}$ was determined using several parameters, like the remaining fraction of neutron events for a given selection efficiency of γ-ray events

of 99 %. For visible energies of $1.0 - 1.5\,\mathrm{MeV}$ this parameter was found to be between $(2.14 \pm 0.17) \cdot 10^{-4}\,\%$ in case of the Borexino scintillator and $(31.4 \pm 0.4)\,\%$ for the Double Chooz gamma catcher scintillator. The results for the various LAB-based scintillators show a decreasing PSD performance for decreasing PPO concentrations below $\sim 5\,\mathrm{g/l}$ and a saturating performance above this concentration. Furthermore, the concentration of bisMSB was found to have no significant influence on the PSD performance, while an increasing dilution with nonscintillating n-paraffine results in a decreasing performance. The obtained results for the PSD performance are consistent with the behavior observed for the results on the quenching effect.

Zusammenfassung

Für zukünftige Flüssigszintillator-basierte Neutrinodetektoren, wie dem vorgeschlagenen LENA und dem geplanten JUNO Detektor, ist die elastische Neutrino-Proton-Streuung ein wichtiger Kanal zur Detektion von Neutrinos aus einer Kernkollaps-Supernova in unserer Galaxie. Um die gemessenen Daten richtig interpretieren zu können, müssen die Nichtlinearitäten der Lichtausbeute des Szintillators als Funktion der Protonenenergiedeposition verstanden werden. Diese Arbeit beschreibt eine quantitative Studie dieser Nichtlinearitäten, die als Quenching bezeichnet werden. Mit Hilfe eines gepulsten, monoenergetischen Neutronen-Strahls wurden Protonenrückstöße in Flüssigszintillatoren hervorgerufen. Der Neutronen-Strahl wurde am Maier-Leibnitz-Laboratorium (MLL) in Garching unter der Verwendung der Kernreaktion $p(^{11}B, n)^{11}C$ produziert.

Diverse organische Flüssigszintillatoren wurden bei verschiedenen Neutronenenergien zwischen ~ 4.7 MeV und ~ 11.2 MeV untersucht. Die Messungen umfassten die Szintillatoren der zur Zeit laufenden Experimente Double Chooz und Borexino sowie die bevorzugten Szintillatoren für die LENA und JUNO Detektoren. Des Weiteren wurde eine beispiellose Vielzahl von Szintillatoren basierend auf linearem Alkylbenzol (LAB) untersucht. Diese enthielten verschiedene Konzentrationen des primären Wellenlängenschiebers 2,5-Diphenyloxazol (PPO) und des sekundären Wellenlängenschiebers 1,4-Bis(2-methylstyryl)benzol (bisMSB), sowie unterschiedliche Mengen an nichtszintillierendem n-Paraffin.

Mit Hilfe eines gepulsten Strahls war es möglich die Neutronenenergie durch eine Flugzeitmessung zu bestimmen. Dadurch konnte die Lichtausbeute für Protonen aus Neutronen-induzierten Protonen-Rückstoß-Spektren gewonnen werden. Das energieabhängige Verhalten der Lichtausbeute konnte erfolgreich durch das semiempirische Birks-Modell beschrieben werden. Für den Birks-Parameters kB ergaben sich für die verschiedenen Szintillatoren Werte zwischen (0.0095 ± 0.0005) cm/MeV und (0.0149 ± 0.0007) cm/MeV. Ein in der Stärke steigender Quenching-Effekt wurde für LAB-basierte Szintillatoren mit sinkender PPO-Konzentration unterhalb von ~ 3 g/l beobachtet. PPO-Konzentrationen oberhalb von ~ 3 g/l führten jedoch zu keiner signifikanten Verstärkung oder Abschwächung des Quenching-Effekts. Außerdem zeigen die Resultate keinen signifikanten Einfluss des sekundären Wellenlängenschiebers bisMSB auf den Quenching-Effekt. Eine Verdünnung von LAB-basierten Szintillatoren mit nichtszintillierendem n-Paraffin resultiert in einer Verstärkung des Quenching-Effekts mit ansteigendem Anteil an n-Paraffin. Das beobachtete Verhalten des Quenching-Effekts für die verschiedenen LAB-basierten Szintillatoren ist in guter Übereinstimmung mit dem heutigen Verständnis der Szintillationsprozesse in Mehrkomponenten-Flüssigszintillatoren.

Rückstoß-Protonen, hervorgerufen durch schnelle Neutronen, stellen einen bedeutenden Untergrund in Flüssigszintillator-basierten Neutrinoexperimenten dar. Dieser Untergrund kann prinzipiell von Ereignissen durch γ-Strahlen und Elektronen mit Hilfe der Unterschiede in der charakteristischen Szintillationspulsform für die jeweilige Teilchensorte unterschieden werden. Unter Verwendung der Flugzeitmessung wurden untergrundarme Datensätze von Ereignissen infolge von γ-Strahlen-induzierten Elektronen und Neutronen-induzierten Protonen erstellt. Aus diesem Grund bietet der experimentelle Aufbau am MLL eine ex-

zellente Möglichkeit Flüssigszintillatoren bezüglich ihrer Leistungsfähigkeit für Pulsform-analyse zu untersuchen.

Um die Unterschiede in den Pulsformen für γ- und Neutronen-induzierte Ereignisse zu para-metrisieren, wurde der sogenannte 'tail-to-total'-Parameter verwendet. Die Leistungsfähig-keit der Pulsformanalyse in Abhängigkeit der sichtbaren Energie zwischen $0.25\,\mathrm{MeV}$ und $4.00\,\mathrm{MeV}$ wurde mit Hilfe verschiedener Parameter quantifiziert. Beispielhaft für die Cha-rakterisierung der Leistungsfähigkeit ist der verbleibende Anteil an Neutronen-induzierten Ereignissen bei einer Effizienz von $99\,\%$ in der Selektion von γ-induzierten Ereignissen zu nennen. Im Energiebereich von $1.0-1.5\,\mathrm{MeV}$ wurden für diesen Parameter Werte zwischen $(2.14\pm0.17)\cdot10^{-4}\,\%$ für den Borexino-Szintillator und $(31.4\pm0.4)\,\%$ für den Double Chooz-Gamma-Catcher-Szintillator bestimmt. Die Resultate der verschiedenen LAB-basierten Szintillatoren zeigen eine geringere Leistungsfähigkeit der Pulsformanalyse mit sinkender PPO-Konzentration unterhalb von $\sim 5\,\mathrm{g/l}$ und eine Sättigung in der Leistungsfähigkeit oberhalb dieser Konzentration. Des Weiteren wurde kein signifikanter Einfluss der bisMSB-Konzentration auf die Leistungsfähigkeit der Pulsformanalyse beobachtet. Eine zunehmen-de Verdünnung mit nichtszintillierendem n-Paraffin resultiert dagegen in einer zunehmen-den Verschlechterung. Die Resultate für die Leistungsfähigkeit der Pulsformanalyse aller untersuchten Szintillatoren sind konsistent mit den Ergebnissen der gemessenen Quenching-Effekte.

Contents

1. Introduction

After the first postulation of neutrinos by Wolfgang Pauli in 1930 to ensure conservation of energy, momentum and spin in the β-decay of radioactive nuclei neutrino physics got a major field in particle physics [1]. In 1953 Cowan and Reines could perform a first detection of (anti)neutrinos at a nuclear power plant, using a liquid scintillator detector [2, 3].

In the following decades major progress in the field of neutrino physics and astrophysics was achieved: Radiochemical experiments, like Homestake [4], SAGE [5] and GALLEX/GNO [6, 7], and water Cherenkov based experiments, like Super-Kamiokande [8] and SNO [9] were leading the field. However, in the present time organic liquid scintillator based detectors play an important role again. In particular, the KamLAND long baseline reactor neutrino experiment [10] gave first precise results on the oscillation parameters governing solar neutrino oscillations. Additionally, the Borexino experiment [11] could perform first direct measurements of solar ^{7}Be-neutrinos [12], pep-neutrinos [13] and pp-neutrinos [14] (see section 2.2.5), improving the knowledge on the fusion processes in the sun. Furthermore, the liquid scintillator experiments Double Chooz [15] (see section 2.1), Daya Bay [16] and RENO [17] determined a rather high value for the last mixing angle θ_{13} (see sections 1.1 and 1.3), opening the possibility to determine the neutrino mass hierarchy and CP violation in the fermion sector in future experiments (see sections 1.1 and 1.4).

Currently, there are two proposed next generation organic liquid scintillator based neutrino detectors: Firstly, the 50 kt Low Energy Neutrino Astronomy (LENA) experiment [18], which is addressing a rich physics program mainly focused on natural neutrino sources and secondly, the Jiangmen Underground Neutrino Observatory (JUNO) [19], which is mainly aiming for the determination of the neutrino mass hierarchy with a 20 kt detector. Due to their huge size and conceptional similarities, both experiments have a significant overlap regarding their physics potentials. The major overlaps of the physics goals are the real time detection of neutrinos from a galactic core collapse supernova (SN) (see section 1.5) and the first time measurement of the cumulative flux of neutrinos, which were emitted from all SNe in the causal universe up to now, the so-called diffuse supernova neutrino background (DSNB) (see section 1.5.4).

For both, the detection of neutrinos from a galactic SN and the DSNB, energy depositions by proton recoils play an important role. While elastic neutrino-proton scattering is one of the main detection channels for neutrinos from a galactic SN (see section 2.2.3), proton recoils induced by neutrons, produced by neutral current interactions of atmospheric neutrinos on ^{12}C, pose the major background for the measurement of the DSNB (see section 2.2.4). Furthermore, proton recoils, caused by cosmic muon induced neutrons in the materials surrounding the detector, are a major background to the detection of reactor

electron antineutrinos. In all cases mentioned above, the response of the used organic liquid scintillator to protons needs to be well understood. Therefore, an experiment at the Maier-Leibnitz-Laboratorium (MLL), using a pulsed neutron beam, was built to investigate the response of organic liquid scintillators regarding neutron induced proton recoils.

A brief introduction to neutrino oscillations and to the current knowledge in neutrino physics is given in sections 1.1 and 1.2 of the present chapter. Additionally, the status of the determination of the third mixing angle θ_{13} (see section 1.3) and different possibilities to determine the neutrino mass hierarchy are discussed (see section 1.4). Finally, an introduction to core collapse supernovae and the expected neutrino signal is given in section 1.5.

The liquid scintillator experiments Double Chooz, LENA and JUNO are introduced in chapter 2 along with the results obtained by Double Chooz and the physics goals of LENA and JUNO. In chapter 3 the scintillation mechanisms of aromatic organic liquids are introduced briefly. Furthermore, a summary of the used scintillator components and investigated samples is given. The experimental setup at the Maier-Leibnitz-Laboratorium (MLL), which was used to investigate different scintillator mixtures under irradiation with neutrons, is presented in chapter 4. The data taken for the investigated scintillator samples in three beam times at the MLL in 2013 and 2014 was analyzed with regard to ionization quenching due to protons. This analysis and the obtained results are described and discussed in chapter 6. Additionally, the data from the beam times was analyzed with regard to pulse shape discrimination performance regarding proton and electron recoil events in the scintillator. The analysis and the results for the different scintillator samples are presented in chapter 7.

1.1. Neutrino Oscillations

1.1.1. Neutrinos in the Standard Model

In the *standard model of particle physics* (SM) neutrinos are considered as massless and electrically neutral particles, which are produced and interact by the weak interaction [1, 20, 21]. Neutrinos and their antiparticles exist in three flavors: ν_e and $\bar{\nu}_e$, ν_μ and $\bar{\nu}_\mu$ and ν_τ and $\bar{\nu}_\tau$. The weak interaction is mediated by the exchange of either a Z^0-boson ($m_Z \approx 91\,\mathrm{GeV}$ [20]) in so-called *neutral current* (NC) interactions or $W^\pm$-bosons ($m_W \approx 80\,\mathrm{GeV}$ [20]) in *charged current* (CC) interactions. Due to the high masses of the Z^0- and $W^\pm$-bosons both the range and cross section of the weak interaction are very small: For neutrinos with energies in the MeV range typical values for the cross section are in the order of 10^{-44} to $10^{-43}\,\mathrm{cm}^{-2}$. Furthermore, the weak interaction violates parity maximally, which means that $W^\pm$ couple only to left-handed particles and right-handed antiparticles. Therefore, the massless neutrinos in the SM are produced exclusively left-handed, while antineutrinos are generated right-handed.

1.1.2. Neutrino Oscillations in Vacuum

The assumption of massless neutrinos in the SM is in conflict with the observations by several neutrino experiments that neutrinos can change their flavor depending on their energy and travelled distance [8, 9, 10] - a phenomenon known as *neutrino oscillations*. The neutrinos ν_e, ν_μ and ν_τ are eigenstates of the weak interaction[1]. Allowing non-zero masses for the neutrinos, the resulting eigenstates of the propagation Hamiltonian - the mass eigenstates ν_1, ν_2 and ν_3 - are in general not equal to the flavor eigenstates. It is possible to express the flavor eigenstates by a superposition of the orthogonal mass eigenstates by [1, 23]:

$$\begin{pmatrix} \nu_e \\ \nu_\mu \\ \nu_\tau \end{pmatrix} = U \begin{pmatrix} \nu_1 \\ \nu_2 \\ \nu_3 \end{pmatrix} = \underbrace{\begin{pmatrix} U_{e1} & U_{e2} & U_{e3} \\ U_{\mu1} & U_{\mu2} & U_{\mu3} \\ U_{\tau1} & U_{\tau2} & U_{\tau3} \end{pmatrix}}_{\text{PMNS matrix}} \begin{pmatrix} \nu_1 \\ \nu_2 \\ \nu_3 \end{pmatrix} \tag{1.1}$$

where U is the unitary *Pontecorvo-Maki-Nakagawa-Sakata* (PMNS) matrix, which can be parameterized by three mixing angles θ_{12}, θ_{23}, θ_{13} and a CP violating phase δ as follows [1]:

$$U = \begin{pmatrix} 1 & 0 & 0 \\ 0 & c_{23} & s_{23} \\ 0 & -s_{23} & c_{23} \end{pmatrix} \begin{pmatrix} c_{13} & 0 & s_{13}e^{-i\delta} \\ 0 & 1 & 0 \\ -s_{13}e^{i\delta} & 0 & c_{13} \end{pmatrix} \begin{pmatrix} c_{12} & s_{12} & 0 \\ -s_{12} & c_{12} & 0 \\ 0 & 0 & 1 \end{pmatrix} \tag{1.2}$$

with s_{ij} and c_{ij} being abbreviations for $\sin\theta_{ij}$ and $\cos\theta_{ij}$. In case of neutrinos being Majorana particles, i.e. particles, which are their own antiparticles, two additional CP violating phases need to be introduced [20]. These will be omitted in the following, as these phases have no influence on the oscillation probability.

In the following, the concept of neutrino oscillations is derived based on the assumption that the neutrino mass eigenstates can be treated as plain waves. Additionally, effects resulting from the exact nature of the neutrino production and the neutrino detection reactions are not taken into account. For a more accurate theoretical treatment please refer to [24].

The time evolution of the mass eigenstates ν_i is given by the Schrödinger equation[2]:

$$|\nu_i(t)\rangle = e^{-iE_it}|\nu_i(t=0)\rangle \tag{1.3}$$

where E_i is the energy of mass eigenstate ν_i. Assuming that the masses of the neutrinos m_i are finite but small compared to the momentum p, i.e. $m_i \ll p$ and $p \approx E$, the energy of the mass eigenstate i can be approximated to be:

$$E_i = \sqrt{p^2 + m_i^2} \stackrel{m_i \ll p}{\approx} p + \frac{m_i^2}{2p} \stackrel{p \approx E}{\approx} E + \frac{m_i^2}{2E} \tag{1.4}$$

---

[1] There are experimental indications for the existence of additional sterile neutrinos. However, explaining all experimental data, even with the addition of sterile neutrinos, is still difficult [22].

[2] In the following natural units are used, i.e. $c = \hbar = 1$.

Using equation (1.1) and equation (1.3), the time evolution of the flavor eigenstate $|\nu_\alpha\rangle$ ($\alpha = e, \mu, \tau$) can be written as follows:

$$|\nu_\alpha(t)\rangle = \sum_{i=1}^{3} U_{\alpha i}|\nu_i(t)\rangle = \sum_{i=1}^{3} U_{\alpha i}\, e^{-iE_i t}|\nu_i(t=0)\rangle \tag{1.5}$$

The time dependent probability $P_{\nu_\alpha \to \nu_\beta}(t)$ of detecting a neutrino with flavor $|\nu_\beta\rangle$, which was originally produced in flavor state $|\nu_\alpha\rangle$ at $t = 0$, can be expressed by [25, 26]

$$P_{\nu_\alpha \to \nu_\beta}(t) = |\langle \nu_\beta|\nu_\alpha(t)\rangle|^2 \overset{\langle \nu_i|\nu_j\rangle = \delta_{ij}}{=} \left| \sum_{i=1}^{3} U_{\alpha i} U_{\beta i}^* e^{-iE_i t} \right|^2 . \tag{1.6}$$

Using equation (1.4) and $t \approx L$, where L is the traveled distance of an ultrarelativistic neutrino ($v \approx c$), one obtains [25, 26]:

$$
\begin{aligned}
P_{\nu_\alpha \to \nu_\beta}(L) =\ & \delta_{\alpha\beta} - 4 \sum_{i>j} \mathrm{Re}\left(U_{\alpha i} U_{\beta i}^* U_{\alpha j}^* U_{\beta j}\right) \sin^2\left(\frac{\Delta m_{ij}^2 L}{4E}\right) \\
& + 2 \sum_{i>j} \mathrm{Im}\left(U_{\alpha i} U_{\beta i}^* U_{\alpha j}^* U_{\beta j}\right) \sin\left(\frac{\Delta m_{ij}^2 L}{2E}\right)
\end{aligned}
\tag{1.7}
$$

with $\Delta m_{ij}^2 = m_i^2 - m_j^2$ being the squared mass differences between the mass eigenstates. Therefore, the oscillation probability $P_{\nu_\alpha \to \nu_\beta}$ is only non-vanishing, if at least one of the squared mass differences is different from zero. As a consequence neutrinos require a finite mass to allow for oscillations.

In case of antineutrinos, the sign of the third term in equation (1.7) has to be changed. Hence, the oscillation probabilities for neutrinos and antineutrinos differ, if the imaginary part in the third term in equation (1.7) does not vanish. This would imply CP-violation [26]. The only parameter in the PMNS-matrix affecting the existence of an imaginary part of the oscillation probability is the CP-violating phase δ. CP is only violated in the neutrino sector, if $\delta \neq 0$ and $\delta \neq \pi$. Note that the CP-violating phase has no influence on the survival probability $P_{\nu_\alpha \to \nu_\alpha}$, as the imaginary part in equation (1.7) fully vanishes ($\mathrm{Im}(U_{\alpha i} U_{\alpha i}^* U_{\alpha j}^* U_{\alpha j}) = \mathrm{Im}(|U_{\alpha i}|^2 |U_{\alpha j}|^2) = 0$). Therefore, δ cannot be measured in disappearance experiments, like reactor neutrino experiments. Therefore, it has to be determined in beam based appearance experiments, which is rather challenging. Thus, the value of the phase δ could not be determined until today.

1.1.3. Neutrino Oscillations in Matter

The above described oscillation probability was derived for neutrinos moving in vacuum. For neutrinos traversing matter, coherent forward scattering with the electrons, protons and neutrons has to be taken into account [27]. NC-reactions have equal cross sections for all neutrino flavors and, therefore, have practically no effect on neutrino oscillations. In

contrary, CC-reactions are only relevant for electron neutrinos in matter with no muons or tauons available, as it is the case, for example, in earth or solar matter.

The resulting asymmetry between the coherent scattering amplitudes for electron neutrinos and the other flavors can be expressed by an additional potential for the ν_e [26]:

$$V = \sqrt{2}\, G_{\mathrm{F}}\, N_{\mathrm{e}} \tag{1.8}$$

with G_{F} being the Fermi coupling constant and N_{e} being the electron number density of the matter traversed by the neutrinos. For antineutrinos the sign of the potential needs to be changed ($V \to -V$). As the potential V has to be added to the Hamiltonian, the mass eigenstates and, in consequence, the mixing angles change for neutrinos traversing matter. In the simplified two-flavor case, the oscillation in vacuum can be described by one mixing angle θ and one squared mass differences Δm^2. The corresponding effective values for the parameters in case of oscillation in matter θ_{m} and Δm_{m}^2 reed [26]:

$$\Delta m_{\mathrm{m}}^2 = \Delta m^2 \, \sqrt{\sin^2 2\theta + \left(\cos 2\theta - \tfrac{2EV}{\Delta m^2}\right)^2} \tag{1.9}$$

$$\sin^2 2\theta_{\mathrm{m}} = \frac{\sin^2 2\theta}{\sin^2 2\theta + \left(\cos 2\theta - \tfrac{2EV}{\Delta m^2}\right)^2} \tag{1.10}$$

Three special cases can be derived from equations (1.9) and (1.10):

- $\frac{2EV}{\Delta m^2} \ll \cos 2\theta \Rightarrow \theta_{\mathrm{m}} \approx \theta$: Almost no effect on the mixing due to matter.

- $\frac{2EV}{\Delta m^2} \approx \cos 2\theta \Rightarrow \theta_{\mathrm{m}} \approx 45°$: Maximal mixing between the two flavors due to matter effect; independent on actual value of θ.

- $\frac{2EV}{\Delta m^2} \gg \cos 2\theta \Rightarrow \theta_{\mathrm{m}} \approx 90°$: Independent on the value of θ; almost no mixing occurs.

For example, the third case applies to electron neutrinos produced by fusion processes in the center of the sun with energies above $\sim 10\,\mathrm{MeV}$. Here, the matter effect leads to electron neutrinos ν_{e} consisting practically of the mass state $\nu_{2,\mathrm{m}}$ with mass $m_{2,\mathrm{m}}$. Due to the oscillation length being long compared to the radial density gradient in the sun the electron neutrinos stay in this mass state until they leave thw sun. Consequently, almost no further oscillation appears on the way from the sun to the earth, leading to a detection probability for electron neutrinos of $P_{\nu_e \to \nu_e} = |\langle \nu_2 | \nu_e \rangle|^2 \approx \sin^2 \theta_{12} \approx 30\,\%$ [25]. This resonant conversion of the electron neutrinos ν_{e} into other flavors is commonly known as the *Mikheyev-Smirnov-Wolfenstein* (MSW) *effect* [28]. It is only possible, when the condition $m_2 > m_1$ is fulfilled, and, therefore, $\Delta m_{12}^2 > 0$. While solar neutrinos below about $\sim 1\,\mathrm{MeV}$ oscillate basically as in vacuum (first of above shown cases), oscillation of neutrinos with energies above about $\sim 5\,\mathrm{MeV}$ is dominated by matter effects (third of above shown cases).

1.2. Current Status of Neutrino Physics

The three-neutrino flavor oscillations, introduced in section 1.1.2, feature six independent free parameters affecting the oscillation probabilities: the three mixing angles θ_{12}, θ_{13} and

parameter	mass hierarchy case	best fit	1σ range
Δm_{21}^2 $(10^{-5}\,\text{eV}^2)$	NH or IH	7.54	$(7.32 - 7.80)$
Δm_{31}^2 $(10^{-3}\,\text{eV}^2)$	NH	2.47	$(2.41 - 2.53)$
	IH	-2.42	$-(2.36 - 2.48)$
$\sin^2\theta_{12}$	NH or IH	0.308	$(0.291 - 0.325)$
$\sin^2\theta_{13}$	NH	0.0234	$(0.0215 - 0.0254)$
	IH	0.0240	$(0.0218 - 0.0259)$
$\sin^2\theta_{23}$	NH	0.437	$(0.414 - 0.470)$
	IH	0.455	$(0.424 - 0.594)$
δ	NH	$1.39\,\pi$	$(1.12 - 1.77)\,\pi$
	IH	$1.31\,\pi$	$(1.98 - 1.60)\,\pi$

Table 1.1.: Best fit three-flavor oscillation parameters from a global analysis of the experimental results from long baseline accelerator, solar, short baseline reactor, and the KamLAND and Super-Kamiokande experiments [29]. The results and the corresponding 1σ error intervals are given for the cases of normal mass hierarchy (NH, $m_1 < m_2 < m_3$) and inverted hierarchy (IH, $m_3 < m_1 < m_2$).

θ_{23}, two independent squared mass differences Δm_{21}^2 and Δm_{31}^2 and the CP-violating phase δ. In table 1.1 the current knowledge on the oscillation parameters from a global analysis [29] is summarized. The mixing angle θ_{12} and the squared mass difference Δm_{21}^2 are mainly constricted by the precise results from solar and the KamLAND [30] experiments, while the observation of the MSW effect fixes the sign of Δm_{21}^2 (see section 1.1.3). The parameters θ_{23} and Δm_{31}^2 are mainly constrained by the long baseline accelerator neutrino experiments MINOS [31] and T2K [32], which are also sensitive to θ_{13} and subdominantly to θ_{12} and δ and, therefore, suffer from parameter correlations. Major constraints on θ_{13} arise from the short baseline reactor experiments Double Chooz [33], Daya Bay [34] and RENO [17]. Further improvement on the results on Δm_{31}^2 and δ are obtained, when most recent results on atmospheric neutrino data from Super-Kamiokande [35] are included.

Besides the mostly well determined oscillation parameters shown in table 1.1, there are still unsolved topics, which need to be addressed in running and future experiments:

- While the absolute value for Δm_{31}^2 is known rather precisely, the sign could still not be determined. In consequence, there are still two possible mass orderings: normal hierarchy (NH) for $m_1 < m_2 < m_3$ or inverted hierarchy (IH) for $m_3 < m_1 < m_2$.

- The value of the CP-violating phase δ is still not known. Results from global analyses, like that described in [29], hint for $\delta > \pi$ on a 1σ-level in case of NH and slightly below the 1σ-level for IH (see table 1.1).

- The amplitude of the oscillation due to θ_{23} ($\sin^2 2\theta_{23}$) is known to be close to max-

imum, which means $\theta_{23} \approx 45°$. Due to the resulting ambiguity the octant of angle θ_{23}, i.e. whether $\theta_{23} < 45°$, $\theta_{23} > 45°$ or $\theta_{23} = 45°$ is still not known. The results from the global analysis shown in table 1.1 show hints for $\theta_{23} < 45°$ in case of normal mass hierarchy [29].

- A major topic in neutrino physics is the determination of the absolute masses of neutrinos, for which up to now only upper limits exist. Direct measurements of the electron antineutrino mass from the β^+-decay of tritium resulted in an upper limit on the effective electron neutrino mass of $m_e < 2\,\mathrm{eV}$ [36]. The KATRIN experiment, which is currently in its final steps of construction, aims for a sensitivity of $0.2\,\mathrm{eV}$ [37]. Furthermore, results from cosmology constrain the sum of the three neutrino masses to $\sum_i m_i < 0.39\,\mathrm{eV}$ (at $95\,\%$ CL) [20].

- Oscillation data from accelerator and reactor experiments and calibration data from gallium based radiochemical experiments show hints for at least one additional neutrino, mixing with the three known neutrino flavors ν_e, ν_μ and ν_τ [36]. As the observed decay width of the Z^0-boson is not compatible with a fourth weakly interacting neutrino flavor [20, 38], an additional mixing neutrino must not couple to weak interactions (or any other of the known interactions). Such neutrinos are, therefore, commonly referred to as *sterile neutrinos*. In case of the existence of sterile neutrinos, the additionally introduced oscillation parameters need to be in the range of $\sin^2 2\theta \sim 0.001 - 0.1$ and $\Delta m^2 > 0.1\,\mathrm{eV}^2$ for compatibility with present oscillation data [36].

In the following sections the experimental status in the determination of the mixing angle θ_{13} (see section 1.3) and the experimental prospect of the determination of the mass hierarchy and the CP-violating phase δ (see section 1.4) will be discussed in more detail, as this thesis is connected to the Double Chooz experiment (see section 2.1), the LENA project (see section 2.2) and the JUNO project (see section 2.3).

1.3. Status of the Neutrino Mixing Angle θ_{13}

The mixing angle θ_{13} can be measured in two complimentary ways [39]: on the one hand, with short baseline reactor neutrino experiments and, on the other hand, with long baseline accelerator experiments. In the following, both possible approaches are introduced briefly. Furthermore, the experimental status is summarized.

1.3.1. Reactor Neutrino Experiments

Nuclear reactors are powerful artificial neutrino sources. The neutrinos are produced in β^--decays of the fission products solely in the form of electron antineutrinos $\bar{\nu}_e$, featuring a mean energy of $\sim 3\,\mathrm{MeV}$ [20]. Expanding equation (1.7) the survival probability of electron
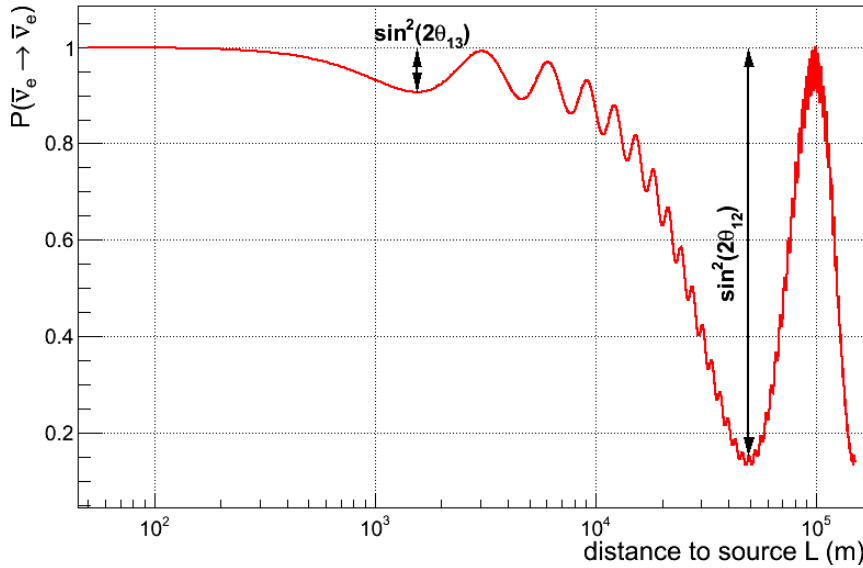
Figure 1.1.: Survival probability $P(\bar{\nu}_e \rightarrow \bar{\nu}_e) = P_{\bar{\nu}_e \rightarrow \bar{\nu}_e}$ according to equation (1.11) for electron antineutrinos with an energy of $3\,\mathrm{MeV}$ as a function of the distance L between source and detector. To calculate $P_{\bar{\nu}_e \rightarrow \bar{\nu}_e}$ the values for the oscillation parameters given in table 1.1 have been used, assuming normal mass hierarchy and $\Delta m^2_{32} \approx \Delta m^2_{31}$.

antineutrinos can be expressed in the following way [36]:

$$
\begin{aligned}
P_{\bar{\nu}_e \rightarrow \bar{\nu}_e} = 1 \; &- \; \cos^4 \theta_{13} \, \sin^2 2\theta_{12} \, \sin^2 \Delta_{21} \\
&- \; \sin^2 2\theta_{13} \left(\cos^2 \theta_{12} \, \sin^2 \Delta_{31} + \sin^2 \theta_{12} \, \sin^2 \Delta_{32} \right)
\end{aligned}
\tag{1.11}
$$

with $\Delta_{ij} = \frac{\Delta m^2_{ij} L}{4E}$. In figure 1.1 $P_{\bar{\nu}_e \rightarrow \bar{\nu}_e}$ is shown for electron antineutrinos with an energy of $3\,\mathrm{MeV}$ produced by a source in a distance L, using the values for the oscillation parameters given in table 1.1 for normal mass hierarchy. For a detector placed at the oscillation maximum due to Δm^2_{31} in a distance of $\sim 1-2\,\mathrm{km}$ to a powerful nuclear reactor (far detector) the survival probability can be approximated to be

$$
P_{\bar{\nu}_e \rightarrow \bar{\nu}_e} \approx 1 - \sin^2 2\theta_{13} \, \sin^2 \left(\frac{\Delta m^2_{31} L}{4E} \right)
\tag{1.12}
$$

using $\Delta m^2_{21} \ll \Delta m^2_{31}$ and $\Delta m^2_{31} \approx \Delta m^2_{32}$. With known Δm^2_{31} a precise measurement of θ_{13} without degeneracies is possible in this configuration. By placing a second detector at a distance of $\lesssim 400\,\mathrm{m}$ to the reactor (near detector), systematic effects arising from the limited knowledge on the energy spectrum of the reactor neutrinos and the cross section of the detection reaction can be reduced efficiently [36].

Currently there are three short baseline reactor neutrino experiments running: Double Chooz [33], Daya Bay [34] and RENO [17]. The detector concepts of all three experiments are very similar. While the Double Chooz experiment features two identical detectors, one far and one near (completed in 2014), detecting neutrinos from two reactors [33], the two detectors in the RENO experiment detect neutrinos from six reactors [17]. In

experiment	$\sin 2\theta_{13}$	year	reference
Double Chooz	$0.090^{+0.032}_{-0.029}$	2014	[42]
Daya Bay	0.090 ± 0.005	2015	[40]
RENO	$0.101 \pm 0.008\,(\text{stat}) \pm 0.010\,(\text{syst})$	2014	[43]

Table 1.2.: Recent results on the mixing angle θ_{13} from the reactor neutrino experiments Double Chooz, Daya Bay and RENO. Note that the result from Double Chooz corresponds to measurement with the far detector only. The systematic uncertainty is expected to decrease significantly, when data from the near detector (completed end of 2014) is included.

the final configuration of the Daya Bay experiment eight detectors are distributed in two near laboratories and one far laboratory, detecting neutrinos from the six reactors of the Daya Bay nuclear power complex [40]. In section 2.1 a detailed description of the Double Chooz experiment will be presented. For detailed descriptions of the Daya Bay and RENO experiments please refer to [41] and [17], respectively. The latest results from the three experiments are listed in table 1.2.

All three experiments reported an excess of $\bar{\nu}_e$ events between $\sim 4-6\,\text{MeV}$ when comparing the measured to the expected neutrino spectra [42, 43, 44]. A correlation between the excess and the reactor power was reported by both the Double Chooz [42] and the RENO [43] collaboration. An unknown background contribution is thereby disfavored, but not fully excluded.

1.3.2. Accelerator Neutrino Experiments

In accelerator neutrino oscillation experiments a beam consisting of muon (anti)neutrinos ν_μ ($\bar{\nu}_\mu$) is directed to a far detector in a distance of several $100\,\text{km}$ at the oscillation maximum corresponding to Δm_{31}^2. While a near detector is used to monitor the unoscillated neutrino beam, the far detector searches for the appearance of ν_e ($\bar{\nu}_e$). In such accelerator appearance experiments matter effects for neutrinos traversing the earth mantle have to be taken into account (see section 1.1.3). Assuming a constant matter density and neglecting subleading terms in θ_{13}, one obtains for the appearance probability for the oscillation $\nu_\mu \rightarrow \nu_e$ [20, 45]:

$$
\begin{aligned}
P_{\nu_\mu \rightarrow \nu_e} \approx \quad & \sin^2 \theta_{23} \, \frac{\sin^2 2\theta_{13}}{(A-1)^2} \, \sin^2\left((A-1)\,\Delta\right) \\
& + \alpha^2 \, \frac{\cos^2 \theta_{23} \, \sin^2 2\theta_{12}}{A^2} \, \sin^2\left(A\,\Delta\right) \\
& + \alpha \, \frac{8\,J_{CP}}{A\,(1-A)} \cdot \sin\left(A\,\Delta\right) \cdot \sin\left((1-A)\,\Delta\right) \cdot \left(\cot \delta \, \cos \Delta - \sin \Delta\right)
\end{aligned}
\tag{1.13}
$$

where

$$
\alpha = \frac{\Delta m_{21}^2}{\Delta m_{31}^2}, \quad \Delta = \frac{\Delta m_{31}^2 \, L}{4\,E}, \quad A = \sqrt{2}\,G_\mathrm{F}\,N_\mathrm{e}\,\frac{2E}{\Delta m_{31}^2} \quad \text{and}
$$

$$8\,J_{CP} = \sin\delta\,\cos\theta_{13}\,\sin 2\theta_{12}\,\sin 2\theta_{13} 2\theta_{23}$$

In case of $\bar{\nu}_\mu \to \bar{\nu}_e$, equation (1.13) needs to be modified by $A \to -A$ and $J_{CP} \to -J_{CP}$, while $(J_{CP} \cdot \cot\delta)$ remains unchanged [20, 45].

From equation (1.13) it becomes obvious that the measurement of θ_{13} by long baseline accelerator experiments is challenging, which is caused by degeneracies resulting from the unknown sign of Δm^2_{31} (mass hierarchy), the θ_{23}-octant and the CP-violating phase δ. Nevertheless, with such experiments it is possible to establish $\theta_{13} \neq 0$ with a high sensitivity [20].

In the T2K experiment a ν_μ-beam with $0.6\,\text{GeV}$ is produced at J-PARC[3] and directed to the Super-Kamiokande detector in a distance of $295\,\text{km}$ [46]. In a recent result on the appearance of electron neutrinos the observation of 28 ν_e appearance events with an expectation of 4.92 ± 0.55 background events was presented. Assuming $\sin^2 2\theta_{23} = 1$ and $\delta = 0$, $\theta_{13} = 0$ could be excluded by $7.3\,\sigma$ [46]. Furthermore, results on the value of θ_{13}, assuming NH (IH), were obtained with $\sin^2 2\theta_{13} = 0.140^{+0.038}_{-0.032}$ $(0.170^{+0.045}_{-0.037})$. Compared to the values on $\sin^2 2\theta_{13}$ obtained by the reactor neutrino experiments (see table 1.2) the best fit results from T2K are by a factor of about 1.5 (1.8) higher. This tension may imply $\delta \neq 0$ and/or $\sin^2 \theta_{23} \neq 0.5$ to obtain compatibility between the results from reactor and accelerator experiments [20].

The MINOS experiment in the USA consists of two detectors: a near detector at a baseline of $1.04\,\text{km}$ and a far detector at a baseline of $735\,\text{km}$ to the beam. A neutrino beam of ν_μ or $\bar{\nu}_\mu$ with a peak energy of $3\,\text{GeV}$ is produced at the FNAL[4]. Results from the $\nu_\mu \to \nu_e$ appearance disfavor $\theta_{13} = 0$ at a $89\,\%$ CL [47]. Recent results from both $\nu_\mu \to \nu_e$ and $\bar{\nu}_\mu \to \bar{\nu}_e$ appearance are compatible with the results from the reactor neutrino experiments and are $\delta = 0$ and $\theta_{23} < \pi/4$, $0.01\,(0.03) < 2\sin^2\theta_{23}\sin^2 2\theta_{13} < 0.12\,(0.18)$ $(90\,\%$ CL), assuming NH (IH) [48].

---

[3] Japan Proton Accelerator Research Complex
[4] Fermi National Accelerator Laboratory

1.4. Status on Mass Hierarchy and CP-Violation

The results on θ_{13} from reactor neutrino experiments show a rather high value for θ_{13} with relatively high precision (see table 1.2). This precision will be further improved with results from Double Chooz for both far and near detector running in parallel. The gained knowledge on θ_{13} and its high value now opens the possibility to search for the mass hierarchy (MH), i.e. the sign of Δm_{31}^2, and the CP-violating phase δ.

Currently two different ways to determine the MH are feasible [49]. The first approach explores the small difference between Δm_{31}^2 and Δm_{32}^2 in the three-flavor framework, utilizing neutrinos from nuclear power plants (see section 1.4.1). The second way to measure the MH takes advantage of matter enhanced oscillation of neutrinos traveling through earth matter (see section 1.1.3). This approach can either be realized in long baseline accelerator neutrino experiments (see section 1.4.2) or in experiments detecting atmospheric neutrinos (see section 1.4.3).

1.4.1. Mass Hierarchy from Reactor Experiments

The complete formula for the survival probability for electron antineutrinos $\bar{\nu}_e$ from nuclear reactors was already given in equation (1.11) and shown graphically in figure 1.1 for $\bar{\nu}_e$ with an energy of 3 MeV. The optimal place for a reactor experiment with the aim to determine the MH is the first oscillation minimum due to Δm_{21}^2 in a distance of ~ 50 km to the neutrino source, where the terms due to Δm_{21}^2 are suppressed in equation (1.11) [36]. In consequence, the contributions due to Δm_{31}^2 and Δm_{32}^2 are relatively enhanced.

Reactor experiments are typically scintillator based and the reactor-$\bar{\nu}_e$ are detected by the inverse β-decay (see section 2.1.2), which provides a direct measurement of the energy of the incident neutrino. A Fourier analysis of the resulting energy spectrum should feature three peaks at frequencies corresponding to Δm_{21}^2, Δm_{31}^2 and Δm_{32}^2. As the size of Δm_{21}^2 is about 3 % the size of Δm_{31}^2 and Δm_{32}^2, the corresponding peak in the Fourier spectrum is expected to be at much lower frequencies than those caused by Δm_{31}^2 and Δm_{32}^2. According to equation (1.11), the amplitude of the oscillation due to Δm_{32}^2 is $\sin^2\theta_{12} \sim 0.3$, while that due to Δm_{31}^2 is larger with $\cos^2\theta_{12} \sim 0.7$ (see table 1.1). In consequence, the power of the peak due to Δm_{31}^2 in the Fourier analysis is expected to be larger than that due to Δm_{32}^2 [36]. Therefore, the position of the larger peak relative to the smaller peak determines the MH case, which is shown schematically in figure 1.2. In case of normal hierarchy, which corresponds to $\Delta m_{31}^2 > \Delta m_{32}^2$, the larger peak is expected to be at a higher frequency than the smaller peak, while in case of inverted hierarchy, i.e. $\Delta m_{31}^2 < \Delta m_{32}^2$, the larger peak is expected at lower frequency than the smaller peak [36]. Due to the small difference between Δm_{31}^2 and Δm_{32}^2, the difference in the corresponding oscillation frequencies is also very small. To resolve this difference the energy resolution of the detector used in such an experiment needs to be very high, exceeding resolutions reached in all previous scintillator detectors.

Currently, there are two planned experiments aiming for the determination of the mass
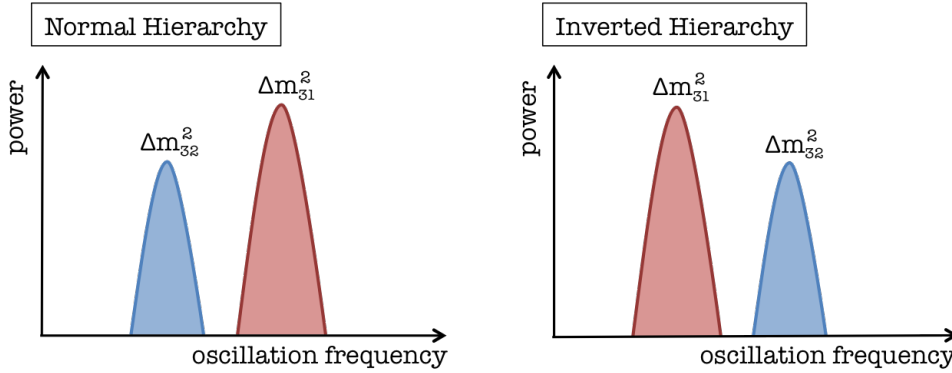
Figure 1.2.: Schematic representation of the frequency spectra obtained in a Fourier analysis of the energy spectrum measured by a reactor neutrino experiment at a baseline of $\sim 50\,\text{km}$ for the cases of normal and inverted hierarchy, reproduced according to [36]. The horizontal axis corresponds to the oscillation frequency, while the vertical axis shows the power of the Fourier analysis. The mass hierarchy case can be determined by the position of the larger peak due to Δm_{31}^2 relative to the smaller one due to Δm_{32}^2.

hierarchy using reactor neutrinos. Both, the JUNO experiment in China [19], which will be introduced in section 2.3, and the RENO-50 experiment in Korea [50] propose scintillator based detectors with a mass in the order of $20\,\text{kt}$.

1.4.2. Mass Hierarchy from Long Baseline Experiments

The mass hierarchy can also be measured by long baseline accelerator neutrino experiments, similar to those described in section 1.3.2, but featuring longer baselines beyond $1000\,\text{km}$ [49]. The most important channel with regard to the mass hierarchy determination is the appearance of electron (anti)neutrinos in a beam, which was originally produces primarily in the muon flavor. As the beam traverses the earth mantle on the way to the detector, matter effects need to be considered in the corresponding oscillation probability $P_{\nu_\mu \to \nu_e}$ ($P_{\bar{\nu}_\mu \to \bar{\nu}_e}$) as given in equation (1.13). In figure 1.3 the oscillation probability $P_{\nu_\mu \to \nu_e}$ is shown for the T2K baseline of $L = 259\,\text{km}$ [46] and the baseline of a proposed beam from CERN to the Pyhäsamli mine in Finland of $L = 2300\,\text{km}$ [51] for both the normal and the inverted mass hierarchy case.

To match the oscillation maximum due to Δm_{31}^2 to the baseline of the respective experiment the beam energy needs to be adjusted (see equation (1.13)). Therefore, the energy scale of the first oscillation maximum in terms of L/E is shifted to higher energies with rising baseline and correspondingly rising beam energy. Furthermore, a longer baseline means a longer path traversed by the neutrinos through the earth mantle. This and the increased neutrino energy result in an increased matter effect, which affects the oscillation probabilities for normal hierarchy (NH) and inverted hierarchy (IH) differently. This is impressively shown by the red (NH) and blue (IH) bands in figure 1.3, which correspond to the oscillation probabilities $P_{\nu_\mu \to \nu_e}$ for all possible values for the unknown CP-violating
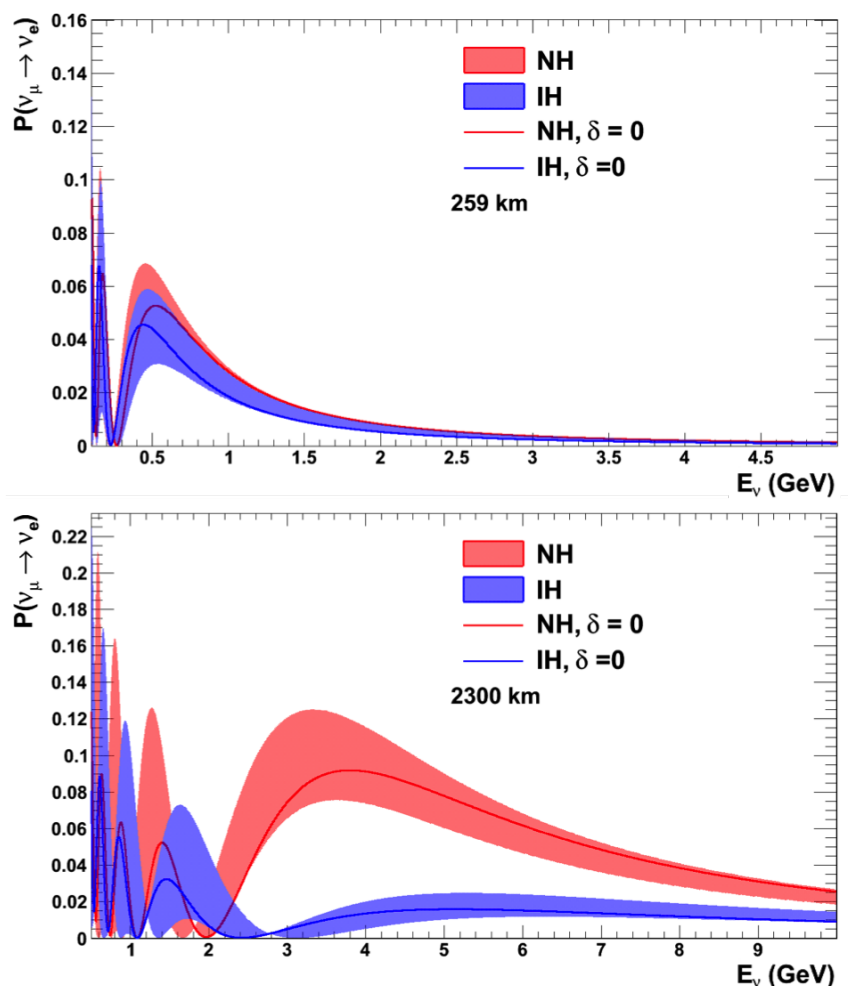
Figure 1.3.: The appearance probability for the $\nu_\mu \rightarrow \nu_e$ channel as a function of the neutrino energy in case of normal (red) and inverted hierarchy (blue). The upper panel refers to the T2K baseline of $259\,\mathrm{km}$ [46], while the lower corresponds to a baseline of $2300\,\mathrm{km}$ for a proposed beam from CERN to Pyhäsalmi [51]. The solid curves correspond to the oscillation probabilities in case of $\delta = 0$, while the shaded areas cover the oscillation probabilities for all possible values for the CP-violating phase $0 \leq \delta \leq 2\pi$. The different energy scales are caused by different beam energies to obtain the oscillation maximum due to Δm_{31}^2 at the respective used baseline (see equation (1.13)). The data was taken from [52] and generated with the GLoBES library [53] based on the earth density profile according to the Preliminary Reference Earth Model [54].

phase $0 \leq \delta \leq 2\pi$. The difference in $P_{\nu_\mu \to \nu_e}$ for NH and IH is most prominent in case of the longer baseline from CERN to Pyhäsalmi, where both bands are well separated above $\sim 2.5 \, \text{GeV}$. In case of the T2K baseline both bands overlap almost completely. Hence, a determination of the MH, independent of the actual value of δ, is only possible for longer baselines. In case of an antineutrino beam, the behavior of the corresponding oscillation probability $P_{\bar{\nu}_\mu \to \bar{\nu}_e}$ is reversed for NH and IH and the respective bands in figure 1.3 are interchanged [49].

Besides the determination of the MH, long baseline experiments are the only currently known possibility for a reliable direct measurement of the CP-violating phase δ[49]. While the difference in $P_{\nu_\mu \to \nu_e}$ for the different MH cases become rather large with rising baseline (almost $10\,\%$ in case of $L = 2300 \, \text{km}$), the difference between extreme values of δ is in the order of few percent. Therefore, a very good energy resolution and particle identification are needed to determine δ.

LBNO[5] in Europe [51] and LBNE[6] in the USA [55] were proposed accelerator experiments with baselines of $2300 \, \text{km}$ (see figure 1.3) and $1300 \, \text{km}$, respectively, aiming for the determination of the MH and the CP-violating phase δ. Although the sensitivity would be better with the longer baseline of LBNO, parts of both collaborations currently combine efforts in a common experiment in the USA, featuring a proposed baseline of $1300 \, \text{km}$: the DUNE/LBNF experiment[7] [56]. The proposed far detector is a liquid argon time projection chamber with a fiducial volume of $> 35 \, \text{kt}$ detecting neutrinos from a beam produced at Fermilab.

1.4.3. Mass Hierarchy from Atmospheric Neutrinos

Atmospheric neutrinos are produced by decays of pions, muons and kaons induced by interactions of cosmic rays in the upper atmosphere [49]. The primary flux of atmospheric neutrinos contains ν_e, $\bar{\nu}_e$, ν_μ and $\bar{\nu}_\mu$ and features a ratio of muon neutrinos to electron neutrinos of about two-to-one below $\sim 2 \, \text{GeV}$, which rises towards higher energies. The ratio between the produced neutrinos and antineutrinos is also slightly larger than one, which is caused by differing production yields for positively and negatively charged pions [49].

Similarly to long baseline experiments, the matter effect can be used to determine the MH with atmospheric neutrinos. As atmospheric neutrinos are produced in the earth's atmosphere, they travel all possible distances through the earth's interior on there way to the detector. Therefore, the matter density profile of the earth has to be taken into account in such experiments. Essentially, the following oscillation behaviors are expected in the different oscillation channels in case of normal hierarchy (NH) [49]:

- Muon (anti)neutrino disappearance $\nu_\mu \to \nu_\mu$ ($\bar{\nu}_\mu \to \bar{\nu}_\mu$): A resonant oscillation ap-

---

[5] Long Baseline Neutrino Oscillations
[6] Long Baseline Neutrino Experiment
[7] Deep Underground Neutrino Experiment at the Long Baseline Neutrino Facility

pears around $5\,\text{GeV}$ for neutrinos traveling the maximal distance through the earth's interior, which is not present for antineutrinos.

- Muon to electron (anti)neutrino appearance $\nu_\mu \to \nu_e$ ($\bar{\nu}_\mu \to \bar{\nu}_e$): The oscillation amplitude for neutrinos is much larger than for antineutrinos.

- Electron (anti)neutrino disappearance $\nu_e \to \nu_e$ ($\bar{\nu}_e \to \bar{\nu}_e$): The oscillation amplitude for neutrinos is much larger than for antineutrinos.

- Electron to muon (anti)neutrino appearance $\nu_e \to \nu_\mu$ ($\bar{\nu}_e \to \bar{\nu}_\mu$): The oscillation amplitude for neutrinos is much larger than for antineutrinos.

In case of inverted mass hierarchy, the oscillation behavior of neutrinos and antineutrinos has to be exchanged [49]. All features described above appear with a dependency on the energy and the zenith angle. Hence, the main requirement for a detector, aiming for the determination of the MH using atmospheric neutrinos, is a good tracking performance for charged leptons, which are produced by CC-interactions of the neutrinos in the detector. Thereby, the direction of the incident neutrino and the corresponding distance, the neutrino traveled through the earth's interior, can be reconstructed. Obviously, a detector, which could discriminate between interactions due to neutrinos and antineutrinos, would be a powerful tool to determine the MH. Usually, atmospheric neutrino detectors are only sensitive to the neutrino flavor. In consequence, it is impossible to disentangle the $\nu_\mu \to \nu_\mu$ ($\bar{\nu}_\mu \to \bar{\nu}_\mu$) oscillation channel from the $\nu_e \to \nu_\mu$ ($\bar{\nu}_e \to \bar{\nu}_\mu$) channel and the $\nu_e \to \nu_e$ ($\bar{\nu}_e \to \bar{\nu}_e$) channel from the $\nu_\mu \to \nu_e$ ($\bar{\nu}_\mu \to \bar{\nu}_e$) channel. Due to the matter effect, the higher neutrino flux compared to antineutrinos and the higher detection cross section for neutrinos, a sizable sensitivity for the MH can be achieved. A discrimination between muon neutrinos and antineutrinos could be achieved by magnetizing the detector, which is very challenging, as atmospheric neutrino detectors are usually rather large.

Proposed high energy atmospheric neutrino experiments aiming for the determination of the MH are the PINGU[8] experiment, which is a proposed upgrade to the already existing IceCupe experiment at the South Pole [57], and the ORCA[9] option for the KM3NeT[10] project, which uses a similar detection technique as IceCube, but is placed in the deep Mediterranean sea on the northern hemisphere [58, 59]. Both PINGU and ORCA are large scale Cherenkov telescopes with an energy threshold of a few GeV. Furthermore, the India-based Neutrino Observatory (INO) aims for the MH determination with a proposed $52\,\text{kt}$ magnetized iron calorimeter [60], while the Hyper-Kamiokande water Cherenkov experiment aims at this goal with a detector mass of $0.99\,\text{Mt}$ [61].

---

[8] Precision IceCube Next Generation Upgrade
[9] Oscillation Research with Cosmics in the Abyss
[10] A multi-km^3 Neutrino Telescope

1.5. Neutrinos from Supernovae

Supernova (SN) explosions, marking the end of massive stars, are among of the most energetic events in the universe. SNe appear in two main types [62]: core collapse and thermonuclear SNe. The latter can in principle be understood as fusion bombs, most likely appearing for binary systems with white dwarfs. While neutrino emission plays an insignificant role in thermonuclear SNe, the energy carried away by neutrinos in a core collapse SN accounts for about $99\,\%$ of the total energy released in such an event [62]. The current understanding of the explosion mechanism (section 1.5.1) and the neutrino signal (section 1.5.2) of core collapse are presented briefly in the following. Furthermore, the neutrino signals, which could be detected from the SN1987A by the IMB, Kamiokande and BST experiments, are presented in section 1.5.3. Finally, the so-called diffuse supernova neutrino background (DSNB), which is the cumulative neutrino flux created from all core collapse SNe throughout the universe, is introduced briefly in section 1.5.4.

1.5.1. Standard Core Collapse Supernova Model

At the end of their life, massive stars with $M > 8\,M_\odot$[11] feature a core mainly consisting of iron, surrounded by an onion shell like structure built by the ashes of earlier burning phases [63]. As the binding energy per nucleon is maximal for iron, no fusion processes occur in the core, while it is kept stable by an equilibrium between gravitation and the pressure of the degenerate relativistic electron gas. The mass of the iron core increases successively by shell burning until the Chandrasekhar mass ($\sim 1.4\,M_\odot$) is reached. At this time the densities in the core are in the order of $\sim 10^{10}\,\mathrm{g\,cm^{-3}}$ and temperatures of $\sim 10^{10}\,\mathrm{K}$ are reached [64]. In this environment electron capture on iron takes place via

$$e^- + {}^{56}\mathrm{Fe} \rightarrow {}^{56}\mathrm{Ni} + \nu_e \; . \tag{1.14}$$

Thereby, the pressure due to the degenerate electron gas is reduced and energy is emitted in form of neutrinos. In consequence, the core starts to contract, which is further accelerated by endothermic photodissociation of iron nuclei. The energy released by the core contraction is thereby exhausted and the pressure support is reduced even further [64].

As the core collapses, densities in the order of $10^{11} - 10^{12}\,\mathrm{g\,cm^{-3}}$ are reached. At this stage, the mean free paths of the ν_e become smaller than the core radius, caused by coherent scattering off heavy nuclei. In consequence, the neutrinos are trapped in the core, which is why this stage is commonly called *neutrino trapping* [62], and neutrino spheres can be defined analogously to the photosphere in the sun. Outside these flavor-dependent spheres neutrinos can move freely, as the density decreases with the radius.

Despite the neutrino trapping, the homologous and subsonic contraction of the core continues until reaching nuclear densities of $\sim 10^{14}\,\mathrm{g\,cm^{-3}}$. Repulsive nuclear forces stop the collapse of the inner core, causing the supersonically infall to rebound from this solid wall

---

[11] $M_\odot$ is the solar mass of $\sim 2 \cdot 10^{30}\,\mathrm{kg}$.

(commonly called the *bounce*) [63]. Consequently, a shock wave is formed, which moves outwards, dissociating nuclei of the core material into free nucleons. A huge amount of electron neutrinos is generated in the regions behind the shock by [64]

$$e^- + p \to n + \nu_e . \tag{1.15}$$

Initially these neutrinos are trapped. When the shock crosses the neutrino sphere, all produced ν_e can escape within about $20\,\text{ms}$, which is often referred to as the *prompt ν_e burst* or *neutronization burst*.

Almost simultaneously to the ν_e burst, the production of other neutrino species begins to start. In the post-bounce region thermally created positrons produce electron antineutrinos $\bar{\nu}_e$ via [64]:

$$e^+ + n \to p + \bar{\nu}_e . \tag{1.16}$$

Muon and tau neutrinos are produced in this stage of the SN by electron-positron annihilation

$$e^+ + e^- \to \nu_{\mu,\tau} + \bar{\nu}_{\mu,\tau} , \tag{1.17}$$

nucleon-nucleon bremsstrahlung

$$N + N' \to N + N' + \nu_{\mu,\tau} + \bar{\nu}_{\mu,\tau} \tag{1.18}$$

and neutrino-antineutrino annihilation

$$\nu_e + \bar{\nu}_e \to \nu_{\mu,\tau} + \bar{\nu}_{\mu,\tau}. \tag{1.19}$$

Each of these processes also contributes to the production of ν_e and $\bar{\nu}_e$, but the dominant production channels for ν_e and $\bar{\nu}_e$ are the reactions (1.15) and (1.16), respectively. The radii of the neutrino spheres for the different neutrino species vary due to the different possible interactions. While the ν_e and $\bar{\nu}_e$ can interact predominantly via the CC reactions $\nu_e + n \to p + e^-$ and $\bar{\nu}_e + p \to n + e^+$, for muon and tau (anti)neutrinos (often summarized by ν_x) only neutral current reactions are possible, of which coherent scattering off heavy nuclei is the dominant interaction channel. Due to the limited interaction possibilities the ν_x decouple from the matter at smaller radii. Hence, they have higher energies than ν_e and $\bar{\nu}_e$. Due to the higher abundance of neutrons the ν_e decouple at a larger radius than the $\bar{\nu}_e$. Inside the respective sphere the neutrinos are thermalized. As the temperature decreases with increasing radius, the mean energies $\langle E \rangle$ of the different neutrino species are dependent on the radii of the respective neutrino spheres. This results in a typical energy hierarchy of the emitted neutrinos: $\langle E_{\nu_e} \rangle < \langle E_{\bar{\nu}_e} \rangle < \langle E_{\nu_x} \rangle$.

The shock propagation through the outer iron core is efficiently cooled by photodissociation, which consumes $\sim 8.8\,\text{MeV}$ per nucleon, and neutrino emission. Therefore, it finally stalls at a radius of $\sim 100 - 200\,\text{km}$ [63]. While matter from the surrounding core keeps on falling into the newly-born proto-neutron star with a radius of $\sim 50 - 80\,\text{km}$, the released gravitational energy is largely cooled by emission of high energy neutrinos, produced by the processes shown above. According to the current understanding of core collapse SNe these neutrinos reheat the regions behind the stalled shock by the reverse reactions of (1.15)
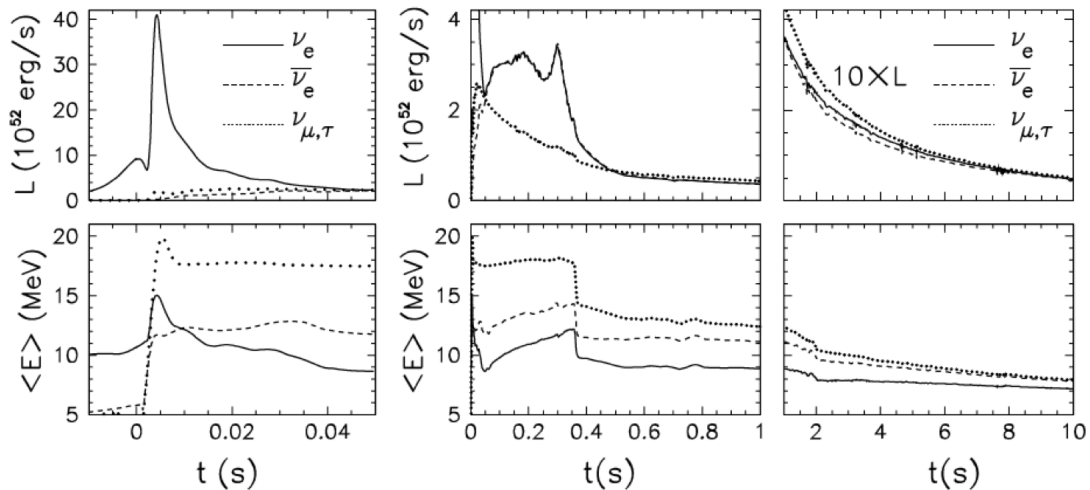
Figure 1.4.: Neutrino signal from a core collapse SN of a progenitor star with a mass of $10.8\,M_\odot$ according to a spherically symmetric simulation of the Basel group [65]. The upper panels show the luminosities for the different neutrino species as a function of time, while the lower panels show the evolution of the mean neutrino energies for each species. The left panels correspond the signal from the prompt neutrino burst, while the central panels show that from the accretion phase. In the right panels the cooling phase is depicted. The figure was taken from [18].

and (1.16). After several hundred ms the shock wave finally takes off and expels the surrounding shell materials, what causes the actual visible SN [62].

In the following the neutron star is cooled by diffuse neutrino emission on a time scale of several seconds and settles at a radius of about $12\,\mathrm{km}$ [62]. Matter, which is mainly composed of isotopes produced by neutrino interactions, is blown off. In this *hot bubble* region nucleosynthesis takes place and heavy neutron rich elements may be produced via the r-process.

1.5.2. Neutrino Signal from SNe

The neutrino signal of a core collapse SN can be divided into three main phases, as shown in figure 1.4 for a SN of a $10.8\,M_\odot$ star from a simulation of the Basel group [65]:

1. **Prompt ν_e burst:** This first phase of neutrino emission is caused by the electron neutrinos produced behind the shock front and released after the shock reaches the neutrino sphere. This phase of the emission marks the most luminous neutrino emission from the SN and lasts up to $\sim 20\,\mathrm{ms}$ (see left panel figure 1.4). Simultaneously, the production of $\bar{\nu}_e$, $\nu_{\mu,\tau}$ and $\bar{\nu}_{\mu,\tau}$ begins.

2. **Accretion phase:** After the shock stalls at a radius of $\sim 100-200\,\mathrm{km}$, the neutrino emission is driven by the released gravitational energy of infalling matter [62]. The luminosities of the ν_e and $\bar{\nu}_e$ emission are similar, while the flux of ν_e is larger (see

figure 1.4). This is caused by the larger radius of the neutrino sphere for ν_e than for $\bar{\nu}_e$, which is caused by the higher abundance of neutrons for the charge current reverse reactions of (1.15). The $\nu_{\mu,\tau}$ and $\bar{\nu}_{\mu,\tau}$ (often summarized to ν_x) are emitted closer to the core, featuring smaller fluxes, but higher energies. Typically, in this stage the hierarchy in the luminosities is $L_{\nu_e} \sim L_{\bar{\nu}_e} > L_{\nu_x}$, while the hierarchy in the mean energy is $\langle E_{\nu_e} \rangle < \langle E_{\bar{\nu}_e} \rangle < \langle E_{\nu_x} \rangle$, with $\langle E_{\bar{\nu}_e} \rangle \sim 12 - 15\,\mathrm{MeV}$ (see central panel figure 1.4) [62]. The accretion phase typically lasts several hundred ms.

3. **Cooling phase:** After the shock wave went off and accretion stops, the newborn neutron star settles and cools by neutrino emission. The neutrinos are produced deep inside and emerge on a diffusion time scale of several seconds [62]. The neutrino species are produced with comparable luminosities. Due to the decreasing abundance of protons the hierarchy in the mean energy changes to $\langle E_{\nu_e} \rangle < \langle E_{\bar{\nu}_e} \rangle \sim \langle E_{\nu_x} \rangle$ (see right panel figure 1.4).

In total an energy of $\sim 2 - 4 \cdot 10^{53}\,\mathrm{erg}$[12] is emitted in the form of neutrinos, depending on the mass of the progenitor star [62]. The energy is distributed approximately in equal amounts among the different neutrino flavors.

1.5.3. Neutrinos from the SN 1987A

The SN 1987A is one of the most important events happening in neutrino astrophysics up to now [62]. It appeared on 23rd of February in 1987 in the Large Magellanic Cloud, which is a satellite galaxy of the Milky Way, at a distance of about $50\,\mathrm{kpc}$ ($\sim 160\,000\,\mathrm{ly}$). The SN 1987A was the first SN associated with observation of the progenitor star and the closest SN visible in modern times.

Three neutrino detectors were online, when the SN 1987A happened, and could detect a total of 24 $\bar{\nu}_e$ events via the secondary positron emitted in the inverse beta decay $\bar{\nu}_e + p \to n + e^+$ (see also section 2.1.2) [66]. The two water Cherenkov detectors of the Kamiokande experiment in Japan [67, 68] and of the Irvine-Michigan-Brookhaven (IMB) experiment in the USA [69, 70] measured 11 events in a time span of $12.4\,\mathrm{s}$ and 8 $\bar{\nu}_e$ events in $5.6\,\mathrm{s}$, respectively. Additionally, the Baksan Scintillation Telescope (BST) [71, 72] in the Caucasus mountains detected 5 events appearing within $14.3\,\mathrm{s}$. According to the expectations, the signals in all three experiments were detected a few hours before the SN could be observed with optical telescopes [62]. Several analyses of the shape in time and energy of the detected events could confirm the general understanding of core collapse SNe [62]. Nevertheless, high statistics measurements, ideally by several different detectors, are needed to test the core collapse models quantitatively and to learn more about the different processes contributing to the explosion of a core collapse SN. To detect neutrinos from a galactic SN in the lifetime of a neutrino detector requires some luck, as several measurements indicate an average rate of core collapse SNe in the Milky Way below 3 per century [62].

---

[12] $1\,\mathrm{J} = 10^7\,\mathrm{erg}$

1.5.4. Diffuse Supernova Neutrino Background

The Diffuse Supernova Neutrino Background (DSNB) is the cumulative neutrino flux emitted by all core collapse SNe in the causally reachable universe [73]. The energy spectrum of the DSNB results from the quasi-thermal neutrino spectra emitted in core collapse SNe convoluted with the redshift dependent supernova rate. The energy density in neutrinos from cosmic core collapse SNe is of the order of $\sim 0.01\,\mathrm{eV\,cm^{-3}}$ and comparable to the energy density of photons from stars throughout the universe. Therefore, the DSNB offers a unique probe to stellar birth and death, which is unobscured and unaffected by other astrophysical sources [62].

Unfortunately, the DSNB could not be detected, yet. The best upper limit on the flux was set by the Super-Kamiokande experiment of $2.8 - 3.0\,\bar{\nu}_\mathrm{e}\,\mathrm{cm^{-2}\,s^{-1}}$ (90 % C.L.) for $E_{\bar{\nu}_e} > 17.3\,\mathrm{MeV}$, depending on different DSNB models [74]. The predictions of different models are between one order of magnitude and a factor of two below the obtained upper limit.

Even if neutrinos from a galactic SN are observed, the detection of the DSNB would offer unique information on the average neutrino spectra from SNe and, hence, would provide a test for different core collapse SN models. The proposed LENA project (see section 2.2) could possibly measure the DSNB flux, predicted by current models, after 10 years of measurement (see section 2.2.4). Also the JUNO project (see section 2.3) will be able to detect the DSNB with comparable sensitivity.

2. Neutrino Experiments

In the scope of this thesis the organic liquid scintillators used in the currently running Double Chooz experiment and favored for the proposed LENA and the planned JUNO experiments were studied regarding their response to incident neutrons. In this chapter all three experiments are introduced briefly. Furthermore, the scintillator used in the Borexino experiment was investigated due to a request from the Borexino collaboration. Please refer to [11, 14, 75] for a detailed description and results of the Borexino experiment.

2.1. The Double Chooz Experiment

The Double Chooz experiment is located at the EDF[1] nuclear power plant at Chooz in the French Ardennes [15, 33, 42]. The power plant features two reactors with a nominal thermal power of $4.25\,\mathrm{GW}$. The experiment consists of two identical liquid scintillator detectors optimized for the detection of electron antineutrinos, which are emitted in the β^--decays of the fission products of $^{235}\mathrm{U}$, $^{239}\mathrm{Pu}$, $^{241}\mathrm{Pu}$ and $^{238}\mathrm{U}$. A far detector (FD) is placed at an average distance of $1.05\,\mathrm{km}$ to the two reactor cores, which is close to the oscillation minimum corresponding to Δm_{31}^2 (see equation (1.11) and figure 1.1). A second near detector (ND) is placed closer to the two reactors in a mean distance of $400\,\mathrm{m}$ to measure the mostly unoscillated reactor neutrino spectrum. In Figure 2.1 the locations of both the ND and the FD relative to the two reactors are shown. Both detectors are placed underground to reduce the background caused by high energetic muons produced by cosmic rays in the atmosphere. The FD was constructed in a depth of $300\,\mathrm{meter}$ water equivalent (m.w.e.) rock overburden, in a cavern already used by the preceding CHOOZ experiment [76]. For the ND a new laboratory in a depth of $120\,\mathrm{m.w.e.}$ was built.

The two detector concept offers the possibility of a relative measurement of the rates and the energy spectra of the reactor neutrinos. Thus, systematic uncertainties due to the limited knowledge on the reactor neutrino spectrum and the cross section of the detection reaction can be eliminated. The Double Chooz FD is taking data since April 2011. As the ND was completed just recently in the end of 2014, all results published by the collaboration until now are based on a comparison of the $\bar{\nu}_e$ rate and energy spectrum measured by the FD with a prediction of the rate an energy spectrum in case of no oscillation, i.e. $\sin^2 2\theta_{13} = 0$.

---

[1] Électricité de France
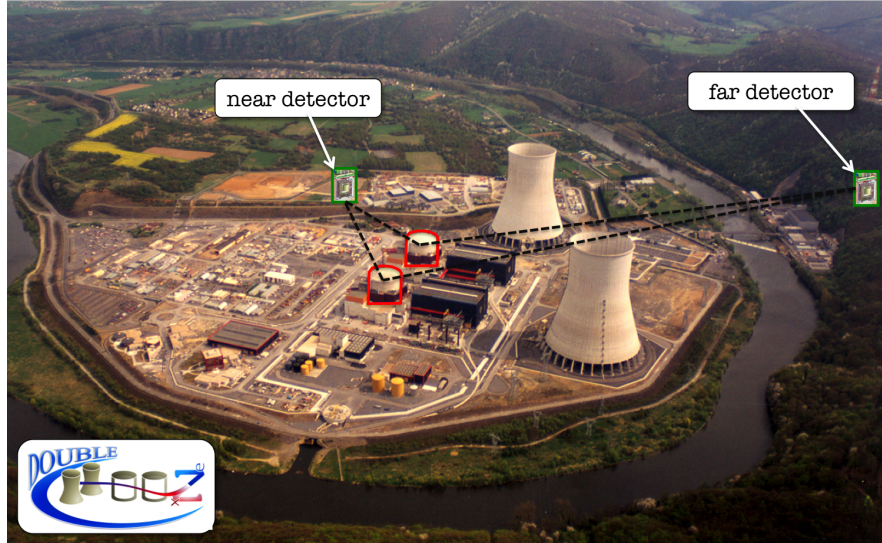
Figure 2.1.: The Double Chooz Experiment at the Chooz nuclear power plant according to [77]. Neutrinos from two reactors (red) are detected at a far and a near detector.

2.1.1. Detector Setup

The two Double Chooz detectors were designed to detect electron antineutrinos with high efficiency, using the inverse beta decay (IBD) reaction (see section 2.1.2). Each detector consists of four interlaced cylindrical volumes, which are aligned to their rotation symmetry axis (see figure 2.2). These subvolumes are filled with different organic liquids suitable to the purpose of each detector volume. The three innermost volumes comprise the *inner detector* (ID), while the outermost volume represents the so-called *inner veto* (IV), which is optically separated from the ID. All volumes can be accessed via chimneys at the top of the detector. On top and around the side of each detector a 15 cm thick steel shielding is placed to protect the ID and IV from external γ-rays. Furthermore, an additional muon veto system, the *outer veto* (OV), is placed on top of the main detector. In the following each of the detector subsystems will be introduced in more detail:

- **The Neutrino Target:** The innermost volume of each Double Chooz detector is the neutrino target, which consists of $10.3\,\mathrm{m}^3$ of Gd-loaded liquid scintillator contained in an 8 mm thin transparent acrylic vessel [33]. Gadolinium, added with a concentration of 1 g/l, features a high cross section for neutron capture [78] and is, therefore, used to increase the efficiency in the detection of the neutrons produced in the inverse beta decay (see section 2.1.2). The detailed composition of the scintillator is given in table 3.4 in chapter 3.

- **The Gamma Catcher:** The neutrino target is surrounded by a 55 cm layer of $22.5\,\mathrm{m}^3$ Gd-free liquid scintillator contained in a 12 mm thin acrylic vessel [33]. The main purpose of this volume is to increase the efficiency of detecting the full energy of γ-rays escaping the neutrino target. Therefore, this part of the detectors is called gamma catcher. The light yield of the gamma catcher scintillator (for detailed com-
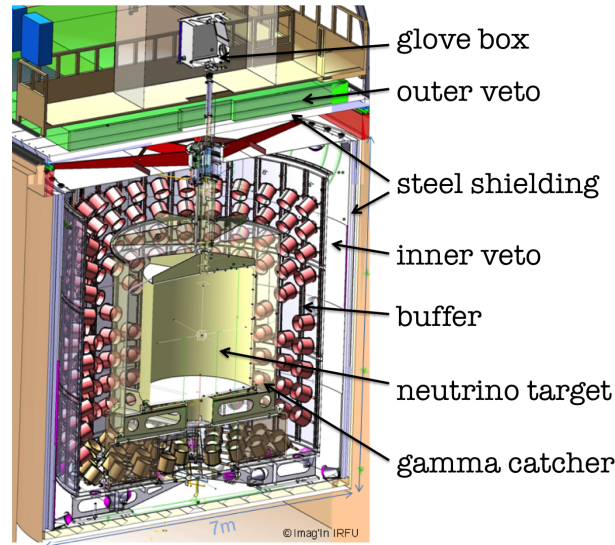
Figure 2.2.: Layout of the Double Chooz detectors according to [33, 79].

position see table 3.4) was matched to that used for the neutrino target to guarantee a homogeneous energy response in the inner detector.

- **The Buffer:** The outermost volume of the inner detector is the so-called buffer, consisting of $\sim 100\,\mathrm{m}^3$ of transparent non-scintillating organic liquid[2] contained in a 3 mm thin stainless steel vessel [33]. This insensitive volume has a thickness of 105 cm and acts as a passive shielding for the neutrino target and for the gamma catcher from radioactivity in the surrounding rock and the outer parts of the detector. 390 10 inch photomultiplier tubes[3] (PMTs), which are mounted on the inner wall of the buffer vessel, detect the scintillation light produced by particle interactions in the target or gamma catcher scintillator. The buffer is one of the major improvements compared to the previous CHOOZ experiment.

- **The Inner Veto:** The inner detector is surrounded by 50 cm of liquid scintillator (see table 3.4) with a total volume of $90\,\mathrm{m}^3$, contained in a stainless steel tank [33]. Being optically separated from the ID, this part of the detector acts as a active veto against cosmic muons, muon-induced spallation products like fast neutrons and natural radioactivity from the rock. The inner veto is instrumented with 78 8 inch PMTs[4], which are distributed in such way that the efficiency in the detection of muons is maximized [80]. In case of the far detector, the inner wall of the inner veto tank is covered with reflective white paint, while reflective VM2000 foil was attached to the outer wall of the buffer tank to increase the collection efficiency for the scintillation photons. Instead of reflective white paint, the ND IV tank wall is covered with VM2000 foil.

---

[2] The buffer liquid is a mixture of n-praffine and Ondina 917 (Dinol) in case of the far (near) detector.

[3] Hamamatsu R7081

[4] The used Hamamatsu R1408 PMTs have been used in the IMB and Super-Kamiokande experiments before and have seen the Cherenkov light due to neutrinos from the supernova 1987A [33].

- **The Outer Veto:** On top of the main detector an active muon veto, which is called
  the outer veto (OV), was built. The OV covers an area of $13\,\text{m} \times 7\,\text{m}$ and consists
  of two orthogonal layers of plastic scintillator strips, which are read out by PMTs
  [33]. The region around the chimneys of the inner detector volumes is left free by an
  area of $110\,\text{cm} \times 30\,\text{cm}$. Therefore, another two layers of plastic scintillator strips are
  mounted $3.9\,\text{m}$ above the main OV, covering the chimney region.

To prevent buoyancy forces between the four volumes of the main detector, the densities of
the neutrino target, gamma catcher and inner veto scintillators and the buffer liquid were
matched to $0.804 \pm 0.001\,\text{g/cm}^3$ at $15\,^\circ\text{C}$. Furthermore, all detector liquids needed to fulfill
high requirements regarding optical transparency, chemical compatibility and stability and
radiopurity. Additionally, the stability of the Gd-loaded target scintillator, which was the
limiting issue for the CHOOZ experiment [76], had to be ensured.

The signals from all ID and IV PMTs are digitized using 8 bit flash-ADC[5] electronics with
a sampling frequency of $500\,\text{MHz}$ [33]. When a trigger occurs, all PMT signals are read out
simultaneously for a $256\,\text{ns}$ time window. The data acquisition is triggered either when the
deposited energy in the ID exceeds a threshold of $350\,\text{keV}$ or when an energy of $\sim 10\,\text{MeV}$
is exceeded in the IV.

The Double Chooz detectors are calibrated by various calibration systems [33, 42]. The
time and gain responses of the ID and IV PMTs and the readout electronics are calibrated
regularly by multi-wavelength LED-fiber systems. The relative time response of ID PMTs
was additionally calibrated with high precision using a laser system attached to a diffuser
ball, which was deployed inside the neutrino target. The energy scale is calibrated using
various radioactive sources (^{60}Co, ^{68}Ge, ^{137}Cs and ^{252}Cf), which are deployed into the
neutrino target along the symmetry axis and into the gamma catcher volume using a guide
tube. Additionally, captures of muon-induced neutrons on H, Gd and C and Bi-Po decays
from radio-impurities are used for energy calibration and the extraction of time stability
and position dependence corrections.

2.1.2. Detection of Electron Antineutrinos

The electron antineutrinos from the reactors are detected by the so-called inverse beta
decay (IBD) reaction [81]:
$$\bar{\nu}_e + p \rightarrow e^+ + n \tag{2.1}$$
The energy threshold of this charged current reaction is $E_{\text{thr}} \approx 1.8\,\text{MeV}$. The generated
positron rapidly deposits its kinetic energy E_{e^+} in the scintillator, which leads to a prompt
scintillation signal. Annihilation of the positron and an ambient electron results in the
production of two $511\,\text{keV}$ γ-rays, which deposit additional $1.022\,\text{MeV}$ in the liquid scintil-
lator. Therefore, the energy $E_{\bar{\nu}_e}$ of the incident $\bar{\nu}_e$ can be reconstructed from the deposited
energy made visible by the scintillation light (visible energy) E_{vis} [33]:
$$E_{\text{vis}} \approx E_{\bar{\nu}_e} - (m_n + m_e - m_p) + 2\,m_e \approx E_{\bar{\nu}_e} - 0.78\,\text{MeV} \tag{2.2}$$

---

[5] Analog-to-Digital Converter
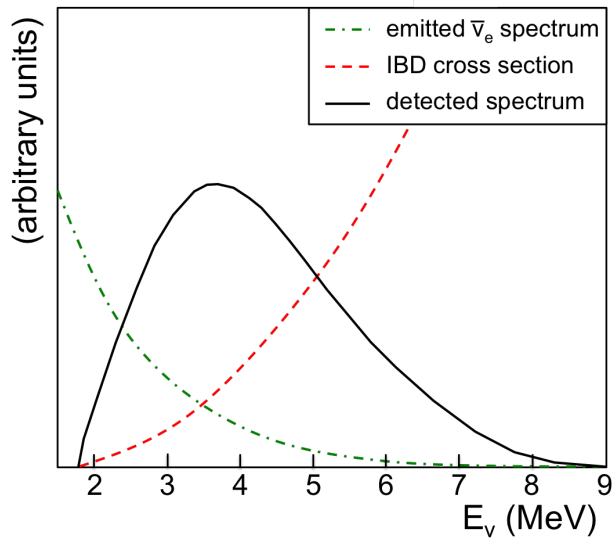
Figure 2.3.: Schematic plot of the unoscillated reactor neutrino spectrum (green), the cross section for the inverse beta decay (red) and the product of both showing the detected energy spectrum in an experiment (black). The horizontal axis represents the neutrino energy (E_ν), while the vertical axis is in arbitrary units. The plot was produced based on [82].

with m_n, m_p and m_e being the masses of neutron, proton and electron. Furthermore, the recoil energy of the neutron produced in the IBD reaction (2.1) can be neglected. The expected visible energy spectrum of electron antineutrinos from a reactor basically results from the product of the neutrino spectrum emitted by a reactor and the energy dependent cross section for the IBD. This is shown schematically in figure 2.3.

The neutron produced in the IBD reaction (2.1) undergoes thermalization followed by a capture on gadolinium after a mean time of $31.1\,\mu$s [42]. Gadolinium has a high cross section for capture of thermal neutrons in the order of several 10^5 barn [78]. The capture is followed by the emission of several γ-rays with a total energy of about $8\,$MeV:

$$^{\mathrm{A}}\mathrm{Gd} + n \rightarrow {}^{\mathrm{A}+1}\mathrm{Gd}^* \rightarrow {}^{\mathrm{A}+1}\mathrm{Gd} + \gamma s \quad (\textstyle\sum_i E_{\gamma,i} \approx 8\,\mathrm{MeV}) \qquad (2.3)$$
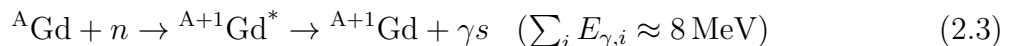
The energy deposition of the γ-rays, following the neutron capture, causes a delayed scintillation signal after a mean time of $31.1\,\mu$s compared to the prompt signal from the IBD-positron. The prompt energy deposition of the positron, containing information on the $\bar{\nu}_e$ energy, and the delayed energy deposition following the neutron capture on gadolinium form a distinct *delayed coincidence* signature, which significantly reduces the possible background contributions (see section 2.1.3). Furthermore, the high total energy of the delayed signal in succession to the neutron capture on Gd is well above the energy range of natural radioactivity, reducing the contribution of accidental background.

Additionally, there is a probability of $\sim 13\,\%$ that an IBD-neutron is captured by hydrogen in the neutrino target (cross section $\sigma \sim 0.3\,$barn) [83]. In the gamma catcher, where no

gadolinium is admixed to the scintillator, this reaction dominates[6]. The mean capture time for neutrons on hydrogen in the gamma catcher was measured to be about $200\,\mu$s [83]. The neutron capture results in the formation of deuterium and the emission of a $2.2\,$MeV γ-ray [78]. This energy is well within the range of natural radioactivity. Therefore, an analysis of IBD events in the gamma catcher is accompanied by a significantly higher accidental background compared to an analysis of the Gd-capture IBD events in the target.

2.1.3. Backgrounds

The background contributions in Double Chooz are limited to those mimicking the delayed coincidence signature of IBD events and can be classified into two groups: accidental and correlated backgrounds. In the analyses of the Gd-capture IBD events three correlated backgrounds sources are considered: the cosmic muon induced β-n emitting isotopes ^{9}Li and ^{8}He, fast neutrons and muons being stopped and decaying in the inner detector [33, 42]. A possible contribution of correlated background due to an (α, n)-reaction on ^{13}C and the decay of ^{12}B, which is produced by cosmic muons in the scintillator, was found to be negligible [42]. In the analysis of H-capture IBD events another minor background source was found: correlated events due to light produced in the PMT bases[7] [83]. In the following the main backgrounds will be discussed in more detail.

Accidental Background

Random coincidences of a positron-like prompt event and a neutron capture-like delayed event are called accidental background. The prompt-like events are caused by α-, β- and γ-decays in and around the ID. Neutron captures on Gd and H can also cause prompt-like events, as the energy region for the positron events from the IBD reaction ranges up to $\sim 10\,$MeV [42]. As delayed-like events in the Gd-capture IBD analysis need to have a high energy around $8\,$MeV, mainly captures of muon-induced neutrons on Gd and high energy γ-rays from muon-spallation in the surrounding rock contribute to the delayed-like events of accidental background. Therefore, this background is reduced significantly in the Gd-data. The reduced capture time of the IBD neutrons on Gd around $30\,\mu$s (compared to $200\,\mu$s for capture on H) also accounts for the reduction of accidental background. In the analysis of H-capture IBD events delayed-like events can be due to those also contributing to the prompt-like events, as the released energy following the neutron capture on H is around $2.2\,$MeV. Therefore, accidental background is the major background in the H-capture analysis and has a similar rate as the reactor neutrino signal [83].

---

[6] In organic scintillators neutron capture on carbon is also possible, but the cross sections are by two orders of magnitude smaller than for capture on hydrogen [78].

[7] So-called light noise, which are events due to light emitted by the ID PMT bases, was found to have a significant contribution to the Double Chooz far detector trigger rate. Nevertheless, accidental background resulting from these events can be reduced efficiently by cuts on the hit pattern of the ID PMTs. The light noise events feature a much less homogeneous pattern compared to physics events [33].

By means of an off-time window analysis, the rate and prompt-like energy spectrum of accidental background can be measured with high precision. The selection time window for IBD events is shifted by 1 s with respect to the prompt event [42]. Thereby, only random coincidences are selected. Statistics can be further improved by adding successive selection windows to the selection of random coincidences.

Cosmogenic Isotopes

Muon-spallation of carbon atoms, abundant in the organic scintillators, can produce radioisotopes [84, 85]. Some of these isotopes, namely ^{9}Li and ^{8}He, are so-called β-n emitters. ^{9}Li and ^{8}He both have significantly high branching ratios of 50.8 % and 16 %, respectively, for β^--decays accompanied by an additional emission of a neutron (and two α-particles in case of ^{9}Li) [86]:

$$\begin{aligned}
^9\text{Li} &\xrightarrow{50.8\,\%} e^- + \bar{\nu}_e + n + 2\,\alpha \\
^8\text{He} &\xrightarrow{16\,\%} e^- + \bar{\nu}_e + n + {^7}\text{Li}
\end{aligned} \tag{2.4}$$
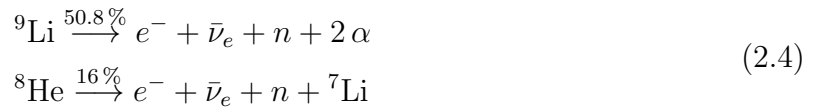
While the energy of the electron and the kinetic energy of the neutron, in the form of recoil protons, account for the prompt-like signal, the delayed capture of the thermalized neutron on Gd or H completes the perfect imitation of an IBD event. Both ^{9}Li and ^{8}He have rather long half lives of 178 ms and 119 ms [86]. With a muon rate of 46 Hz [33] in both IV and ID it is not possible to apply a veto of several half lives, as this would lead to an exceedingly high dead time of the detector of up to 100 %.

The determination of the rate and spectral shape of correlated background due to ^{9}Li and ^{8}He in Double Chooz is based on the correlation of IBD candidates in space and time with preceding muons. Based on this correlation a likelihood method was established, which is used to determine both rate and shape of the background and to reduce it in the IBD selection. Please refer to [33, 42] for more details on the cosmogenic isotope background in Double Chooz.

Fast Neutrons

Fast neutrons, which are produced by muon spallation in the rock surrounding the detectors, can penetrate both IV and the buffer volume and enter the central scintillating volumes. The delayed-coincidence of the IBD can be mimicked by a proton recoil with enough energy[8] followed by the delayed capture of the neutron on Gd or H after thermalization.

A powerful tool to determine the shape of the fast neutrons background is the IV. As it contains liquid scintillator and the IV PMT signals are read out in case of an ID trigger,

---

[8] Mind that the scintillation light output due to protons is quenched by a factor of $\gtrsim 2$. The determination of proton quenching is a major topic of this thesis and was measured, amongst others, for the Double Chooz scintillators (see chapter 6). See also section 3.2 for details on the quenching effect in organic scintillator.

although the IV threshold is not exceeded, it is possible to detect even low energy proton recoils due to fast neutrons in the IV. Therefore, the spectral shape of the fast neutron background could be determined by coincidences of prompt IBD candidate events in the ID and energy depositions in the IV [42]. The rate of the fast neutron background is determined from an extrapolation of an IBD selection allowing prompt-like events with energies exceeding the reactor neutrino energy region. In later analyses additional information from the IV tagging is used to determine the rate. The shape of the fast neutron background in the analyses of the Gd-capture IBD events was found to be flat [15, 33, 42], while the background rises towards low energies in case of the H-capture analysis [83].

Further improvement in the knowledge of the fast neutron background may be achieved using pulse shape discrimination (PSD) of the scintillation signal (see section 3.3). This way, proton recoil events in the ID may be distinguished from IBD positron energy depositions. In the scope of this thesis the Double Chooz scintillators for target, gamma catcher and muon veto where tested with regard to their PSD performance showing promising results. Nevertheless, up to now it was found to be challenging to apply PSD with regard to fast neutrons in Double Chooz.

Due to similar characteristics of the background signatures, the fast neutron background described above is strongly connected to the stopping muon background. Actually, the rate and shape are determined for the sum of both background contributions [33, 42].

Stopping Muons

Stopping muons are a class of events, in which a muon enters, is stopped and decays in the ID without being identified by the IV and OV due to no or a too small signal. For example, this is possible for muons entering the ID through the chimney region. A short enough track of stopping muons can lead to a prompt-like IBD signal. The electron or positron from the following decay of the muon by

$$\mu^- \longrightarrow e^- + \nu_\mu + \bar{\nu}_e$$
$$\mu^+ \longrightarrow e^+ + \bar{\nu}_\mu + \nu_e$$

(2.5)

with a lifetime of $2.2\,\mu$s [20] can mimic the delayed IBD neutron capture signal.

The OV, especially the upper part covering the chimney region, is a powerful tool to remove most of the stopping muon background. A further reduction of this background can be achieved by a cut on the goodness of the vertex reconstruction in the ID, which is suitable for point like events and fails for (short) muon tracks [33, 42]. Furthermore, the OV can be used to reduce the fast neutron background, as it also tags muons, which do not cross the main detector, but the surrounding rock.

2.1.4. Prediction of the Unoscillated Spectrum

As the near detector was completed only recently in end of 2014, all Double Chooz results on θ_{13} are based on the prediction of the expected unoscillated neutrino flux and spectrum

in the far laboratory [15, 33, 42, 83, 87]. The $\bar{\nu}_e$ are produced in the β-decays of the fission product from the main nuclear fuel isotopes ^{235}U, ^{239}Pu, ^{241}Pu and ^{238}U in the two Chooz reactor cores. The prediction of the unoscillated $\bar{\nu}_e$-flux for each reactor includes the time dependent thermal power and the fuel composition and evolution of each fuel element during its lifetime. Furthermore, reference $\bar{\nu}_e$-spectra for ^{235}U, ^{239}Pu and ^{241}Pu from measurements at the ILL reactor [88, 89, 90] and ^{238}U, recently measured at the FRM II research reactor[9] [91, 92], are used. To reduce the flux uncertainty from the reactors the prediction is normalized to the rate measurement performed by the Bugey4 experiment [93]. Thereby, the total reactor flux and IBD detection cross section correlated systematic error could be reduced to 1.8 % [15, 33, 83] (and 1.7 % in the most recent analysis [42]).

The results from the normalized $\bar{\nu}_e$-spectra and information about the IBD cross section are used to simulate IBD interactions in the Double Chooz detector Monte-Carlo simulation (MC). Besides the physical interactions and scintillation light production due to the IBD products, the simulation includes the detector response and electronic readout effects, which yields an output similar to the actual output of the real detector. Therefore, all cuts used in the analysis of the data can also be applied to the simulation output. For further details on the reactor neutrino spectrum prediction please refer to [33].

2.1.5. Results

Double Chooz released several analysis results on θ_{13} since the start of data taking with the far detector in April 2011 [15, 33, 42, 83, 87]. With increasing amount of data also the analysis techniques, such as calibration of the energy scale and background determination and rejection, have been improved successively.

Double Chooz published its first result in March 2012 from an analysis of the Gd-capture events on data from 96.8 live days[10] taken with the far detector [15], labeled as Gd-I in the following. In September 2012 an updated Gd-capture analysis of 227.93 live days of data (Gd-II) was published [33]. The same dataset was used for an analysis of the H-capture events in the gamma catcher (H-II) and published in 2013 [83]. Due to a difference in the applied veto cuts the H-II live time is increased to 240.1 days in comparison to the Gd-II analysis. In October 2014 an improved measurement of θ_{13}, based on the analysis of Gd-capture IBD events from a total of 467.9 live days of data (Gd-III), was published [42]. Furthermore, in 2011 and 2012 a total of 7.53 days of background data could be taken with both reactors being switched off, which is unique for all currently running reactor neutrino experiments. In the beginning of 2013 an analysis of this reactor off data only was published [94]. This data is fully included in the Gd-III analysis and used to constrain the background rate [42]. In the Gd-I and Gd-II analyses 22.5 hours of reactor off data

---

[9] The measured ^{238}U spectrum was used in the most recent Double Chooz analysis only. Before, calculations for the ^{238}U contribution were used to predict the reactor $\bar{\nu}_e$ spectrum [42].

[10] The live days correspond to the effective days of taken data after correction for the data taking efficiency and dead times due to applied analysis cuts.

IBD analysis	Gd-I	Gd-II	H-II	Gd-III
live days	96.8	227.93	240.1	460.67
IBD candidates	**4121**	**8249**	**36284**	**17351**
reactor $\bar{\nu}_e$ pred.	4009	8439.6	17690	17530
^{9}Li $+^8$ He	222.6	284.9	680	447
fast n + stopp. μ	80.3	152.7	600	278
accidental bkg.	31.9	59.5	17630	32.3
corr. light noise	-	-	80	-
total prediction	**4344**	**8937**	**36680**	**18290**

Table 2.1.: IBD candidate events, estimated background events and predicted unoscillated reactor neutrino signal events for the different Double Chooz analyses of the IBD events for neutron capture on Gd and H, respectively [15, 33, 42, 83]. In case of the Gd-III analysis the live days are given for the reactor on period only. Please refer to table 2.2 for the determined background rates in each analysis.

background rate (d^{-1})	Gd-I	Gd-II	H-II	Gd-III
^{9}Li $+^8$ He	2.3 ± 1.2	1.25 ± 0.54	2.8 ± 1.2	$0.97^{+0.41}_{-0.16}$
fast n + stopp. μ	0.83 ± 0.38	0.67 ± 0.20	2.5 ± 0.47	0.604 ± 0.05
accidental bkg.	0.33 ± 0.03	0.261 ± 0.002	73.45 ± 0.16	0.070 ± 0.003
corr. light noise	-	-	0.32 ± 0.07	-

Table 2.2.: Background rate estimates with total errors, determined in the Double Chooz analyses of the IBD events for neutron capture on Gd and H, respectively [15, 33, 42, 83]. A brief description of the background contributions is given in section 2.1.3. For details on the determination of the background rates or the reduction of each background contribution please refer to the respective publication.

(present at that time) were used to verify the background estimations [15, 33].

In table 2.1 the selected IBD candidates, estimated backgrounds and expected reactor neutrino signal events are given for the Gd-I, Gd-II and Gd-III and the H-II analyses. The determined background rates for all analyses are summarized in table 2.2. As the analysis techniques and background vetos could be improved, the background rates and uncertainties could be reduced in the succeeding analyses. Furthermore, the results show that in case of the H-II analysis the accidental background event rate approximately equals that of the reactor neutrino signal, while it plays a minor role in the Gd-capture analyses.

The most precise results on θ_{13} by Double Chooz are obtained in a *rate+shape* (R+S) *analysis*. In such an analysis the measured IBD candidate rate is compared to the predicted rate for different energy regions of the prompt event spectrum of the IBD events. In order to accomplish this, the shape of the energy spectra for all background contributions need to
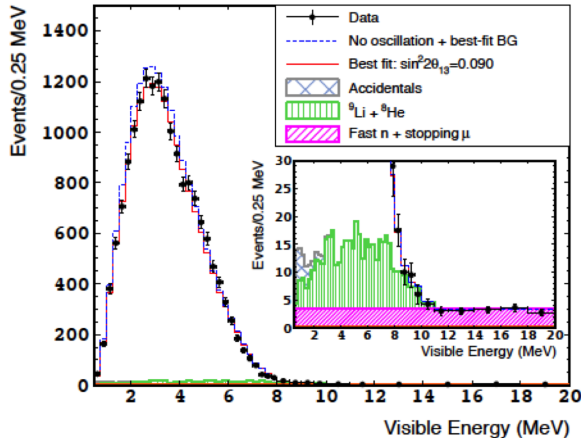
Figure 2.4.: The measured prompt energy spectrum (black data points) superimposed with the predicted spectrum for no oscillation (blue dashed line) and the $\sin^2 2\theta_{13} = 0.090$ best-fit result (red line) as given in [42]. The contributions of accidental background (grey, cross-hatched), cosmogenic $^9\text{Li} + ^8\text{He}$ (green, vertical-hatched) and fast neutron and stopping muon background (magenta, slant-hatched) are shown.
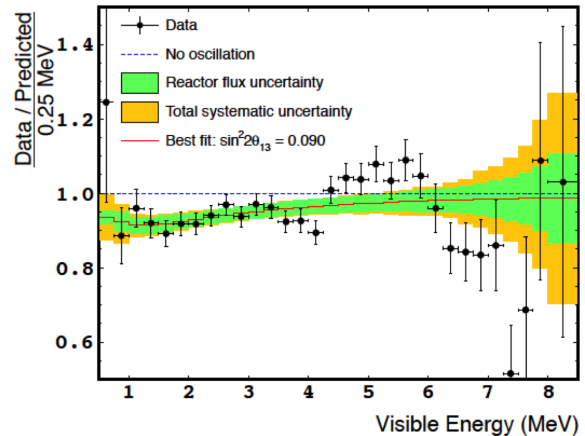
Figure 2.5.: The ratio of background subtracted data (black points) and the no oscillation prediction as a function of the prompt event visible energy from [42]. The ratio of the predicted spectrum for the best-fit result of $\sin^2 2\theta_{13} = 0.090$ and the no oscillation prediction is shown by the red line. The systematic uncertainty arising from the reactor flux prediction is shown in green, while the orange area denotes the total systematic error.

be determined and understood, while the total amount of each background is constrained by the respective rate estimates (see table 2.2). As an example, figure 2.4 shows the measured prompt IBD event spectrum obtained in the Gd-III analysis. Additionally, the result of the oscillation fit, the predicted spectrum in case of $\theta_{13} = 0$ (no oscillation) and the spectra for each background contribution are depicted. The corresponding ratio of the background-subtracted spectrum and the no-oscillation prediction is depicted in figure 2.5, which also shows the best-fit result with the uncertainty arising from the reactor flux prediction and the total systematic uncertainty. Furthermore, in figure 2.6 the prompt IBD event spectrum for the H-II analysis is shown along with the best-fit result and the individual background contributions.

A background model independent analysis on the same data as used for Gd-II and H-II was published in 2013 [87]. This *Reactor Rate Modulation* (RRM) analysis is based on the variations in the total thermal power of the two reactors. For both the Gd- and H-capture IBD data seven data points arise from different states of the two reactors: three points for both reactors running, three points for one of the reactors not running and one point for the reactor off period [87]. The data point resulting from the reactor off period corresponds to a direct measurement of the background rate. Plotting the resulting rates for each period against the expected rate, the resulting data for each the Gd- and H-data can be fitted with a linear function. A non-zero oscillation is visible in form of the deviation of the
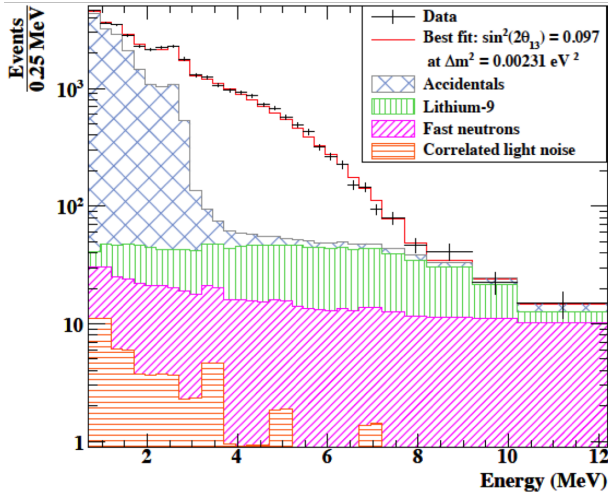
Figure 2.6.: The measured prompt energy spectrum from the H-II analysis (black data points) plotted together with the prediction from the best-fit oscillation result of $\sin^2 2\theta_{13} = 0.097$ (red line) as given in [83]. The background contribution are given for accidentals (blue, cross-hatched), cosmogenic ^{9}Li + ^{8}He (green, vertical-hatched), fast neutrons and stopping muons (magenta, slant-hatched) and correlated light noise (red, horizontal-hatched).
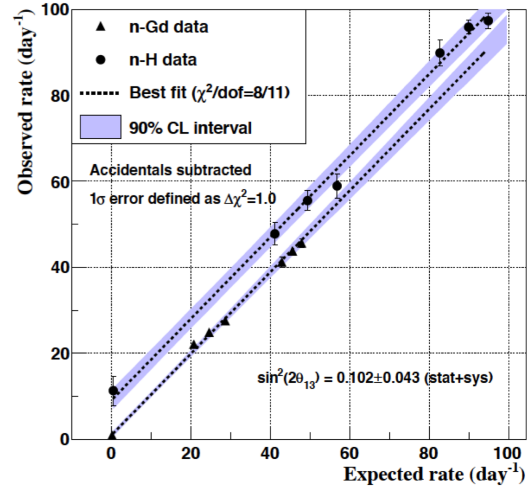
Figure 2.7.: Correlation between the measured Gd-II (black triangles) and H-II (black circles) daily IBD candidate rates and the expected daily neutrino rate for different conditions of the two reactors as given in [87]. The period, in which both reactor were switched off, represents the respective data point at an expected rate of $0\mathrm{day}^{-1}$ and represents a direct measurement of the background rate. The black dashed line shows the best-fit result of $\sin^2 2\theta_{13} = 0.102$.

slope from one, while the finite background rate leads to an offset. Figure 2.7 shows the result for the RRM analysis including the Gd-II and H-II data. For an update of the RRM analysis for the Gd-III analysis please refer to the Gd-III publication [42].

In table 2.3 the results on θ_{13} from the Gd-I, Gd-II, Gd-III and H-II R+S analyses are given as well as the result from the published RRM analysis on the combined Gd-II and H-II data. All results are in good agreement. The current best result is obtained by the R+S analysis of the Gd-III data. An analysis of the H-capture IBD events in the dataset corresponding to the Gd-III period is in preparation.

2.1.6. Outlook

As Double Chooz took data with the far detector only up to now, the results on θ_{13} were limited by the uncertainties on the reactor flux and IBD cross section. In a parallel measurement with both the far and the near detector these uncertainties will be reduced significantly, while the systematic uncertainties on the background contributions are expected to dominate, decreasing with increasing statistics.

analysis	result on $\sin^2 2\theta_{13}$	publication
Gd-I	$0.086 \pm 0.041\,(\text{stat}) \pm 0.030\,(\text{syst})$	[15]
Gd-II	$0.109 \pm 0.030\,(\text{stat}) \pm 0.025\,(\text{syst})$	[33]
Gd-III	$0.086\,^{+0.032}_{-0.029}\,(\text{stat} + \text{syst})$	[42]
H-II	$0.097 \pm 0.034\,(\text{stat}) \pm 0.034\,(\text{syst})$	[83]
RRM (Gd-II & H-II)	$0.102 \pm 0.028\,(\text{stat}) \pm 0.033\,(\text{syst})$	[87]

Table 2.3.: Published Double Chooz rate+shape fit results from the analyses of the Gd-capture (Gd-I, Gd-II and Gd-III) and the H-capture (H-II) IBD events. In addition, the result from the background model independent reactor rate modulation analysis (RRM) using the combined Gd-II and H-II data is given.

Figure 2.8 shows the projected sensitivity of Double Chooz in case of $\sin^2 2\theta_{13} = 0.1$. The sensitivity is depicted for the IBD selections according to the Gd-II (black) and Gd-III (blue) analyses for the measurement with the far detector only and for the measurement with both the near and far detectors [42]. To determine the sensitivity for the two detector case a $0.2\,\%$ uncertainty on the relative detection efficiency and a remaining uncorrelated flux uncertainty of $0.1\,\%$ were assumed. The background levels in the near detector were scaled from the far detector using muon flux measurements performed in the near and far laboratories. The blue shaded area in figure 2.8 shows the possible improvement in the systematic uncertainties of the Gd-capture IBD analysis, while the lower dotted blue line refers to the case, in which only the reactor flux uncertainty remains.

After three years of data taking with both the near and far detector running an error on $\sin^2 2\theta_{13}$ of $\sigma(\sin^2 2\theta_{13}) = 0.015$ can be reached, using the current Gd-III analysis, which represents the current knowledge of the systematic uncertainties. Improvements in the analysis techniques might further reduce the error to about 0.010.
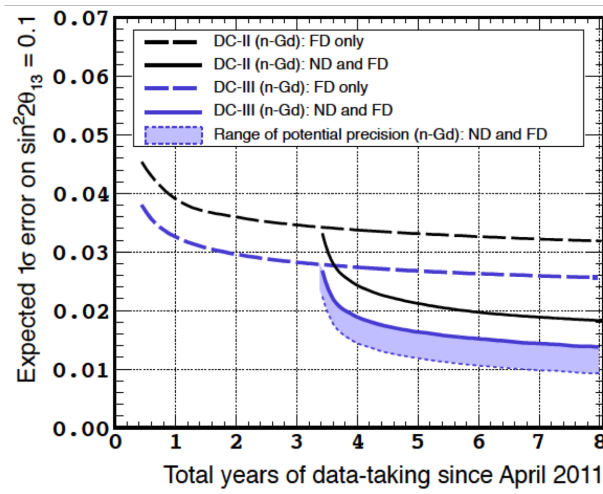
Figure 2.8.: The projected sensitivity for Double Chooz in case of $\sin^2 2\theta_{13} = 0.1$ with the far detector only (dashed curves) and both the far and near detector (solid curves) running [42]. The sensitivity is depicted for both the Gd-II (black, [33]) and Gd-III (blue, [42]) analyses. The shaded region represents the potential improvements for further reduction of the current systematic uncertainties. The lower blue dotted line corresponds to the sensitivity, when the reactor flux uncertainty is the only systematic uncertainty.

2.2. The LENA Project

The LENA (Low Energy Neutrino Astronomy) project is a proposed next generation liquid scintillator detector with a desired target mass of ~ 50 kt [18]. It is planned as a follow-up experiment to currently running scintillator detectors, like KamLAND [30] and Borexino [11, 75], which demonstrated the huge potential of large scale scintillator detectors in neutrino oscillation physics and neutrino astrophysics.

Using liquid scintillator, a low energy threshold of down to ~ 200 keV and an excellent particle discrimination performance can be achieved. This combined with the huge size of LENA offer a rich physics program, ranging from precision measurements of solar neutrinos and geoneutrinos to searches for the proton decay [18]. Furthermore, neutrinos emitted in a possibly appearing galactic supernova (SN) could be detected with high statistics. Additionally, LENA would allow for a first detection of the cumulative flux of neutrinos from earlier SNe, the so-called diffuse supernova neutrino background (DSNB). The huge size enables the detection of neutrinos with energies in the GeV-range expanding the physics program to atmospheric neutrinos and using LENA as a far detector for a long baseline neutrino beam experiment. A summary of the LENA physics goals will be given in sections 2.2.2-2.2.8.

As part of the LAGUNA-LBNO design study, which had been funded by the European Union until end of August 2014, the feasibility of the LENA physics program and of the construction the detector deep underground was investigated.

2.2.1. Detector Setup

A schematic overview of the currently favored LENA detector design is shown in figure 2.9 [95]. Due to the limited attenuation lengths of organic liquid scintillators in the order of $10-20$ m, the detector shape was chosen to be cylindrical [18], in contrast to currently running scintillator detectors, like Borexino [11] and KamLAND [30], which are spherical. The liquid scintillator will be contained in a sensitive volume of 96 m in height and 14 m in radius. The favored scintillator mixture is based on linear alkylbenzene (LAB) with the wavelength shifters 2,5-diphenyloxazole (PPO) and 1,4-bis(2-methylstyryl)benzene (bisMSB) admixed in concentrations of 3 g/l and 20 mg/l, respectively (refer to chapter 3 for more details on organic liquid scintillators). The emission spectrum is effectively shifted to wavelengths around ~ 430 nm, where the scintillator features high transparency and the photosensors used to detect the light are most sensitive.

The scintillation light will be read out by $\sim 30\,000$ 12 inch PMTs. The PMTs are planned to be equipped with light collectors to increase the effective sensitive area and to be contained in composite steel and acrylic pressure encapsulations. The PMTs in the pressure encapsulations and the light collectors represent the optical modules (OMs), which will be mounted on a support structure with the aperture at a radius of 14 m. Thereby, an effective optical coverage of about 30 % is achieved. To shield the sensitive scintillator volume from radioactive impurities in the PMT glass and encapsulation materials the OMs are filled
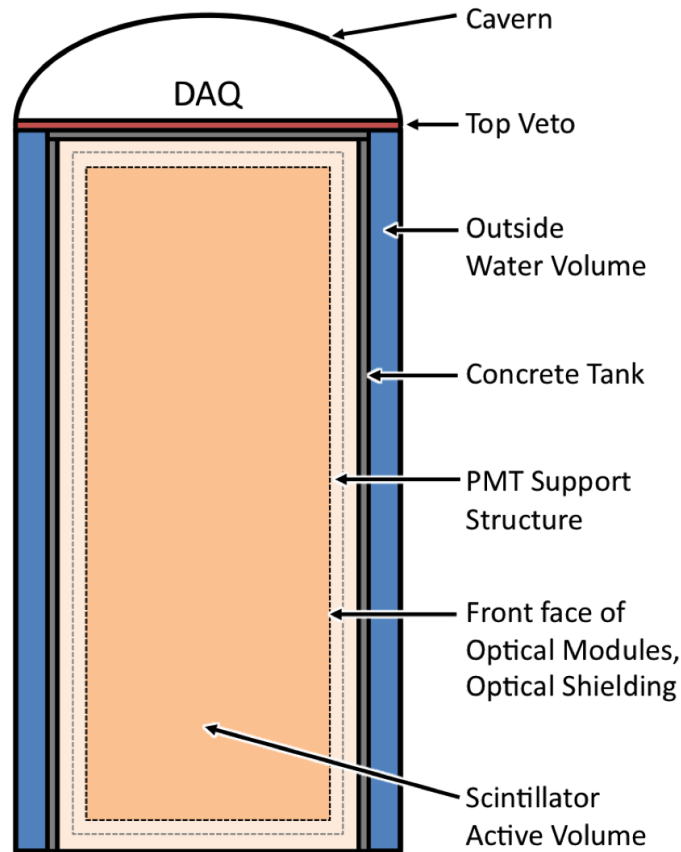
Figure 2.9.: Schematic view of the current LENA detector design according to [95]. The active volume will contain $\sim 50\,\text{kt}$ of LAB based liquid scintillator. The scintillation light is read out by $\sim 30\,000$ optical modules (OMs) consisting of $12\,\text{inch}$ PMTs equipped with light collectors and contained in pressure encapsulations. The apertures of the OMs face the active volume at a radius of $14\,\text{m}$. Both the scintillator and the OMs are contained in a concrete tank with an inner radius of $16\,\text{m}$ and a hight of $100\,\text{m}$. The region between the front face of the OMs and the concrete tank is optically separated from the active volume by an opaque foil. Outside the concrete tank a water tank instrumented with additional PMTs acts as an active muon veto and passively shields the scintillator volume from fast neutrons. Furthermore, an active muon veto, possibly consisting of plastic scintillator strips, will be placed above the detector.

with nonscintillating mineral oil.

The scintillator and the OMs on the support structure are contained in a 60 cm thick concrete tank with an inner height of 100 m and an inner diameter of 16 m. An opaque foil will be attached between the front apertures of the OMs to optically separate the sensitive volume from the region between the concrete tank and the OMs, which will be filled with the same scintillator. Therefore, this region acts as a passive shielding of the active volume against radiation from the concrete and beyond.

The space between the concrete tank and the wall of the cavern will be filled with clean water to passively shield the inner detector from external γ-rays and fast neutrons from radioactivity or muon spallation in the surrounding rock. To achieve an optimal shielding, the thickness of the water shielding is planned to be at least 2 m. Cherenkov light produced by cosmic muons crossing the water volume will be detected by PMTs mounted on the outer concrete tank wall. Additionally, an active muon veto system will be placed on top of the detector, where no water shielding will be present. Possible options for this system are plastic scintillator panels, resistive plate chambers or limited streamer tubes.

The currently favored location for the LENA detector is the Pyhäsalmi mine in Finland. The detector could safely be constructed in a depth of 1400 m, which corresponds to about 4000 m of water equivalent. Compared to Borexino at the LNGS[11] featuring a cosmic muon flux of $1.2\,\mathrm{m^{-2}h^{-1}}$ [75] a lower muon flux in the order of $0.4\,\mathrm{m^{-2}h^{-1}}$ is expected at Pyhäsalmi [18].

2.2.2. Physics Goals

The rich physics program of LENA ranges from low energy neutrinos in the MeV range produced by astrophysical sources, like the sun and supernova, or emitted in radioactive decays in the earth, so-called geoneutrinos, to high energy beam neutrinos in the GeV range [18]. Furthermore, the search for the proton decay is an important topic in the LENA program. In the following sections 2.2.3 to 2.2.8 the main physics goals of LENA are summarized briefly.

The currently running Borexino detector[12] is an optimal opportunity to test analysis methods for the LENA experiment, although the sensitivity is limited by the small size. Furthermore, methods used to determine and discriminate different background contributions can be developed and refined using the data taken with the Borexino detector. Most of all, the exceedingly high radiopurity in the Borexino detector sets the standards for future neutrino experiments.

---

[11] Laboratori Nazionali del Gran Sasso
[12] Most of the groups contributing to studies for LENA are also members of the Borexino collaboration.

2.2.3. Supernova Neutrinos

A high statistics measurement of neutrinos from core collapse supernova (SN) in our galaxy would be an important test of the current knowledge on these energetic events (see section 1.5). A galactic SN appearing in the life-time of LENA ($\sim 30\,\mathrm{a}$) would allow for such a high statistics measurement. In [96] event rates in LENA for a galactic core collapse SN of a progenitor star with a mass of $8\,\mathrm{M}_\odot$ at a distance of $10\,\mathrm{kpc}$ were estimated, using the SNOwGLoBES[13] software package [97] and the GVKM[14] model for the SN neutrino fluxes [98]. As a result, a total of about 16000 events in different detection channels are expected. In table 2.4 the expected numbers of events in the different possible detection channels are given.

Almost 10000 events are expected in the inverse β-decay (IBD) channel (see equation 2.1 and section 2.1.2). The delayed coincidence signature and the possible reconstruction of the neutrino energy from the prompt positron signal allow for a high statistics test of the evolution of the $\bar{\nu}_e$-flux in time and energy. Due to the short period of the SN signal this channel is expected to be practically background free.

Charge current reactions of ν_e and $\bar{\nu}_e$ on ^{12}C in the scintillator offer further detection channels for supernova neutrinos [18, 96]:

$$\nu_e + {}^{12}\mathrm{C} \to {}^{12}\mathrm{N} + e^- \qquad (E_\mathrm{thr} = 17.3\,\mathrm{MeV})$$
$$^{12}\mathrm{N} \to {}^{12}\mathrm{C} + e^+ + \nu_e \tag{2.6}$$

$$\bar{\nu}_e + {}^{12}\mathrm{C} \to {}^{12}\mathrm{B} + e^+ \qquad (E_\mathrm{thr} = 14.4\,\mathrm{MeV})$$
$$^{12}\mathrm{B} \to {}^{12}\mathrm{C} + e^- + \bar{\nu}_e \tag{2.7}$$
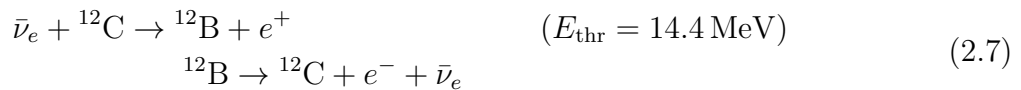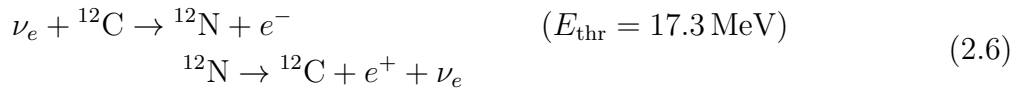
The prompt energy deposition by the produced electron or positron, respectively, and the delayed re-decay of the produced nuclei can be used to identify events caused by these CC reactions. As the life times for ^{12}N and ^{12}B are $11.0\,\mathrm{ms}$ and $20.2\,\mathrm{ms}$ [99], respectively, both channels cannot be distinguished on and event by event basis. With slightly less than 500 expected events for each of both channels in LENA it is possible to extract the contribution of each detection channel from a simultaneous fit to the cumulative energy and time spectra of the re-decay events. This way, the total flux of ν_e from the SN can be extracted for energies above the threshold for reaction (2.6) of $E_\mathrm{thr} = 17.3\,\mathrm{MeV}$.

In addition to the described charged current interactions a neutral current interaction on ^{12}C, leading to a higher excited state of ^{12}C, is possible for all neutrino species [18]:

$$\nu + {}^{12}\mathrm{C} \to \nu + {}^{12}\mathrm{C}^* \qquad (E_\mathrm{thr} = 15.1\,\mathrm{MeV})$$
$$^{12}\mathrm{C}^* \to {}^{12}\mathrm{C} + \gamma \tag{2.8}$$
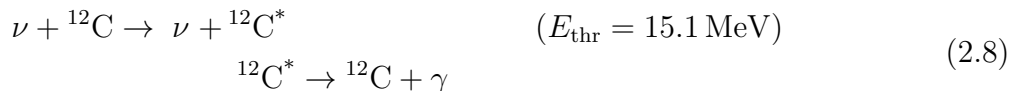
The resulting monoenergetic deexcitation of ^{12}C* deposits an energy of $15.1\,\mathrm{MeV}$ in the detector, which is well above the energy region of natural radioactivity. Unfortunately, this

---

[13] SuperNova Observatories with GLoBES
[14] Gava-Kneller-Volpe-McLaughlin

detection channel	type	abbreviation	exp. events
$\bar{\nu}_e + p \to e^+ + n$	CC	IBD	9250
$\nu + p \to \nu + p$	NC	ν-p	4179
$\nu + {}^{12}C \to {}^{12}C^* + \nu$	NC	NC-^{12}C	1296
$\nu + e^- \to \nu + e^-$	NC	ν-e	496
$\nu_e + {}^{12}C \to {}^{12}N + e^-$	CC	ν_e-^{12}C	468
$\bar{\nu}_e + {}^{12}C \to {}^{12}B + e^+$	CC	$\bar{\nu}_e$-^{12}C	459
total number of expected events:			16148

Table 2.4.: Expected number of events from a SN of a progenitor star with a mass of $8\,M_\odot$ at a distance of $10\,\mathrm{kpc}$ for different detection channels in LENA ($50\,\mathrm{kt}$) according to [96]. The estimated values are based on calculations using the SNOwGLoBES software package [97] and SN neutrino fluxes according to the GVKM model [98]. For the event rate in the ν-p channel a Birks-factor $kB = 0.01\,\mathrm{cm}\,\mathrm{MeV}^{-1}$ was assumed to account for the quenching of protons in liquid scintillator (see section 3.2 and equation (3.8)).

channel offers no information about the energy of the incident neutrino. Therefore, only the cumulative flux of all neutrino flavors above the threshold energy of $15.1\,\mathrm{MeV}$ can be measured using the NC-^{12}C channel.

Further NC detection channels are elastic neutrino-electron (ν-e) and neutrino-proton (ν-p) scattering [18, 96]. While both channels are sensitive to all neutrino species, no information on the initial neutrino energy is provided. Nevertheless, comparison of the measured spectrum with the expectations can provide important information about the processes in SNe. Despite the high expected signal rates of about 500 events in the ν-e channel and almost 4200 events in the ν-p channel within the short timescale of $\sim 10\,\mathrm{s}$, the enormous intrinsic background due to ^{14}C in the scintillator limits the detection threshold to about $200\,\mathrm{keV}$. In case of ν-p scattering quenching has to be taken into account (see section 3.2 and equation (3.8)), which has a strong impact on the event rate above the threshold. For the expected events in this channel, given in table 2.4, a Birks-factor of $kB = 0.01\,\mathrm{cm}\,\mathrm{MeV}^{-1}$ was used.

In the scope of this thesis, measurements with regard to proton quenching for the favored LENA scintillator and other scintillator mixtures, were performed in a small scale experiment at the Maier-Leibnitz-Laboratorium in Garching (see chapters 4-6). Furthermore, the measurements include investigations of the pulse shape discrimination (PSD) performance of the favored LENA scintillator with regard to energy depositions due to protons and electrons (see chapter 7). PSD could be used to separate the spectra from ν-e and ν-p scattering. A dedicated study was performed in [96] showing promising results.

In [100] the possibility of the detection of neutrinos from late burning stages of a massive star before the actual SN explosion was investigated. As a result neutrinos from the late

burning stages of stars in the closer vicinity of up to $\sim 2\,\mathrm{kpc}$ could be detected within LENA in the ν-e and IBD channels. In consequence, LENA could give an early warning for smaller neutrino detectors and optical telescopes even before the first SN neutrinos are detected.

2.2.4. Diffuse Supernova Neutrino Background

As described in section 1.5.4, the measurement of the DSNB flux would provide important information on the average neutrino spectrum from core collapse SNe. The current best upper limit for the DSNB $\bar{\nu}_e$-flux of $2.8 - 3.1\,\bar{\nu}_e\,\mathrm{cm}^{-2}\,\mathrm{s}^{-1}$ ($E_{\bar{\nu}e} > 17.3\,\mathrm{MeV}$) was obtained by the Super-Kamiokande experiment detecting the $\bar{\nu}_e$ via the secondary positrons from the inverse β-decay (IBD) [74].

In [101, 102] the feasibility of a DSNB detection with LENA was studied for different DSNB models with varying mean neutrino energies $\langle E_\nu \rangle$ between 12 and 21 MeV. An important advantage of the liquid scintillator detector LENA compared to Super-Kamiokande is the possibility to detect the neutrons from the IBD by the delayed capture on hydrogen (see section 2.1.2). Thus, the contributing backgrounds can be reduced significantly.

Nevertheless, for LENA at the Pyhäsalmi mine an irreducible background due to reactor neutrinos arrises below $9.5\,\mathrm{MeV}$[15]. Above about 25 MeV the DSNB signal ($\langle E_\nu \rangle = 12\,\mathrm{MeV}$) is surpassed by atmospheric $\bar{\nu}_e$ background. Therefore, an analysis window between 9.5 and 25 MeV was chosen to reduce the atmospheric and reactor $\bar{\nu}_e$ background to 11 remaining events in 10 a, while expecting $50 - 100$ DSNB events, depending on $\langle E_\nu \rangle$ [102]. Background due to cosmogenic muon induced $^9\mathrm{Li}$ (see section 2.1.3) can efficiently be reduced to a negligible contribution of 0.01 events in 10 a, applying a 2 m cut around every muon for 2.5 s, which introduces a dead time of only 0.2 % [102]. The background contribution due to fast neutrons produced in the surrounding rock can be lowered to 4.9 events per 10 a by reducing the fiducial volume radius to 11 m, which also reduces the expected DSNB events to 32.4 ($\langle E_\nu \rangle = 12\,\mathrm{MeV}$).

The most important background arrises from neutral current (NC) reactions of atmospheric neutrinos and antineutrinos with $^{12}\mathrm{C}$, which all have in common that a fast neutron is emitted [102]. Except for reaction $\nu_x + {}^{12}\mathrm{C} \rightarrow \nu_x + n + {}^{11}\mathrm{C}$, which has the largest contribution with a branching ratio of 38.8 %, the emission of the neutron is accompanied by protons, deuterons, tritium nuclei or α-particles. The IBD signature is mimicked by the prompt energy deposition of the charged products or by the neutron scattering off a proton in the scintillator, followed by the neutron being captured on hydrogen. A simulation of this atmospheric neutrino NC background resulted in $3.27 \cdot 10^3$ expected events in 10 a, which would surpass the DSNB signal by more than one order of magnitude [102]. Tagging these NC events by the decays of the produced isotopes would work for only $\sim 40\,\%$ of the background events and would require a reduction of the fiducial mass to 30 kt to prevent accidental coincidences of IBD events and external background.

---

[15] The reactor neutrino background at Pyhäsalmi is low compared to locations in Central Europe.

A powerful tool to reduce the NC background due to atmospheric neutrinos was found to be pulse shape discrimination (PSD). Neutron-induced protons, alphas and heavier particles cause different scintillation pulse shapes than positrons or electrons (see section 3.3). It could be shown in [102] that the NC background can be reduced to 21.8 events in 10 years, while reducing the efficiency for the DSNB signal to 40 %. Additionally, the applied PSD analysis could reduce the background due to muon-induced fast neutrons to 1.8 events in 10 a. Using a 44 kt fiducial volume, the achieved DSNB signal efficiency would result in 17.9 ($\langle E_\nu \rangle = 12$ MeV) to 35.2 ($\langle E_\nu \rangle = 21$ MeV) expected DSNB events in 10 a, while the total background is estimated to 27.8 events. Assuming a knowledge of the background rates with a 5 % precision, the DSNB flux could be measured by LENA with more than 3 σ accuracy after 10 years of measurement. If no DSNB signal is detected, all current DSNB models would be ruled out at a 90 % C.L..

The PSD analysis is based on data taken in a beam time at the Maier-Leibnitz-Laboratorium in August 2012 with the setup also used in this thesis. The setup was developed in collaboration with Jürgen Winter, who analyzed the data of the August 2012 beam time with regard to the scintillation pulse shape caused by neutron- and γ-induced events [100]. Results obtained for the PSD performance of the favored LENA scintillator from data taken in the scope of this thesis in beam times cunducted in 2013 and 2014 will be presented in chapter 7.

2.2.5. Solar Neutrinos

The energy in the sun is produced by the fusion of hydrogen to helium. This can either take place via the pp-chain or the CNO-cycle, in which isotopes of carbon, nitrogen and oxygen serve as catalysts. In both cases the fusion can be summarized by the following net reaction [36]:

$$4\,p \longrightarrow {}^4\text{He} + 2\,e^+ + 2\,\nu_e + 26.73\,\text{MeV} \tag{2.9}$$
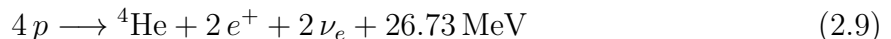
In the sun, fusion via the CNO-cycle plays a minor role with less than about 2 % [36]. The neutrino spectra resulting from the different steps of the pp-chain and the CNO-cycle are shown in figure 2.10. As solar neutrinos are solely produced as electron neutrinos ν_e the main detection reaction in liquid scintillator is elastic neutrino electron scattering. The expected rates in LENA, using a fiducial volume of 36 kt and a threshold of 200 keV, are given in table 2.5.

A detection of the pp-neutrino flux in LENA is challenging. Despite an expected rate of about 2300 events per day [101], the signal is almost fully covered by background due to decays of ^{14}C in the scintillator. ^{14}C decays via β^--decay with a halflife of 5730 a and a Q-value of 156.5 keV [99]. Due to the limited energy resolution of scintillator based detectors, a ^{14}C trigger rate in the order of 1 kHz above the threshold of 200 keV is expected in LENA, which is orders of magnitudes above the pp-neutrino signal [101].

The high rate of ^{7}Be-neutrinos in LENA offers the possibility to search for periodic modulations in the ^{7}Be-flux. LENA will be sensitive to modulations with periods ranging from several minutes to more than 10 years, reaching an accuracy below 1 % after a 10 years
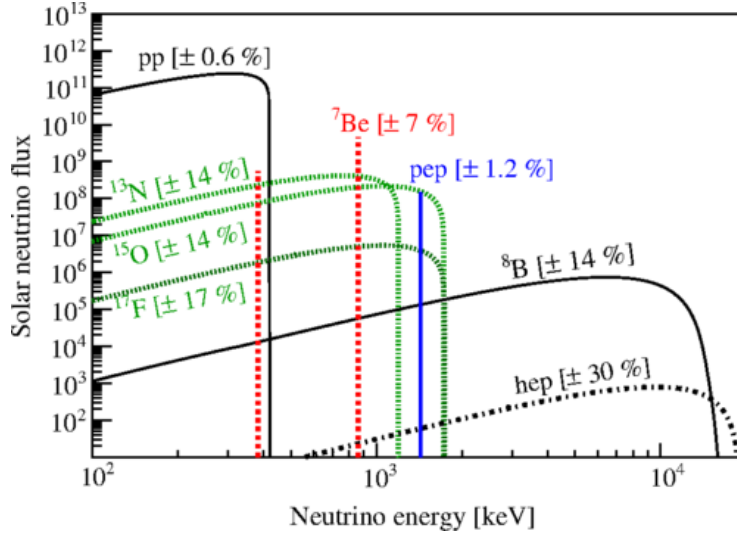
Figure 2.10.: Energy spectra of solar neutrinos from different subreactions of the pp-chain (black, red and blue) and CNO-cycle (green) as given in [75]. The vertical axis corresponds to the flux in $\mathrm{cm}^{-2}\,\mathrm{s}^{-1}\,(10^3\,\mathrm{keV})^{-1}$ for the continuous spectra and shows the flux in $\mathrm{cm}^{-2}\,\mathrm{s}^{-1}$ for the monoenergetic lines. The theoretical uncertainties on the fluxes are given by the numbers in brackets.

measurement [103]. Therefore, a search for day-night variations in the neutrino flux and modulation due to the 11 a lasting solar cycle can be performed by LENA. Furthermore, possible gravity and buoyancy driven helioseismic waves may affect the fusion processes in the sun. While such helioseismic waves cannot be observed on the surface of the sun, LENA would be able to detect such so-called g-modes with periods down to several minutes [103].

As LENA at the Pyhäsamli mine features a lower muon background compared to Borexino, the background due to cosmogenic ^{11}C is expected to be reduced with respect to the pep-neutrino flux. Furthermore, the theoretical uncertainty on the pep-flux is rather small and causes a high event rate of $\sim 850\,\mathrm{d}^{-1}$ in LENA. Therefore, a precision measurement of the pep-flux by LENA would allow to test the ν_e survival probability near the MSW transition region (see section 1.1.3).

Due to background by cosmogenicaly produced ^{11}C and intrinsic ^{210}Bi, a measurement of the neutrino flux from the CNO-cycle with LENA is challenging. Compared to Borexino, which could only put an upper limit on the CNO-flux [75], LENA expects a reduced ^{11}C background. The rate of the ^{210}Bi decays to ^{210}Po with a half life of 5 d can be measured by the rate of ^{210}Po, using pulse shape discrimination as it is an α-emitter [101]. Mind that the determination of the ^{210}Bi rate is only possible if ^{210}Bi and ^{210}Po are in radioactive equilibrium, which should be the case as soon as the ^{210}Po rate in the detector is stable. As the half life of ^{210}Po is 138 d, works affecting the inner volume of LENA may introduce additional ^{210}Po and, therefore, endanger a measurement of the CNO-flux. Knowing the rate of ^{210}Bi, the background could be subtracted statistically.

ν_e source reaction:	pp	^{7}Be	pep	CNO	^{8}B	hep
expected rate (d^{-1}):	2300	11 000	850	880	130	0.4

Table 2.5.: Expected solar neutrino event rates in LENA using a fiducial volume of 36 kt and a threshold of 200 keV as given by [101].

As the ^{8}B-neutrinos feature energies ranging up to 15 MeV [75], they can be used to probe the electron neutrino survival probability in the matter dominated as well as the transition region caused by the MSW effect (see section 1.1.3). In Borexino the energy threshold for ^{8}B-measurements was limited by external radioactivity to be at 3 MeV [75]. Due to the huge size of LENA, this background can be removed almost completely by applying a stringent fiducial volume cut. This way, ^{8}B-neutrinos can be detected down to 2 MeV[101, 104]. It could be shown, that LENA would exclude a constant behavior of the electron neutrino survival probability down to 2 MeV by 5 σ after a 5 a measurement, even if the background level is by a factor of 100 higher than in Borexino [101, 104].

2.2.6. Geoneutrinos

A significant contribution to the heat generated in the earth interior is caused by β^--decays of ^{40}K and isotopes from the decay chains of ^{238}U and ^{232}Th [18]. The electron antineutrinos emitted in these β^--decays are called geoneutrinos and can be detected in LENA via the inverse beta decay (IBD) on protons in the scintillator (see equation (2.1) and section 2.1.2). As the energy threshold for the IBD reaction is ~ 1.8 MeV, geoneutrinos emitted in the ^{40}K-decay cannot be detected.

Geoneutrinos have already been detected by the KamLAND [30] and the Borexino [105] experiments, while both suffered from low statistics. Making use of the huge size of LENA a first high statistics measurement with an expected geoneutrino rate in the order of ~ 1000 events per year would be possible [106].

Due to the delayed coincidence signature of the IBD events background contributions are suppressed efficiently. The main background for geoneutrinos are reactor neutrinos. The energy spectrum of reactor $\bar{\nu}_e$ ranges up to ~ 10 MeV and, therefore, exceeds the spectrum of geoneutrinos with energies of $1.8 - 3.2$ MeV [106]. Hence, the background contribution of reactor neutrinos can be determined from the energy region above 3.2 MeV, making use of the good knowledge of the reactor neutrino spectrum. The expected background due to reactor $\bar{\nu}_e$ at Pyhäsalmi is ~ 240 events per year in the relevant energy region [106]. Furthermore, several nuclear reactors are planned or already under construction in Finland. The reactor background will, therefore, almost double, when all reactors are running.

Further background sources are fast neutrons and the cosmogenic β-n emitting isotopes ^{9}Li and ^{8}He (see section 2.1.3 for details). The background due to fast neutrons is expected to be less than 10 events per year [18] and may be further reduced, using pulse shape

discrimination[16]. With a relatively low muon rate in LENA, the background due to ^{9}Li and ^{8}He can be reduced to about one event per year, applying a spacial cut of 2 m around the muon track and a time cut of 2 s after the muon. The thereby introduced dead time would be small with about 0.1%. Additionally, neutrons produced by the nuclear reaction ^{13}C$(\alpha, n)^{16}$O can cause a background, which is similar to fast neutrons. The α-particles leading to this reaction are mainly produced by decays of ^{210}Po in the scintillator. Assuming a radiopurity level similar to Borexino this background is expected to be about 10 events per year [18].

LENA will be able to perform a high statistics measurement with low background. After one year of measurement at the Pyhäsalmi mine the total geoneutrino flux could be determined with a precision of 3 % (4 % with future Finish reactors) [18]. The ratio between the contributions of geoneutrinos from the Th and U decay chains could be measured with a precision of 10 % after 3 years. Both the total flux and the ratio are important inputs to geochemical and geophysical models, which could be tested by LENA with high precision.

2.2.7. Proton Decay

In the standard model of particle physics the proton is considered to be stable, which is described by the empirically introduced baryon number conservation [107]. Nevertheless, several extensions to the standard model predict a finite proton lifetime [108]. The Super-Kamiokande experiment achieved the best limits on the proton lifetime up to now. The minimal grand unified theory SU(5) predicts a decay of the proton by $p \rightarrow e^+\pi^0$ with a lifetime far below 10^{32} a, which is ruled out by the current best limit obtained by Super-Kamiokande of $\tau_{\mathrm{p}}(p \rightarrow e^+\pi^0) > 8.2 \cdot 10^{33}$ a (90 % C.L.) [109]. Supersymmetric models favor the decay of the proton by $p \rightarrow K^+\bar{\nu}$ [108]. The current best limit on this channel was also obtained by the Super-Kamiokande experiment to be $\tau_{\mathrm{p}}(p \rightarrow K^+\bar{\nu}) > 2.3 \cdot 10^{33}$ a (90 % C.L.) [110].

While LENA cannot contribute to a improvement in the limit of the decay to $e^+\pi^0$, the limit on the $K^+\bar{\nu}$ decay channel could be improved by more than one order of magnitude[18]. This is caused by the distinct event characteristics of the prompt energy deposition by the K^+ followed by a delayed decay of the K^+ after $\tau_{K^+} \approx 12.4$ ns mainly by $K^+ \rightarrow \mu^+\nu_\mu$ (63.6 %) or $K^+ \rightarrow \pi^0\pi^+$ (20.7 %) [20]. As the energy of the initial K^+ is below the Cherenkov threshold, a water Cherenkov detector like Super-Kamiokande cannot benefit from this event topology. Therefore, the sensitivity of such a detector is limited by background due to atmospheric neutrinos. In a liquid scintillator detector, with good enough time resolution to resolve the two energy depositions, this background can be reduced efficiently by pulse shape discrimination. With LENA a sensitivity of $\tau_{\mathrm{p}}(p \rightarrow K^+\bar{\nu}) > 4 \cdot 10^{34}$ a (90 % C.L.) could be reached after 10 a of measurement, probing most of the allowed proton

---

[16] In the scope of this thesis, the favored scintillator mixture for LENA and other LAB based mixtures were investigated with regard to pulse shape discrimination performance for neutron and γ-ray induced events (see chapter 7).

lifetime range predicted by supersymmetric theories [18].

2.2.8. Long Baseline Neutrino Oscillations

As discussed in section 1.4, a promising way to determine the mass hierarchy (i.e. the sign of Δm_{23}^2) are long baseline neutrino beam experiments with baselines longer than $1000\,\text{km}$. Furthermore, there is a chance for the determination of the CP violating phase δ in such experiments.

A neutrino beam can be produced by shooting protons on a light target to create charged pions. These pions are focused into a decay tunnel, using a magnetic horn. In the decay tunnel the pions decay mainly via $\pi^\pm \to \mu^\pm + \overset{(-)}{\nu_\mu}$ [20]. By setting the polarity of the magnetic horn a beam of either ν_μ or $\bar{\nu}_\mu$ can be obtained. A detector searching for the mass hierarchy and CP violation in the leptonic sector will mainly use the electron neutrino appearance channel, i.e. the $\overset{(-)}{\nu_\mu} \to \overset{(-)}{\nu_e}$ oscillation [51].

In the scope of the LAGUNA-LBNO design study such a neutrino beam from the CERN to the Pyhäsalmi mine in a distance of $2300\,\text{km}$ was investigated. An upgrade of the SPS accelerator could deliver $1.5 \cdot 10^{20}$ protons with an energy of $400\,\text{GeV}$ per year, which corresponds to a power of $750\,\text{kW}$ [51]. The energy of the produced $\overset{(-)}{\nu_\mu}$-beam would range up to about $10\,\text{GeV}$. Therefore, the energy region around $4\,\text{GeV}$ is covered, for which the difference in the oscillation probabilities for normal and inverted hierarchy, caused by matter enhanced oscillations (see section 1.1.3), is maximal (see figure 1.3).

As the neutrino energies in the order of several GeV are rather high, a large enough detector is needed to fully contain the electron and muon tracks produced by charged current (CC) interactions. The size of LENA is sufficient, but to determine the mass hierarchy it is necessary to distinguish the CC interactions by the $\overset{(-)}{\nu_e}$ and $\overset{(-)}{\nu_\mu}$. This can be realized by analyzing the light signals resulting from the different track lengths for electrons and muons for a given energy. Background contributions are caused by oscillation of $\overset{(-)}{\nu_\mu}$ to $\overset{(-)}{\nu_\tau}$, which results in interactions mimicking both the $\overset{(-)}{\nu_e}$ and $\overset{(-)}{\nu_\mu}$ CC interactions, and the indistinguishable intrinsic contamination of the beam with $\overset{(-)}{\nu_e}$[17]. Furthermore, neutral current (NC) interactions can cause events similar to $\overset{(-)}{\nu_e}$ CC interactions. Nevertheless, this background can be discriminated by a small difference in the pulse shape compared to the $\overset{(-)}{\nu_e}$ CC interactions, resulting in a reduction by $89\,\%$, while the signal efficiency is reduced to about $27\,\%$ [111].

On the one hand, LENA is large enough to gather enough statistics with sufficient energy resolution in a long baseline experiment. On the other hand, the limited discrimination performance of different CC and NC interactions reduces the sensitivity. Nevertheless, LENA could allow for a determination of the mass hierarchy case with a significance of $5\,\sigma$ after 10 years of measurement, independent on the actual value of δ [52]. The sensitivity to determine the CP-violating phase δ with LENA is very low.

---

[17] This contamination is caused by the suppressed decay of the pions by $\pi^\pm \to e^\pm + \overset{(-)}{\nu_e}$ [20].

2.3. The JUNO Project

The Jiangmen Underground Neutrino Observatory (JUNO) is a planned reactor neutrino experiment in southern China with the purpose to determine the neutrino mass hierarchy (see sections 1.2 and 1.4), using a 20 kt liquid scintillator detector [19]. JUNO is designed to perform a high precision measurement of the electron antineutrino survival probability $P_{\bar{\nu}_e \to \bar{\nu}_e}$ (see equation (1.11) and figure 1.1) around the first oscillation minimum due to Δm_{21}^2 in order to unravel the small difference in the oscillation frequencies driven by Δm_{31}^2 and Δm_{32}^2 (see section 1.4.1). Due to the similarities to the proposed LENA detector, described in section 2.2, a comparable physics program apart from the determination of the mass hierarchy is possible.

2.3.1. Detector Setup

The JUNO detector is planned to be placed in a laboratory 700 m underground at an average distance of ~ 53 km to the Yangjiang and Taishan[18] nuclear power plants, which feature a total of 10 reactor cores with a summed thermal power of ~ 36 GW [112]. In order to resolve the small difference between the oscillations driven by Δm_{31}^2 and Δm_{32}^2 an unprecedented energy resolution of $3\,\%/\sqrt{E\,(\mathrm{MeV})}$ is needed. This corresponds to a photoelectron (p.e.) yield of at least 1200 p.e./MeV, which can be achieved under the requirements of an optical coverage by the PMTs of $\geq 75\,\%$, a PMT quantum efficiency of $\geq 35\,\%$ and an attenuation length[19] of the scintillator of ≥ 20 m [19].

The proposed scintillator is very similar to that favored by LENA and will be based on linear alkylbenzene (LAB) with the same amount of first wavelength shifter 2,5-diphenyloxazole (PPO) of 3 g/l. Compared to LENA, the currently favored concentration of the secondary wavelength shifter 1,4-bis(2-methylstyryl)benzene (bisMSB) is slightly lower with 15 mg/l [19]. The scintillator will have to be cleaned by combining different techniques in order to achieve the attenuation length needed to obtain the desired energy resolution and to reduce radioactive impurities.

In the currently favored configuration the scintillator with a total mass of ~ 20 kt will be contained in an acrylic sphere with an inner diameter of 35.4 m [19] (see figure 2.11). The emitted scintillation light will be read out by $\sim 17\,000$ 20 inch PMTs, which are planned to be installed on a stainless steel support structure at a radius of ~ 19.5 m. The same support structure will be used to stabilize the acrylic sphere. The detector will be contained in a cylindrical cavern and the volume outside the acrylic sphere will be filled with water, shielding the scintillator target from background due to radioactivity from the PMT glass, the support structure and the surrounding rock. The water volume will be instrumented with additional ~ 1600 PMTs and serve as an active muon veto with an estimated tagging efficiency of 99.8 %. In addition, an active muon veto with tracking capability will be placed on top of the detector.

---

[18] The Taishan nuclear power plant is still under construction.

[19] The attenuation length is defined as the distance, at which the intensity of a light beam is reduced to $1/e$ of its initial intensity [113].
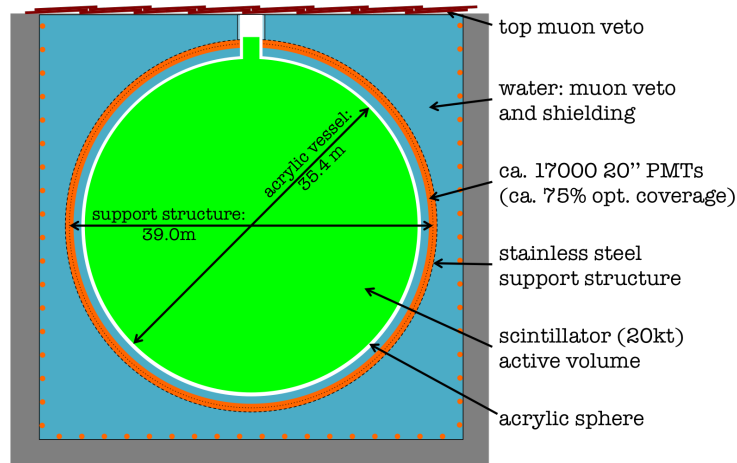
Figure 2.11.: Schematic view of the currently favored JUNO detector setup, reproduced based on [19].

2.3.2. Physics Program

The main goal of JUNO is the determination of the neutrino mass hierarchy. The reactor electron antineutrinos are detected via the inverse β-decay (IBD) described in section 2.1.2. As the scintillator will not be loaded with gadolinium, the produced IBD-neutrons are captured on hydrogen causing an energy deposition of $2.2\,\mathrm{MeV}$ about $200\,\mu\mathrm{s}$ after the prompt energy deposition of the positron. Due to the delayed coincidence signature the backgrounds are limited to those mimicking this coincidence. These are accidental coincidences, muon-induced fast neutrons, cosmogenic β-n-emitters ($^9\mathrm{Li}$ and $^8\mathrm{He}$) and fast neutrons produced through $^{13}\mathrm{C}(\alpha, n)^{16}\mathrm{O}$ reactions (see section 2.1.3). Due to the huge size of JUNO the contributions of the different backgrounds can be reduced efficiently by cuts on the spacial distance and time of the prompt and delayed events (mainly accidental background) and by vetoing events correlated to muons in time and space [19]. A reactor-$\bar{\nu}_e$ signal of about 67 events per day and a total background of about 3 events per day are expected. Based on a Fourier analysis of the measured reactor-$\bar{\nu}_e$ spectrum the mass hierarchy could be determined with a $\sim 4\,\sigma$ precision after a measurement of six years [112]. Figure 2.12 shows the expected $\bar{\nu}_e$ spectra without oscillation, for oscillation in case of normal neutrino mass hierarchy and for oscillation in case of inverted hierarchy [114]. As the differences in the oscillation pattern are on a scale of $\sim 100\,\mathrm{keV}$ the need for an excellent energy resolution of $3\,\%/\sqrt{E\,(\mathrm{MeV})}$ or better becomes obvious.

Besides the determination of the mass hierarchy, JUNO will be able to perform a high precision measurement of the oscillation parameters θ_{12}, Δm_{21}^2 and Δm_{32}^2 on a sub-percent level[20] [115]. This measurement will be complementary to the results, which will be obtained by long baseline accelerator neutrino experiments. Combining the results will offer an access to all seven neutrino mixing parameters within the three-neutrino framework, including the CP-violating phase δ [49].

---

[20] Mind that a precise determination of Δm_{32}^2 requires the knowledge of the mass hierarchy.
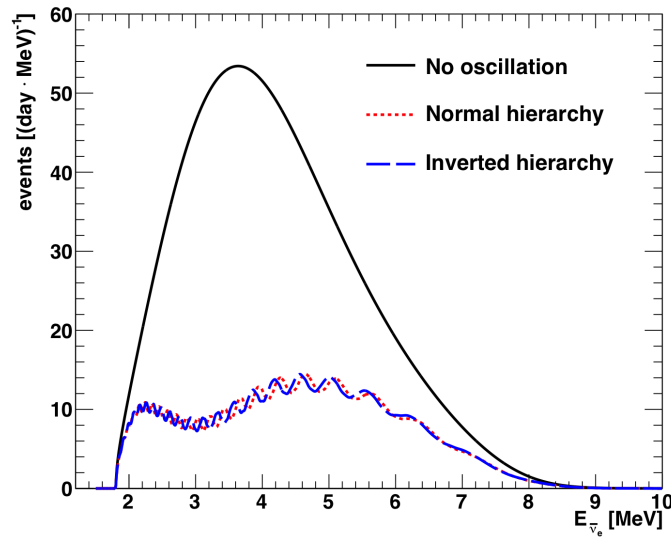
Figure 2.12.: Expected reactor $\bar{\nu}_e$ spectrum in the JUNO detector in case of no oscillation, for normal neutrino mass hierarchy and inverted hierarchy from [114].

Due to the similarities in size and detector technology JUNO can access similar neutrino physics fields as LENA. The measurement of geoneutrinos (see section 2.2.6) and solar neutrinos from different reactions of the pp-cycle (see section 2.2.5) seem to be challenging. While the detection of the geoneutrino flux is limited by the huge background of reactor neutrinos, the measurement of the solar neutrino fluxes is limited by a significantly increased muon induced background caused by the much smaller overburden compared to LENA [19].

Nevertheless, the detection of neutrinos from a galactic core collapse supernova (see section 1.5) is possible with high statistics, as this measurement is practically background free aside from ^{14}C background, which limits the detector threshold of scintillator detectors to about 200 keV. The expected supernova neutrino event rate in the different channels described in section 2.2.3 for LENA basically scales with the detector size, particularly if the used scintillator is almost the same. Under this assumption one would expect about 40 % (= 20 kt/50 kt) of the event rate expected in LENA, which results to a total of ~ 6500 events in case of a supernova at a distance of 10 kpc (compare to table 2.4). As neutrino-proton scattering is a major detection channel for supernova neutrinos of all flavors, a measurement regarding proton quenching (see chapter 6) is necessary in order to reconstruct the energy scale of the recoil protons. Furthermore, the pulse shape discrimination (PSD) performance regarding proton and electron recoils was measured for the favored LENA scintillator and other LAB based mixtures with different concentrations of PPO and bisMSB. PSD is a powerful tool to discriminate the neutrino-proton scattering events from background events due to ^{14}C and from SN neutrino events due to elastic neutrino-electron scattering.

Furthermore, JUNO will be sensitive to measure the diffuse supernova neutrino background (DSNB) (see section 1.5.4), which was studied in an analysis similar to the one used for

LENA (see section 2.2.4) [101, 116]. The main backgrounds for the detection of $\bar{\nu}_e$ from the DSNB are reactor neutrinos, charged current (CC) and neutral current (NC) interactions of atmospheric neutrinos. As JUNO is a reactor neutrino experiment, the reactor-$\bar{\nu}_e$ background will be orders of magnitudes higher compared to LENA. To compensate for that the lower analysis threshold needs to be increased from 9.5 MeV to 11 MeV. Due to the low geographical latitude of JUNO, background caused by atmospheric neutrinos is significantly reduced in comparison to LENA. In consequence, the upper analysis threshold can be increased from 25 MeV to 30 MeV. The background due to NC interactions of atmospheric neutrinos on ^{12}C (see section 2.2.4) can be reduced efficiently by PSD analysis. The signal efficiency of 50 % and the background reduction to 1.1 % were assumed to be similar to LENA, while a positive effect due to the substantially increased light collection of JUNO is expected. As a result of the analysis a DSNB signal of $6.1 - 30.8$ events for different mean neutrino energies $\langle E_\nu \rangle$ between 12 MeV and 21 MeV and a total background of 9.2 events are expected after 10 years of measurement. With an assumed 5 % systematical uncertainty of the backgrounds the DSNB can be detected with a significance of almost $2\,\sigma$ for $\langle E_\nu \rangle = 12$ MeV and more than $3\,\sigma$ for $\langle E_\nu \rangle \geq 15$ MeV [116]. As for the analysis performed for LENA, the results are based on PSD parameters measured in a beam time at the Maier-Leibnitz-Laboratorium (MLL) in August 2012 [100]. In chapter 7 results for the PSD performance regarding proton and electron recoils of different LAB-based scintillator samples, obtained from measurements in two beam times in 2014, will be presented.

As a part of the JUNO collaboration is also involved in the Borexino experiment [11, 75], this well understood detector can be used to test analysis methods and study background contributions and rejection techniques.

3. Organic Liquid Scintillator - an Overview

Organic liquid scintillators are widely-used in neutrino physics Experiments, like Borexino [75], KamLAND [10] and Double Chooz [33] use and future experiments, like the LENA [18] and JUNO [19] projects, plan to use organic liquid scintillators to detect neutrinos from various sources. Organic liquid scintillators are rather cheap detector materials, making large scale detectors with up to several kilotons of target material possible. In comparison to water, in which light is only produced by the Cherenkov effect, low energy thresholds in the region of few hundred keV can be realized [75].

The scintillation mechanisms in organic liquid scintillators originates from the electronic structure of conjugated aromatic molecules. An introduction to the scintillation mechanism and the energy transfer processes in scintillator mixtures containing multiple aromatic compounds will be given in section 3.1.

A feature of liquid scintillators is the so-called quenching effect, which is a nonlinear response to different amounts of energy deposited by a certain particle type and will be introduced in more details in section 3.2. This nonlinearity needs to be characterized for each scintillator mixture and particle type. The characterization of the energy response to neutron induced protons with energies up to $\sim 11\,\mathrm{MeV}$ is a major topic of this thesis (see chapter 6).

A further characteristic of organic liquid scintillators is the scintillation pulse shape in terms of the photon emission time, which varies for different kinds of ionizing particles and is somehow correlated to the quenching effect. In section 3.3 this effect will be discussed in more detail. The differences in the shape can be used to identify and distinguish between different particle types. Measurements for various scintillator mixtures regarding the pulse shape differences for energy depositions by electrons and protons will be presented in chapter 7. The used scintillator ingredients and investigated mixtures will be introduced in section 3.4.

3.1. Optical Model of Liquid Scintillators

Organic liquid scintillators are based on conjugated aromatic molecules - mostly benzene rings. To understand the light emission of organic liquid scintillators one has to understand the electronic structure of the scintillator molecules.

3.1.1. Electronic Structure of Aromatic and Conjugated Organic Molecules

While the electronic configuration of a C atom is $1s^2 2s^2 2p^2$, the configuration for C atoms in chemical bonds is considered to be $1s^2 2s^1 2p^3$, which means that one of the $2s$ electrons is excited into a $2p$ state [117]. In aromatic and conjugated organic molecules the orbitals corresponding to the $2s$ electron and two of the $2p$ electrons form three equivalent hybrid orbitals, which lie in the same plane forming angles of $120°$ to each other [117]. This configuration is called sp^2 *hybridization* and is responsible for the planar and hexagonal ring structure of benzene. These three hybrid orbitals are called σ-electrons and the corresponding bonds are known as σ-bonds. Figure 3.1(a) shows a schematic view of the σ-bonds of benzene. The σ-bonds form the rigid skeletons for the organic molecules and are too strong to contribute to the production of scintillation photons in the desired optical range (wavelenths $\lambda > 200\,\text{nm}$).

The third and remaining $2p$ orbital of the C atoms is called π-electron and is symmetric to a nodal plane, which coincides with the plane formed by the three σ-bonds [117]. These orbitals from the six C atoms, which build the benzene ring, combine to six fully delocalized orbitals, so-called π-orbitals. Effectively, three additional bonds, which are fully delocalized in the hexagonal structure of the benzene molecule, are formed. A schematic picture of these π-bonds in benzene is shown in figure 3.1(b). In other aromatic and conjugated organic molecules similar systems of delocalized π-electrons are formed. The excited states of the π-electrons are responsible for the scintillation light in the desired optical range above $\lambda \gtrsim 200\,\text{nm}$.

(a)   (b)
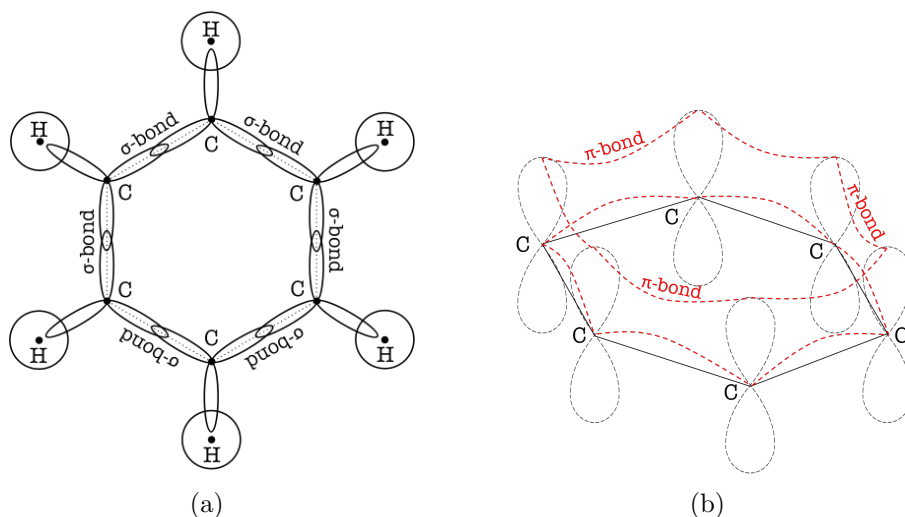
Figure 3.1.: Schematic views of the electronic structure of benzene according to [117]. (a) depicts the σ-bonds responsible for the hexagonal structure and (b) illustrates the formation of the delocalized π-bonds.

3.1.2. Exited π-States and Luminescence

Figure 3.2 shows a Jabłoński diagram [118] for the energy states of the π-electrons of a general aromatic or conjugated organic molecule. The singlet states, corresponding to antiparallel spin configuration of the two electrons in a π-bond, are denoted by S_i, where $i = 0$ belongs to the ground state and $i \geq 1$ to the excited states. The triplet states, in which both electrons have parallel spins, are marked by T_i $(i \geq 1)$. The energy levels of the triplet states are different to those of the singlet states and, therefore, drawn separately.

The energy spacing between singlet states was found to be in the region of $\sim 2 - 4.5\,\mathrm{eV}$ [117]. The energy levels shown by the dashed lines in figure 3.2 indicate the vibrational substates. They are labeled by S_{ij}, where i gives the electromagnetic state and j the vibrational substate. The energy differences of these vibrational substates are in the order of $0.1\,\mathrm{eV}$.

Figure 3.2.: Schematic Jabłoński diagram of the energy levels of π-electrons in an aromatic or conjugated molecule according to [117]. S_0 is the ground state and $S_1, S_2, \ldots$ are the excited singlet states. $T_1, T_2, \ldots$ denote the excited triplet states. $S_{00}, S_{01}, \ldots$ are vibrational sub-levels and I_π the ionization energy for the π-electrons. Luminescence photons are emitted by radiative deexcitation of either the singlet state S_1 (fluorescence) or the triplet state T_1 (phosphorescence) to vibrational sub-levels of the ground state.

Molecules in the ground state S_0 can be excited by photons or ionizing particles to the higher singlet states $S_1, S_2, \ldots$ and their vibrational substates $S_{i0}, S_{i1}, \ldots$. States with $i > 1$, which have a lifetime in the order of 10^{-11} s, rapidly deexcite to vibrational substates of S_1 by radiationless internal conversion between adjacent electronic states [117]. The vibrational substates thermalize even more quickly with lifetimes of $\sim 10^{-12}$ s, until the molecule finally reaches in the S_{10} state. The radiative lifetime of this state is in the order of 10^{-9} to 10^{-8} s. Molecules in the S_{10} state deexcitite to the ground state and its vibrational substates with relative intensities given by the Franck-Condon factors [119, 120], which take the overlap of the vibrational wavefunctions into account. The radiation emitted in the transition from S_1 to the S_0 states is called *fluorescence* and accounts for the fast component of the *luminescence* occurring in organic liquid scintillators.

Excited triplet states $(T_1, T_2, \ldots)$ cannot be populated directly from the ground state due to a necessary spin-flip of one of the contributing π-electrons [117]. Nevertheless, the first excited triplet state T_1 can be populated by the transition $S_1 \rightarrow T_1$. The underlying process is called *inter-system crossing* and causes a spin flip by a spin-orbit coupling. Triplet states are populated more efficiently by preceding ionization of organic molecules. The ion recombines with an electron mainly to excited states, from which about 75% are triplet states [117]. In analogy to the singlet states, higher excited triplet states rapidly decay to the T_{10} state by internal conversion followed by a quick thermalization of the vibrational substates. The radiative transition of the T_{10} state to one of the vibrational substates of ground state S_0 is highly forbidden. Therefore, the lifetime in the order of 10^{-4} s is rather long compared to the timescale of fluorescence. The emitted radiation is called *phosphorescence*.

At higher temperatures the lifetime of the T_1 state can be reduced by several processes. A molecule excited to the T_1 state may gather enough thermal energy during its lifetime to return to S_1. Another possible process is the interaction of two excited molecules in T_1 by

$$T_1 + T_1 \longrightarrow S_i + S_0 \longrightarrow S_0 + S_0 + \textit{fluorescence} \,, \tag{3.1}$$
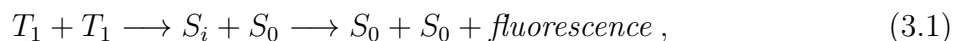
resulting in one molecule in an exited singlet state S_i ($i \geq 1$) and the other in the ground state. Both examples result in a *delayed fluorescence* with a lifetime in the order of $\sim 10^{-7} - 10^{-6}$ ns, depending on the energy gap between S_1 and T_1, the temperature and the ionization density. The latter directly affects the density of excited triplet states and, therefore, the probability for a process according to equation (3.1). Delayed fluorescence mainly accounts for the slow component of the luminescence of organic scintillators. The contribution of phosphorescence to the luminescence of liquid scintillators plays a minor role due to its long decay time compared to delayed fluorescence.

3.1.3. Multicomponent Scintillators

Organic liquid scintillators commonly consist of a *solvent* with one or two admixed *solutes* or *fluors*. The solvent as well as the solutes consist of aromatic or conjugated molecules. Due to a significant overlap of the emission and absorption spectra of the solvent self-

absorption reduces the amount of detectable luminescence photons in single-component scintillators. This can be resolved by adding a second aromatic or conjugated organic substance with a smaller energy gap between the ground state S_0 and the first excited singlet state S_1 than the solvent. The concentration of the first solute are normally in the order of $\sim 1-10\,\mathrm{g/l}$, which corresponds to a mass fraction of $\lesssim 1\,\%$. The emission spectrum of the solute is shifted to longer wavelengths compared to that of the solvent. Therefore, solutes are also commonly called *wavelength shifters*. Due to the low concentration self-absorption of the solute only plays a role for large scale detectors. By admixing a second solute with concentrations in the order of $\sim 10\,\mathrm{mg/l}$ the emission spectrum can be shifted to even longer wavelengths, which further reduces the effect of self-absorption.

Figure 3.3 shows a simplified diagram of the energy transfer processes in a three-component liquid scintillator mixture. The contribution of each scintillator component is highlighted by a colored box. Essentially, all π-electron excitation energy caused by a ionizing particle ends up in excited solvent molecules (in the following refered to as *primary excitation*) [117, 121]. Due to typically small concentrations of the first solute and a even smaller concentrations of the second solute primary excitation of those can be neglected. As described above (see section 3.1.2) the excitation energy of molecules in higher singlet states rapidly dissipate energy by internal conversion and thermalization of vibrational states until the first excited singlet state S_1 is reached. The remaining excitation energy is either emitted radiatively or dissipated thermally with a certain probability - a process refered to as *internal quenching* (processes (1), (8) and (15) for solvent and both solutes in figure 3.3) and not to be confused with quenching due to high ionization and excitation densities as described in section 3.2.

The primary excitation energy of the solvent molecules is rapidly (timescale of $\sim 10^{-11}\,\mathrm{s}$) brought to the vicinity of a primary solute molecules by thermal diffusion and nonradiative solvent-solvent transfer [117, 121] (process (5) in figure 3.3). Radiative transfer of excitation energy between solvent molecules (process (4) in figure 3.3) appears on a timescale similar to that of fluorescence emission and therefore plays a minor role.

The energy transfer to a molecule of the first solute is mainly nonradiative and caused by a long-range dipole-dipole interaction [117, 121] (process (6) in figure 3.3). The rate k of the transfer by this dipole-dipole interaction between two molecules with a distance R to each other, which is also called Förster interaction, is given by [122]:

$$k = \frac{1}{\tau_0}\left(\frac{R_0}{R}\right)^6 \tag{3.2}$$

where τ_0 is the lifetime of the first excited singlet state of the solvent. R_0 is the critical distance at which the excitation transfer has an equal probability as the deexcitation by emission or internal quenching and is commonly called *Förster rasius*. Typical values of R_0 are in the range of $\sim 20-60\,\text{Å}$ and depend on the overlap between the emission spectrum of the solvent and the absorption spectrum of the first solute [121]. Compared to typical diameters of organic molecules in the order of about 6 Å this is rather large distance.

Due to the small concentration of the second solute in the order of $\sim 10\,\mathrm{mg/l}$ it is rather
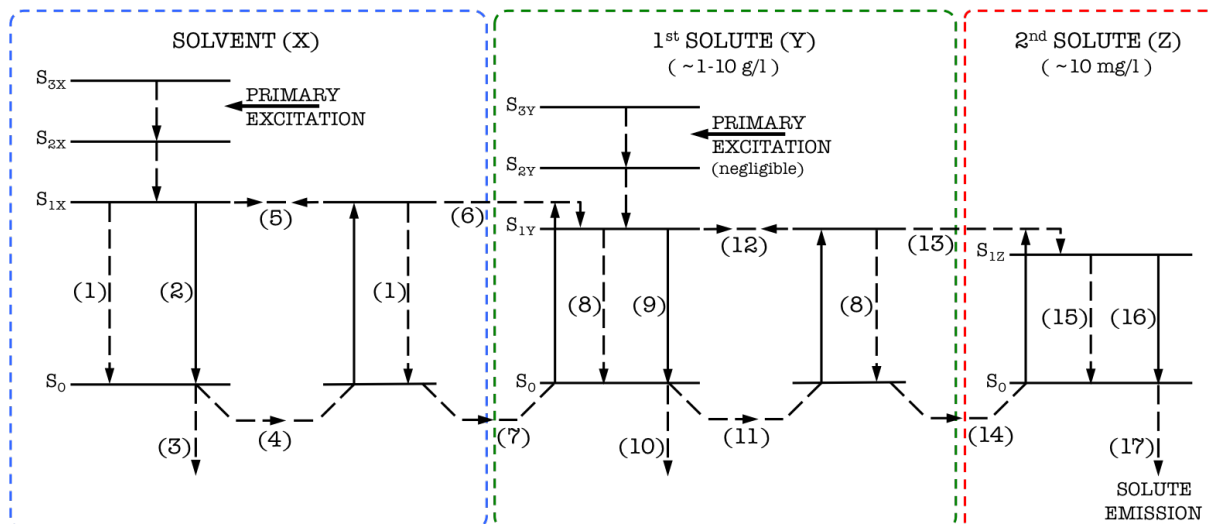
Figure 3.3.: Simplified diagram of the energy transfer processes in a three-component liquid scintillator solution according to [117, 121]. The transfer processes within and between solvent molecules (blue box) are: (1) internal quenching, (2) emission, (3) escape of light, (4) radiative migration and (5) nonradiative migration. The excitation energy can be transfered to the first solute either (6) nonradiatively or (7) radiatively. The transfer processes within and between molecules of the first solute (green box) are: (8) internal quenching, (9) emission, (10) escape of light, (11) radiative migration and (12) nonradiative migration. (13) and (14) denote the nonradiative and radiative transfer from the first to the second solute. The processes within a molecules of the second solute (red box) are: (15) internal quenching, (16) emission and (17) escape of light. The primary excitation by a ionizing particle basically ends up in primary excitation of the solvent molecules. Due to a normally small concentration of the first and a even smaller concentration of the second solute primary excitation of solute molecules can be neglected.

unlikely to find a molecule in the closer vicinity of an excited molecule of the first solute. Therefore, the transfer of excitation energy from the first to the second solute is only partly caused by the dipole-dipole interaction described above (process (13) in figure 3.3). Radiative transfer, i.e. emission by the first solute and absorption by the second solute, plays an important role here [117] (process (14) in figure 3.3). With increasing concentration the contribution of the radiative component decreases while that of the nonradiative transfer increases.

In some applications of organic liquid scintillators it is beneficial to dilute the solvent with a nonscintillating organic component, which is typically free of aromatic and conjugated compounds. For example, this can be useful to increase the transparency of the scintillator solution. Furthermore, adding saturated hydrocarbons increases the number of protons in the liquid and, therefore, the target density for the detection of electron antineutrinos by the inverse β-decay (see equation (2.1) in section 2.1.2). Admixture of such *diluters* reduces the efficiency of the solvent-solvent energy transfer, which is partly based on direct contact of the molecules. Nonscintillating molecules do not participate in the energy transfer process,

but rather block the solvent molecules to get in direct contact to each other. Therefore, diluters can inhibit the solvent-solvent energy transfer, which brings the primary excitation to the vicinity of molecules of the first solute.

The emission spectrum of a multicomponent scintillator solution is essentially that of the first solute in case of a two-component and that of the second solute in case of a three-component scintillator. Commonly, a second solute is chosen in that way that it matches the sensitive region of the used photosensors thereby increasing the number of detected photons for a given deposited energy.

3.2. Light Output and Quenching

A minimal ionizing particle depositing its kinetic energy E (for example an electron with an energy of $1\,\mathrm{MeV}$) creates primary excitations and ionizations of solute molecules spaced several molecular distances apart from each other. Hence, the probability for interactions between the excited or ionized molecules are rather small. In that case, the light output L of an organic scintillator per unit path length $\mathrm{d}x$ can be described by a linear relation [117]:

$$\frac{\mathrm{d}L}{\mathrm{d}x} = S\,\frac{\mathrm{d}E}{\mathrm{d}x} \tag{3.3}$$

with $\frac{\mathrm{d}E}{\mathrm{d}x}$ being the energy loss of the ionizing particle and S being the absolute scintillation light yield, which can be derived for a two-component scintillator by [117]:

$$S = \frac{PC}{E_{1\mathrm{X}}}\,f_{\mathrm{XY}}\,q_{0\mathrm{Y}}\cdot 10^6\,\tfrac{\mathrm{ph}}{\mathrm{MeV}} \tag{3.4}$$

where P is the primary excitation efficiency and $C = \frac{E_{1\mathrm{X}}}{E_{\mathrm{eX}}}$ is the fraction of the mean excitation energy E_{eX}, which contributes to fluorescence transitions of the solvent (X) from the first excited singlet state $E_{1\mathrm{X}}$ or is transfered to the solute (Y). The quantum efficiency of this transfer of excitation energy to the solute is given by f_{XY}. $q_{0\mathrm{Y}}$ describes the fluorescence quantum efficiency of the solute, which is limited by internal quenching. About $\frac{2}{3}$ of the energy deposited by a ionizing particle is expended in molecular excitation and ionization of both σ- and π-electrons. With the fraction of π-electrons $F_\pi \sim 0.1-0.15$ in the used aromatic compound P can be estimated to be

$$P \sim \tfrac{2}{3}\,F_\pi \lesssim 0.1\ . \tag{3.5}$$

For a three-component scintillator equation (3.4) has to be modified as follows [117]:

$$S = \frac{PC}{E_{1\mathrm{X}}}\,f_{\mathrm{XY}}\,f_{\mathrm{YZ}}\,q_{0\mathrm{Z}}\cdot 10^6\,\tfrac{\mathrm{ph}}{\mathrm{MeV}} \tag{3.6}$$

where the additional factor f_{YZ} is the quantum efficiency of the transfer of excitation energy from the first solute (Y) to the second solute (Z). The fluorescence quantum efficiency of the first solute $q_{0\mathrm{Y}}$ is replaced by that of the second solute $q_{0\mathrm{Z}}$.

Slow electrons or heavier ionizing particles, like protons or α-particles, are not minimal ionizing, featuring a higher energy loss $\frac{\mathrm{d}E}{\mathrm{d}x}$ in the scintillator. Energy depositions by such particles result in higher densities of excited and ionized solvent molecules, which can interact by reactions like:

$$S^* + S^* \longrightarrow S^+ + S_0 + e^- \tag{3.7}$$

Ionized π-electrons recombine preferably to excited triplet states with a fraction of about 75 % [117]. Excited triplet states are only partly converted to excited singlet states by reactions as given in equation (3.1), which decreases the quantum efficiency f_{XY}. In consequence, the fluorescence light yield is reduced for higher excitation and ionization densities. This effect is called *ionization quenching* and causes a nonlinear behavior of the scintillation light yield for energy depositions by a certain particle type.

A semi-empirical model, which takes the influence of an increased excitation and ionization density due to a higher energy losses $\frac{\mathrm{d}E}{\mathrm{d}x}$ into account, is given by Birk's formula, which is a modification of equation (3.3) [117]:

$$\frac{\mathrm{d}L}{\mathrm{d}x} = \frac{S\,\frac{\mathrm{d}E}{\mathrm{d}x}}{1 + kB\,\frac{\mathrm{d}E}{\mathrm{d}x}} \tag{3.8}$$

where $B\,\frac{\mathrm{d}E}{\mathrm{d}x}$ is the specific density of excited and ionized molecules along the particle path and k a parameter describing the strength of the quenching effect. With time the parameters B and k were combined to the so-called kB- or Birks-factor. The energy loss of different ionizing particles $\frac{\mathrm{d}E}{\mathrm{d}x}$ can be obtained for example from the Bethe-Bloch-formula or the ESTAR, ASTAR and PSTAR databases [123], which provide the energy losses of electrons, α-particles and protons for various materials.

To obtain the light output L due to a particle depositing its kinetic energy E_{dep} in the scintillator equation (3.8) has to be integrated over the whole particle path:

$$L = \int_0^R \frac{S\,\frac{\mathrm{d}E}{\mathrm{d}x}(x)}{1 + kB\,\frac{\mathrm{d}E}{\mathrm{d}x}(x)}\,\mathrm{d}x = \int_0^{E_{\mathrm{dep}}} \frac{S}{1 + kB\,\frac{\mathrm{d}E}{\mathrm{d}x}(E)}\,\mathrm{d}E \tag{3.9}$$

with R being the range of the particle. The energy loss $\frac{\mathrm{d}E}{\mathrm{d}x}$ is thereby dependent on the current energy of the particle at each integration step.

Figure 3.4 shows the resulting light output for protons for different values of the quenching parameter kB. The light output is given in terms of visible energy, which is the energy detectable by emitted scintillation photons compared to electron depositing the same amount of energy. In case of no quenching ($kB = 0\,\mathrm{cm/MeV}$) the visible energy equals the deposited energy. The values for the energy dependent proton energy loss were calculated for linear alkylbenzene (see section 3.4.1) from data based on the PSTAR-database [123] (see section 6.5.1 for details). Figure 3.4 shows that with rising values for kB the amount of emitted light (here visible energy) decreases drastically. Especially at lower energies the energy response is highly nonlinear. Typically, liquid organic scintillator have kB-values in the order of $\sim 0.01\,\mathrm{cm/MeV}$, which results in a reduction of the emitted light by protons by a factor of $\sim 2-3$ compared to electrons depositing the same amount of energy.
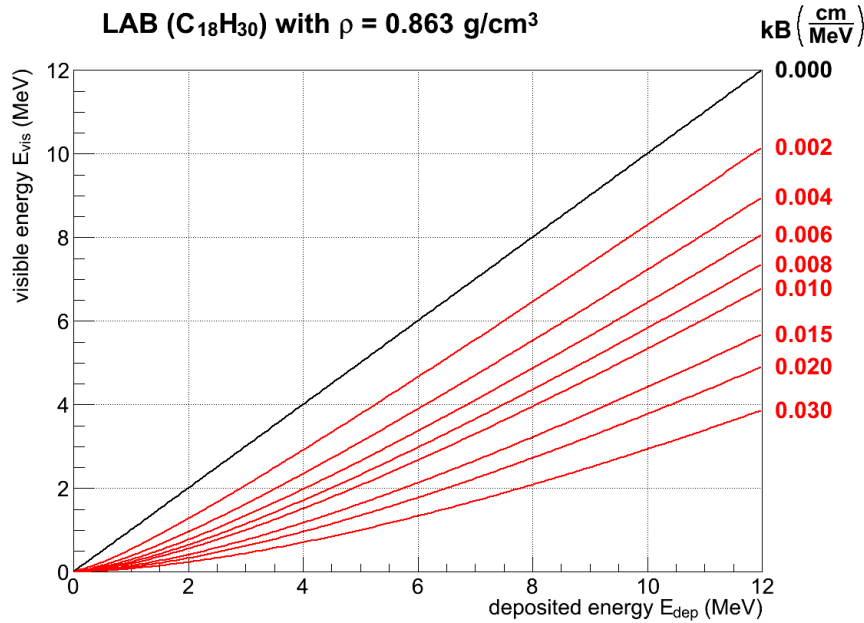
Figure 3.4.: The scintillation output in terms of visible energy for protons in LAB and different values for kB according to equation 3.9. Values for the energy dependent energy loss were calculated for LAB (effective formula $C_{18}H_{30}$) with a density of $0.863\,\mathrm{g\,cm^{-3}}$ based on data from the PSTAR database [123] as described in section 6.5.1.

It was found that ionization quenching shows no effect on the scintillation decay times [117]. Therefore, quenching appears at a time scale, which is faster than that of fluorescence emission. The quenching time scale lies in the order of $\sim 10^{-9}\,\mathrm{s}$ and is limited by the time scale of the ion recombination, rapid dissipation of excessive vibrational energy to neighboring isotopes and migration of π-electronic excitation energy away from the ionization column (see solvent-solvent energy transfer in section 3.1.3).

3.3. Scintillation Pulse Shape and Particle Identification

As discussed in section 3.1.2, fluorescence emission following direct excitation of π-electronic states of organic molecules accounts for the fast component of the emission in the order of $\sim 1-10\,\mathrm{ns}$. Due to the underlying deexcitation of the first excited singlet state S_1 to the vibrational sublevels of the ground state S_0 the time behavior follows an exponential decay:

$$N(t) = N_0 \cdot e^{-\frac{t}{\tau}} \tag{3.10}$$

with $N(t)$ and N_0 the number of excited states at time t and $t = 0$, respectively, and τ the lifetime of S_1.

The slow component of a liquid scintillator is mainly caused by the deexcitation of π-electronic triplet states populated by recombination of ionized molecules. Different possible processes for the deexcitation of the first excited triplet state T_1 to the ground state S_0

(like those described in section 3.1.2) lead to different individual time behaviors, which are not necessarily exponential. The timescale of those processes range from several 10 ns to several μs. Therefore, the shape of the decay of the slow component is complex and cannot be described by a single exponential. The processes leading to the shape of the slow component are not fully understood to this point.

A commonly used empiric approach to model the scintillation time decay is the approximation by a sum of several exponential decays (see for example [100, 124, 125]):

$$N(t) = \sum_{i=0}^{N_{\mathrm{max}}} N_i \cdot e^{-\frac{t}{\tau_i}} \qquad (3.11)$$

where N_i are the numbers of excited states at $t = 0$ contributing to component i and τ_i the corresponding lifetime. Typically, the scintillation pulse shape is empirically described by a total number of three or four components (i.e $N_{\mathrm{max}} = 3, 4$) [100, 124, 125].

In case of multicomponent scintillators a finite rise time has to be taken into account, which originates from the different flourescence decay times of solvent and solutes [117]. Furthermore, the timescales for the migration of excitation energy between solute molecules and transfer to the first (and second) solute (see section 3.1.3) play a role.

The shape of the fast and slow component were found to be basically independent of the excitation and ionization density, i.e. the energy loss $\frac{\mathrm{d}E}{\mathrm{d}x}$ of an ionizing particle [117]. Nevertheless, the relative amplitudes of the fast and slow component change for different types of ionizing particles. For higher excitation and ionization densities due to energy depositions by heavy particles the fraction of excited triplet states is increased as already described in section 3.2. In consequence the relative amplitude of the slow scintillation component is enhanced.

This dependency of the scintillation pulse shape on the particles energy loss can be used to distinguish energy depositions by different types of particles by pulse shape discrimination (PSD). Figure 3.5 shows a qualitative comparison of the pulse shapes for electrons, protons and α-particles in an organic scintillator. The normalization to the pulse height highlights the enhanced slow component for increasing mass of the incident particle.

There are various methods to parameterize the pulse shape differences. In this thesis the so-called *tail-to-total* method will be used, which is based on the ratio of two integrals over the recorded scintillation pulse. One integral covers the total pulse - the *total* - and the other the tail region - the *tail*. Please see chapter 7 for more details on this method. Another example for a method commonly used for pulse shape discrimination is the so called *Gatti* method [126], which is based on the comparison between each recorded pulse and average template pulses for each particle type. See for example [100] for a more detailed explanation.
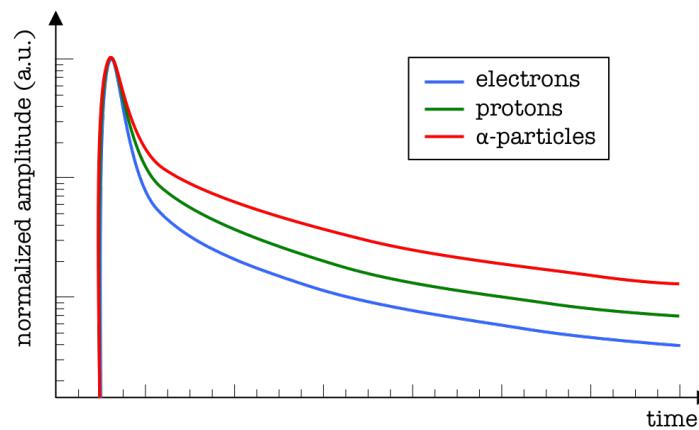
Figure 3.5.: Qualitative comparison of the scintillation pulse shape for electrons, protons and α-particles based on [117]. The pulse amplitude (normalized to the pulse height) is shown as a function of time on a logarithmic scale.

3.4. Properties of The Used Scintillator Components and Sample Preparation

There are various kinds of organic solvent and solute materials available to be used for liquid scintillator solutions. Here those used for the scintillator mixtures investigated in this thesis will be presented briefly.

3.4.1. Solvents

In table 3.1 the main properties of the solvents used for the investigated scintillator mixtures are summarized, featuring the names, densities, chemical and structural formulae, the CAS-numbers[1] and providing companies. Furthermore, the peak absorption and emission wavelengths are given according to [124, 127].

The solvent *phenyl-o-xylylethane* (PXE) was used for the Double Chooz scintillators for the neutrino target and gamma catcher volumes (see section 2.1) [131]. *Pseudocumene* (PC) or *1,2,4-trimethylbenzene* is the solvent used in the Borexino experiment [11]. Compared to PXE and PC *linear alkylbenzene* (LAB) is a scintillator solvent, which is rather new in neutrino physics. LAB is already used for the muon veto scintillator in Double Chooz (see section 2.1) and is, for example, planned to be used in the SNO+ experiment [132]. Furthermore, the future projects LENA (see section 2.2) and JUNO (see section 2.3) favor LAB-based liquid scintillators because of its good performance and low cost - it is a common ingredient of commercial detergents and, therefore, produced industrially in huge amounts. In this thesis various LAB-based mixtures were investigated with regard to future use in the proposed LENA and JUNO detectors.

---

[1] Unique identifier for chemical substances assigned by the Chemical Abstracts Service (CAS).
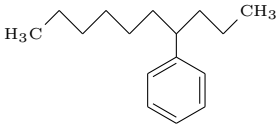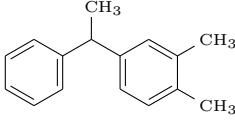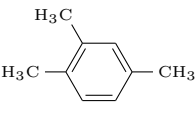
name	**LAB** linear alkylbenzene	**PXE** phenyl-o-xylylethane	**PC** pseudocumene
structural formula			
chemical formula	$C_9H_{12}(CH_2)_n$ ($n = 7$-10)	$C_{16}H_{18}$	C_6H_{12}
density	$0.863\,g/cm^3$	$0.986\,g/cm^3$	$0.880\,g/cm^3$
emission max.	$283\,nm$	$290\,nm$	$290\,nm$
absorption max.	$260\,nm$	$270\,nm$	$267\,nm$
CAS number	67774-74-7	6196-95-8	95-63-6
company	Helm [128]	Dixie Chemicals [129]	EniChem [130]

Table 3.1.: Main properties of the used scintillator solvents LAB, PXE and PC. Wavelengths for maximum absorption and emission are given according to [124, 127].

3.4.2. Wavelength Shifters

Solvents usually feature a significant overlap of their emission and absorption spectra and, therefore, suffer from selfabsorption. To resolve this problem additional luminescent aromatic substances are added. These are called *solutes*, *fluors* or *wavelength shifters*. Table 3.2 shows the main properties of the solutes used for the scintillator mixtures studied in this thesis.

Both used solutes are solids and can be purchased in form of powders. *2,5-diphenyloxazole* (PPO) is commonly used as primary solute with an absorption maximum close to the emission maxima of LAB, PXE and PC. It is used in typical concentrations in the range of $1 - 10\,g/l$ and efficiently shifts the emitted scintillation light by $\sim 60\,nm$ to longer wavelengths. Due to the selfabsorption of PPO, which can be relevant in case of large scintillator detectors, a second solute is used. A commonly used second solute is *1,4-bis(2-methylstyryl)benzene* (bisMSB), which has an emission spectrum nicely matching the sensitive wavelength region of most photosensors. It further shifts the emitted scintillation light by another $\sim 55\,nm$ to longer wavelengths. Typical concentrations in the order of few $10\,mg/l$ significantly reduce the effect of selfabsorption.

3.4.3. Diluters

There are several reasons to dilute the scintillator solvent with nonscintillating organic liquids, which contain no aromatic compounds. Firstly, those liquids feature a high op-

name	**PPO**	**bisMSB**
	2,5-diphenyloxazole	1,4-bis(2-methylstyryl)benzene
structural formula		
chemical formula	$C_{15}H_{11}NO$	$C_{24}H_{22}$
absorption max.	303 nm	345 nm
emission max.	365 nm	420 nm
CAS number	92-71-7	13280-61-0
company	PerkinElmer [133]	
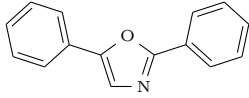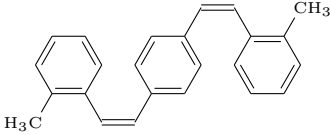
Table 3.2.: Main properties of the used first solute PPO and second solute bisMSB. Wavelengths for maximum absorption and emission are given according to [124, 127].

tical transparency and, therefore, increase the transparency of the scintillator solution. Additionally, nonscintillating organic liquids, which are typically saturated hydrocarbons, increase the number of protons in the mixture. This is important for reactor neutrino experiments, which detect electron antineutrinos via the inverse beta decay (see equation (2.1) and section 2.1.2). In table 3.3 the diluters used in the investigated scintillator solutions are summarized.

Dodecane and *n-paraffine* are both liquids containing saturated hydrocarbon chains. While dodecane has a chainlength with twelve carbon atoms, n-paraffine consists of a mixture with chainlengths between $10-13$. Dodecane was used to increase the proton number in the target and gamma catcher scintillators for Double Chooz (see section 2.1)[131]. To reduce buoyant forces in the Double Chooz detectors, which consist of four interlaced volumes, the densities of the different liquids needed to be matched. To do so, *Ondina 909*, which is a highly refined mineral oil, was used to adjust the density of the gamma catcher to that of the target scintillator [131]. Like dodecane and n-paraffine it consists of saturated hydrocarbons, but contains branched chains (isoalkenes) and saturated cyclic components. The number of carbon atoms per molecule ranges from 13 to 23. To adjust the density of the Double Chooz muon veto scintillator n-paraffine was used [137]. Furthermore, LAB-based scintillators diluted with different amounts of n-paraffine were studied regarding PSD performance and quenching in the scope of this thesis.

name	**n-dodecane**	**n-paraffine**	**Ondina 909** mineral oil
structural formula			saturated hydrocarbons (linear & cyclic)
chemical formula	$C_{12}H_{26}$	C_nH_{2n+2} (n = 10-13)	C_{13} to C_{23}
density	$0.749\,g/cm^3$	$0.749\,g/cm^3$	$0.825\,g/cm^3$
CAS number	112-40-3	929-018-5	8042-47-5
company	Japan Energy [134]	CBR [135]	Shell [136]

Table 3.3.: Main properties of the used diluters n-dodecane, n-paraffine and the light mineral oil Ondina 909.

3.4.4. Investigated Scintillator Mixtures

In total 15 different scintillator mixtures were studied in three beam times performed at the Maier-Leibnitz-Laboratorium (Garching) in the scope of this thesis (see section 4.5). Four of the investigated samples stem from the presently running neutrino experiments Double Chooz and Borexino.

For Double Chooz the scintillators from target (DCTarget), gamma catcher (DCGC) and muon veto (DCMV) were studied. The compositions of these scintillators are summarized in table 3.4. The DCTarget and DCGC scintillators were developed and produced by a group of MPIK[2] Heidelberg [131], while the DCMV scintillator was developed at TUM [137, 138]. The DCTarget and DCMV samples both stem from the Double Chooz far detector[3]. The sample of the DCGC scintillator was taken from the batch produced for the Double Chooz near detector (prior to the filling of the detector).

The Borexino scintillator consists of PC as solvent and 1.5 g/l PPO as solute [11]. Due to the use of photosensors matching the emission spectrum of PPO no second solute was added. The investigated sample was taken in 2013 from the Borexino detector.

A total of eleven LAB-based scintillator mixtures with different concentrations of the solutes PPO and bisMSB and dilutions with n-paraffin were investigated in the scope of this thesis. All samples were prepared at TUM by Dr. Hong Hanh Trinh Thi[4] using LAB, PPO, bisMSB and n-paraffine from the same batch, respectively [137]. The investigated LAB-based scintillator mixtures can be divided into three groups:

---

[2] Max-Planck-Institut für Kernphysik

[3] The samples were extracted not from the detector directly, but from the last vessel of the filling system before the detector.

[4] Chemist at the TUM chair in experimental physics and astroparticle physics (E15)

scintillator	composition	
Target [131]	$80\,\%_{vol}$	dodecane
(DCTarget)	$20\,\%_{vol}$	PXE
	$4.5\,g/l$	Gd-(thd)$_3$
	$0.5\,\%_{wt.}$	oxolane
	$7\,g/l$	PPO
	$20\,mg/l$	bisMSB
Gamma Catcher [131]	$66\,\%_{vol}$	Ondina 909
(DCGC)	$30\,\%_{vol}$	dodecane
	$4\,\%_{vol}$	PXE
	$2\,g/l$	PPO
	$20\,mg/l$	bisMSB
Muon Veto [137, 138]	$51.6\,\%_{vol}$	n-paraffine
(DCMV)	$48.4\,\%_{vol}$	LAB
	$2\,g/l$	PPO
	$20\,mg/l$	bisMSB

Table 3.4.: Compositions of the scintillators used in the Double Chooz experiment. The components Gd-(thd)$_3$ ((Gd(III)-tris-(2,2,6,6-tetramethyl-heptane-3,5-dionate)) and oxolane (also called tetrahydrofuran) of the target scintillator are used to stably dissolve gadolinium in the scintillator (please refer to [131] for more details). See tables 3.1-3.3 for the main properties of the other components.

1. LAB with fixed bisMSB-concentration and varying PPO-concentration:

$$\text{LAB} + X \,\text{g/l PPO} + 20 \,\text{mg/l bisMSB} \quad (\text{with } X \in \{1, 3, 5, 7, 9\})$$

2. LAB with fixed PPO-concentration and varying bisMSB-concentration:

$$\text{LAB} + 3 \,\text{g/l PPO} + X \,\text{mg/l bisMSB} \quad (\text{with } X \in \{0, 10, 20, 40, 80\})$$

3. LAB with fixed bisMSB- and PPO-concentration diluted by different amounts of n-paraffine:

$$(100 - X) \,\%_{\text{vol}} \,\text{LAB} + X \,\%_{\text{vol}} \,\text{n-paraffine} + 3 \,\text{g/l PPO} + 20 \,\text{mg/l bisMSB}$$
$$(\text{with } X \in \{0, 25, 50\})$$

After the arrival of the samples from Double Chooz and Borexino at TUM and the mixing of the LAB-based samples, all samples were flushed thoroughly with nitrogen before they were stored in glass bottles[5] in a dark and cool cabinet. The sample container used in the measurements will be presented in detail in the following chapter (see section 4.2.1) as well as the procedure of cleaning the container and filling with the samples (see section 4.4). A summary of each of the three conducted beam times with the respective investigated scintillator samples will be given in section 4.5.

---

[5] The used bottles are chemically compatible with all scintillator samples.

4. Experimental Setup at the Maier-Leibnitz-Laboratorium

For organic liquid scintillator based neutrino experiments, like Borexino, Double Chooz, LENA and JUNO (see chapter 2), a precise knowledge of energy response and time behavior of the scintillator used is mandatory. In particular, organic liquid scintillators are known for their nonlinear energy response, which is commonly called quenching. Their light output differs dependent on the kind of ionizing particles, like electrons, protons and heavier nuclei (see chapter 3). Neutron induced proton recoil events are of special interest to the mentioned experiments, as they can pose an important background for the detection of electron antineutrinos, for example, from nuclear reactors, the earth's interior or the diffuse supernova neutrino background. Furthermore, a major detection channel for supernova neutrinos is neutrino-proton scattering. Here the energy scale for the scattered protons has to be reconstructed precisely at low energies to test supernova models.

There are two main methods to investigate scintillators with neutron induced proton recoils. On the one hand, neutron sources such as AmBe or ^{252}Cf can be used to irradiate scintillator samples. Such sources provide neutrons with continuously distributed energies of up to $\sim 10\,\text{MeV}$. On the other hand, neutrons can be produced by (p,n)-reactions at ion- and proton-accelerators. Depending on the reaction used, neutrons with a continuous energy spectrum or monoenergetic neutrons can be obtained. By pulsing the incident beam, a time-of-flight (ToF) measurement can be used to determine the energy of the produced neutrons.

The neutron scattering facility at the Maier-Leibnitz-Laboratorium (MLL) in Garching provides an excellent environment to investigate neutron induced proton recoils in organic liquid scintillators. In this chapter the experimental setup at the MLL is described. The first part is focused on the neutron production using the MLL tandem accelerator (see section 4.1). The detector, experimental and electronic setups, which were used, are introduced in section 4.2, followed by a description of the reconstruction applied to the recorded pulses (see section 4.3). Furthermore, the preparation of the samples for the measurements is discussed in section 4.4 before an experimental summary of the three performed beam times is given in the last part (see section 4.5).
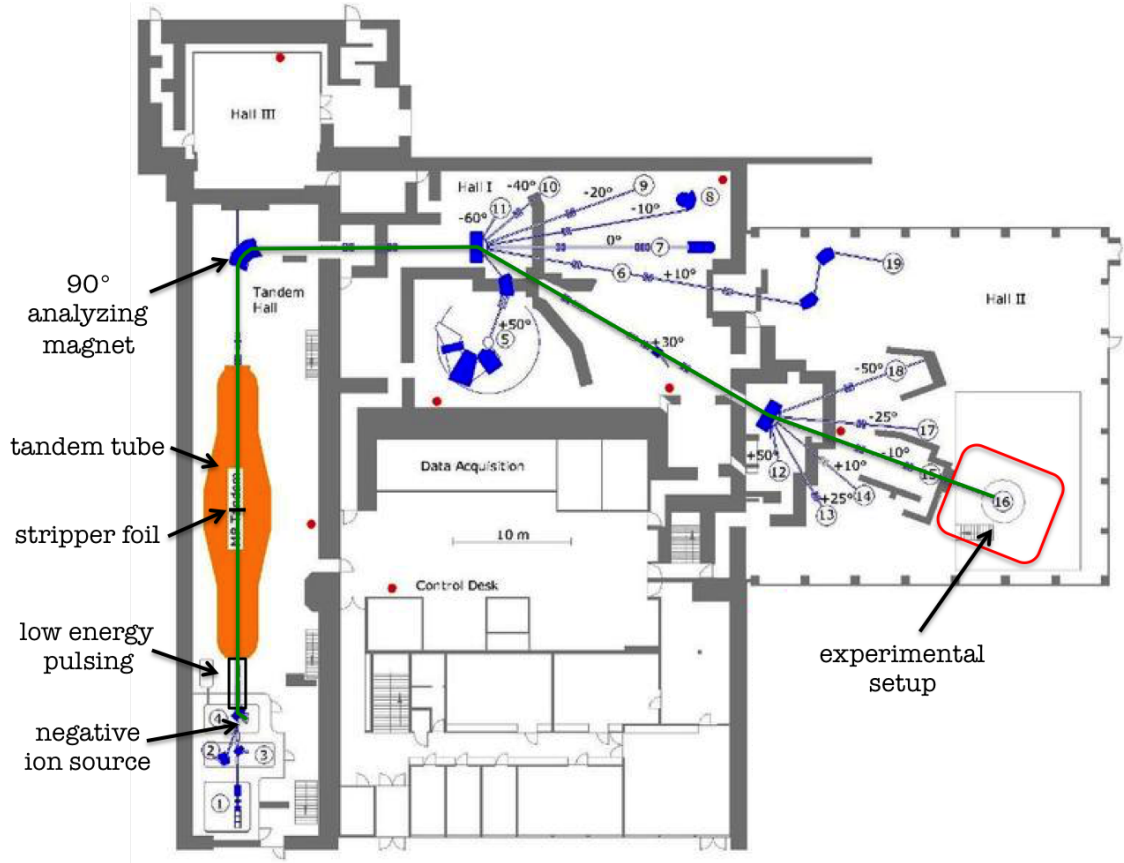
Figure 4.1.: A site plan of the MLL accelerator facility highlighting relevant accelerator components. The green line shows the path of the ^{11}B-beam to the experimental site in hall II (red).

4.1. Accelerator Setup at the MLL

The Maier-Leibnitz-Laboratorium (MLL) features a tandem-van de Graaff-accelerator with a maximum acceleration voltage of $2 \times 15\,\mathrm{MV}$. The experimental setup for the investigation of organic liquid scintillators is situated at the neutron scattering facility in hall II (see figure 4.1), which is used by the CRESST collaboration to study neutron induced nuclear recoils in $CaWO_4$ low temperature detectors [139, 140, 141]. The experimental setup for the investigation of liquid scintillators was improved successively in collaboration with another PhD thesis [100] and in the scope of several Diploma theses [138, 142, 143] in several joint beam times with the CRESST group until August 2012. This thesis uses the data taken in three beam times performed between September 2013 and June 2014 largely for studies of liquid scintillators only.

The tandem accelerator is used to guide a pulsed ^{11}B ion beam onto a gaseous hydrogen target to produce a neutron beam by the following nuclear reaction:

$$^{11}\mathrm{B} + p \; \rightarrow \; ^{11}\mathrm{C} + n \, . \tag{4.1}$$

Details related to the pulsed ion beam and the neutron production will be described in the following sections 4.1.1-4.1.3.

4.1.1. Ion Beam Acceleration

To produce an ion beam at the MLL ions have to be produced first. The MLL provides a negative-ion injector, which allows for the production of negative ions for a wide range of elements and isotopes [141]. A schematic description of the ion source is given in appendix A. The negative ^{11}B ions are extracted from the ion source by a positive extraction voltage and preaccelerated by a voltage of 100 kV before passing the low energy pulsing (see section 4.1.2) and accessing the tandem accelerator. Here the applied voltage of ~ 10.2 MV is used twice. After the ions passed once through the terminal voltage a thin carbon foil in the center of the tandem accelerator strips off electrons from the ions. Resulting maximally ionized ^{11}B^{5+} ions (all electrons are stripped off) traverse the acceleration voltage one more time. In consequence, the ions obtain an energy of 6×10.2 MeV $= 61.2$ MeV. Summing up all acceleration steps, like the extraction voltage and preacceleration, the ions gain a total energy of 61.5 MeV. A 90° analyzing magnet after the tandem accelerator tube is used to select boron ions with the right charge and energy.

4.1.2. Low Energy Pulsing

The low energy pulsing at the MLL consists of the low energy chopper followed by a buncher [141, 144]. The low energy chopper consists of five consecutive synchronized AC coupled capacitors followed by a small aperture. With a frequency of 5 MHz$/2^i$ (with the so called *Untersetzung* $i = 0, 1, 2, ...$) the beam is chopped into slices of up to about 70 ns. For the data presented in this thesis a *Untersetzung* of 1 was used, which means a time difference between two successive bunches of ~ 400 ns.

The low energy buncher consists of consecutive tubes with gaps, between which voltages are applied. The working principle is similar to a linear electron accelerator. The falling edge of a saw-tooth voltage is synchronized with the beam bunches exiting the chopper. Thereby the first ions in each bunch are decelerated, while the last ones are accelerated. The saw-tooth voltage is approximated by two sine voltages with 5 MHz and 10 MHz applied at two separated gaps. The voltage amplitudes of and the phase between both frequencies can be adjusted to obtain a stable approximately saw-tooth shaped voltage.

After successfully synchronizing the chopper and buncher, very short bunch widths in the order of $\sim$ 2-3 ns (FWHM) can be reached. The shape and width of those bunches directly affect the precision of the results for the measurements presented in this thesis (see chapter 6).

To enable a measurement of the neutron energies by time-of-flight a logical signal from the low energy pulsing facility is used as a clock for the experiment's trigger electronics presented in section 4.2.3.
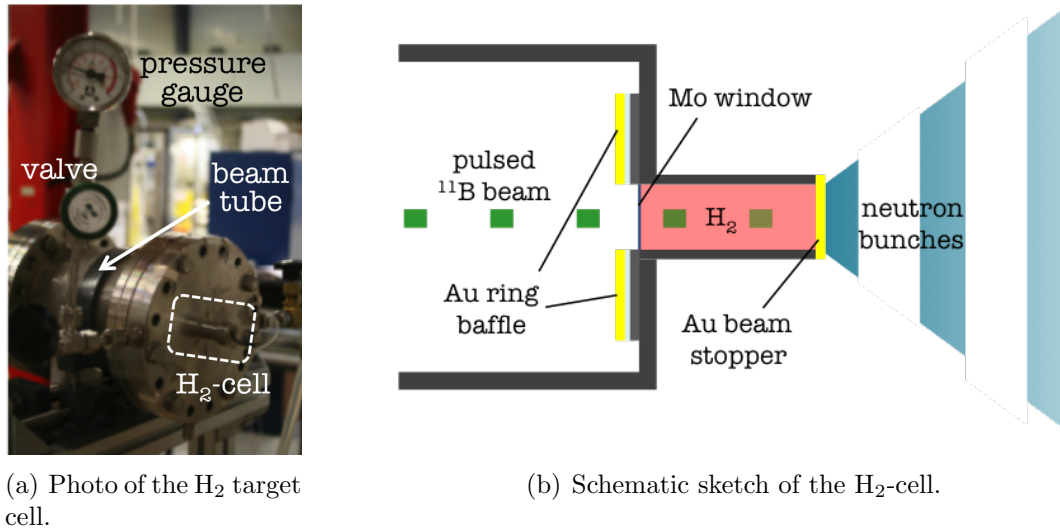
(a) Photo of the H_2 target cell.

(b) Schematic sketch of the H_2-cell.

Figure 4.2.: A photo and a schematic drawing of the H_2-target cell. (a) shows the flange with the H_2-cell at the beam end. The pressure gauge can be seen at the top of the picture. (b) is a schematic view of the H_2-cell setup.

4.1.3. Gaseous H_2-Target and Neutron Production

To produce the neutrons the reaction given in equation (4.1) has been chosen [145] by the CRESST group due to best feasibility [139, 141]. Gaseous hydrogen with a pressure of ~ 2 bar contained in a cell with a diameter of 1 cm and a length of 3 cm serves as a target for the incoming ^{11}B beam. To separate the hydrogen gas from the evacuated beam tube a 5 μm thin molybdenum window is used (see figure 4.2). The incident 61.5 MeV ^{11}B nuclei lose an average energy of about 4.9 MeV to pass the molybdenum window and another 1.3 MeV of energy in the hydrogen gas before reaction (4.1) takes place [139, 146]. The beam energy of 61.5 MeV was chosen to obtain a high neutron yield, while avoiding the excitation of the first excited state of ^{11}C. That would lead to an additional production of lower energetic neutrons (see figure 4.3) [145].

Due to inverse kinematics[1], the neutrons produced in the (p,n) reaction (4.1) are scattered in forward direction with a maximum angle of $\sim 40°$ with respect to the beam axis. According to momentum and energy conservation, the neutron energy decreases with rising scattering angle with respect to the forward direction (beam axis), which was utilized by the experiment described in this thesis to obtain different neutron energies between $\sim 4.7 - 11.2$ MeV.

---

[1] When a heavy projectile is shot on a light target, the center of mass is moving rapidly.
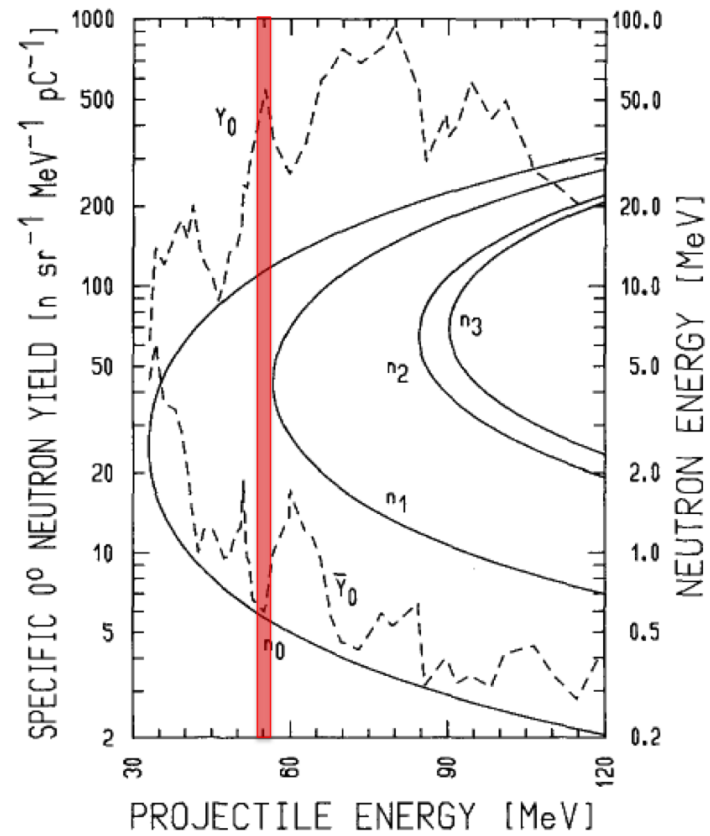
Figure 4.3.: Dependence of the neutron energy on the incident ^{11}B energy (solid curves) and neutron yield at 0° (dashed curve) for the reaction ^{1}H(^{11}B, n)^{11}C. $n_0 - n_3$ denote the ground and first excited states of ^{11}C, respectively. Y_0 shows the neutron yield at 0° for the high energy branch and $\bar{Y}_0$ the 0° neutron yield for the low energy branch (both for n_0, i.e. no excitation of ^{11}C). The highlighted region corresponds to the optimal ^{11}B energy after losses in the molydenum foil and the hydrogen gas. Plot taken from [145].

4.2. Experimental Setup for Liquid Scintillator Characterization

4.2.1. Scintillation Light Detector Setup

The setup for the detection of scintillation light from different organic liquid scintillators was designed and realized in collaboration with Jürgen Winter [100]. It consists of two main components: the cell containing the scintillator samples and a photomultiplier tube (PMT) in a polyvinyl chloride (PVC) housing. Figure 4.4 shows a cross section of the full detector module, which is described in the following.

The scintillator sample is contained in a polytetrafluoroethylene (PTFE) cell and a 2 mm thick quartz glass window. The PTFE cell is screwed into a polyvinyl chloride (PVC) flange and sealed with a PTFE coated O-ring, which is placed between the PTFE cell and the quartz glass window. Figure 4.5 shows photos of the assembled sample container. The inner diameter of the PTFE cell was matched to the PMT diameter of 3 inch, while the depth was chosen to be 1 inch. This results in ~ 120 ml of volume for the liquid scintillator samples. The sample container is filled through a small opening at the side of the PTFE cell, which is sealed by a PTFE screw during measurements. Therefore, liquids filled into the fully assembled container will only be exposed to PTFE or quartz glass. Both PTFE and quartz glass have very good chemical compatibility with all organic liquids used (see section 3.4). The base of the cell, which points to the H_2-cell during measurement, was manufactured with a thickness of only 1 mm to reduce scattering of the neutrons before entering the liquid scintillator volume. Three identical sample containers where constructed to allow for a smooth operation of the beam times described in section 4.5.

To detect the scintillation light, an ETEL 9822KB photomultiplier tube (PMT) with good timing characteristics and a wide dynamic range was used [147] (see figure 4.6(a)). To shield the PMT from ambient magnetic fields a shielding was manufactured using mumetal with a thickness of 0.25 mm (see figure 4.6(b)). To increase the shielding effectivity, the manufactured mumetal shielding was tempered under hydrogen atmosphere at more than 1000 °C by the Vacuumschmelze Hanau [148].

The PMT covered by the mumetal shielding is integrated in a PVC encapsulation. The sample container described above was designed to be flanged to the PVC encapsulation, in such way that the PMT faces the quartz glass window. This allows for a fast change of samples and, therefore, makes an efficient usage of the limited beam time possible. An additional cap consisting of PVC at the sides and 1 mm thin Aluminum sheet in direction of the H_2-cell is needed to make the whole assembly light-tight.

The vacant space behind the PMT in figure 4.4 houses the voltage divider for the PMT. This region is accessible via another flange at the back of the detector module. The two pipe shaped structures at the back flange are used as light-tight feedthroughs of the high voltage and signal cables. For additional light tightness the connections of the flanges and the front cap are covered with black tape. The whole detector was covered with black felt
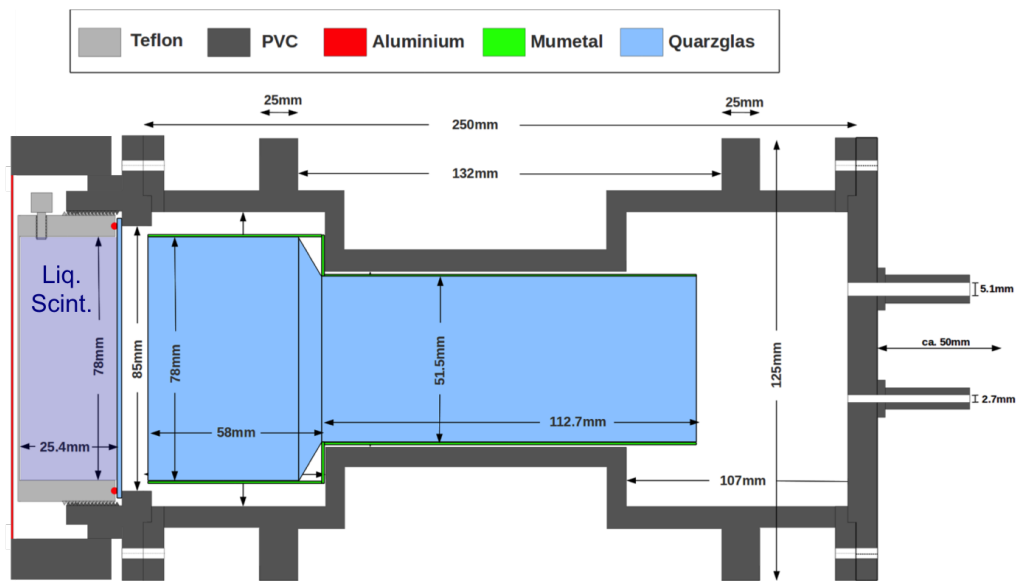
Figure 4.4.: Cross section of the detector module for liquid scintillator investigations at the MLL. The sample container (left side of the drawing) can be flanged on the PVC housing of the PMT (blue). The vacant space on the right side of the drawing houses the voltage divider (not shown) for the PMT. This region can be accessed by an additional flange. The high voltage and signal cable are fed through the pipe structures shown on the right.
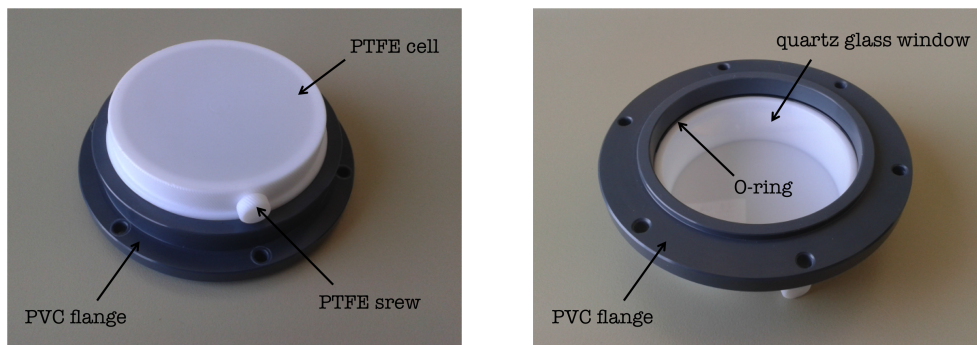
(a) Sample container view facing the PTFE container.

(b) Sample container view facing the quartz glass window.

Figure 4.5.: Photos of a sample container. The scintillator samples are contained in a white PTFE cell (1 inch inner depth and 3 inch inner diameter) and a 2 mm thick quartz glass window. The cell is screwed into a PVC flange and sealed by a PTFE coated O-ring between the cell and quartz glass window. The sample container is filled through a hole at the side of the PTFE cell, which can be sealed by a PTFE screw. Three identical sample containers were constructed and used in the measurements.
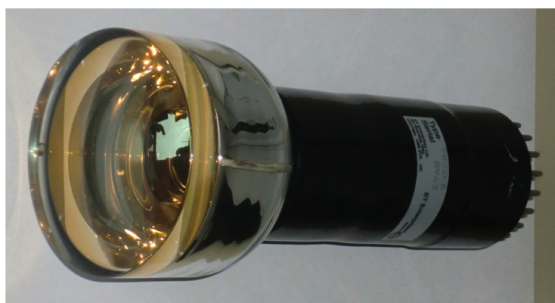
(a) 3 inch ETEL 9822KB photomultiplier tube.

(b) Mumetal shielding with a thickness of 0.25 mm.

Figure 4.6.: Photos of the photomultiplier tube and mumetal shielding. The mumetal shielding was tempered at the Vacuumschmelze Hanau after construction at the workshop at TUM.

during measurements to further reduce influence from ambient light.

Figure 4.7 shows the fully mounted detector module. Additionally, a holder for radioactive sources for calibration with γ-rays is shown. It can be attached to the detector module using two metal tubes, which also serve as a rail to position the sources. The source holder was designed to guarantee a precisely reproducible positioning of the different γ-sources used in the calibration measurements. It is easily mountable and was removed during data taking under neutron irradiation to reduce systematic effects from scattered neutrons.

4.2.2. Experimental Setup and Geometry

The full detector module is mounted on an Item-rail [149]. Up to ten different selected detector positions between 1.0° and 35.3° with respect to the beam axis can be accessed easily by moving the detector on the rail. This way, different incident neutron energies of about 4.7 MeV to 11.2 MeV [2] can be accessed, while using the same ^{11}B beam energy in all measurements. In figure 4.8 the experimental setup at the neutron scattering facility is shown schematically. The cryostat used by the CRESST group, which is shown as a red circle in figuee 4.8, was dismounted during almost all measurements presented in this thesis in order to reduce systematic effects due to neutron activation and scattering in the cryostat materials.

For all selected positions the distance between detector and H_2-cell and the angle to the beam axis (0°) have been measured with respect to the centers of the scintillator and the H_2-cell by triangulation using a laser distance measurement device [150]. In table 4.1 the measured distances and angles are shown along with the estimated errors due to the measurement. Additionally, the systematic error caused by the dimensions of both the scintillator and the H_2-cell is given for each position. The numbering of the detector

---

[2] Please refer to section 6.3 for details on the determination of the neutron energy at each position using the time-of-flight technique.
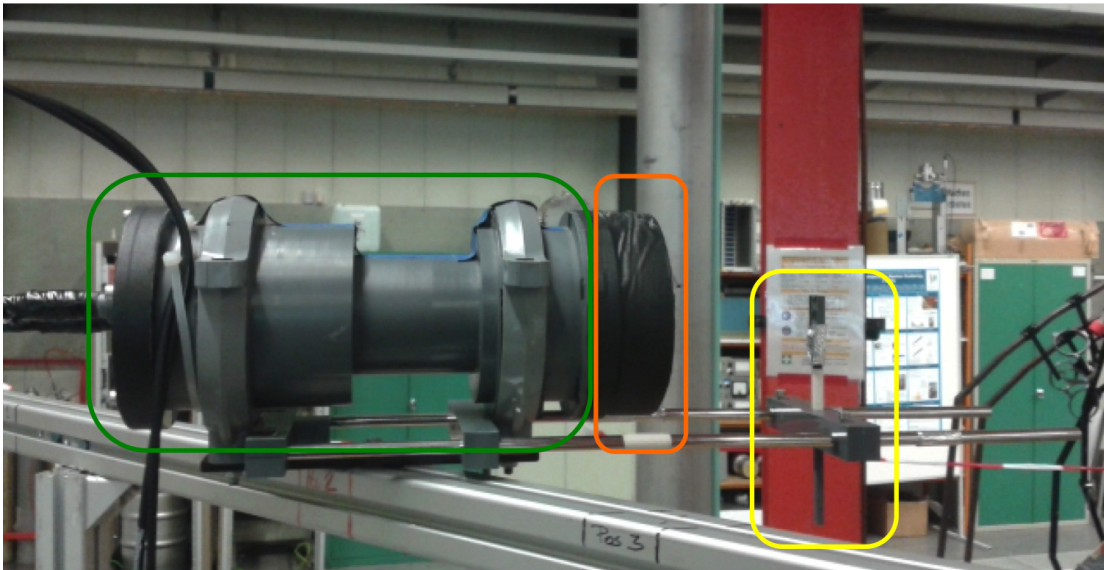
Figure 4.7.: Fully assembled detector mounted on an Item-rail. The PVC encapsulation housing the PMT is highlighted in green. The position of the sample container flanged to the PVC housing, covered by a cap and tape for light tightness is pointed out by the orange box. On the right, the holder used for calibration with radioactive γ-sources (yellow) is shown. It is attached to the detector module by two metal sticks, which are also used to adjust the source position, and was removed during measurements with the neutron beam. Mind that the detector is flipped by 180° compared to the schematic drawing shown in figure 4.4.
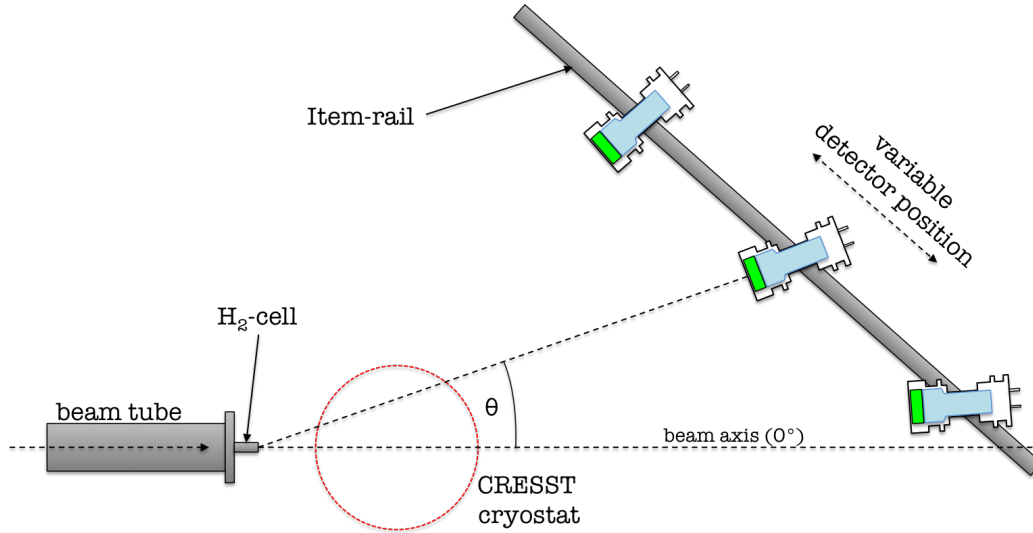
Figure 4.8.: Schematic drawing of the experimental setup at the neutron scattering facility at the MLL. The CRESST cryostat (red circle) was dismounted during most of the measurements to reduce systematic effects due to neutrons scattering inside the cryostat. The detector can be moved easily on an Item-rail [149] and placed at up to ten selected positions between $1.0° \leq \theta \leq 35.3°$ with respect to the beam axis ($\theta = 0°$). Thereby, neutron energies between $4.7\,\text{MeV}$ and $11.2\,\text{MeV}$ are obtained.

positions from Pos-1 to Pos8 has historical reason. In previous beam times only Pos0 to Pos7 have been used because of an additional scintillator detector on the beam axis, used by the CRESST group. This detector was in the line of sight to the H_2-cell and, therefore, caused systematic effects due to neutron scattering and activation. In the beam times performed in the scope of this thesis, this detector was moved to a position, at which the influence on the measurements was minimal.

The error on the distance measurement was estimated to be $5\,\text{mm}$ for Pos0 to Pos8 and $10\,\text{mm}$ for Pos-1. Due to the dimensions of the scintillator volume and the hydrogen cell a geometrical error on the distance of $25.0 - 27.7\,\text{mm}$ arises, which is used as an input to the neutron energy determination by time-of-flight described in section 6.3. The measurement error on the angle to the beam axis results from error propagation on the triangulation and is between $0.3°$ and $2.8°$, depending on the detector position. Due to the $3\,\text{inch}$ diameter of the scintillator cell, an additional geometrical error on the angle to the beam axis was derived to be $0.6° - 1.1°$.

4.2.3. Electronic Setup and Data Acquisition

To perform a time of flight measurement a coincidence between the PMT signal and a signal correlated to the pulsing is needed. The signal provided by the MLL pulsing system is synchronous to the actual neutron production in the H_2-cell, but features an unknown time shift. Therefore, this signal can only be used as a clock for the trigger. The actual

detector position	angle θ to beam axis	angle error due to det. size	distance d	uncertainty on d due to cell and det. size
Pos-1	$1.0° \pm 1.0°$	$0.6°$	$(3592 \pm 10)\,\mathrm{mm}$	$27.7\,\mathrm{mm}$
Pos0	$3.6° \pm 2.8°$	$0.7°$	$(3282 \pm 5)\,\mathrm{mm}$	$27.7\,\mathrm{mm}$
Pos1	$8.2° \pm 1.1°$	$0.8°$	$(2951 \pm 5)\,\mathrm{mm}$	$27.5\,\mathrm{mm}$
Pos2	$14.1° \pm 0.6°$	$0.8°$	$(2664 \pm 5)\,\mathrm{mm}$	$27.3\,\mathrm{mm}$
Pos3	$17.2° \pm 0.6°$	$0.9°$	$(2527 \pm 5)\,\mathrm{mm}$	$27.0\,\mathrm{mm}$
Pos4	$21.6° \pm 0.5°$	$0.9°$	$(2386 \pm 5)\,\mathrm{mm}$	$26.7\,\mathrm{mm}$
Pos5	$25.0° \pm 0.5°$	$1.0°$	$(2292 \pm 5)\,\mathrm{mm}$	$26.3\,\mathrm{mm}$
Pos6	$27.7° \pm 0.4°$	$1.0°$	$(2230 \pm 5)\,\mathrm{mm}$	$26.0\,\mathrm{mm}$
Pos7	$31.5° \pm 0.4°$	$1.0°$	$(2150 \pm 5)\,\mathrm{mm}$	$25.5\,\mathrm{mm}$
Pos8	$35.3° \pm 0.3°$	$1.1°$	$(2085 \pm 5)\,\mathrm{mm}$	$25.0\,\mathrm{mm}$

Table 4.1.: Measured distances between the detector and the H_2-cell and angles with respect to the beam axis (0°) for all detector positions used. Both the errors resulting from the measurement and the systematic errors due to the finite dimensions of the H_2-cell and the scintillator sample are given. The distances and angles were measured with respect to the centers of the scintillator container and the H_2-cell by triangulation using a laser distance measurement device.

time of flight has to be determined in an offline analysis (see section 6.3).

In figure 4.9 schematic views of the NIM[3]-based electronic setups used in the different beam times are shown. The working principle of both displayed setups is the same: One part of the split PMT signal is fed directly into the data acquisition, while the other half is amplified to obtain a low threshold. A passive signal splitter was used to avoid additional electronic noise. The amplified signal is discriminated and generates a logical gate with a length of about 370 ns, which is passed on to a coincidence unit. The provided pulsing signal, appearing every $\sim$ 400 ns, is first discriminated to obtain a logical signal. The obtained signal is successively delayed in a delay generator and also fed into the coincidence unit. In case of a coincidence a logical signal is emitted to trigger the data acquisition. An additional discriminated pulsing signal is passed on to the data acquisition to be recorded for further analysis. See also figure 4.10 for a more descriptive view of the trigger working principle. The relative position of the PMT signal to the trigger position already gives an uncalibrated time of flight. A more precise value for the time of flight is obtained from the difference of the reconstructed start times of the recorded PMT and pulsing signals (see section 4.3).

The changes in the electronic setups used in the beam time in September 2013 and the ones in February and May/June 2014 (see figure 4.9) were mainly implemented to reduce electronic noise. In the 2014 beam times a different fast amplifier with less noise was

---
[3] Nuclear Instrumentation Module
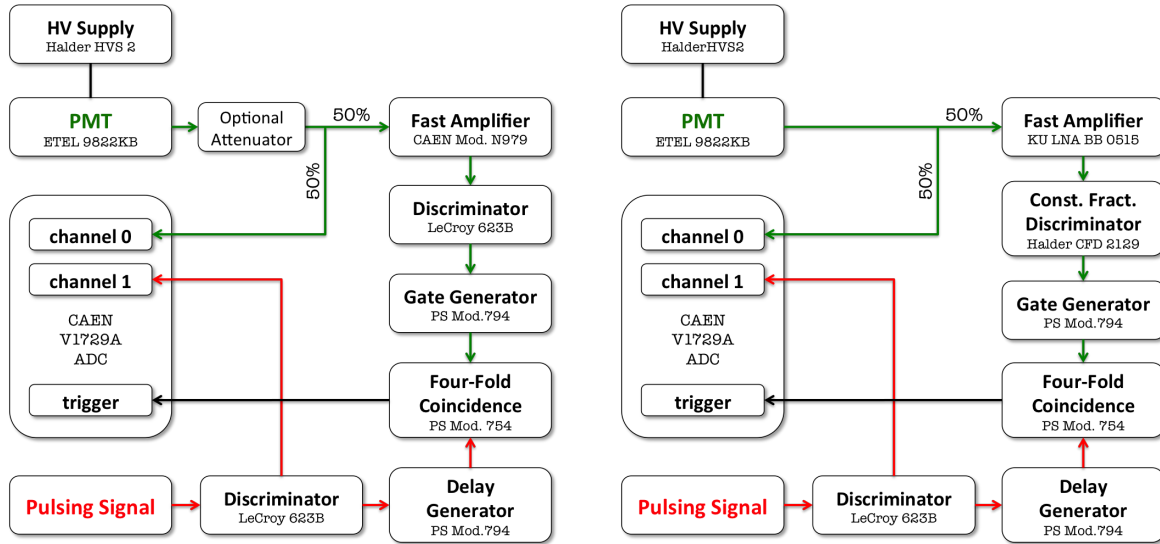
(a) Electronic setup used during the beam time in September 2013.

(b) Electronic setup used during the beam times in February and May/June 2014.

Figure 4.9.: The electronic setups used in the beam time in September 2013 (a) and that used in the beam times in February 2014 and May/June 2014 (b) to perform a time of flight measurement. The main difference is the usage of a constant fraction discriminator and a different low noise fast amplifier during the 2014 beam times. In September 2013 optional attenuators have been used to match the PMT signal with the sensitive range of the ADC used, while not changing the PMT high voltage for the different scintillator samples. In the 2014 beam times the matching was done by changing the PMT high voltage. The working principle of both shown setups is the same: The PMT signal is split with one part being fed into the ADC and the other part being amplified. The amplified part of the PMT signals is discriminated and fed into a gate generator, which produces a logic signal. This signal is fed into a coincidence unit. The signal from the pulsing is discriminated, delayed and also passed on to the coincidence unit. In case of a coincidence a logical signal is emitted to trigger the ADC, which records the split PMT signal and an additional discriminated pulsing signal.
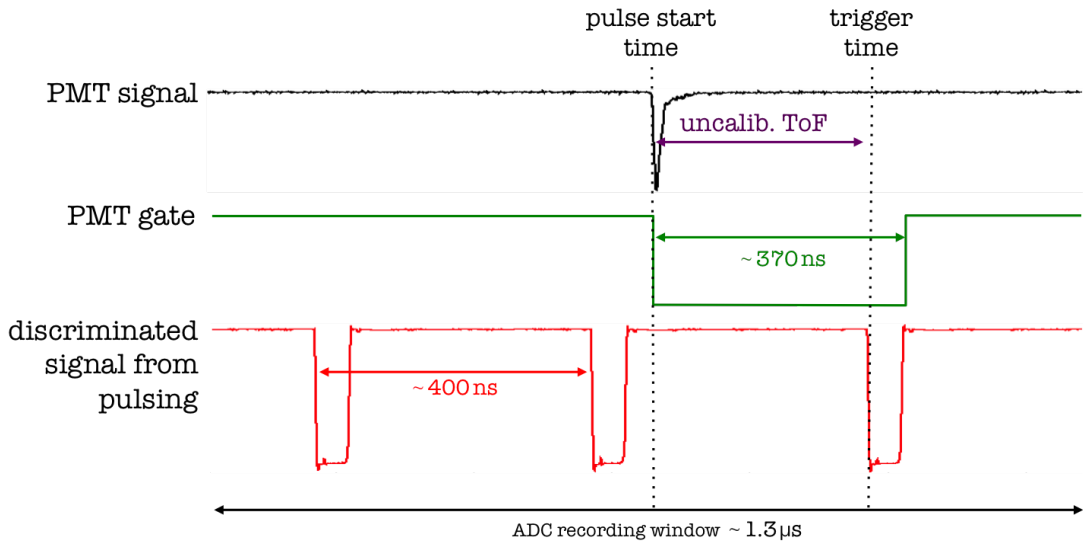
Figure 4.10.: Working principle of the trigger logic used for the time of flight (ToF) measurement. The PMT signal opens a gate of about 370 ns, waiting for a signal from the beam pulsing, which is discriminated and delayed to adjust the desired time of flight spectrum. Both the shown PMT and discriminated pulsing signal were recorded with the ADC used in the measurements presented in this thesis.

used. Furthermore, a constant fraction discriminator was utilized in order to obtain a pulse height corrected trigger position. In the 2013 beam time, optional attenuators were used to match signal hight to the sensitive range of the ADC. During the 2014 beam times this matching was done by adjusting the PMT high voltage instead.

The PMT signal and the discriminated signal from the pulsing were recorded using a CAEN V1729A 14 bit switched capacitor ADC[4] [151, 152], which has a fixed sensitive range of ± 1 V and a maximum sampling rate of 2 GS/s. Up to four channels can be used to simultaneously record signals with a fixed window length of 1.26 μs. The software for operating the ADC was custom made and developed by Dominikus Hellgartner at TUM. In figure 4.10 recorded PMT and pulsing signals were used to illustrate the working principle of the trigger. In the experiment described in this thesis only negative pulses from PMT and the discriminated pulsing signal were present. In consequence, only the negative half of the sensitive region of the ADC and, therefore, effectively 13 bit were used. The obtained precision in the pulse height was therefore limited by the ADC to $(1000\,\text{mV})/2^{13} = 0.122\,\text{mV}$, which is more than sufficient for the measurements presented in this thesis.

---

[4] Analog to Digital Converter
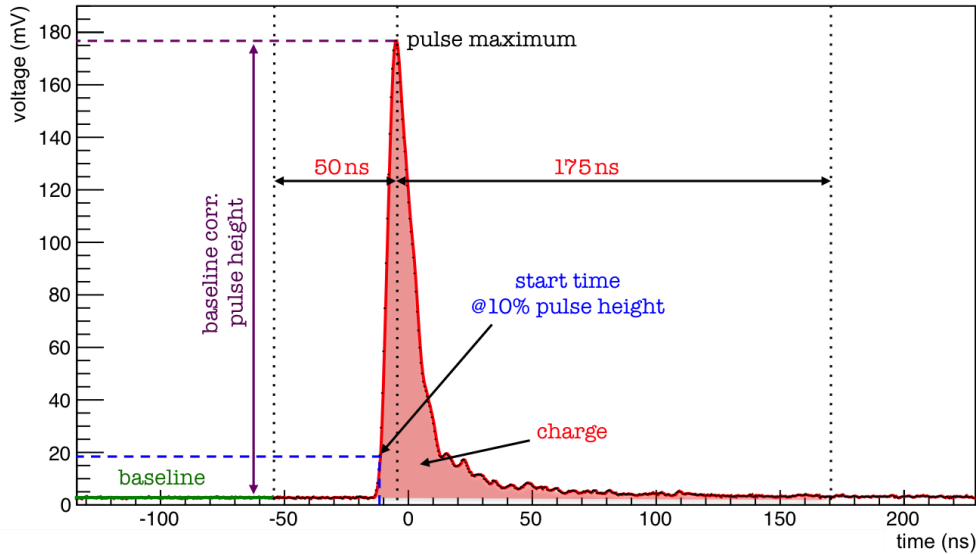
Figure 4.11.: An example for an inverted PMT signal illustrating the main reconstructed pulse parameters. The inverse of the recorded voltage is shown versus the time of each sample in the ADC recording window. A constant baseline (green) is determined from a range of 200 ns ending 50 ns before the pulse maximum. The pulse start time (blue) is determined at 10% of the baseline corrected pulse height (violet). To obtain a precise variable proportional to the energy deposited in the scintillator the pulse charge is determined as the baseline corrected integral over the pulse from 50 ns before to 175 ns after the maximum (red shaded area).

4.3. Pulse Reconstruction

The pulses recorded by the ADC are stored in a format compatible with the ROOT framework [153, 154, 155]. From each of the saved pulses several parameters are determined for further analyses. In Figure 4.11 the definition of the main pulse parameters *constant baseline*, *pulse height*, *start time* and *charge*, as determined for the recorded PMT pulses, are depicted schematically.

PMT Pulse Reconstruction: Firstly, the *pulse maximum* is determined from the inverted pulse[5] before a *constant baseline* is derived from a 200 ns interval, ending 50 ns before the pulse maximum, by averaging over all contributing samples. The *baseline width* is calculated as the standard deviation from the mean value using the same 200 ns interval. For data quality checks, the baseline interval is fitted with a linear function (*linear baseline*) to determine the slope. Having values for the constant baseline and the voltage corresponding to the pulse maximum, the *pulse height* can be calculated as the difference of both values. This parameter is mainly used to remove saturated pulses (i.e. pulses exceeding the

---

[5] All recorded pulses were negative. The pulse reconstruction was designed for positive pulses and, therefore, negative pulses $p(t)$ need to be inverted by $p(t) \rightarrow -p(t)$.

sensitive range of the ADC) in succession to cosmic muons crossing the scintillator.

The *start time* of the pulses is estimated from the position, at which the pulse reaches 10% of its pulse height. To increase the time resolution beyond the ADC sample width of 0.5 ns, linear interpolation between the two recorded samples below and above the 10% pulse height threshold is used. In order to obtain a parameter proportional to the energy deposited in the scintillator, which is more precise than the pulse height, the pulse *charge* Q is determined using the baseline corrected integral over a fixed window from 50 ns before to 175 ns after the maximum at t_{max}:

$$Q = \int_{t_s}^{t_e} (p(t) - b)\, \mathrm{d}t \tag{4.2}$$

with $t_s = t_{max} - 50$ ns and $t_e = t_{max} + 175$ ns the integration start and end time, $p(t)$ the recorded pulse amplitude in mV at time t and b the constant baseline, which was determined beforehand. The upper integration boundary was chosen to prevent a systematic effect on the charge due to a reflection of the PMT pulse around 220 ns, present in the data recorded in the September 2013 beam time and caused by a wrongly used $1\,\mathrm{M\Omega}$ load resistance for the PMT signal at the PMT voltage devider (see also section 4.5.1). To guarantee comparability of the results the same upper charge integration boundary was used for all measurements, including those in the 2014 beam times.

For pulse shape discrimination (PSD) of calibration data taken with an AmBe-source (see chapter 5) the commonly used *tail-to-total* ratio t_2t was determined:

$$t_2t = \frac{\int_{t_t}^{t_e} (p(t) - b)\, \mathrm{d}t}{\int_{t_s}^{t_e} (p(t) - b)\, \mathrm{d}t} \tag{4.3}$$

with $t_s = t_{max} - 50$ ns, $t_e = t_{max} + 200$ ns and $t_t = t_{max} + 25$ ns being the integration boundaries, $p(t)$ the recorded pulse height in mV at the time t and b the determined constant baseline. The t_2t parameter was calculated in the same way for all investigated scintillator samples.

Discriminated Pulsing Signal Reconstruction: As shown in figure 4.10, which illustrates the trigger logic using actual pulses recorded with the ADC, the discriminated pulsing signal appears three times in the sampling window of the ADC. The time distance between two successive pulses is ~ 400 ns, which corresponds to the time difference between two consecutive beam bunches. As the offset between the actual time, at which the ^{11}B beam bunch hits the H$_2$-cell, and the time of the corresponding signal from the pulsing is not known, the choice which of the three recorded discriminated pulsing signals to use for further analysis is arbitrary. Obviously, it should always be the same in the respective data set recorded in each measurement. As the pulsing signal is correlated to the trigger time, the pulses appear at the same position in the ADC recording window in all events of the respective measurement. A 400 ns analysis window was defined for each measurement, starting at least 200 ns before the onset of the selected pulse.

As for the PMT signal, the *pulse maximum* is determined from the inverted pulse. Then a *constant baseline* and its *width* are determined from a 100 ns interval, which ends 50 ns before the pulse maximum, in the same way as for the PMT pulses. The smaller used interval compared to that used in the reconstruction of the PMT pulses is caused by the size of the analysis window, described above. Furthermore, the *pulse height* is calculated as the difference between the value for the pulse maximum and the determined constant baseline. The *start time* of each discriminated pulsing signal is determined from the time, at which the signal reaches 50 % of its pulse height, using linear interpolation. The higher threshold compared to the reconstruction of the PMT signal was chosen arbitrarily, which is possible due to the fact that the pulse shape of the discriminated pulsing signal is always the same.

4.4. Scintillator Sample Preparation

The liquid scintillators, which are currently used in the running experiments Double Chooz and Borexino, and those, which are intended to be used in the future projects LENA and JUNO (see chapter 2), were investigated in the three conducted beam times. Furthermore, different LAB-based scintillators with varying concentrations of the first wavelength shifter PPO and the second wavelength shifter bis-MSB (see section 3.4) were examined. The different LAB-based scintillator samples were prepared by Dr. Hong Hanh Trinh Thi[6]. To remove the oxygen contamination introduced during mixing and handling, all liquids were flushed extensively for at least 20 minutes with nitrogen gas and stored in a dark and conditioned cabinet. The importance of removing the oxygen contamination from the samples is shown in [100], where the influence of oxygen on the PSD performance of LAB-based scintillators was investigated with the same experimental setup as used in this thesis. A clear degradation was found for scintillators exposed to air.

Before each beam time, all three sample containers (see section 4.2.1) were disassembled and all parts were cleaned thoroughly using an aromatic free detergent. Afterwards, all parts were rinsed with high-purity water exhaustively and air-dried during about one day in a dust reduced flow box. Then all parts - especially those in contact with liquid scintillator - were cleaned with ethanol and isopropanol using lint-free cloth and blown off with pressurized gaseous nitrogen to remove remaining dust. Finally, all parts of the respective sample container were reassembled again.

To further clean the cells before the actual filling, each container was flushed 3-4 times with about 20-30 ml of either the solvent liquid of the scintillator to be investigated (e.g. LAB for all LAB-based mixtures) or the desired scintillator mixture itself. At the same time, all items used in the filling process, like glass beakers and pipettes, were cleaned by using them for the flushing. In the next step the sample cells, all filling tools and the scintillator mixture (in a sterile bottle) were brought into a glove-bag [156], which then was thoroughly flushed with nitrogen gas to remove oxygen and avoid contamination in

---

[6] Chemist at the TUM chair in experimental physics and astroparticle physics (E15)

this regard. The remaining oxygen concentration was checked using an oxygen monitor [157] and kept below 1%.

Inside the glove-bag the sample containers were purged another 3-4 times with about 20-30 ml of the scintillator to be investigated. Finally, about 120 ml of the desired liquid were filled directly into the sample cells. Outside of the glove-bag, the containers - especially the quartz glass window facing the PMT - were cleaned on the outside with ethanol and isopropanol and wrapped in lint free cloth for transport to the MLL.

During a running beam time, the sample cells were emptied after the measurement and flushed with the next scintillator (or scintillator base liquid) to be filled into the cell. Thereafter, the next scintillator was filled into the respective cell without fully disassembling it. This is sufficient, because all scintillators used dissolve in each other and, therefore, are perfectly suitable for cleaning. Furthermore, possible contamination in additional working steps were thereby eliminated.

4.5. Performed Beam Times at the MLL

Three beam times have been performed at the MLL to investigate a various number of liquid scintillator samples regarding proton quenching and neutron-gamma pulse shape discrimination (PSD) performance. Before these beam times, others had been conducted in collaboration with the CRESST group mainly in order to further develop the setup. Results regarding PSD performance from a beam time in August 2012 can be found in [100]. In the following each of the three beam times conducted and analyzed in the scope of this thesis will be summarized.

4.5.1. Beam Time September 2013

The first beam time was performed from 9th to 16th of September 2013 without the CRESST group, meaning the cryostat (see figure 4.8) being dismounted for background reduction. Due to problems with the accelerator and beam guidance control system and a not working pulsing, no data under neutron irradiation could be taken until afternoon of the 11th of September. Nonetheless, measurements for five different scintillator samples could be completed. Experimental information, like applied PMT voltage and attenuators used, is given in table 4.2 along with the abbreviations for the investigated samples, which are used in the following. A summary of the measurements performed for all investigated samples at each detector position with respect to the beam axis is given in table 4.3.

The high voltage applied to the PMT was the same for all investigated samples in this beam time, while matching the PMT signal range to the sensitive ADC region was done by attenuators (see figure 4.9(a)). Furthermore, a different amplifier and discriminator for the PMT signal than in the two later beam times in 2014 were used for the trigger logic.

Additionally, an important difference to the beam times in 2014 was that the load resistance

scintillator sample	PMT voltage	attenuation	abbreviation
Double Chooz muon veto scint.	1788 V	none	DCMV
LAB + 3 g/l PPO + 20 mg/l bisMSB	1788 V	none	LAB-3-20
Borexino (PC + 1.5 g/l PPO)	1788 V	3 dB + 2 dB	Borexino
LAB + 5 g/l PPO + 20 mg/l bisMSB	1788 V	2 dB	LAB-5-20
LAB + 3 g/l PPO + 40 mg/l bisMSB	1788 V	none	LAB-3-40

Table 4.2.: Scintillator samples investigated in the September 2013 beam time sorted chronologically in the order of measurement. In all measurements, the same high voltage was applied to the PMT. The PMT signals were attenuated in order to match to the sensitive region of the ADC. Furthermore, abbreviations for the scintillator samples are given and will be used in the following. Please refer to table 3.4 for the detailed composition of the Double Chooz muon veto scintillator.

sample	Pos-1	Pos0	Pos1	Pos2	Pos3	Pos4	Pos5	Pos6	Pos7	Pos8
DCMV		×	×	×	×	×	×	×	×	
LAB-3-20		×	×	×	×	×	×	×	×	
Borexino	×	×	×	×	×	×	×	×	×	×
LAB-5-20		×	×	×	×	×	×	×	×	
LAB-3-40		×		×	×	×	×	×	×	

Table 4.3.: Summary of performed measurements (marked by crosses) for all samples studied in the September 2013 beam time at the different detector positions with respect to the beam axis. The Borexino sample was the only one used to take data at Pos8 in all three conducted beam times. See table 4.1 for information on the detector positions and table 4.2 for the scintillator compositions.

of the signal at the PMT voltage divider side was $1\,M\Omega$ instead of $50\,\Omega$. This has a significant effect on the signal, which has a long decay in case of $1\,M\Omega$ load resistance and, therefore, affects the results on the PSD performance. Hence, the data taken during this beam time was only analyzed regarding proton quenching. For PSD studies additional measurements were performed in the 2014 beam times.

4.5.2. Beam Time February 2014

A second beam time has been conducted from 10th to 17th of February 2014 without the CRESST group and, therefore, with the cryostat (see figure 4.8) being dismounted. The main goal of this beam time was the measurement of the Double Chooz neutrino target and gamma catcher scintillators in collaboration with a group from MPIK in Heidelberg, where these scintillators were developed and produced. Unfortunately, the gamma catcher

scintillator sample	PMT voltage	abbreviation
LAB + 3 g/l PPO + 20 mg/l bisMSB	1860 V	LAB-3-20(2)
Double Chooz target scint.	1884 V	DCTarget
LAB + 3 g/l PPO + 10 mg/l bisMSB	1860 V	LAB-3-10
LAB + 3 g/l PPO + 0 mg/l bisMSB	1860 V	LAB-3-0
LAB + 7 g/l PPO + 20 mg/l bisMSB	1800 V	LAB-7-20
LAB + 9 g/l PPO + 20 mg/l bisMSB	1800 V	LAB-9-20
LAB + 3 g/l PPO + 80 mg/l bisMSB	1836 V	LAB-3-80

Table 4.4.: Scintillator samples investigated in the February 2014 beam time sorted chronologically in the order of measurement. To match the sensitive region of the ADC the high voltage applied to the PMT was varied for different scintillator samples. Furthermore, abbreviations for the investigated scintillator samples are given and will be used in the following. See table 3.4 for the detailed composition of the Double Chooz target scintillator.

sample seemed to be contaminated and could not be used. A new uncontaminated sample was measured in the beam time in May/June 2014 instead.

Seven different scintillators could be studied under neutron irradiation in this beam time. During the measurement of LAB + 3 g/l PPO + 0 g/l bisMSB a problem with the pulsing occurred, which affected the data taken at Pos1, Pos2, Pos4 and Pos6 (see table 4.1) and caused the ^{11}B-beam pulse width to be larger than 4 ns (FWHM[7]) instead of about 3 ns.

See tables 4.4 and 4.5 for the applied PMT voltages, the abbreviations used for the investigated samples and the data taken for each scintillator mixture. See figure 4.9(b) for the electronic setup used during this beam time.

4.5.3. Beam Time May/June 2014

The last beam time with focus on the investigation of the liquid scintillator response to neutron induced proton recoils was performed from 30th of May to 5th of June 2014. In contrast to the two earlier beam times this one was partially conducted in collaboration with the CRESST group, which tested a new detector during this beam time. After finishing the tests the cryostat was dismounted on 2nd of June. The measurements of three scintillator samples were affected: 50LAB-50nPar, LAB-1-20 and DCMV-PSD. The measurement with all other samples could be performed with the cryostat being dismounted.

See tables 4.6 and 4.7 for the applied PMT voltages, the abbreviations used and the taken data for each scintillator sample. In this beam time the electronic setup depicted in figure 4.9(b) was used. For the samples DCMV-PSD, LAB-5-20-PSD and LAB-3-40-PSD

---

[7] Full Width at Half Maximum

sample	Pos-1	Pos0	Pos1	Pos2	Pos3	Pos4	Pos5	Pos6	Pos7	Pos8
LAB-3-20(2)	×	×	×	×	×	×	×	×	×	
DCTarget		×	×	×	×	×	×	×	×	
LAB-3-10		×	×	×	×	×	×	×	×	
LAB-3-0		×	×	×	×	×	×	×	×	
LAB-7-20		×	×	×	×	×	×	×	×	
LAB-9-20		×	×	×	×	×	×	×	×	
LAB-3-80		×		×	×		×	×	×	

Table 4.5.: Summary of performed measurements (marked by crosses) for all samples studied in the February 2014 beam time at the different detector positions with respect to the beam axis. During the measurement with LAB-3-0 the pulsing performance was decreased for data taken at Pos1, Pos2, Pos4 and Pos6. See table 4.1 for information on the detector positions and table 4.4 for the scintillator compositions.

data was taken with high statistics at only one position. This data was analyzed with focus on PSD performance only. Measurements for those scintillators regarding proton quenching were already performed in the earlier beam times.

scintillator sample	PMT voltage	cryostat	abbreviation
50% LAB + 50% n-paraffin + ...	1836 V	yes	50LAB-50nPar
LAB + 1 g/l PPO + 20 mg/l bisMSB	1884 V	yes	LAB-1-20
Double Chooz muon veto scint.	1884 V	yes	DCMV-PSD
Double Chooz gamma catcher scint.	1920 V	no	DCGC
LAB + 5 g/l PPO + 20 mg/l bisMSB	1788 V	no	LAB-5-20-PSD
75% LAB + 25% n-paraffin + ...	1860 V	no	75LAB-25nPar
LAB + 3 g/l PPO + 40 mg/l bisMSB	1800 V	no	LAB-3-40-PSD
Borexino (PC + 1.5 g/l PPO)	1740 V	no	Borexino(2)
LAB + 3 g/l PPO + 0 mg/l bisMSB	1836 V	no	LAB-3-0(2)

Table 4.6.: Scintillator samples investigated in the May/June 2014 beam time sorted chronologically in the order of measurement. The beam time has been performed partly in collaboration with the CRESST group, i.e. the cryostat was mounted for a part of the measurements. To match the sensitive region of the ADC the high voltage applied to the PMT was varied for different scintillator samples. Furthermore, abbreviations for the scintillator samples are given and will be used in the following. The suffix *PSD* for some of the scintillator abbreviations denote measurements taken for PSD performance studies only. For details on the compositions of the Double Chooz muon veto and gamma catcher scintillators please refer to table 3.4.

sample	Pos-1	Pos0	Pos1	Pos2	Pos3	Pos4	Pos5	Pos6	Pos7	Pos8
50LAB-50nPar		×	×	×		×	×	×	×	
LAB-1-20		×	×	×	×	×	×	×	×	
DCMV-PSD		×								
DCGC	×	×	×	×	×	×	×	×	×	
LAB-5-20-PSD		×								
75LAB-25nPar		×	×	×	×	×	×	×	×	
LAB-3-40-PSD			×							
Borexino(2)		×		×		×		×		
LAB-3-0(2)	×		×	×		×		×		

Table 4.7.: Summary of the performed measurements (marked by crosses) for all samples studied in the May/June 2014 beam time at the different detector positions with respect to the beam axis. For DCMV-PSD, LAB-5-20-PSD and LAB-3-40-PSD data has been taken with high statistics at only one position, as those samples have been studied regarding PSD performance only. See table 4.1 for information on the detector positions and table 4.6 for the scintillator compositions.

5. Detector Calibration

The measurement of the proton quenching, which is the nonlinear response of the scintillator to energy depositions by proton recoils (see section 3.2), is based on the comparison between the amount of light emitted by the scintillator due to an energy deposition by a proton and that caused by an electron with the same initial energy (see chapter 6). Therefore, the precision of the measurement of proton quenching strongly depends on the accuracy of the detector calibration for electrons.

A standard approach is the calibration using γ-rays, which create electron recoils all over the scintillator. Due to the low Z of organic scintillators the dominating interaction of γ-rays in the relevant energy region is Compton scattering, resulting in a continuous energy recoil spectrum. The so-called Compton edge marks the end of this part of the spectrum at an energy of [158]

$$E_{\mathrm{CE}} = \frac{2E_\gamma^{\,2}}{m_\mathrm{e}c^2 + 2E_\gamma} \tag{5.1}$$

with E_{CE} the Compton edge energy, E_γ the energy of the γ-ray, m_e the electron mass and c the speed of light. The γ-ray sources used to calibrate the detector for each investigated scintillator sample are presented in section 5.1 before the taken calibration data and the applied data quality cuts are discussed in section 5.2.

To obtain a conversion from the energy dependent pulse parameter used (pulse charge, see section 4.3) to the deposited energy in the scintillator the Compton edge needs to be reconstructed from the measured spectra, which is the main challenge of the energy calibration with γ-sources. Due to the finite energy resolution of scintillator detectors, which is mainly determined by the number of detected photons, the Compton edge is smoothed out, which complicates the reconstruction of E_{CE} from the measured spectrum. An additional complication is introduced by multiple Compton scattering and pile up events. Therefore, a model based on input from a Monte Carlo (MC) simulation (see section 5.3) was developed to fit the measured spectra in order to extract the Compton edge position (see section 5.4).

The calibration fit to the results from the MC-based Compton edge reconstruction in order to obtain the energy response of the detector to electrons for each scintillator sample is described in section 5.5. Furthermore, the detected number of photoelectrons at a given energy was estimated for each investigated scintillator sample as described in section 5.6. Data from earlier beam times indicated that the gain of the PMT shows variations over time and for different detector positions of up to several percent, while having a constant high voltage applied. Therefore, correction factors were determined from comparing ^{22}Na Compton spectra, which were recorded for each sample and detector position before or after

neutron beam measurements, with the corresponding spectrum obtained during energy calibration (see section 5.7).

5.1. Deployed Calibration Sources

Table 5.1 sumarizes the deployed calibration sources - ^{137}Cs, ^{22}Na, ^{228}Th and AmBe[1] - with corresponding γ-ray and Compton edge energies. For each scintillator sample calibration measurements with all sources were performed.

source type	decay/reaction	E_γ (keV)	E_{CE} (keV)
^{137}Cs	$^{137}\text{Cs} \xrightarrow{\beta^-} {}^{137}\text{Ba} + \gamma$	661.7	477.4
^{22}Na	$^{22}\text{Na} \xrightarrow{\beta^+} {}^{22}\text{Ne} + \gamma$	1274.5	1061.7
	$\text{e}^+ + \text{e}^- \longrightarrow 2\,\gamma$	511.0	340.7
^{228}Th	$^{208}\text{Tl} \xrightarrow{\beta^-} {}^{208}\text{Pb} + \gamma$	2614.5	2381.7
AmBe	$^9\text{Be}\,(\alpha,\text{n})\,^{12}\text{C}^* \rightarrow {}^{12}\text{C} + \gamma$	4438.9	4197.3

Table 5.1.: γ-ray sources used for calibration of the detector. The respective decay or nuclear reaction, which produce the γ-rays are given. The Compton edge energies E_{CE} were derived from the γ-energies E_γ (from [99]) using equation (5.1).

The ^{137}Cs- and ^{22}Na-source both have a diameter of $\sim 1\,\text{mm}$ and are contained in a $20 \times 10 \times 2\,\text{mm}$ carrier made of glass, while the ^{228}Th-source is a small cylinder with a diameter of $2\,\text{mm}$ and a height of $1\,\text{cm}$. The AmBe-source is contained in a cylindrical metal container with a diameter of $1.74\,\text{cm}$ and a height of $1.94\,\text{cm}$. Due to the lack of detailed information about the source, the geometry of the volume holding the actual AmBe source was reconstructed from a technical drawing to be a cylinder with $1.42\,\text{cm}$ diameter and $1.54\,\text{cm}$ height. The source geometries described above are implemented in the simulation described below in section 5.3.

Using the source holder already described in section 4.2.1 and shown in figure 4.7, the sources could be reproducibly positioned on the symmetry axis of the detector setup. While the AmBe-source was positioned in a distance of $11.1\,\text{cm}$ to the detector in the September 2013 beam time and of $13.6\,\text{cm}$ in the 2014 beam times, the other sources were placed in a distance of $3.25\,\text{cm}$ to the detector[2]. The distances of the sources were selected in order to reduce pile up events. Especially, physical pile up is present in the ^{22}Na-spectra, where the $1274.5\,\text{keV}$ γ and the two $511\,\text{keV}$ annihilation-γs are emitted simultaneously, and in spectra recorded with the AmBe-source, which emits neutrons and the $4.4\,\text{MeV}$ γ-rays

---

[1] ^{241}AmBe is a neutron source, which produces neutrons by the nuclear reaction $^9\text{Be}\,(\alpha,\text{n})\,^{12}\text{C}$. As the produced ^{12}C may end up in the first excited state, the source also emits highly energetic $4.4\,\text{MeV}$ γ-rays.

[2] The distances are given for the source center relative to the the front of the fully assembled detector module, which is shown in figure 4.7.

(a) ^{22}Na   (b) AmBe
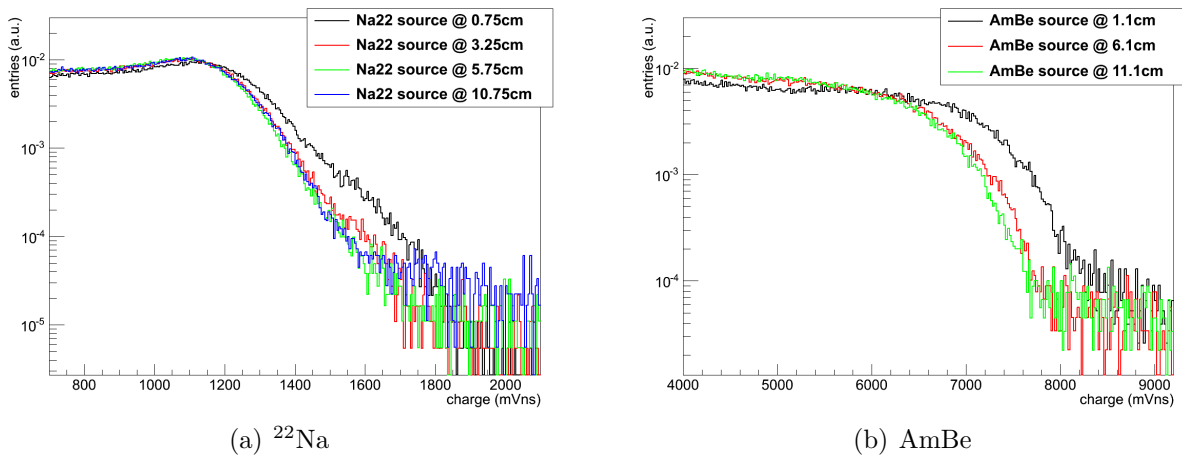
Figure 5.1.: Compton spectra taken with the ^{22}Na- (a) and the AmBe-source (b) at different distances to the detector and normalized to the total integral over histogram region. The spectra for the respective sources were recorded with the same high voltage applied to the PMT and using the same trigger threshold. The major differences in the region of the Compton edges in both plots are caused by pile up of simultaneously emitted γ-rays and/or neutrons (see text). In case of ^{22}Na, a distance to the detector of 3.25 cm was chosen, while the AmBe-source was positioned in a distance of 11.1 cm in the September 2013 beam time and of 13.6 cm in the 2014 beam times. Mind that the AmBe-spectra (b) include events due to γ-rays and neutrons.

at the same time. Figure 5.1 shows Compton spectra taken with the ^{22}Na- and AmBe-source at different distances to the detector. The high voltage applied to the PMT and the trigger threshold was the same for all measurements with the respective source. The obvious differences in the region around the Compton edges are caused by the described physical pile up of simultaneously emitted γ-rays and/or neutrons. The above mentioned source positions with respect to the detector were defined according to the results shown in figure 5.1 for the ^{22}Na- and AmBe-source.

5.2. Measured Calibration Data and Data Handling

For each investigated scintillator sample, data with all four γ-ray calibration sources (see table 5.1) was recorded at the same detector position to avoid systematic effects (see section 4.2.2 and table 4.1). The internal trigger of the ADC was used for all calibration measurements. The applied trigger thresholds were chosen low enough to record the full Compton edge regions. Calibration data with the ^{22}Na-source has been taken with two different applied trigger thresholds: The lower one was chosen to record the full spectrum including the Compton edges of the 511 keV and the 1274.5 keV γ-rays, while the higher threshold was used to obtain higher statistics at the Compton edge due to the 1274.5 keV γs. The number of events recorded in each calibration measurement for the investigated

scintillator samples are given in table B.1 in appendix B.2 along with the detector position, at which the calibration was performed.

The relevant parameters of the recorded PMT pulses were reconstructed as described in section 4.3. For further analysis quality cuts were applied to the data. To remove saturated pulses (mainly caused by cosmic muons) a cut on the reconstructed pulse heights above a threshold chosen well above the region of the Compton edge events was used. Furthermore, a cut on the position and the width of the baseline was applied to remove events affected by noise or additional small pulses in the region used to determine the baseline (see figure 5.2(a)). To reduce effects due to a tilted baseline, the reconstructed linear baseline slope and its fit error were used in order to remove all events with a slope value larger than three times its fit error. Due to significantly reduced electronic noise in the two 2014 beam times compared to the September 2013 beam time, this cut could be loosened to accepting all events with a slope value smaller than five times its fit error. All described cuts on the baseline are a priori independent of the determined charge, as the baseline is determined for samples well before the pulse onset and is, therefore, not affected by the pulse. Hence, the cuts on the position, on the width and on the slope of the baseline do not affect the intrinsic energy spectrum of the detector setup.

To further reduce influences on the measured spectra from additional pile up pulses in the recorded time window and electronic noise, a cut on the baseline corrected integral over all samples not used for the charge determination, named the anticharge, was used as shown in figure 5.2(b). As this parameter includes parts of the decaying flank of the pulse, a cut on the anticharge can have an effect on the resulting spectrum. Therefore, the applied cut is kept loose enough, removing only outliers towards high positive values of the anticharge, in order to prevent effects on the energy spectrum, especially in the region of the Compton edges. This way, events with larger additional pulses in the ADC recording window could be removed. Furthermore, the anticharge could be used to remove events featuring a tilted baseline outside the window used to determine the baseline parameters (see section 4.3) from data recorded in the September 2013 beam time, as shown in figure 5.2(b).

Figure 5.3 shows the calibration spectra measured for LAB-3-20 in the September 2014 beam time using the pulse charge as a measure for the deposited energy in the scintillator. All cuts described above were applied. The shown spectrum for the AmBe-source contains both the γ-ray and neutron induced events. For further analysis, the neutron events have to be rejected as described in section 5.4.2.

5.3. Detector Simulation

Due to multiple scattering of the calibration γ-rays in the scintillator the determination of the Compton edge position in the recorded spectra is not trivial [143]. Therefore, a method to reconstruct the Compton edge from the data, which is based on input from a Monte Carlo (MC) simulation, was developed. The Monte Carlo simulation of the detector setup (see section 4.2.1) is based on the widely used GEANT4 simulation

(a) cut on baseline position and width (b) cut on baseline and anticharge
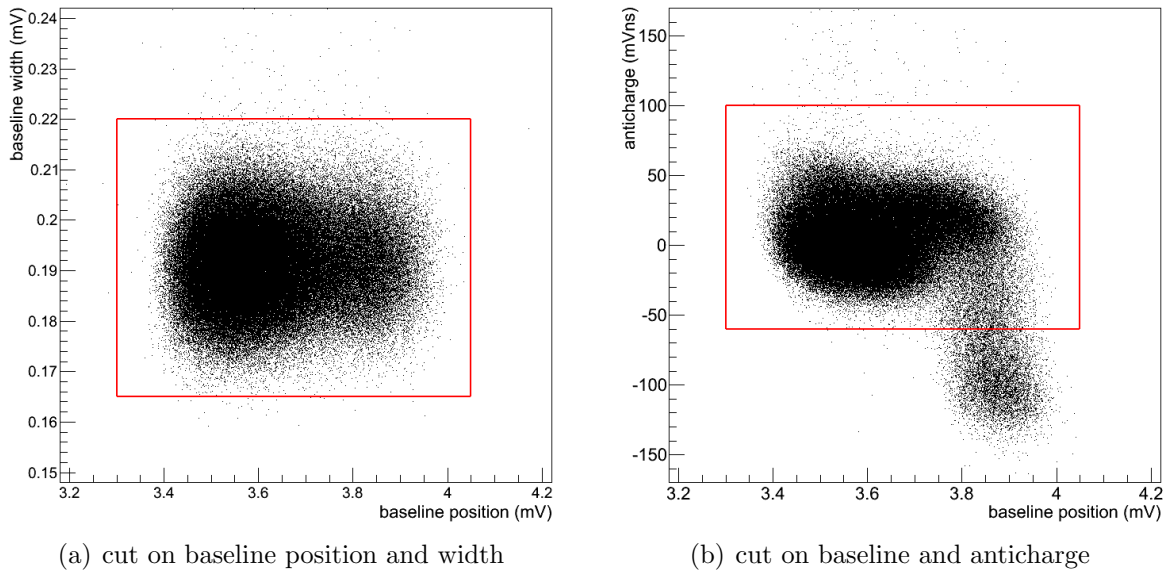
Figure 5.2.: Cuts on the position and width of the baseline (a) and on the baseline position and the anticharge (b), applied to the calibration data recorded with the ^{137}Cs-source for the LAB-3-20 scintillator sample (September 2013). All events outside the respective red box were rejected. The parameter labeled as anticharge is the baseline corrected integral over all samples not used for the charge determination (see section 4.3) and was mainly used to remove pile up pulses outside the charge integration window. Furthermore, this parameter could be used to remove pulses featuring a tilted baseline outside the interval, in which the baseline parameter is determined as described in section 4.3. These events account for the population on the lower right in figure (b) and were not present in the data recorded in the 2014 beam times due to significantly reduced electronic noise.

framework (version 4.9.6.p01) [159, 160].

The detector geometry and materials as described in section 4.2.1 were implemented into the simulation. Most of the PVC-encapsulation, the detailed scintillator sample container with quartz glass window, PTFE cell and PVC flange were included. Furthermore, the PMT was realized as a hollow glass tube surrounded with the mumetal shielding. The cap made of PVC and aluminum to make the whole detector assembly light tight was also implemented, as well as the respective source holders used in the calibration measurements. The calibration sources were included with their respective geometries as described in section 5.1. The whole simulation setup is depicted in figure 5.4 showing both source holders used in one picture, while only one was used in the respective measurement and simulation at a time. The following parts of the detector setup were not included in the simulation (see figure 4.7 for comparison):

- the Item-rail and all structures to mount the detector on it
- the back part of the detector module housing the voltage divider
- the two metal sticks and PVC part used to position and mount the source holder
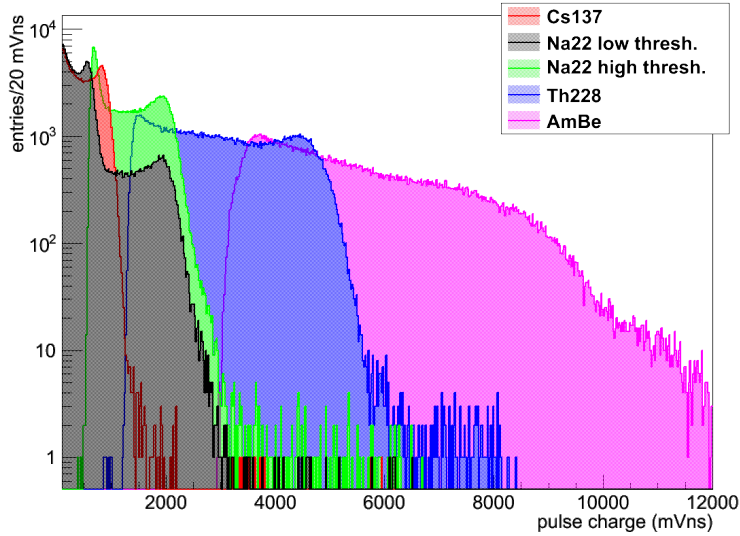
Figure 5.3.: Measured spectra for the different used calibration sources for the scintillator sample LAB-3-20 (September 2013). The pulse charge is used as a measure for the energy. All cuts described in section 5.2 have been applied. The plotted AmBe spectrum contains both γ-ray and neutron events. The neutron events need to be rejected before further analysis (see section 5.4.2 for details). In case of the ^{22}Na-source, the obtained spectra for both the lower (black) and the higher (green) used trigger thresholds are shown.

- the inner structure of the PMT

For each type of scintillator, simulations were performed using the corresponding densities and effective chemical formulas. The used values are summarized in table 5.2. In the simulations performed for the LAB-based scintillators, the same density and effective chemical formula were utilized.

To simulate the decays of the particular isotopes and the interactions of the decay products in the scintillator and the surrounding materials the predefined GEANT4 physics list `QGSP_BERT_HP` was used. Please refer to [161] for details and [162] and [163] for validation and testing.

The events for each calibration source were simulated in different ways. In case of the ^{137}Cs- and ^{22}Na-source the respective isotope was placed randomly distributed in the spherical source volumes with 1 mm diameter (see section 5.1), while the actual decay and its products were simulated by GEANT4. Accordingly, events for the ^{228}Th-source were simulated by placing ^{208}Tl, which is the isotope producing the desired 2.6 MeV γ-rays, uniformly distributed in the cylindrical source volume (see section 5.1). In case of the AmBe-source, 4.4 MeV γ-rays were started with a random position and direction in the corresponding source volume, while the neutrons produced in the AmBe-source were not included in the simulation. In the simulation the sources were placed at the same distance to the detector front as in the respective calibration measurement.

The numbers of simulated events for each calibration source and the corresponding po-
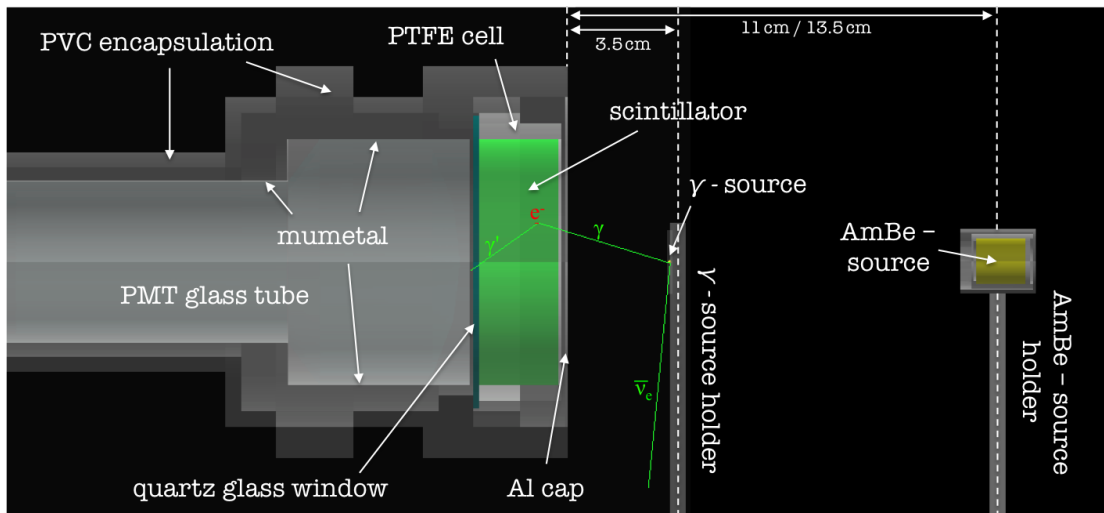
Figure 5.4.: GEANT4 based simulation of the detector setup for calibration. The detailed geometry and all materials of the setup described in section 4.2.1 have been implemented. Both source holders used are shown, while only one of both was used in the particular calibration measurement. The green lines indicate the trajectories of the electron antineutrino and the γ-ray resulting from a simulated ^{137}Cs-decay. The scattered off Compton electron is shown in red. The depicted distances between the centers of the respective sources and the detector front correspond to the distances used in the measurements as given in section 5.1.

sition of the sources center with respect to the detector front are given in table B.2 in appendix B.3. From each simulation, the deposited energies in the liquid scintillator were extracted in each simulated event. Furthermore, the deposited energy of the single interaction steps of the primary γ-ray in the scintillator were recorded. Therefore, it was possible to extract events from the obtained simulation data, in which the primary γ-ray interacted once or multiple times in the scintillator. An example spectrum for the simulated deposited energies in a LAB-based scintillator for the ^{137}Cs-source is shown in figure 5.5. The total deposited energy in the scintillator volume is shown for all events (black curve), for events, in which the γ-ray is scattered once (green curve), and for events, in which multiple scattering of the γ-ray in the scintillator occurs (red curve). The Compton edge due to the 662 keV γ-rays is clearly visible at 477 keV and, expectedly, not exceeded by single scattering events, while multiple scattering account for all events above the Compton edge energy. The small peak at about 80 keV is mainly caused by γ-rays undergoing Compton scattering in the quartz glass window, the PMT glass or other surrounding materials before being scattered in the scintillator. In case of multiple scattering in the scintillator, this peak is shifted slightly to higher energies in the corresponding spectrum.

scintillator type	eff. chem. formula	density ($\mathrm{g\,cm^{-3}}$)	used for
LAB	$C_{18}H_{30}$	0.863	LAB-X-Y
DCTarget	$C_{10}H_{19}$	0.804	DCTarget
DCGC	$C_{100}H_{205}$	0.804	DCGC
DCMV	$C_{15}H_{28}$	0.804	DCMV
PC	C_9H_{12}	0.880	Borexino
50% LAB + 50% n-paraffin	$C_{15}H_{28}$	0.805	50LAB-50nPar
75% LAB + 25% n-paraffin	$C_{33}H_{58}$	0.830	75LAB-25nPar

Table 5.2.: Effective chemical formulas and densities used in the simulation for the different scintillator samples. The last column refers to abbreviation for the different samples introduced in tables 4.2, 4.4 and 4.6. For all LAB-based scintillator mixtures the same density and hydrogen-to-carbon were used.

5.4. Reconstruction of the Compton Edge Position

As shown in figure 5.5 for simulated ^{137}Cs events, the multiple scattering of the calibration γ-rays in the scintillator has a significant contribution to the energy spectrum in the scintillator. Obviously, this is also the case in the measured calibration spectra (see figure 5.3), hidden by the limited resolution of the detector. A method to reconstruct the Compton edge position from the recorded calibration spectra, which uses the results from the simulations described above in section 5.3, was developed and will be described in the following [3].

5.4.1. Fit Model

To obtain a Compton spectrum from the recorded data, first the cuts described in section 5.2 were applied. As a measure for the deposited energy in the scintillator the *charge* of the recorded pulses was used, which is more precise than the pulse height (see section 4.3).

To obtain a conversion from the pulse charge to the energy deposited in the scintillator it is necessary to extract the Compton edge position from the measured calibration spectra. Thus, the total deposited energy provided by the simulation, including single and multiple scattering events (see section 5.3 and figure 5.5), is used as input to a likelihood fit[4].

A probability density function (PDF) for the charge distribution in the region around the Compton edges is obtained by scaling the simulated deposited energies E_{dep} to the

---

[3] The analysis method was developed in collaboration with Ludwig Prade, who studied the response of organic liquid scintillators to electrons in the scope of his diploma thesis at TUM [143].

[4] The fit is based on the ROOT framework [153, 154, 155] and the MINUIT function minimization tool [164]
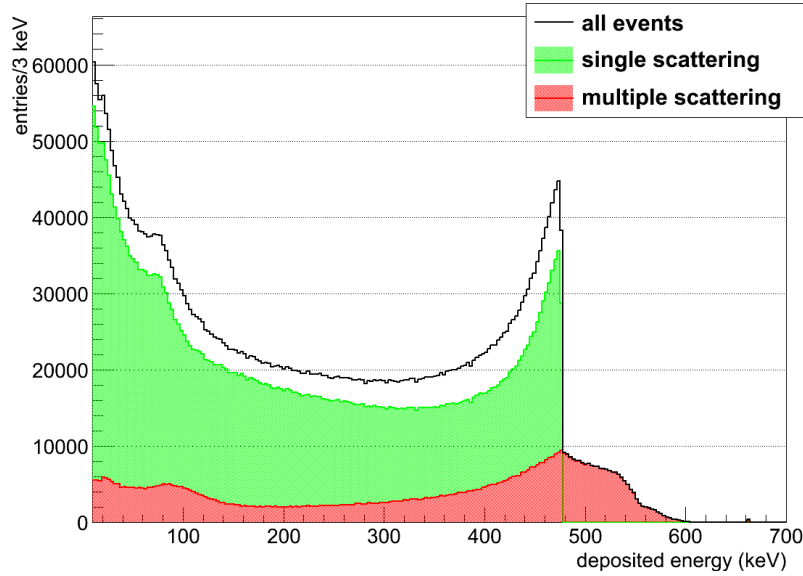
Figure 5.5.: Simulated distribution of deposited energies in LAB-based scintillator using the ^{137}Cs-source. The black histogram shows all events, while the green spectrum shows only those, in which the primary 662 keV γ-ray interacted only once in the scintillator (including previous scattering in the surrounding materials). The red spectrum corresponds to multiple scattering of the γ-ray in the scintillator, resulting in deposited energies exceeding the Compton edge at ∼ 477 keV.

parameter space of the pulse charge Q using a factor f_{scale}:

$$Q(E_{\text{dep}}) = f_{\text{scale}} \cdot E_{\text{dep}} \tag{5.2}$$

This corresponds to a transformation of the simulated deposited energy spectrum $\frac{\mathrm{d}N}{\mathrm{d}E_{\text{dep}}}$ to the spectrum in terms of the charge $\frac{\mathrm{d}N}{\mathrm{d}Q}$:

$$\frac{\mathrm{d}N}{\mathrm{d}Q} = \frac{\mathrm{d}E_{\text{dep}}}{\mathrm{d}Q} \cdot \frac{\mathrm{d}N}{\mathrm{d}E_{\text{dep}}} = \frac{1}{f_{\text{scale}}} \cdot \frac{\mathrm{d}N}{\mathrm{d}E_{\text{dep}}} \tag{5.3}$$

The resulting spectrum is convoluted with a gaussian energy resolution in the form of

$$g(Q) = \frac{1}{\sigma(Q)\sqrt{2\pi}} \cdot e^{-\frac{1}{2}\left(\frac{Q}{\sigma(Q)}\right)^2} \tag{5.4}$$

where $\sigma(Q)$ is an energy dependent resolution determined by

$$\sigma(Q) = A \cdot \sqrt{Q} = A \cdot \sqrt{f_{\text{scale}} \cdot E_{\text{dep}}} \ . \tag{5.5}$$

The square root dependency of the resolution is used because of Poisson statistics of the number of detected photons. Furthermore, A is a parameter to account for the conversion from the number of detected photons to the reconstructed charge. The convolution of

the transformed energy spectrum $\frac{\mathrm{d}N}{\mathrm{d}Q}(Q)$ and the energy resolution $g(Q)$ can be written as

$$S(Q) = \int_{-\infty}^{\infty} g(q) \cdot \frac{\mathrm{d}N}{\mathrm{d}Q}(Q-q)\,\mathrm{d}q \tag{5.6}$$

and results in the PDF for the signal part of the fit. In addition, a constant background is assumed with the following PDF in the fit range $[a, b[$:

$$B(Q) = \begin{cases} \frac{1}{b-a} & \text{for } a \leq Q \leq b \\ 0 & \text{else} \end{cases} \tag{5.7}$$

The total PDF $F(Q)$ is then constructed in the following way:

$$F(Q) = f_{\mathrm{norm}}\left[(1 - f_{\mathrm{bkg}}) \cdot S(Q) + f_{\mathrm{bkg}} \cdot B(Q)\right] \tag{5.8}$$

with f_{bkg} a parameter describing the background content in the used fit range and f_{norm} a normalization factor. A, f_{scale}, f_{bkg} and the normalization factor f_{norm} are free parameters in a likelihood fit based on the MINUIT minimization framework [164]. The result for f_{scale} is the desired parameter to reconstruct the Compton edge Q_{CE} from the measured charge spectrum

$$Q_{\mathrm{CE}} = f_{\mathrm{scale}} \cdot E_{\mathrm{CE}} \tag{5.9}$$

with E_{CE} being the theoretical Compton edge energy for the respective γ-ray energy according to equation (5.1). The statistical error on Q_{CE} is derived from the error on f_{scale} resulting from the fit by

$$\Delta Q_{\mathrm{CE}} = \Delta f_{\mathrm{scale}} \cdot E_{\mathrm{CE}}\ . \tag{5.10}$$

The errors on the theoretical Compton edge energies E_{CE} depend on the errors of the well known γ-energies and are, therefore, neglected.

Figures 5.6-5.10 show example spectra for LAB-3-20 measured in the September 2013 beam time fitted with the PDF described in this section (see equation (5.8)). All fit results (red curves) show a good agreement with the measured spectra (black data points) within the error bars. The good agreement of the fit model and the measured calibration spectra was observed for all investigated scintillator samples. The obtained statistical errors on the reconstructed Compton edge positions Q_{CE} are in the order of $\sim 0.1\%$. The results for the Compton edge positions are an input to the calibration fit described in section 5.5. As the AmBe source is a strong neutron source, the Compton spectra induced by the 4.4 MeV γ-rays need to be extracted from the recorded data by a pulse shape discrimination (PSD) analysis, which will be described in following section 5.4.2.

5.4.2. Obtaining the AmBe γ-Spectrum by PSD Analysis

To obtain a clean γ-induced spectrum from the calibration data taken with the AmBe-source the neutron-induced events need to be removed. Neutron- and γ-induced events feature different scintillation pulse shapes, which is caused by the differing energy loss of
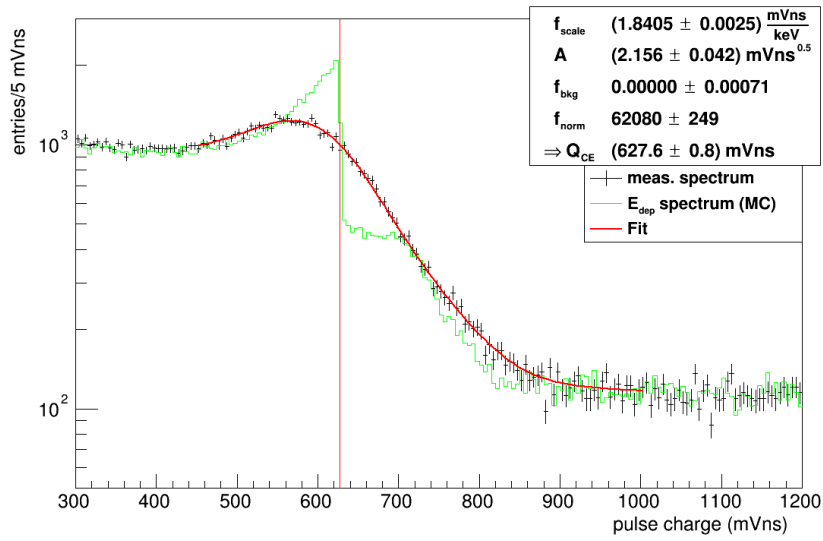
Figure 5.6.: Measured ^{22}Na-spectrum (black) for LAB-3-20 (September 2013) using the low trigger threshold of $-10\,\mathrm{mV}$. The region around the Compton edge of the $511\,\mathrm{keV}$ γ-rays was fitted with the model described in section 5.4.1 (red curve). The simulated deposited energy spectrum (green) was scaled to match the integral of the measured spectrum. The position of the Compton edge was reconstructed at $Q_{\mathrm{CE}} = f_{\mathrm{scale}}\,E_{\mathrm{CE}} = 627.6\,\mathrm{mVns}$ (vertical red line), where $E_{\mathrm{CE}} = 340.7\,\mathrm{keV}$ is the theoretical Compton edge energy according to equation (5.1).
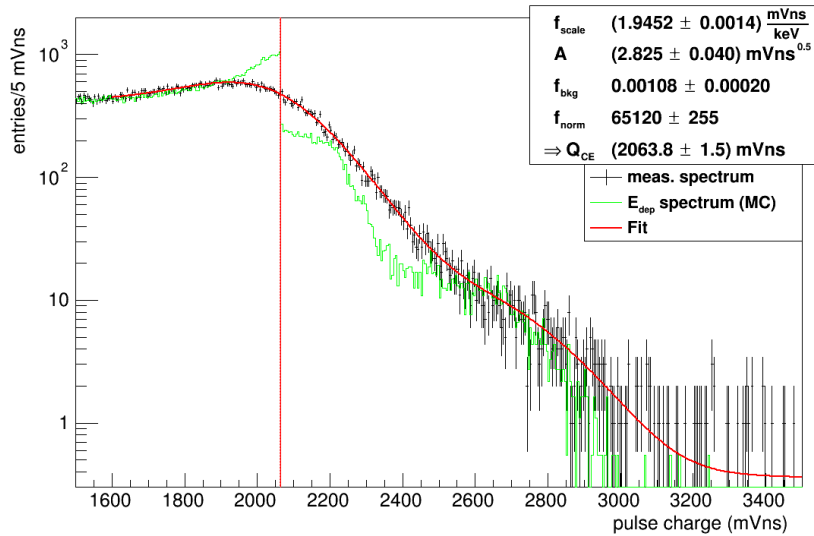
Figure 5.7.: Measured ^{22}Na-spectrum (black) for LAB-3-20 (September 2013) using the low trigger threshold of $-40\,\mathrm{mV}$. The region around the Compton edge of the $1274.5\,\mathrm{keV}$ γ-rays was fitted with the model described in section 5.4.1 (red curve). The simulated deposited energy spectrum (green) was scaled to match the integral of the measured spectrum. The position of the Compton edge was reconstructed at $Q_{\mathrm{CE}} = f_{\mathrm{scale}}\,E_{\mathrm{CE}} = 2063.8\,\mathrm{mVns}$ (vertical red line), where $E_{\mathrm{CE}} = 1061.7\,\mathrm{keV}$ is the theoretical Compton edge energy according to equation (5.1).
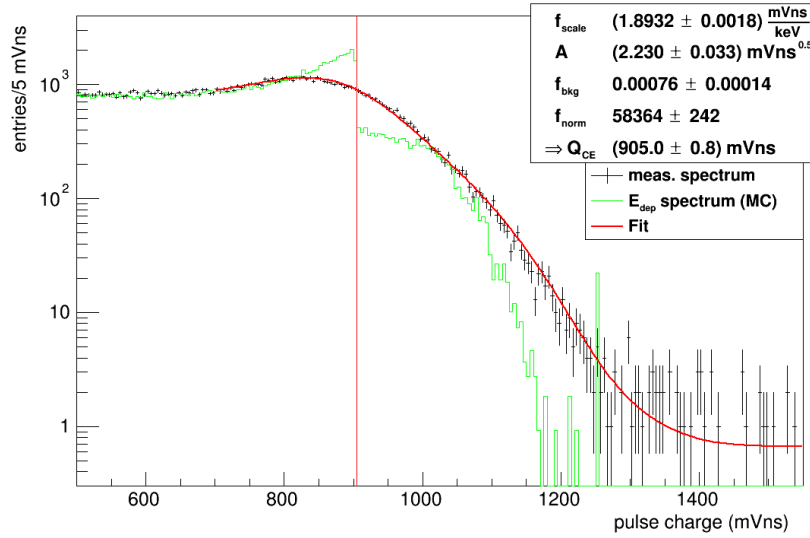
Figure 5.8.: Measured ^{137}Cs-spectrum (black) for LAB-3-20 (September 2013). The region around the Compton edge of the 661.7 keV γ-rays was fitted with the model described in section 5.4.1 (red curve). The simulated deposited energy spectrum (green) was scaled to match the integral of the measured spectrum. The position of the Compton edge was reconstructed at $Q_{\mathrm{CE}} = f_{\mathrm{scale}} E_{\mathrm{CE}} = 905.0$ mVns (vertical red line), where $E_{\mathrm{CE}} = 477.4$ keV is the theoretical Compton edge energy according to equation (5.1).
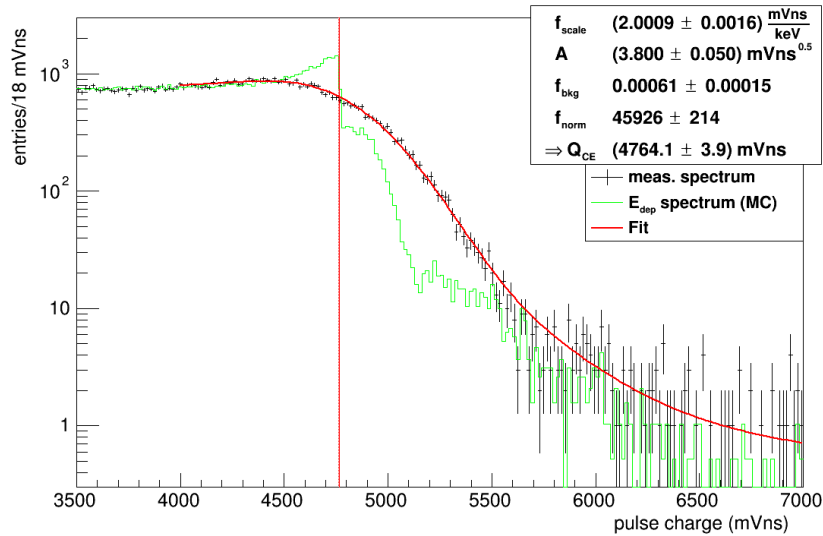
Figure 5.9.: Measured ^{228}Th-spectrum (black) for LAB-3-20 (September 2013). The region around the Compton edge of the 2614.5 keV γ-rays was fitted with the model described in section 5.4.1 (red curve). The simulated deposited energy spectrum (green) was scaled to match the integral of the measured spectrum. The position of the Compton edge was reconstructed at $Q_{\mathrm{CE}} = f_{\mathrm{scale}} E_{\mathrm{CE}} = 4764.1$ mVns (vertical red line), where $E_{\mathrm{CE}} = 2381.7$ keV is the theoretical Compton edge energy according to equation (5.1).

Figure 5.10.: Measured AmBe-spectrum (black) for LAB-3-20 (September 2013). The region around the Compton edge of the 4438.9 keV γ-rays was fitted with the model described in section 5.4.1 (red curve). The simulated deposited energy spectrum (green) was scaled to match the integral of the measured spectrum. The position of the Compton edge was reconstructed at $Q_{\mathrm{CE}} = f_{\mathrm{scale}} E_{\mathrm{CE}} = 8891.3$ mVns (vertical red line), where $E_{\mathrm{CE}} = 4197.3$ keV is the theoretical Compton edge energy according to equation (5.1). The black data 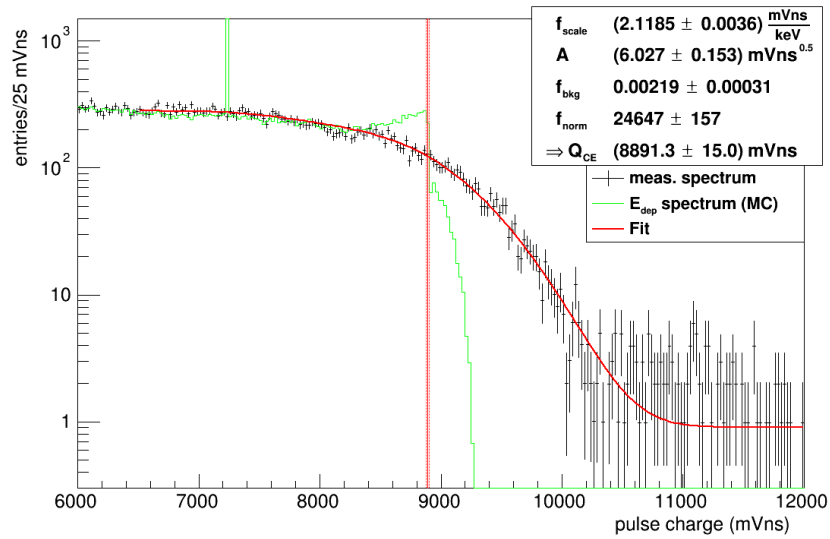was obtained by pulse shape analysis as described in section 5.4.2, which removes the neutron-induced events from the spectrum.

the recoil protons and electron (see section 3.3). Therefore, a discrimination of neutron-
and γ-induced events can be achieved by a pulse shape analysis of the recorded pulses. In
the analysis described in this section the tail-to-total parameter t_2t, determined according
to equation (4.3) in the same way for all investigated scintillator samples, was used to
discriminate between events induced by γ-rays and neutrons.

In a first step the AmBe calibration data taken for the respective scintillator sample was
divided into equally spaced slices in terms of the pulse charge, matching the desired range
for the Compton edge position reconstruction described in the previous section. As an
example, in case of the Compton spectrum for LAB-3-20 shown in figure 5.10 a plot range
from $6000\,\mathrm{mVns}$ to $12000\,\mathrm{mVns}$ was used in the Compton edge reconstruction. In that
particular case slices with a width of $500\,\mathrm{mVns}$ were used. Furthermore, two additional
slices with equal width are defined directly above and below the desired charge range for
the Compton edge reconstruction. The slice widths used in the PSD analyses of the data
taken for the different scintillator samples were chosen between $250 - 500\,\mathrm{mVns}$ depending
on the respective PSD-performance and statistics.

For each defined slice the corresponding determined values of t_2t are filled into a histogram.
In figure 5.11 two example slices are shown for the above mentioned example case of data
taken for LAB-3-20. The obtained spectra feature two peaks: The peak at lower t_2t values
is caused by γ-induced events, while the one at higher t_2t values is due to neutron-induced
protons. This can be explained by the enhanced pulse tail for neutron-induced protons,
caused by the higher energy loss of protons compared to electrons (see section 3.3). Each
of the obtained t_2t spectra is fitted with the sum of two Gaussian distributions:

$$f(t_2t) = g_\gamma(t_2t) + g_\mathrm{n}(t_2t) \tag{5.11}$$

with $g_\gamma(t_2t)$ and $g_\mathrm{n}(t_2t)$ being the Gaussians describing the peak caused by γ- and neutron-
induced events, respectively.

For each successfully fitted slice i, a cut value $t_2t_{\mathrm{cut},i}$ is determined, meeting the require-
ment of a γ-event selection efficiency $\eta_{\gamma,i} = 99\,\%$, which was determined in the following
way:

$$\eta_{\gamma,i} = \frac{\int\limits_{t_2t_{\min}}^{t_2t_{\mathrm{cut},i}} g_{\gamma,i}(t_2t)\,\mathrm{d}t_2t}{\int\limits_{t_2t_{\min}}^{t_2t_{\max}} g_{\gamma,i}(t_2t)\,\mathrm{d}t_2t} \tag{5.12}$$

where $[t_2t_{\min}, t_2t_{\max}]$ is the plot range of the respective t_2t-spectrum and $g_{\gamma,i}(t_2t)$ the Gaus-
sian fit result corresponding to the peak caused by γ-rays in slice i. Furthermore, the
relative neutron contamination $c_{\mathrm{n},i}$ in the remaining sample after rejecting all events with
$t_2t \geq t_2t_{\mathrm{cut},i}$ is determined for each slice i by

$$c_{\mathrm{n},i} = \frac{\int\limits_{t_2t_{\min}}^{t_2t_{\mathrm{cut},i}} g_{\mathrm{n},i}(t_2t)\,\mathrm{d}t_2t}{\int\limits_{t_2t_{\min}}^{t_2t_{\max}} f_i(t_2t)\,\mathrm{d}t_2t} \tag{5.13}$$

(a) Slice 4: $7000\,\mathrm{mVns} \leq Q < 7500\,\mathrm{mVns}$ (b) Slice 10: $10000\,\mathrm{mVns} \leq Q < 10500\,\mathrm{mVns}$
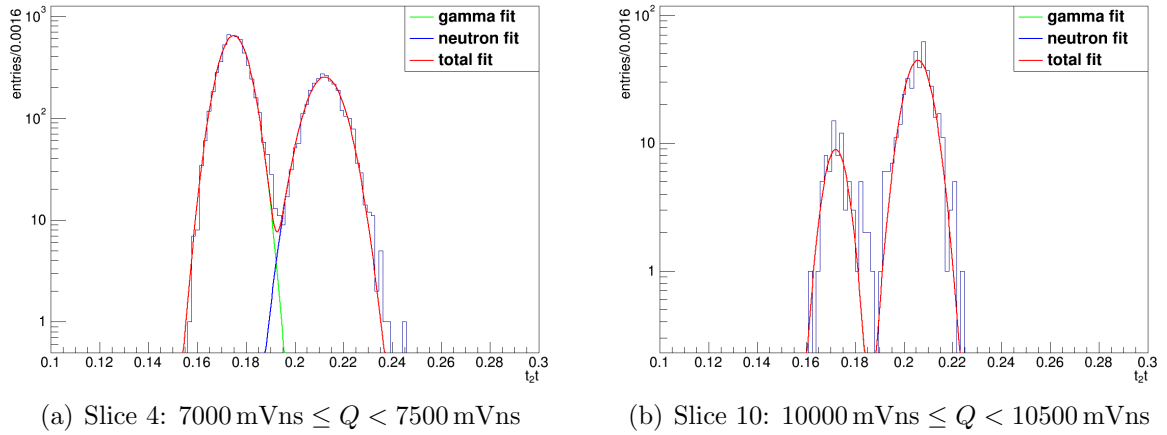
Figure 5.11.: Two example t_2t-spectra for charge (Q) slices obtained in the PSD analysis of the AmBe-calibration data taken for LAB-3-20 (September 2013). The respective peak at lower t_2t values is caused by γ-induced events, while the other one contains neutron-induced events. The spectra were fitted with the sum of two Gaussians according to equations (5.11).

with $f_i(t_2t) = g_\gamma(t_2t) + g_{\mathrm{n},i}(t_2t)$ being the result for the total fit and $g_{\mathrm{n},i}(t_2t)$ being the result for the Gaussian fit to the peak caused by neutrons. Finally, the respective errors for the neutron contaminations $c_{\mathrm{n},i}$ and the γ selection efficiencies $\eta_{\gamma,i}$ are determined from the fit results by Gaussian error propagation.

With results from all slices for the t_2t cut values $t_2t_{\mathrm{cut},i}$ at $\eta_{\gamma,i} = 99\,\%$ and the corresponding neutron contamination $c_{\mathrm{n},i}$, the γ-spectrum is extracted from the respective total AmBe dataset in the following way: First, the cut on t_2t is applied, accepting only events with $t_2t < t_2t_{\mathrm{cut}}(Q)$. Thereby, $t_2t_{\mathrm{cut}}(Q)$ is the charge dependent cut value obtained by linear interpolation between the respective values determined for all slices. The charge values for the events passing the cut are then filled into a histogram with the desired range and binning used for the Compton edge reconstruction fit (see section 5.4.1). For each bin i the expected relative neutron contamination $c_{\mathrm{n}}(Q_i)$ is determined for the bin center Q_i by linear interpolation of the results from the slices and subtracted by

$$N_i^{\mathrm{sub}} = N_i \left(1 - c_{\mathrm{n}}(Q_i)\right) \tag{5.14}$$

with N_i being the content in bin i before subtraction and N_i^{sub} after subtraction. The error on each bin i is determined from the statistical error of bin i and the error on the neutron contamination by Gaussian error propagation of equation (5.14). The respective error on the neutron contamination is determined by linear interpolation of the error obtained for each of the slices.

In the last step all bin entries are corrected for the γ selection efficiency $\eta_\gamma(Q_i)$ by

$$N_i^{\mathrm{final}} = \frac{N_i^{\mathrm{sub}}}{\eta_\gamma(Q_i)} \tag{5.15}$$

where N_i^{final} is the content of bin i after correction for the γ selection efficiency and N_i^{sub} the result from equation (5.14). The error on each bin is again determined by Gaussian error
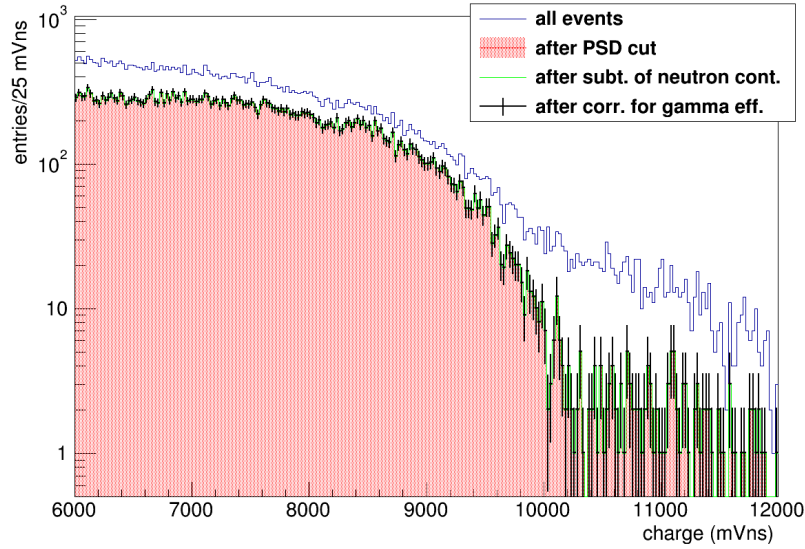
Figure 5.12.: Charge spectra for all steps in the extraction procedure to obtain the γ-ray induced spectrum from the AmBe-calibration data taken for LAB-3-20 (September 2013). The spectrum without applied PSD cut is shown in blue. After cutting on the t_2t-parameter (determined for 99 % selection efficiency for γ events) the red shaded spectrum is obtained, which is hardly distinguishable from the spectrum after subtraction of the neutron contamination (green) according to equation (5.14). The neutron contamination after applied cut on t_2t is smaller than 0.1 % in the plotted range. The spectrum obtained after correcting for the γ selection efficiency is shown by the black data points.

estimation of equation (5.15). Figure 5.12 shows the obtained spectrum for all steps described above for the AmBe-calibration data recorded for LAB-3-20 during the September 2013 beam time. Due to the good PSD performance of this scintillator the contamination of neutron events after the cut on the t_2t-parameter is smaller than 0.1 % in the plotted range. These differences between the individual spectra obtained in the steps after the t_2t-cut are almost invisible.

Due to the limited statistics at higher charges, a fit of the function given in equation (5.11) to the respective slices was not possible and no values for $t_2t_{\text{cut},i}$ and the remaining neutron contamination $c_{\text{n},i}$ could be determined. To extract the γ-spectrum at higher charge values a "last trustful slice" (LTS) with a central value for the charge of Q_{thresh} was identified. For all bins i with $Q_i > Q_{\text{thresh}}$ the values for $t_2t_{\text{cut},i}$ and $c_{\text{n},i}$ obtained for the LTS were used. In the example shown in figure 5.12 slice 10 with a central value of $Q_i = 10250\,\text{mVns}$ was used as LTS. This particular slice was already shown in figure 5.11(b).

5.4.3. Validation and Error Estimation

The reconstruction of the Compton edge position from the measured γ-spectra as described in section 5.4.1 is based on assumptions regarding the linear relation between deposited energy and the charge (see equation 5.2) and regarding the energy dependent resolution

of the detector (see equation 5.5). Furthermore, not all effects present in the experiment can be included in the simulation. Therefore, it was mandatory to test and validate the described method, which was a major goal of the Diploma thesis of Ludwig Prade [143], which was supervised by the author.

A coincidence setup with a high purity germanium (HPGe) detector and the scintillator detector described in section 4.2.1 was developed. The calibration source was placed between both detectors. Taking advantage of the high energy resolution of the HPGe-detector, events, in which the γ-ray did a 180° Compton scattering and deposited the remaining energy in the HPGe-detector, were selected. Thereby, the position of the Compton edge could easily be determined from the charge spectrum of those events measured with the scintillator detector. Additionally, a Compton spectrum was recorded with the same calibration source at the same position with respect to the scintillator detector, triggering on the scintillator detector signals only. On this spectrum the Compton edge reconstruction method described in section 5.4.1 was applied. Based on the comparison of the results from the coincidence measurement and the fit to the additionally taken Compton spectrum the systematic error on the Compton edge reconstruction method could be estimated.

In figure 5.13 a comparison of the result from the coincidence measurement and the fitted Compton spectrum is shown for the 1274.5 keV γ-rays emitted from the ^{22}Na-source. The model described in section 5.4.1 was fitted to the measured spectrum using the deposited energies in the scintillator from a MC-simulation. The results from the Compton edge position reconstruction (vertical red line) and the coincidence measurement (vertical turquoise line) are shown with 1σ statistical error intervals (shaded areas). According to the discrepancy of both obtained results, the systematic error on the reconstructed Compton edge position for the 1274.5 keV γ-rays from the ^{22}Na-source was estimated conservatively to be 1.5 %.

The coincidence measurement could successfully be carried out for the γ-rays emitted by the ^{137}Cs- and the ^{22}Na-source. For the ^{228}Th-source the measurement was not possible due to irreducible background from the various additional emitted γ-ray energies. In case of the AmBe-source the measurement could not be performed because of the source being mainly a strong neutron source. The emitted neutrons would activate the HPGe-detector and could affect the doping of the Ge-crystal. For both the ^{228}Th- and the AmBe-source the errors were estimated conservatively to be 2.0 % and 3.0 %, respectively, based on the results obtained for ^{137}Cs and ^{22}Na. In table 5.3 the estimated systematic errors for the determination of the Compton edge according to the method described in section 5.4.1 are shown for the different γ-energies from the used sources.

To obtain the total error on the reconstructed Compton edge position the relative systematic errors shown in table 5.3 were added linearly with the statistical errors from the fit, which are in the order of 0.1 %. Both the reconstructed position and the corresponding total error are inputs to the calibration fit described in the next section 5.5.
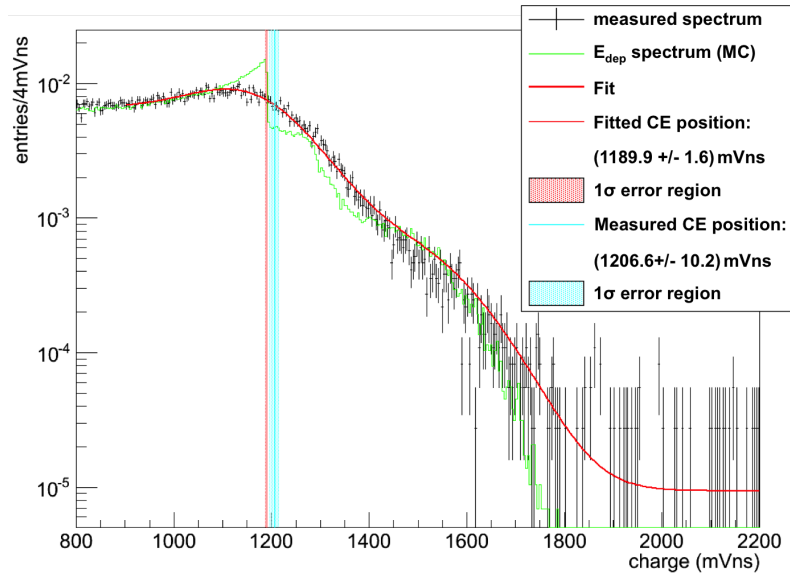
Figure 5.13.: Comparison of the results for the reconstructed Compton edge position due to 1274.5 keV γ-rays (^{22}Na) from the fit and from a coincidence measurement with a HPGe-detector (see [143] for details on measurement). The data (black) was fitted with the model described in section 5.4.1 (red curve) using the deposited energies from the simulation described in section 5.3 (green spectrum). The result for the Compton edge position from the fit (vertical red line) and the result from the measurement (vertical turquoise line) are shown with 1σ statistical errors (shaded areas). Based on the shown results, the error on the Compton edge fit method was estimated conservatively to be 1.5 % in case of the Compton edge due to the 1274.5 keV γ-rays emitted from the ^{22}Na-source.

source	γ-energy (keV)	Compton edge (keV)	rel. syst. error
^{137}Cs	661.7 keV	477.4 keV	1.0 %
^{22}Na	511.0 keV	340.7 keV	1.0 %
	1274.5 keV	1061.7 keV	1.5 %
^{228}Th	2614.5 keV	2381.7 keV	2.0 %
AmBe	4438.9 keV	4197.3 keV	3.0 %

Table 5.3.: Systematic uncertainties on the determination of the Compton edges using the method described in section 5.4.1. The uncertainties corresponding to the calibration using the ^{137}Cs- and the ^{22}Na-source were estimated based on coincidence measurements with an additional HPGe-detector performed by Ludwig Prade [143] in the scope of his Diploma thesis. In case of the ^{228}Th- and the AmBe-source the errors were extrapolated from the results obtained for ^{137}Cs and ^{22}Na, as for these sources no coincidence measurements were possible.

5.5. Calibration Fit

5.5.1. Linear Calibration Fit

After reconstructing the Compton edge positions for all calibration spectra (see section 5.4.1) recorded for the respective scintillator sample it is possible to determine the functional relation between the deposited electron energy and the measured charge. This was achieved by a χ^2-based fit to the obtained data points using the following linear relation:

$$E_{\text{vis}}(Q) = m \cdot Q + t \tag{5.16}$$

with $E_{\text{vis}}(Q)$ the visible energy, Q the determined pulse charge, m the slope and t the constant of the linear fit. Figure 5.14 shows an example fit to the calibration data obtained for the LAB-3-20 sample investigated in the September 2013 beam time. The errors on the reconstructed Compton edge position are the linearly added systematical and statistical errors as described in section 5.4.3. The errors on the well known theoretical Compton edge energies have been neglected. The linear function fits the data quite well. The nonzero value for t is expected due to ionization quenching (see section 3.2), which mainly affects the energy region below ~ 200 keV in case of electrons [143, 165]. Above this region a linear relation between the light output and the deposited energy can be assumed in good approximation. In the representation as shown in figure 5.14 an offset of $t > 0$ due to quenching has to be taken into account.

Furthermore, the data point for the AmBe-calibration at an energy of about 4200 keV seems to be shifted slightly to higher charge values with respect to the fitted curve. This was observed also in case of the other investigated scintillator samples. A possible explanation for this may be pile up of γ- and neutron-induced events in the scintillator. Both are emitted from the AmBe source simultaneously, possibly resulting in a simultaneous energy

Figure 5.14.: Linear fit to the reconstructed and theoretical Compton edge positions according to equation (5.16) obtained for LAB-3-20 (Sept. 2013). The given errors on the reconstructed Compton edge positions include statistical and systematic errors and were estimated as described in section 5.4.3. The errors on the theoretical Compton edge energies (see table 5.1) were neglected.

deposition in the scintillator. Due to the limited time resolution of the PMT both energy depositions would end up in the same pulse and, therefore, cannot be distinguished. Furthermore, events with a high energy deposition of the γ-ray in the region of the Compton edge and a small energy deposition by a simultaneous neutron may be misinterpreted by the pulse shape analysis described in section 5.4.2. In such a case the pulse shape would not differ significantly from an energy deposition of a γ-ray only. As the precise spectrum of the neutrons from the AmBe source is not known, the described effect was not included in the MC-simulation (see section 5.3). Hence, this pile up is not included in the Compton edge reconstruction based on the simulation input as described in section 5.4.1.

Nevertheless, it was decided to use the AmBe calibration point in the linear fit, as it is the only data point at high energies, where the events induced by the beam neutrons are expected. Furthermore, the rather large error on the reconstructed Compton edge position reduces the weight of this data point in the fit.

5.5.2. Quadratic Calibration Fit

In addition to the above described linear fit a quadratic function was fitted to the calibration data, which matches the data including the point for AmBe better for all investigated scintillator samples:

$$E_{\mathrm{vis}}(Q) = a \cdot Q^2 + b \cdot Q + c \tag{5.17}$$

with $E_{\mathrm{vis}}(Q)$ the visible energy, Q the determined pulse charge and a, b and c free parameters of the fit. Figure 5.15 shows an example fit of equation (5.17) to the calibration data
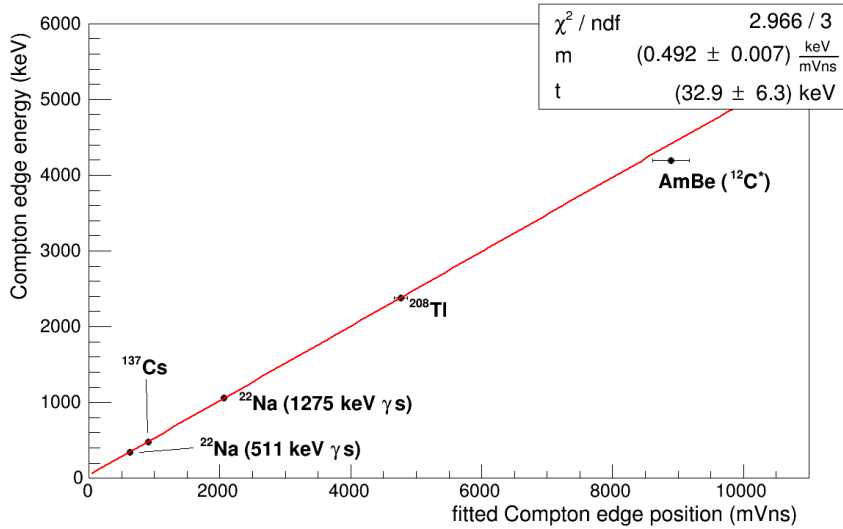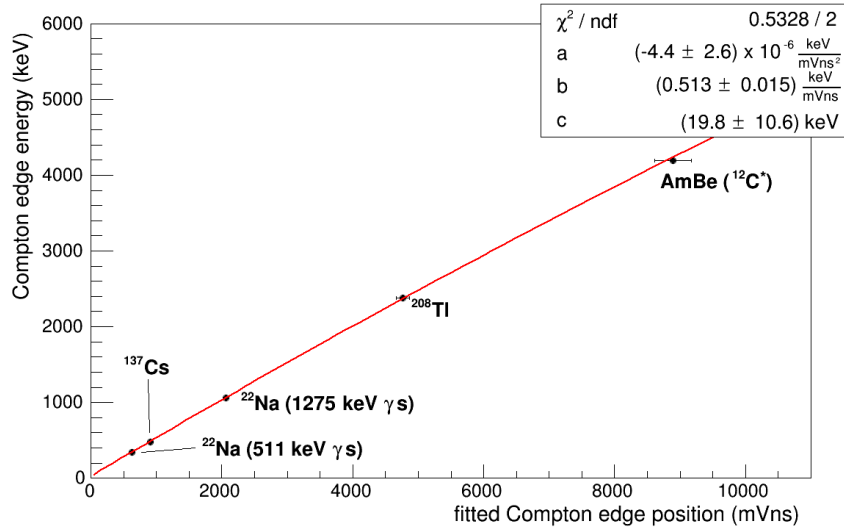
Figure 5.15.: Fit of a quadratic function to the reconstructed and theoretical Compton edge positions according to equation (5.17) obtained for LAB-3-20 (Sept. 2013). The given errors on the reconstructed Compton edge positions include statistical and systematic errors and were estimated as described in section 5.4.3. The errors on the theoretical Compton edge energies (see table 5.1) were neglected.

points obtained for the LAB-3-20 sample (September 2013). The data points are the same as those shown in figure 5.16. While the quadratic function fits the data nicely, the relative errors on the parameters are higher compared to the linear fit. This behavior is observed in the calibration of all investigated scintillator samples. Especially the parameter describing the quadratic term a has a rather huge error in the order of 50 %.

5.5.3. Results

In table B.3 in appendix B.4 the results from the fits of the linear (see section 5.5.1) and quadratic function (see section 5.5.2) to the data obtained from the Compton edge position reconstruction, as described in section 5.4.1, are given for all investigated scintillator samples. The analysis of the beam data with regard to proton quenching presented in chapter 6 was performed for both the calibration using the linear function and the calibration using the quadratic function applied to the data.

5.6. Photoelectron Yield Estimation From Energy Resolution

The pulse shape discrimination (PSD) performance of liquid scintillators (see section 3.3) strongly depends on the number of detected photons, i.e. the number of photoelectrons (p.e.) produced in the photocathode of the photomultiplier tube (PMT). The PSD perfor-

mance improves with the number of detected photoelectrons. As the PMT was operated at moderate high voltages (see section 4.5), which did not allow the detection of single photoelectrons, no dedicated photoelectron calibration of the detector was performed for each investigated scintillator. Therefore, the photoelectron yield for a given energy was estimated from the calibration data, taken for the respective scintillator sample.

The energy resolution of a scintillator detector is strongly related to the number of detected photoelectrons. Estimates for the energy resolution of the detector for each scintillator sample are obtained from the results of the fits to the Compton spectra to the measured calibration spectra, as described in section 5.4.1. Using equations (5.5) and (5.9) the relative energy resolution at the Compton edge $\frac{\sigma_{E_{\mathrm{CE}}}}{E_{\mathrm{CE}}}$ for each of the different γ-ray energies, emitted by the calibration sources used (see section 5.1), can be estimated by:

$$\frac{\sigma_{E_{\mathrm{CE}}}}{E_{\mathrm{CE}}} \approx \frac{\sigma_{Q_{\mathrm{CE}}}}{Q_{\mathrm{CE}}} = \frac{A \cdot \sqrt{Q_{\mathrm{CE}}}}{Q_{\mathrm{CE}}} = \frac{A}{\sqrt{Q_{\mathrm{CE}}}} \tag{5.18}$$

with Q_{CE} being the reconstructed position of the Compton edge in terms of the pulse charge (section 4.3). $\sigma_{Q_{\mathrm{CE}}} = A \cdot \sqrt{Q_{\mathrm{CE}}}$ is the resolution of the detector at the Compton edge according to equation (5.5), which describes the energy dependent Gaussian resolution of the detector in the fit to the measured Compton spectra by a fit parameter A.

Figure 5.16 shows the relative resolutions $\frac{\sigma_{Q_{\mathrm{CE}}}}{Q_{\mathrm{CE}}}$ as a function of the Compton edge energy (see table 5.1) for the LAB-3-20(2) scintillator sample (February 2014). The shown data points were fitted with the following functional relation [20]:

$$\frac{\sigma_{Q_{\mathrm{CE}}}}{Q_{\mathrm{CE}}}(E) = \sqrt{a^2 + \frac{b^2}{E} + \frac{c^2}{E^2}} \tag{5.19}$$

where the parameters a, b and c represent the contributions of the spacial dependance of the light collection efficiency, the statistical fluctuation and the electronic noise to the energy resolution, respectively. As shown in figure 5.16 the data point corresponding to the calibration with the AmBe-source does not seem to follow the functional relation, which is indicated by the other data points. This behavior is observed for all investigated scintillator samples. An explanation for this behavior could again be pile up of γ-ray and neutron induced events in the scintillator, as already described in section 5.5.1. As a consequence, the data point obtained from the AmBe calibration was not included in the fit of equation (5.19) to the data. As indicated by the reduced χ^2/ndf (ndf is the number of degrees of freedom), equation (5.19) describes the data points well.

The photoelectron yield can be estimated from the fit result for parameter b of equation (5.19) as described in the following. Due to Poisson statistics the relative energy resolution $\frac{\sigma_E}{E} \approx \frac{\sigma_{Q_{\mathrm{CE}}}}{Q_{\mathrm{CE}}}(E)$ is limited by the number of detected photoelectrons N_{pe}:

$$\frac{\sigma_E}{E} \geq \frac{\Delta N_{\mathrm{pe}}}{N_{\mathrm{pe}}} = \frac{1}{\sqrt{N_{\mathrm{pe}}}} \tag{5.20}$$

where $\Delta N_{\mathrm{pe}} = \sqrt{N_{\mathrm{pe}}}$ is the error on the number of detected photoelectrons due to Poisson statistics. Parameter b in equation (5.19) describes the contribution of the detected number
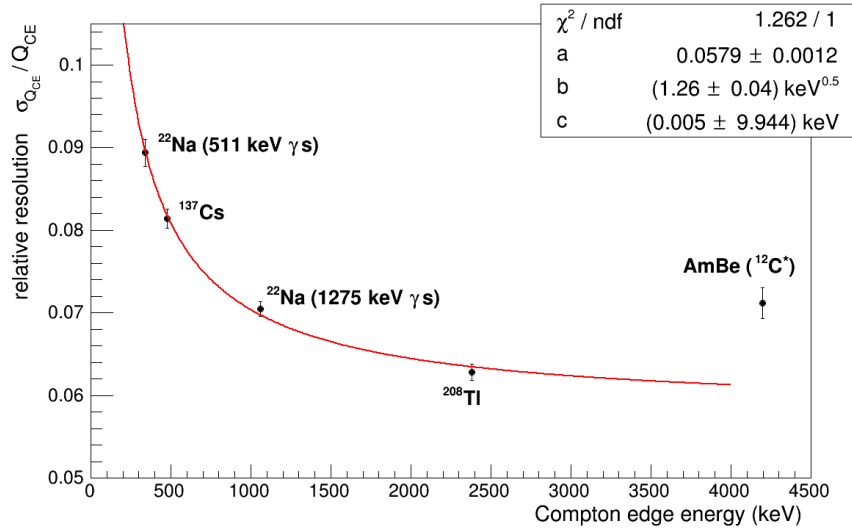
Figure 5.16.: The relative resolution $\frac{\sigma_{Q_{\mathrm{CE}}}}{Q_{\mathrm{CE}}}$ of the detector as a function of the energy for the LAB-3-20(2) scintillator sample (February 2014). The relative resolution for each data points was determined according to equation (5.18) from the results of the fits to the Compton spectra, described in section 5.4.1. The horizontal position of each data point represents the Compton edge energy due to the γ-ray emitted by the respective source (see table 5.1). The data points were fitted with the function given in equation (5.19), where the point corresponding to the calibration with the AmBe-source was not included.

of photoelectrons to the energy resolution of the detector. Therefore, the photoelectron yield can be estimated by:

$$\frac{\Delta N_{\mathrm{pe}}}{N_{\mathrm{pe}}} = \frac{1}{\sqrt{N_{\mathrm{pe}}}} \approx \sqrt{\frac{b^2}{E}} \quad \Longrightarrow \quad N_{\mathrm{pe}}(E) \approx \frac{E}{b^2} \tag{5.21}$$

The error on the estimated photoelectron yield is determined by Gaussian error propagation, using the error on b from the result of the fit. For each scintillator sample, the photoelectron yield is estimated for an energy of 1 MeV. In the example of the LAB-3-20(2) scintillator sample (February 2014), for which the fit to the relative resolution data was shown in figure 5.16, the photoelectron yield at 1 MeV was estimated to be $N_{\mathrm{pe}}(1\,\mathrm{MeV}) = 628 \pm 40$.

The estimated photoelectron yield for all investigated scintillator samples is summarized in table 5.4. The results for some of the scintillator samples show rather high values, like $N_{\mathrm{pe}}(1\,\mathrm{MeV}) = 1244 \pm 606$ obtained for the LAB-5-20 sample (September 2013). Within the large errors this value is compatible with those obtained for comparable scintillators, like LAB-3-20(2) and LAB-7-20 (February 2014). The rather high values for the photoelectron yields, obtained for some scintillator samples, show that additional calibration points would be needed to determine the photoelectron yield more reliably. As the amount of beam time was limited, the time spent for calibration was optimized in order to use the beam times efficiently. Despite the low number of calibration points, the estimated photoelectron

	sample	photoelectrons at 1 MeV
	DCMV	512 ± 98
	LAB-3-20	909 ± 448
Sept. 2013	Borexino	862 ± 272
	LAB-5-20	1244 ± 606
	LAB-3-40	666 ± 45
	LAB-3-20(2)	628 ± 40
	DCTarget	402 ± 17
	LAB-3-10	560 ± 136
Feb. 2014	LAB-3-0	720 ± 228
	LAB-7-20	637 ± 37
	LAB-9-20	600 ± 33
	LAB-3-80	750 ± 228
	50LAB-50nPar	547 ± 30
	LAB-1-20	498 ± 23
	DCMV-PSD	503 ± 24
	DCGC	424 ± 19
May/June 2014	LAB-5-20-PSD	547 ± 27
	75LAB-25nPar	556 ± 30
	LAB-3-40-PSD	664 ± 168
	Borexino(2)	753 ± 214
	LAB-3-0(2)	685 ± 206

Table 5.4.: The estimated photoelectron yield at 1 MeV for all scintillator samples, which were investigated in the three beam times performed in 2013 and 2014 (see sections 3.4.4 and 4.5). The photoelectron yield was estimated as described in section 5.6.

yields show reasonable values for all scintillators within the errors. While for the LAB-3-20(2) sample (September 2013) 628 ± 40 photoelectrons are detected at $1\,\mathrm{MeV}$, estimated photoelectron yield for the DCTarget sample is 402 ± 17. The difference is expected from the different light yields of both scintillators. Furthermore, the photoelectron yield obtained for the DCGC sample (May/June 2014) of 424 ± 19 is in good agreement with the value obtained for the DCTarget sample, which is expected, as both scintillators were developed in such way that the light yields are the same.

The values for the estimated photoelectron yield are of interest for the interpretation of the results for the PSD performance for neutron and γ-ray induced events (see chapter 7). As the PSD performance depends on the photoelectron yield, the estimated values given in table 5.4 provide a possibility to relate the obtained results for the PSD performance to experiments, which feature a different, typically lower, photoelectron yield.

5.7. Detector Position Dependent Gain Correction

It was discovered that the gain of the PMT variates up to several percent, although a constant high voltage is applied. This is mainly due to the noisy electromagnetic environment in hall II at the MLL, which houses strong magnets for beam guidance. Furthermore, the detector is moved to different positions with respect to the beam axis to obtain different incident neutron energies for the proton quenching measurement (see sections 4.2.2 and 6.3). This also has an affect on the gain, as the PMT orientation is changed with respect to ambient electromagnetic fields, which are not fully absorbed by the PMT's mumetal shielding.

5.7.1. Determination of Gain Correction Factors

To correct for the gain variations, calibration data with the ^{22}Na-source has been taken with the low threshold (see section 5.2) for all scintillator samples at each detector position before or after the measurement with the neutron beam[5]. The Compton spectra obtained from this data - the *comparison spectra* - were used to determine the change in the PMT gain by comparison with a *reference spectrum*, for which the corresponding ^{22}Na-calibration data taken for energy calibration was used. For both, the reference and the comparison Compton spectra, the pulse charge determined according to equation (4.2) was used as a measure for the deposited energy in the scintillator.

Based on the assumption of a direct proportionality of the pulse charge and the PMT gain, a correction factor f_{corr} was introduced to parameterize the variations in the gain. This factor was used to scale the charge from each comparison measurement in such way

---

[5] The respective calibration data for gain correction ($2 \cdot 10^5$ events in each measurement) was taken right before and right after moving the detector to a different position with respect to the beam axis. This way, the source holder, used to position the calibration source (see figure 4.7), did not have to be removed between both measurements and the available beam time could be used efficiently.

that the resulting Compton spectrum matches that obtained from the respective reference measurement. For both, the comparison and reference spectrum, a histogram with equal binning and range was defined. While the reference spectrum was filled once with the charge data of the corresponding measurement, the comparison spectrum was recreated in each of the minimization steps in order to find the optimal gain correction factor f_{corr} as described below. The range and binning were set in such way that both Compton edges due to the 511 keV and 1274.5 keV γ-rays emitted by the ^{22}Na-source are fully contained in the reference spectrum.

As a measure for the agreement between the reference spectrum and the respective comparison spectrum obtained for each value for f_{corr} in the minimization steps Pearson's χ^2-test was used. A suitable figure of merit is given by [166] in the following form:

$$\chi^2(f_{\mathrm{corr}}) = \frac{1}{N_{\mathrm{r}} \cdot N_{\mathrm{c}}(f_{\mathrm{corr}})} \sum_{i=1}^{N_{\mathrm{bins}}} \frac{(N_{\mathrm{r}} \cdot n_{\mathrm{c},i}(f_{\mathrm{corr}}) - N_{\mathrm{c}}(f_{\mathrm{corr}}) \cdot n_{\mathrm{r},i})^2}{n_{\mathrm{r},i} + n_{\mathrm{c},i}(f_{\mathrm{corr}})} \tag{5.22}$$

with N_{r} being the total number of entries in the reference spectrum, $N_{\mathrm{c}}(f_{\mathrm{corr}})$ being the total entries in the comparison spectrum depending on the value of f_{corr} and $n_{\mathrm{r},i}$ and $n_{\mathrm{c},i}(f_{\mathrm{corr}})$ being the entries in bin i of the respective spectrum. N_{bins} is the number of used bins, which is limited to those, which have at least 10 entries in both spectra, to ensure an approximate normal distribution of the counts. It can be shown that the quantity determined in equation (5.22) corresponds to the commonly known χ^2-value [166]. Therefore, χ^2/ndf can be used as a parameter for how well the compared spectra match, where the number of degrees of freedom ndf is given by $N_{\mathrm{bins}} - 1$.

As the χ^2, determined using equation (5.22), suffers from statistical fluctuations of the bin contents of the compared spectra, the optimal value for the correction factor f_{corr} cannot be found reliably by the available numeric minimization algorithms. Therefore, the minimization was performed by a scan of the parameter f_{corr} in steps of 0.002 in the interval $[0.8, 1.2]$. For each step, the χ^2 was determined according to equation (5.22) with the corresponding error using Gaussian error propagation as described in appendix B.1.

The values of χ^2 and the corresponding errors obtained by a scan of the parameter f_{corr} is shown in figure 5.17 as a function of f_{corr} for a measurement with the LAB-3-20 sample (September 2013) and the detector at Pos4 (see section 4.2.2). In that particular case, the corresponding reference spectrum was taken at Pos1. The shown errors in x-direction are defined by the step size of the scan of 0.002 to be ± 0.001 for each data point. The data resulting from the scan was approximated by a polynomial of order two in the region around the minimum:

$$\chi^2(f_{\mathrm{corr}}) = p0 + p1 \cdot f_{\mathrm{corr}} + p2 \cdot f_{\mathrm{corr}}^2. \tag{5.23}$$

In all measurements with the different scintillator samples, the fit range was defined to be ± 0.03 around that value of f_{corr} for which the minimum χ^2 was obtained in the scan. The minimum of function (5.23), fitted to the data, determines the best fit value of $f_{\mathrm{corr}}^{\mathrm{min}}$.

An example plot showing the reference spectrum and the scaled comparison spectrum for $f_{\mathrm{corr}}^{\mathrm{min}}$ is given in 5.18 for the example measurement for the LAB-3-20 sample (September

χ² / ndf	1.665 / 28
p0	6.995e+05 ± 105.6
p1	-1.362e+06 ± 107.1
p2	6.632e+05 ± 100
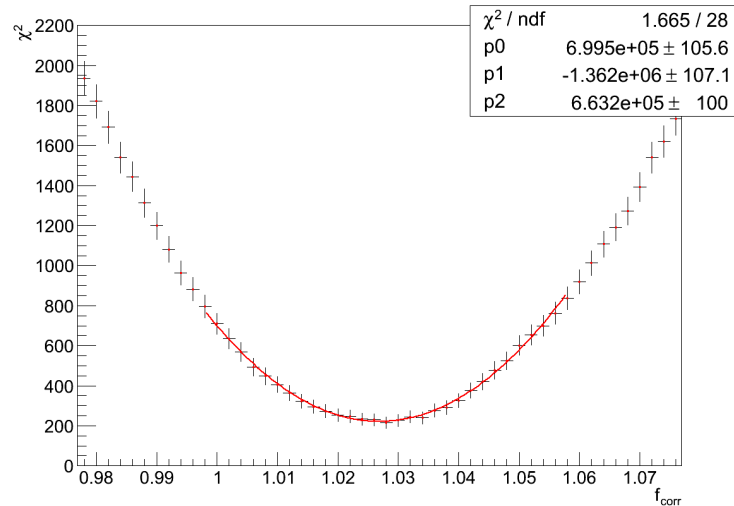
Figure 5.17.: χ^2-values with errors as a function of f_{corr}, obtained for a scan of the gain correction parameter f_{corr} for data taken with the ^{22}Na-source for the LAB-3-20 sample (Sept. 2013) at Pos4 (see section 4.2.2). The corresponding reference spectrum was taken at Pos1. The obtained data was fitted with a polynomial of order two according to equation (5.23). The minimum was calculated from the fit result to be at $f_{\text{corr}}^{\text{min}} = 1.0269 \pm 0.0006$.

2013) already used in figure 5.17. The ^{22}Na charge spectrum measured at Pos4 was scaled with $f_{\text{corr}}^{\text{min}} = 1.0269 \pm 0.0006$ and normalized to the reference spectrum taken for energy calibration at Pos1. Both spectra match nicely with a reduced χ^2/ndf of 0.79208.

5.7.2. Error Estimation and Results

The error on the best fit gain correction factor $f_{\text{corr}}^{\text{min}}$ can be determined by error propagation of the formula obtained for the minimum of function (5.23), which was fitted to the data obtained from the scan of the parameter f_{corr} (see figure 5.17). For the results presented in this thesis a more conservative error was estimated as described in the following. In each measurement, one thousand random spectra were generated according to the probability density function of the reference spectrum. The number of random events per generated spectrum was set to be equal to the number of events in the comparison spectrum, which was scaled with $f_{\text{corr}}^{\text{min}}$. For each generated spectrum i the fit procedure as described in the previous section was applied expecting a result close to $f_{\text{corr},i}^{\text{min}} = 1$. The results for $f_{\text{corr},i}^{\text{min}}$ were filled into a histogram and the resulting spectrum was fitted with a Gaussian. The width from the Gaussian fit is then used as the error on the correction factor $f_{\text{corr}}^{\text{min}}$ as determined in the previous section. In figure 5.19 the distribution of the resulting values for $f_{\text{corr},i}^{\text{min}}$ are shown for the example measurement for LAB-3-20 (September 2013) taken at Pos4. The shown Gaussian fit to the distribution features a mean compatible with 1 and a rounded value for the width of 0.0006, which corresponds to the error on $f_{\text{corr}}^{\text{min}}$ given in figure 5.18.

In addition to the error on the gain correction factor, determined as described above, a
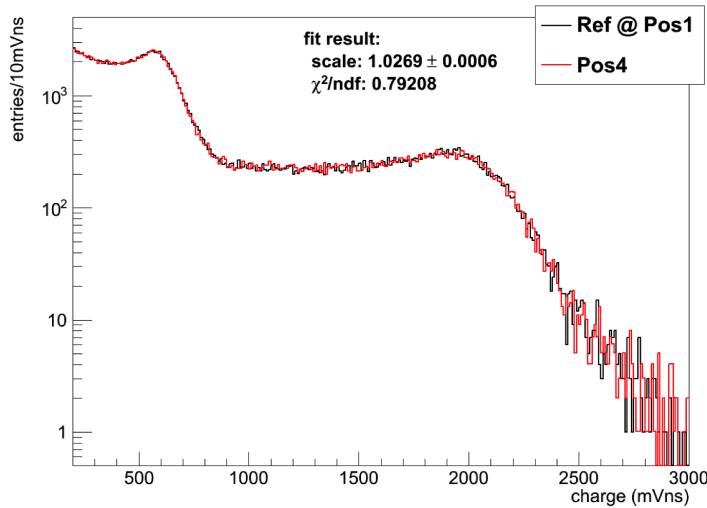
Figure 5.18.: Comparison plot for the LAB-3-20 sample (Sept. 2013) showing the reference ^{22}Na Compton spectrum taken at Pos1 (black) and the spectrum taken at Pos4 (red). The comparison spectrum at Pos4 has been scaled with the best fit value for f_{corr} (given as *scale* in the plot), which was determined as described in the text. The given statistical error on the best fit value for f_{corr} was estimated as given in section 5.7.2.

systematic error of 0.5% due to the gain instability was assumed and used in the analysis of the data taken at the beam times with regard to proton quenching (see chapter 6).

The resulting gain correction factors obtained from the ^{22}Na-measurements for each of the investigated scintillator samples at each detector position before or after the corresponding measurement with the neutron beam are given in tables B.4-B.6 in appendix B.5 for each performed beam time. In addition to the obtained gain correction factors, the respective detector positions, at which the reference spectrum was taken for the energy calibration, are given. The resulting values for the gain correction factors indicate gain variations of up to $\sim 6.4\%$, while the variations are in the region of 3% in most of the cases. Especially the larger discrepancies to the reference measurement should mainly be caused by the strong ambient magnetic fields from magnets used for beam guidance in hall II of the MLL.

The gain correction factors given in tables B.4-B.6 were applied to the pulse charge values from the corresponding measurements with the neutron beam, before further analysis with regard to proton quenching (see chapter 6) or PSD performance (see chapter 7).
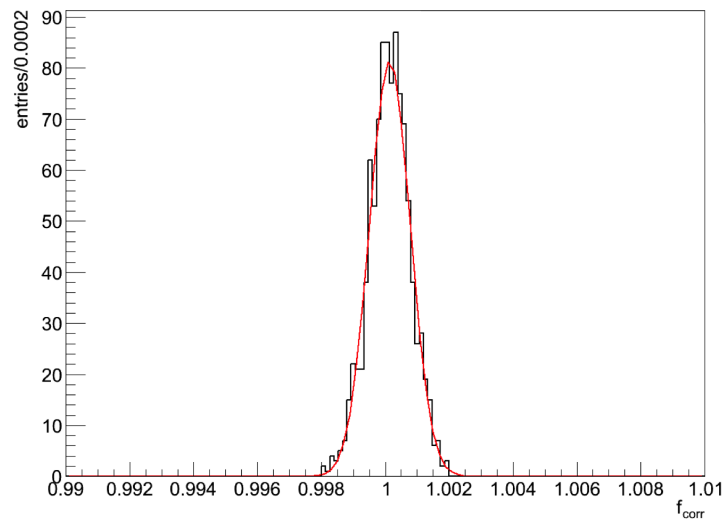
Figure 5.19.: Distribution of $f_{\mathrm{corr},i}^{\min}$ values obtained from fitting 1000 random spectra i to the reference spectrum in order to determine the error on the best-fit gain correction factor obtained for the LAB-3-20 sample (September 2013) at Pos4. The random spectra have been generated with statistics according to the integral over the best-fit comparison spectrum and using the PDF of the reference spectrum (see figure 5.18). The result for the mean of the shown Gaussian fit to the distribution is compatible with 1. A rounded value of 0.0006 was obtained for the width of the Gaussian fit and was used as statistical error on the best-fit gain correction factor $f_{\mathrm{corr}}^{\min}$ determined from the minimum of equation (5.23).

6. Analysis of the Beam Data Regarding Proton Quenching

As discussed in section 2.2.3, neutrino-proton scattering is a major detection channel for neutrinos from core collapse supernovae (see section 1.5). Due to a higher energy loss of protons compared to electrons with equal kinetic energy, the light output of the scintillator features a stronger nonlinearity. This is caused by the effect of ionization quenching, described in section 3.2. For experiments like LENA and JUNO (see sections 2.2 and 2.3), which could perform a high statistics test of current core collapse supernova models, the knowledge of the quenching effect in the used scintillator is of great importance (see section 2.2.3): On the one hand, quenching is an input to the detector simulation, which is used to estimate the expected spectrum in the neutrino-proton scattering channel. On the other hand, the knowledge in the quenching is needed to reconstruct the energy scale of the proton recoil events from the visible energy detected in the actual experiment.

Furthermore, proton recoils due to fast neutrons pose an important background for the detection of electron antineutrinos from nuclear reactors, the diffuse supernova neutrino background or from the earth's interior via the inverse β-decay (see section 2.1.2 and equation (2.1)). In this case, a precise knowledge of the quenching effect is mainly an important input to the detector simulation, which can be used to determine the expected visible energy spectrum and expected rate for this background.

In the scope of this thesis, 15 different scintillator mixtures (see section 3.4.4) were studied with regard to proton quenching in three beam times at the Maier-Leibnitz-Laboratorium (MLL) in Garching (see section 4.5). The measurement is based on proton recoils induced by monoenergetic neutrons produced at the MLL as described in section 4.1. For all measurements the detector and the experimental setup described in chapter 4 have been used. Different neutron energies between $\sim 4.7\,\mathrm{MeV}$ to $\sim 11.2\,\mathrm{MeV}$ were accessed by placing the scintillator detector (see section 4.2.1) at different defined positions with respect to the beam axis (see section 4.2.2).

6.1. Analysis Overview

The quenching effect in organic liquid scintillators can be described by the semi-empiric Birks model, which was introduced in section 3.2. Equation (3.9), which describes the light output for a given deposited energy E_{dep} by an ionizing particle in the scintillator, can be

modified as follows:

$$E_{\mathrm{vis}} = \int_0^{E_{\mathrm{dep}}} \frac{A}{1 + kB \frac{\mathrm{d}E}{\mathrm{d}x}(E)} \, \mathrm{d}E \tag{6.1}$$

where the light output L and the absolute light yield S were substituted by the visible energy E_{vis} and a parameter A, respectively. kB is the commonly called Birks-factor, which describes the dependency of E_{vis} from the energy dependent energy loss $\frac{\mathrm{d}E}{\mathrm{d}x}(E)$ of the ionizing particle. The visible energy E_{vis} is the energy detected in the form of scintillation photons in a detector, which was calibrated with γ-ray induced electron recoils as described in chapter 5. The parameter A corresponds to the fraction $E_{\mathrm{vis}}/E_{\mathrm{dep}}$ in case of no quenching ($kB = 0$) and, hence, should be unity, while an uncertainty arrises from the energy calibration of the detector.

The final goal of the analysis presented in this chapter is the determination of the Birks-factor kB according to equation (6.1). In order to extract kB from the data taken for each scintillator sample (see section 6.2) at the different detector positions (see section 4.2.2) the following input is needed:

- **Deposited Energy (E_{dep}):** In the approximation of $m_p \approx m_n$, where m_p and m_n are the proton and neutron masses[1], the maximal deposited energy of the neutron induced proton recoils $E_{\mathrm{rec}}^{\mathrm{max}}$ corresponds to the energy of the incident neutrons E_n. The neutron energy E_n is determined by a time of flight (ToF) analysis of the data, which was taken in a coincidence setup of the PMT signal and a signal correlated to the beam pulsing (see section 4.2.3). The ToF analysis, which was developed in the scope of this thesis, is described in detail in section 6.3.

- **Visible Energy (E_{vis}):** The visible energy $E_{\mathrm{vis}}^{\mathrm{max}}$, corresponding to the maximal deposited recoil energy of the protons $E_{\mathrm{rec}}^{\mathrm{max}} \approx E_n$, is determined from the energy spectrum of the proton recoils. The proton recoil spectra are gained by a selection based on the ToF-measurement described in section 6.3. The selection and analysis of the proton recoil spectra is presented in section 6.4.

- **Energy Loss of Protons ($\frac{\mathrm{d}E}{\mathrm{d}x}(E)$):** The energy dependent energy loss of protons in the different liquid scintillator mixtures was calculated from data taken from the NIST PSTAR database [123] as described in section 6.5.1.

- **Parameter A:** As discussed above, this parameter can be set to unity, while the uncertainty from the energy calibration (see chapter 5) has to be taken into account. More details are given in section 6.5.

With all these inputs, the Birks-factor kB is determined by a fit to the obtained data points $(E_{\mathrm{vis},i}^{\mathrm{max}}, E_{n,i})$ for the data taken at the different detector positions i. The details on the fit procedure are described in section 6.5. Finally, the results obtained for the investigated scintillator samples are summarized and discussed in section 6.6.

---

[1] $m_p = 938.3 \, \mathrm{MeV}/c^2$ and $m_n = 939.6 \, \mathrm{MeV}/\mathrm{c}^2$ [20]

6.2. Measured Beam Data and Data Handling

The data for the measurements with the neutron beam was recorded with the coincidence setup described in section 4.2.3. Both the PMT pulses and the discriminated signal from the pulsing were recorded with the used ADC (see section 4.2.3). The amount of data recorded in each measurement with the respective scintillator sample at the different detector positions are given in tables C.1-C.3 in appendix C.1 for each of the three beam times performed in 2013 and 2014. While in the beam time in September 2013 about $130 \cdot 10^3$ events were recorded for each measurement, the number of recorded events was increased to at least $\sim 250 \cdot 10^3$ events in the two 2014 beam times. The difference was mainly caused by the the different thresholds of the coincidence setup (see section 4.2.3) in the three beam times. In the September 2013 beam time the threshold was in the region of $\sim 24 \, \text{mV}$, which corresponds to an energy of $\sim 200 \, \text{keV}$ deposited by an electron. The threshold was lowered in the February 2014 beam time to $\sim 13 \, \text{mV}$ ($\sim 130 \, \text{keV}$) and further improved to $\sim 8 \, \text{mV}$ ($\sim 100 \, \text{keV}$) in the May/June beam time.

The recorded pulses from both the PMT and the discriminated pulsing signal were reconstructed as described in section 4.3. Before further analysis, quality cuts were applied to the reconstructed beam data. In case of the PMT data, the cuts were applied in the same way as described for the calibration data in section 5.2, while the data quality cuts for the discriminated pulsing signal were defined as described in the following. The discriminated pulsing signal has a pulse height of $\sim 852 \, \text{mV}$. A loose cut to the pulse height h was applied in such way that all remaining values satisfy the following relation $|h - 852 \, \text{mV}| < 10 \, \text{mV}$. This way extreme outliers could be removed. Furthermore, a cut to the start time was applied. Due to the used coincidence setup (see section 4.2.3), the reconstructed start time of the discriminated pulsing signal is correlated to the trigger time. While a narrow distribution for the start time was expected, it was found that a small fraction of the pulses is reconstructed at too early times (see figure 6.1). This behavior is caused by accidental triggers, when a PMT pulse appears within the finite width of the logical signal, produced for the pulsing signal. To remove those early pulses, a cut on the start time of the discriminated pulsing signal was defined in such way that only events in the narrow peak (see figure 6.1) are included in the analysis. In addition to the cuts on the pulse height and start time of the pulsing signal, loose cuts on the baseline position and width were applied to remove outliers. As the recorded pulsing signals are independent from the amount of energy deposited in the scintillator and, therefore, from the recorded PMT signal, all cuts applied to these pulses have no effect on the spectra obtained from the PMT data.

In addition to the quality cuts on the individual pulses from PMT and pulsing, all periods, in which the beam was off or the pulsing performance worsened significantly, were removed from the data sets before further analysis.
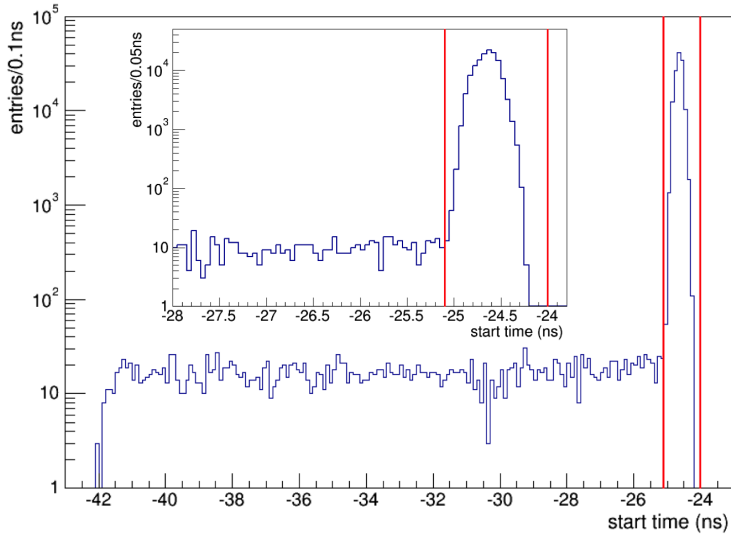
Figure 6.1.: Reconstructed pulse start times of the discriminated pulsing signal (see section 4.3), recorded for the LAB-3-20 sample at Pos0 in the September 2013 beam time. The insert shows a zoom to the region above $-28\,\text{ns}$ with finer binning. As the discriminated pulsing is correlated to the trigger time, a narrow peak is expected, which can be seen around $-24.7\,\text{ns}$. The origin of the distribution towards earlier reconstructed start times is caused by accidental coincidence triggers, when a PMT pulse appears within the finite width of the logical signal, produced for the pulsing signal. The red vertical lines show the values for the applied cut in this particular case.

6.3. Time of Flight Analysis

With the coincidence setup described in section 4.2.3, the kinetic energy of the neutrons E_n produced in the $p(^{11}\text{B}, n)^{11}\text{C}$ reaction (see also equation (4.1)) can be determined by a time of flight (ToF) analysis. E_n was determined for each measurement with the respective scintillator sample (see section 3.4.4) at the different used detector positions (see section 4.2.2).

A value for the time of flight (ToF) with an arbitrary offset $t^*_{\text{ToF},i}$ is obtained for each event i by the difference of the start times of the PMT $t^s_{\text{pmt},i}$ and the discriminated pulsing signal (dps) $t^s_{\text{dps},i}$, reconstructed as described in section 4.3:

$$t^*_{\text{ToF},i} = t^s_{\text{pmt},i} - t^s_{\text{dps},i} \; . \tag{6.2}$$

In figure 6.2 an example for a ToF-spectrum is shown for the LAB-3-20 sample (September 2013 beam time) at Pos0. The following prominent features are visible: The left peak is due to γ-rays produced by the ^{11}B ions in the H_2-cell, while the right peak is caused by the neutrons produced by reaction (4.1), which arrive later at the detector due to their finite mass. The distribution of events on the right of the neutron peak is caused by neutrons, which are scattered in the experiment's surroundings before reaching the detector. Furthermore, a constant background due to accidental coincidences due to γ-rays from radioactive decays is present. The offset of the ToF-spectrum is caused by the
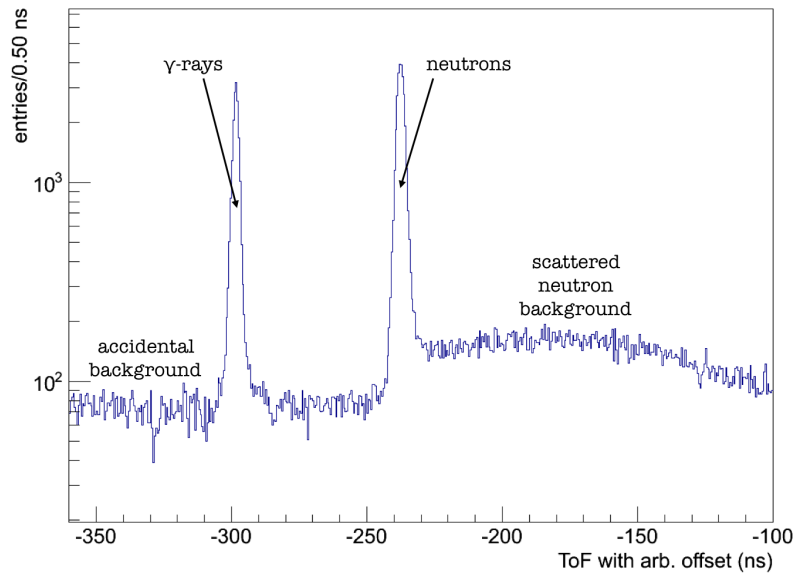
Figure 6.2.: Time of flight (ToF) spectrum recorded for the LAB-3-20 sample (September 2013) at Pos0. The ToF is determined by the difference between the start times of the PMT signal and the pulsing signal (see equation (6.2)). The ToF-spectrum features an offset, which is due to the unknown offset of the pulsing signal from the actual time, at which the ^{11}B bunch hits the H_2-cell.

unknown offset of the pulsing signal with respect to the time, at which the ^{11}B bunch hits the H_2-cell. The peaks in the ToF-spectra as shown in figure 6.2 contain the following information:

- **γ-ray peak:** The width of this peak contains information about the ^{11}B-bunch width, which is convoluted with the time resolution of the PMT and the electronics setup. It is practically independent of the detector position with respect to the beam axis (see section 4.2.2). Furthermore, the offset of the ToF-spectrum can be determined from the position of this peak, as it is expected at a time

$$t_\gamma = \frac{d}{c} \tag{6.3}$$

  with d being the distance between the H_2-cell and the detector at the respective position (see table 4.1) and c being the speed of light in vacuum.

- **neutron peak:** This peak contains information about the energy distribution of the neutrons, produced in reaction (4.1). The energy distribution appears as the transformation from energy to ToF-space. Furthermore, the distribution is convoluted with the time resolution of the whole system, including the ^{11}B-bunch width and the time resolutions of the PMT and the coincidence electronics setup. Depending on the mean kinetic energy of the neutrons $\langle E_n \rangle$ at each detector position at distance d to the H_2-cell (see table 4.1), the neutron peak is expected to be centered around a

ToF of

$$t_n = \frac{d}{c} \cdot \left[1 - \left(\frac{m_n c^2}{\langle E_n \rangle + m_n c^2} \right)^2 \right]^{-\frac{1}{2}} \tag{6.4}$$

with $m_n = 939.6 \, \text{MeV}/c^2$ being the neutron mass and c being the vacuum speed of light. Equation (6.4) can be derived from $E_{n,\text{tot}} = E_n + m_n c^2 \stackrel{!}{=} \frac{m_n c^2}{(1 - \beta^2)^{1/2}}$ with $E_{n,\text{tot}}$ and E_n being the total and kinetic neutron energy and $\beta = \frac{v_n}{c}$, where $v_n = \frac{d}{t_n}$ is the neutron velocity.

The information, contained in the neutron and γ-ray peaks as described above, is extracted via a fit to each ToF-spectrum. This fit and its underlying model are described in the following section 6.3.1.

6.3.1. Fit of the ToF-Spectrum

The main goal of the ToF analysis, described in this section, is to reconstruct the neutron energy distribution from each ToF spectrum, measured with each scintillator at the different detector positions (see sections 4.5 and 6.2). In the following used model will be described. This model consists of four contribution, describing the four features in the spectra: the γ-ray peak, the neutron peak, the scattered neutron background and the flat accidental background.

Model for the γ-ray Peak:

The γ-ray peak contains information about the time resolution of the total setup as described above. As it is not trivial to adjust the pulsing at the MLL to obtain perfectly symmetrical and Gaussian shaped ^{11}B-bunches, the γ-ray peak was approximated by a sum of two Gaussians using the following parameterization:

$$f_\gamma(t) = N_\gamma \cdot \left[\frac{N_{\gamma,1}}{N_\gamma} \cdot g_{\gamma,1}(t) + \left(1 - \frac{N_{\gamma,1}}{N_\gamma} \right) \cdot g_{\gamma,2}(t) \right] \tag{6.5}$$

with N_γ and $N_{\gamma,1}$ being the number of events in the total γ-ray peak and the number of events in the peak corresponding to the first Gaussian $g_{\gamma,1}(t)$, respectively. The normalized Gaussian distribution $g_{\gamma,1}(t)$ and $g_{\gamma,2}(t)$ are parameterized with individual widths of $\sigma_{\gamma,1}$ and $\sigma_{\gamma,2}$ and mean values of $\mu_{\gamma,1} = t_\gamma + t_{\text{offset}}$ and $\mu_{\gamma,2} = \mu_{\gamma,1} - \Delta\mu_\gamma$, respectively. t_γ is determined by equation (6.3), t_{offset} describes the offset of the ToF-spectrum and $\Delta\mu_\gamma$ is the difference in the positions of the two Gaussians. The normalization parameter N_γ, the fraction $\frac{N_{\gamma,1}}{N_\gamma}$, the widths of the Gaussians $g_{\gamma,1}(t)$ and $g_{\gamma,2}(t)$ and the parameters determining the position of the Gaussians, t_{offset} and $\Delta\mu_\gamma$, are free parameters of the fit to the ToF-spectra.

Due to the uncertainty on the distances d between the detector and the H_2-cell, which is caused by the dimensions of the sample container and the H_2-cell (see table 4.1), a broadening of the γ-ray peak is expected. An uncertainty of $\Delta d = 27 \, \text{mm}$, which corresponds to

the value for Pos0, corresponds to a difference in the ToF of the γ-rays of 0.09 ns. Assuming a flat distribution for the interaction probability of the ^{11}B-ions in the H$_2$-cell and for the scattering probability of the γ-rays in the liquid scintillator, the following rectangular function was used:

$$f_{\text{dist},\gamma}(t) = \begin{cases} 1 & \text{if } \frac{d-\Delta d}{c} \leq t \leq \frac{d+\Delta d}{c} \\ 0 & \text{else} \end{cases} \tag{6.6}$$

Therefore, the function $F_\gamma(t)$ used to describe the γ-ray peak is obtained by the convolution of $f_\gamma(t)$ and $f_{\text{dist},\gamma}(t)$, which is determined by

$$F_\gamma(t) \;=\; \int\limits_{-\infty}^{\infty} f_\gamma(\tau) \cdot f_{\text{dist},\gamma}(t-\tau)\,\mathrm{d}\tau \;=\; \int\limits_{\frac{d-\Delta d}{c}}^{\frac{d+\Delta d}{c}} f_\gamma(\tau)\,\mathrm{d}\tau \tag{6.7}$$

and can be solved analytically.

Model for the Neutron Peak:

The energy distribution of the neutrons at the different detector positions is not known. It depends on the energy loss and straggling of the ^{11}B ions before undergoing the $p(^{11}\text{B},n)^{11}\text{C}$ reaction (see also equation (4.1)) and scattering of the produced neutrons in the materials, of which the H$_2$-cell is composed. Furthermore, the detector dimensions play a role, as the neutron energy depends on the scattering angle, i.e. the angle with respect to the beam axis. In the used fit model, a Gaussian neutron energy distribution is assumed, which is mainly motivated by the straggling and the energy loss of the ^{11}B ions before undergoing reaction (4.1). The Gaussian energy distribution $f_n(E)$ is parameterized by a normalization factor N_n, which corresponds to the number of events in the neutron peak, a width of σ_{E_n} and a mean value $\langle E_n \rangle$, which are all free parameters in the fit to the ToF-spectra. For the fit to the ToF-spectrum the energy distribution $f_n(E)$ has to be transformed to the distribution in terms of the time of flight $f_n(t)$. The kinetic energy of the neutrons for a given time of flight is determined by the inverse function of equation (6.4):

$$E_n(t) = m_n c^2 \left[\left(1 - \frac{d^2}{c^2 \cdot t^2} \right)^{-\frac{1}{2}} - 1 \right] \tag{6.8}$$

with m_n being the neutron mass, d being the distance between the detector and the H$_2$-cell and t being the time of flight corresponding to the kinetic energy of the neutron E_n. The transformed energy distribution in the ToF-space $f_n(t)$ is determined by:

$$f_n(t) = \frac{\mathrm{d}E_n(t)}{\mathrm{d}t} f_n(E_n(t)) \tag{6.9}$$

with $\frac{\mathrm{d}E_n(t)}{\mathrm{d}t}$ being the derivative of equation (6.8) with respect to the time of flight t.

Similar to the broadening of the γ-ray peak described above, the dimensions of the H$_2$-cell and the detector cause also a broadening of the neutron peak. The broadening effect on the

neutron peak is stronger than for the γ-ray peak, which is caused by the smaller velocity of the neutrons of $\lesssim 0.15\,c$. To account for the influence of the dimensions of the detector and the H_2-cell, the following rectangular function was used, assuming a flat distribution for the scattering probability of the neutrons in the scintillator:

$$f_{\text{dist,n}}(t) = \begin{cases} 1 & \text{if } E_n(t, d - \Delta d) \leq E_n(t) \leq E_n(t, d + \Delta d) \\ 0 & \text{else} \end{cases} \tag{6.10}$$

where $E_n(t, d)$ is the energy for a given time of flight t and distance d according to equation (6.8) and Δd is the uncertainty on the distance due to the finite dimensions of the H_2-cell and the scintillator volume (see table 4.1). To obtain the transformed energy distribution in the ToF-space, including the uncertainty due to the H_2-cell and detector dimensions, $f_n(t)$ (see equation (6.9)) has to be convoluted with $f_{\text{dist,n}}(t)$ (see equation (6.10)):

$$f_n^*(t) \;=\; \int_{-\infty}^{\infty} f_n(\tau) \cdot f_{\text{dist,n}}(t - \tau)\,\mathrm{d}\tau \;. \tag{6.11}$$

The integral cannot be solved analytically and, therefore, is determined by numerical integration. Furthermore, the time resolution of the whole system $f_{\text{res}}(t)$ has to be taken into account, which is determined according to $f_\gamma(t)$ (see equation (6.5)) to be

$$f_{\text{res}}(t) \;=\; \frac{f_\gamma(t + t_\gamma + t_{\text{offset}})}{N_\gamma} \;. \tag{6.12}$$

The function $F_n(t)$ used to describe the neutron peak is obtained by the convolution of $f_n^*(t)$ and $f_{\text{res}}(t)$, which is determined by

$$F_n(t) \;=\; \int_{-\infty}^{\infty} f_n^*(\tau) \cdot f_{\text{res}}(t - \tau)\,\mathrm{d}\tau \tag{6.13}$$

and needs to be solved numerically.

Model for Accidental and Scattered Neutron Backgrounds:

The background due to accidental coincidences, caused by the ambient natural radioactivity, is expected to be constant and is described by

$$F_{\text{Acc}}(t) = c_{\text{Bkg}} = \text{const.} \tag{6.14}$$

with c_{Bkg} being a free parameter in the fit to the ToF-spectra.

The background due to scattered neutrons is approximated empirically by the sum of two Gaussians with the following parameterization:

$$F_{\text{nBkg}}(t) = N_{\text{nBkg}} \cdot \left[\frac{N_{\text{nBkg,1}}}{N_{\text{nBkg}}} \cdot g_{\text{nBkg,1}}(t) + \left(1 - \frac{N_{\text{nBkg,1}}}{N_{\text{nBkg}}}\right) \cdot g_{\text{nBkg,2}}(t) \right] \tag{6.15}$$

with N_{nBkg} and $N_{\text{nBkg},1}$ being the number of events accounting for the total scattered neutron background and the number of events corresponding to the first Gaussian $g_{\text{nBkg},1}(t)$, respectively. Both normalized Gaussians $g_{\text{nBkg},1}(t)$ and $g_{\text{nBkg},2}(t)$ are parameterized by individual widths $\sigma_{\text{nBkg},1}$ and $\sigma_{\text{nBkg},2}$ and mean values of $\mu_{\text{nBkg},1}$ and $\mu_{\text{nBkg},2} = \mu_{\text{nBkg},2} - \Delta\mu_{\text{nBkg}}$. N_{nBkg}, the fraction $\frac{N_{\text{nBkg},1}}{N_{\text{nBkg}}}$, the parameters $\mu_{\text{nBkg},1}$ and $\Delta\mu_{\text{nBkg}}$ and the widths $\sigma_{\text{nBkg},1}$ and $\sigma_{\text{nBkg},2}$ are free parameters in the fit to the ToF-spectra.

Total Model and χ^2-Fit:

With equations (6.7), (6.13), (6.14) and (6.15) the total function used to describe the ToF-spectra results to

$$F_{\text{ToF}}(t) = w_{\text{bin}} \cdot [F_\gamma(t) + F_n(t) + F_{\text{nBkg}}(t)] + c_{\text{Bkg}} \tag{6.16}$$

with a total of 16 free parameters. w_{bin} is the bin width and is introduced to account for the above given definitions of the parameters N_γ, N_n and N_{nBkg}. The ToF-spectra are fitted by $F_{\text{ToF}}(t)$ in a χ^2-fit based on the ROOT framework [153, 154, 155] and the MINUIT minimization framework [164], where the χ^2 is defined in the following way:

$$\chi^2 = \sum_{i=1}^{n_{\text{bins}}} \frac{(n_i - F_{\text{ToF}}(t_i))^2}{\Delta n_i^2} \tag{6.17}$$

with N_{bins} being the number of bins in the fit range and n_i being the content of bin i with statistical error Δn_i. $F_{\text{ToF}}(t_i)$ is the fit model according to equation (6.16) evaluated at t_i, which is the central value of bin i.

In figure 6.3 an example fit of the model according to equation (6.16) to the ToF-spectrum obtained for the LAB-3-20 sample (September 2013) at Pos0 is shown along with the results for all parameters of the fit. Furthermore, the spectra for the regions around the γ-ray and neutron peak are shown. According to the fit result the used model describes the ToF-spectrum quite well.

6.3.2. Error Estimation and Results

With regard to the proton quenching measurement, the main result of the fit to the measured ToF-spectra, described in the previous section 6.3.1, is the mean energy of the neutrons $\langle E_n \rangle$ at each detector position (see section 4.2.2). The statistical error on the mean neutron energy $\Delta\langle E_n \rangle_{\text{stat}}$ is obtained by the error on this parameter from the fit. $\Delta\langle E_n \rangle_{\text{stat}}$ is typically in the order of $\sim 0.005\,\text{MeV}$ and does not exceed $0.011\,\text{MeV}$. The systematical errors on the obtained values for $\langle E_n \rangle$ consist of two contributions:

- **Error due to distance measurement:** The errors on the measured distances between the H_2-cell and the detector at all used positions with respect to the beam axis are given in table 4.1. As the uncertainties due to the detector and H_2-cell

Entries	102374
$\chi2/ndf$	749/504
N_E	28297 ± 190
$\langle E_n \rangle$	(11.100 ± 0.004) MeV
σ_{E_n}	(0.233 ± 0.006) MeV
N_γ	16816 ± 136
t_{offset}	(-309.363 ± 0.011) ns
$\sigma_{\gamma,1}$	(1.023 ± 0.021) ns
$\sigma_{\gamma,2}$	(2.547 ± 0.193) ns
$\Delta\mu_\gamma$	(-0.366 ± 0.125) ns
$N_{\gamma,1}/N_\gamma$	0.826 ± 0.025
N_{nBkg}	19627 ± 370
$N_{nBkg,1}/N_{nBkg}$	0.861 ± 0.024
$\mu_{nBkg,1}$	(-170.44 ± 1.45) ns
$\sigma_{nBkg,1}$	(37.39 ± 1.00) ns
$\Delta\mu_{nBkg}$	(47.48 ± 1.36) ns
$\sigma_{nBkg,2}$	(13.82 ± 1.44) ns
c_{Bkg}	(71.90 ± 0.70) evts/0.5ns
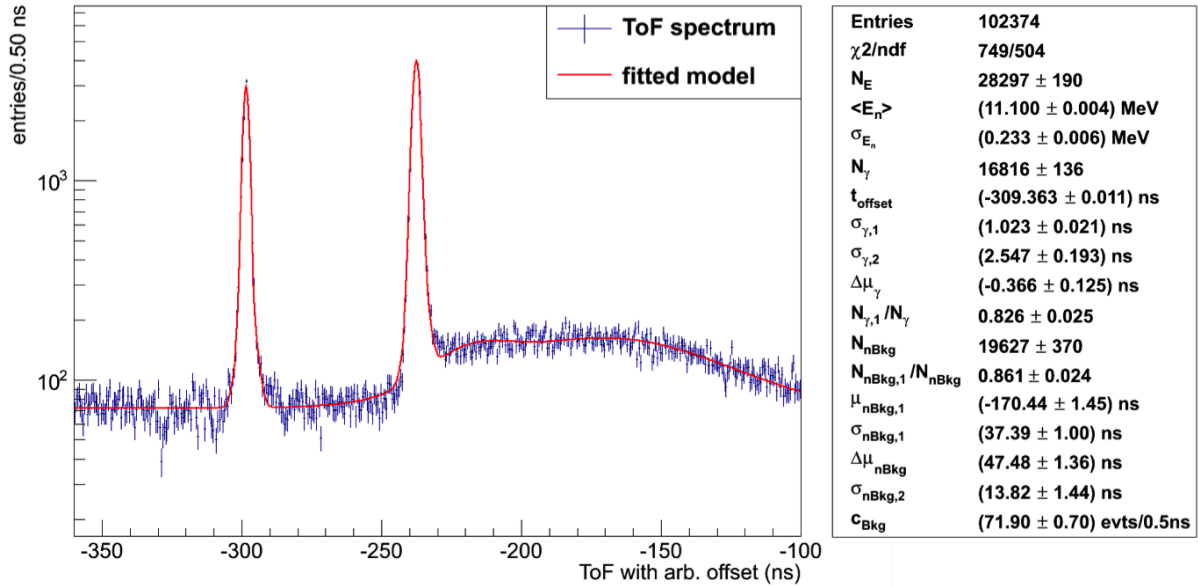
(a)
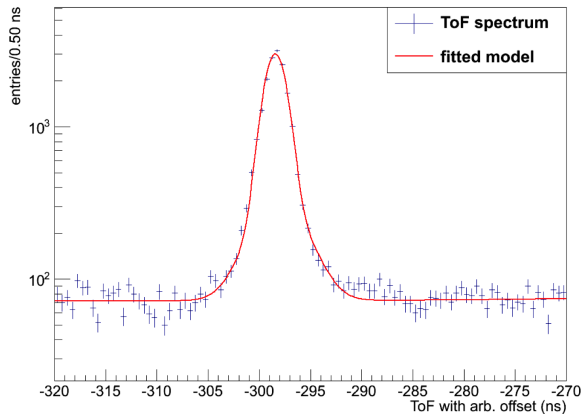
(b)
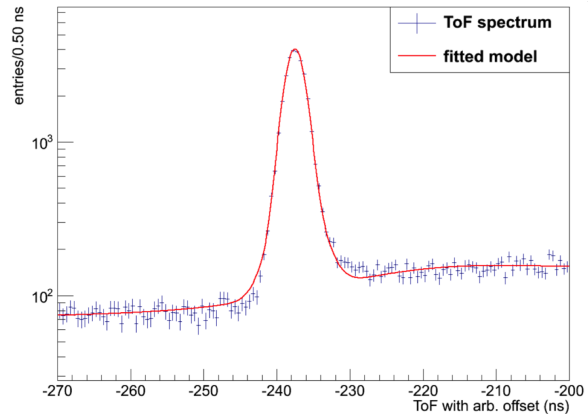
(c)

Figure 6.3.: The ToF-spectrum obtained for the LAB-3-20 sample (September 2013) at Pos0 and fitted with the model according to equation (6.16). (a) shows the total fitted spectrum along with the fit results for all parameters, (b) the region around the γ-ray peak and (c) the region around the neutron peak. The notation for the parameters corresponds to those given for the different contributions to the fit model (see equation (6.16)). The given errors are the statistical errors as obtained from the fit.

dimensions are included in the fit, only the errors from the actual measurement of the distances have to be taken into account. The resulting contributions to the systematic errors on the respective value of $\langle E_n \rangle$ are determined by error propagation of equation (6.8). Depending on the detector position, the absolute errors are in the range of $\sim 0.02 - 0.06\,\mathrm{MeV}$, decreasing with increasing angle of the position with respect to the beam axis (see table 4.1). The corresponding relative errors are in the order of $\sim 0.5\,\%$.

- **Error due to used model:** The error due to the used model is estimated by the standard deviation from the mean value of all fit results for $\langle E_n \rangle$, obtained for the different scintillator samples at a specific detector position (see table C.4 in appendix C.2). The results for the mean values of $\langle E_n \rangle$ and the corresponding standard deviations are given in table 6.1. Only one measurement was performed at Pos8 for the Borexino sample in the September 2013 beam time. Therefore, the given mean value corresponds to the result from this measurement, while the error was assumed to be 0.050 MeV, based on the results obtained for Pos6 and Pos7.

All error contributions to the mean neutron energy $\langle E_n \rangle$ described above are an input to the fit according to the Birks quenching model, which is described in section 6.5.

All individual values for $\langle E_n \rangle$, resulting from the fit to the measured ToF-spectra, are given in table C.4 in appendix C.2 for all investigated scintillator samples and the respectively used detector positions. The results from the fits on the width of the energy distribution of the neutrons σ_{E_n} are used to select the proton recoil events, as described in section 6.4.1. The values of σ_{E_n} obtained in all measurements are listed in table C.5.

detector position	$\langle E_n \rangle_{\mathrm{mean}}$ (MeV)	$\Delta\langle E_n \rangle_{\mathrm{mean}}$ (MeV)
Pos-1	11.15	0.11
Pos0	11.00	0.07
Pos1	10.64	0.08
Pos2	9.99	0.07
Pos3	9.42	0.06
Pos4	8.62	0.07
Pos5	7.78	0.08
Pos6	7.11	0.06
Pos7	5.99	0.04
Pos8	4.71	0.05

Table 6.1.: The mean $\langle E_n \rangle_{\mathrm{mean}}$ and the spread $\Delta\langle E_n \rangle_{\mathrm{mean}}$ of the measured mean neutron energies for each detector position. The values for the individual measurements have been determined by the fit to the ToF-spectra, measured for the different scintillator samples at the respective detector position, using the model described in section 6.3.1. The values for $\Delta\langle E_n \rangle_{\mathrm{mean}}$ are the corresponding standard deviations and are used as the systematic error on the measured $\langle E_n \rangle$ due to the used fit model. In case of Pos8 only one measurement was performed. Therefore, the value given for $\langle E_n \rangle_{\mathrm{mean}}$ corresponds to the result obtained from this measurement, while the given error was estimated based on the results for Pos6 and Pos7. See table C.4 in appendix C.2 for all individual results on $\langle E_n \rangle$ from the fit to each ToF-spectrum measured for the investigated scintillator samples at the different used detector positions.

6.4. Reconstruction of the Maximum Visible Energy from Proton Recoils

As described in section 6.1, the mean neutron energy $\langle E_n \rangle$ at each detector position, reconstructed as described in the previous section 6.3, corresponds to the maximum energy deposited by protons $E_{\text{rec}}^{\max}$, which are scattered off by the neutrons in the scintillator. The determination of the associated maximum visible energy $E_{\text{vis}}^{\max}$ from the recorded data is described in the following.

6.4.1. Obtaining the Proton Recoil Spectrum

To select proton recoil events from the beam data the corresponding results from the time of flight analysis described in the previous section 6.3 are used. After applying the quality cuts on both, the recorded PMT and discriminated pulsing signal, as described in section 6.2, the time of flight $t_{\text{ToF},i}$ is calculated for each event i of the respective measurement by

$$t_{\text{ToF},i} = t_{\text{ToF},i}^* - t_{\text{offset}} , \tag{6.18}$$

where $t_{\text{ToF},i}^*$ is the ToF with an offset, determined by the difference of the reconstructed start times of the PMT and the pulsing signal (see equation (6.2)), and t_{offset} is the ToF offset, which was determined by the fit to the ToF-spectrum (see section 6.3.1).

Using the results from the fit to the ToF-spectrum on the mean neutron energy $\langle E_n \rangle$ and the width of the neutron energy distribution σ_{E_n}, the proton recoil spectrum is obtained by selecting events from the neutron peak in the ToF-spectrum, which meet the following condition for $t_{\text{ToF},i}$:

$$t_{\text{ToF}}(\langle E_n \rangle + 1\sigma_{E_n}) \ \leq \ t_{\text{ToF},i} \ < \ t_{\text{ToF}}(\langle E_n \rangle - 1\sigma_{E_n}) \tag{6.19}$$

where the functional relation between the time of flight and the energy of the neutrons was used:

$$t_{\text{ToF}}(E_n) = \frac{d}{c} \cdot \left[1 - \left(\frac{m_n c^2}{E_n + m_n c^2} \right)^2 \right]^{-\frac{1}{2}} \tag{6.20}$$

with d being the distance of the detector to the H_2-cell at the respective detector position, c being the speed of light in vacuum and m_n being the neutron rest mass. For all events passing the selection, the pulse charge Q_i, reconstructed as described in section 4.3 and used as a measure for the energy, is multiplied by the gain correction factor f_{corr}, determined for the respective measurement as described in section 5.7, to account for the gain variations:

$$Q_{\text{corr},i} = f_{\text{corr}} \cdot Q_i \tag{6.21}$$

Furthermore, the energy calibration performed for each scintillator sample (see section 5.5) is applied to the obtained $Q_{\text{corr},i}$, where both the linear (see section 5.5.1) and quadratic calibration functions (see section 5.5.2) are applied, respectively. An example, illustrating

(a) ToF-spectrum around neutron peak

(b) Selected proton recoil spectra
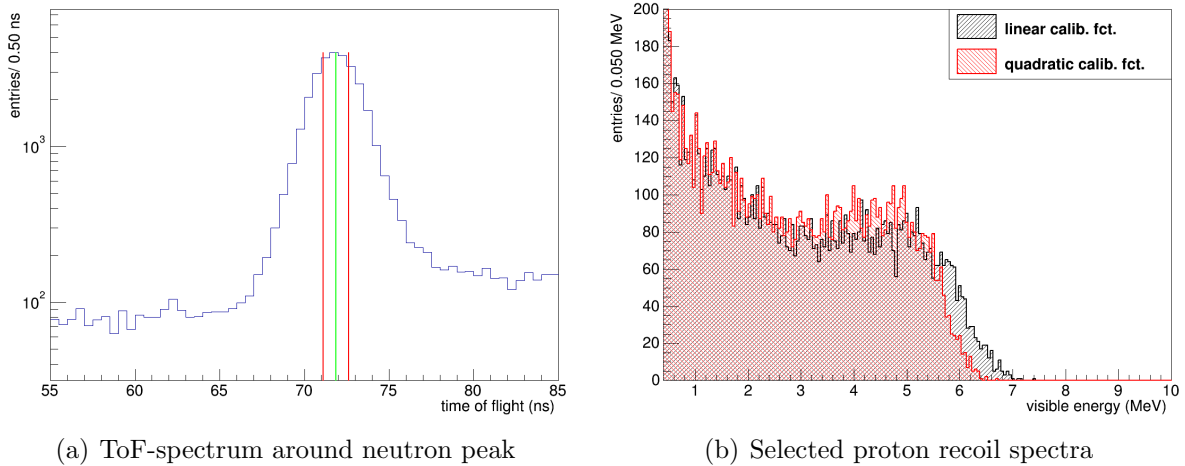
Figure 6.4.: Selection of proton recoil events from the data taken with the LAB-3-20 scintillator (September 2013) at Pos0 (see section 4.2.2). (a) shows the calibrated ToF-spectrum (see equation (6.18)) around the neutron peak, where the red vertical lines indicate the selection interval for the proton recoil events according to the condition given in equation (6.19). The green vertical line represents the ToF corresponding to the mean neutron energy $\langle E_n \rangle$ resulting from the fit to the ToF-spectrum (see section 6.3.1). (b) shows the visible energy spectra from the selection according to equation (6.19) for the linear and quadratic calibration functions applied to the data (see section 5.5).

the selection of the proton recoil events to obtain the proton recoil spectrum, is shown in figure 6.4 for the data taken with the LAB-3-20 sample at Pos0 in the September 2013 beam time. The ToF-spectrum and the result for the ToF fit for this example measurement were already shown in figures 6.2 and 6.3, respectively.

In addition, all proton recoil spectra obtained from the measurements with the LAB-3-20 scintillator at all used detector positions are shown in figure 6.5. For each of the shown spectra the selection according to equation (6.19) was applied, using the results from the fits to the respective ToF-spectra. All shown proton recoil spectra feature a smoothed out edge, which corresponds to the maximum visible proton recoil energy smeared by the energy resolution of the detector. In the region below the edge each spectrum is rather flat and starts to rise towards lower energies. The flatness is expected, as the recoil spectrum of protons scattered off by monoenergetic neutrons is flat [117]. The rise towards lower visible energies is mainly caused by the quenching effect (see section 3.2), while at low energies a small contribution of background due to γ-rays from accidental coincidences is present.

6.4.2. Determination of the Maximum Visible Recoil Energy

The determination of the maximum visible energy $E_{\mathrm{vis}}^{\max}$ from the measured proton recoil spectra (see section 6.4.1) is based on the flat recoil spectrum of protons scattered off by
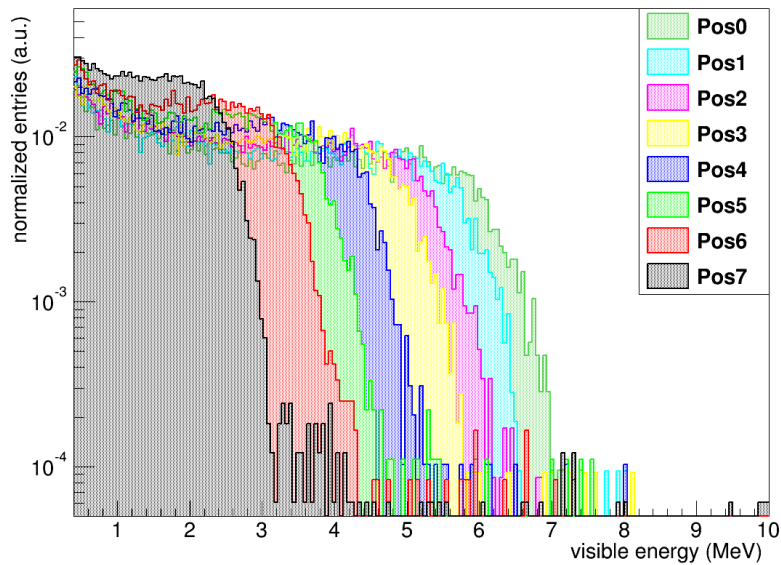
Figure 6.5.: Proton recoil spectra obtained from the measurements with the LAB-3-20 sample at all used detector positions (see section 4.2.2) in the September 2013 beam time. All spectra were normalized to unity. The events for each spectrum were selected according to equation (6.19), using the results on $\langle E_n \rangle$ and σ_{E_n} from the fits to the respective ToF-spectra (see section 6.3.1). The linear calibration function (see section 5.5.1) was applied to the shown data.

monoenergetic neutrons [117]. Despite the fact that the measured spectra are distorted by the quenching effect, the spectra are assumed to be flat in the region around the edge due to the maximum visible recoil energy $E_{\mathrm{vis}}^{\mathrm{max}}$. Thus, the spectrum can be described by a step function $s(E_{\mathrm{vis}})$:

$$s(E_{\mathrm{vis}}) = \begin{cases} 1 & \text{if } E_{\mathrm{vis}} \leq E_{\mathrm{vis}}^{\mathrm{max}} \\ 0 & \text{if } E_{\mathrm{vis}} > E_{\mathrm{vis}}^{\mathrm{max}} \end{cases} \tag{6.22}$$

with E_{vis} being the energy measured with the scintillator detector, which was calibrated with γ-ray induced electrons (see chapter 5). Furthermore, an energy independent Gaussian energy resolution $g_{\mathrm{res}}(E_{\mathrm{vis}})$ is assumed in the region around the edge with a width parameterized by σ_{res}. It can be shown that the convolution of the step function (6.22) and the Gaussian energy resolution results in the complementary error function[2]:

$$g_{\mathrm{res}}(E_{\mathrm{vis}}) * s(E_{\mathrm{vis}}) = N_{\mathrm{norm}} \cdot \mathrm{erfc}\left(\frac{E_{\mathrm{vis}} - E_{\mathrm{vis}}^{\mathrm{max}}}{\sqrt{2}\,\sigma_{\mathrm{res}}}\right) \tag{6.23}$$

with N_{norm} being a normalization factor. The background contribution to the measured proton recoil spectra in the region around the edge due to $E_{\mathrm{vis}}^{\mathrm{max}}$ is assumed to be flat. It is, therefore, parameterized by a constant c_{Bkg}. Thus, the resulting complete functional relation, used to extract the maximum visible proton recoil energy $E_{\mathrm{vis}}^{\mathrm{max}}$ from the measured

---

[2] The complementary error function is defined as [167]: $\mathrm{erfc}\,(x) = \frac{2}{\sqrt{\pi}} \int_x^\infty e^{-\tau^2}\, d\tau$.

(a) p-recoil spectrum for linear calibration

(b) p-recoil spectrum for quadratic calibration
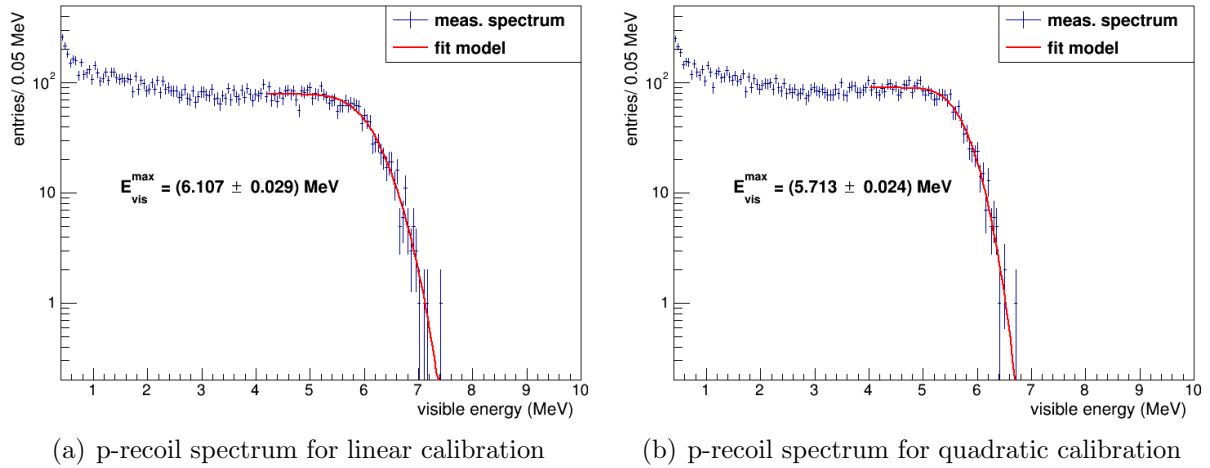
Figure 6.6.: The proton recoil spectra obtained from the measurement with the LAB-3-20 sample (September 2013) at Pos0 fitted with the function given in equation (6.24) in a likelihood fit. (a) shows the fitted spectrum obtained for energy calibration using the linear calibration function (see section 5.5.1), while (b) shows the spectrum, when the quadratic calibration function (see section 5.5.2) is used. The result for the maximum visible proton recoil energy $E_{\mathrm{vis}}^{\mathrm{max}}$ is given in each spectrum along with the statistical error from the fit. The discrepancy in the results for $E_{\mathrm{vis}}^{\mathrm{max}}$ is expected from results obtained for the different used calibration functions (see figures 5.14 and 5.15 and table B.3).

spectra, is:

$$F(E_{\mathrm{vis}}) = N_{\mathrm{norm}} \cdot \mathrm{erfc}\left(\frac{E_{\mathrm{vis}} - E_{\mathrm{vis}}^{\mathrm{max}}}{\sqrt{2}\,\sigma_{\mathrm{res}}}\right) + c_{\mathrm{Bkg}} \tag{6.24}$$

To account for the small number of entries at energies above the edge, the region around the edge in each of the measured recoil spectra is fitted by $F(E_{\mathrm{vis}})$ in a likelihood fit[3]. The result from each fit on the parameter $E_{\mathrm{vis}}^{\mathrm{max}}$ is then used as an input to the determination of the proton quenching, based on the Birks-model described in section 6.5. In figure 6.6 the fitted proton recoil spectra measured for the LAB-3-20 sample (September 2013) at Pos0 are shown for both the linear and quadratic calibration function (see section 5.5) applied to the data. The used fit model, given in equation (6.24), describes the data well.

6.4.3. Error Estimation and Results

The statistical error on the maximum visible proton recoil energy $E_{\mathrm{vis}}^{\mathrm{max}}$ is obtained by the error on this parameter from the fit described in the previous section 6.4.2. All results for $E_{\mathrm{vis}}^{\mathrm{max}}$ with statistical errors from the fits are given in tables C.6 and C.8 in appendix C.3 for both the linear and the quadratic calibration function (see section 5.5) applied to the data.

The systematic errors on the reconstructed maximum visible proton recoil energy $E_{\mathrm{vis}}^{\mathrm{max}}$ are

---

[3] The fit is based on the ROOT framework [153, 154, 155] and the MINUIT minimization toolkit [164]

estimated as described in the following and consist of three contributing uncertainties:

- **Error due to proton recoil event selection:** The energy distribution of the neutrons produced by the ^{11}B at the different detector positions is not perfectly monoenergetic and features a finite width for the assumed Gaussian distribution (see section 6.3.1). Together with the time resolution of the system, including the bunch width and the resolutions of the scintillator detector and the coincidence electronics, the selected proton recoil spectrum actually is a cumulative spectrum produced by neutrons with different energies. To estimate the resulting error on $E_{\mathrm{vis}}^{\max}$ the proton recoil event selection interval given in equation (6.19) is divided into two subintervals:

$$\begin{aligned}\text{high energy selection:} \quad & t_{\mathrm{ToF}}(\langle E_n \rangle + 1\sigma_{E_n}) \ \leq\ t_{\mathrm{ToF},i}\ <\ t_{\mathrm{ToF}}(\langle E_n \rangle) \\ \text{low energy selection:} \quad & t_{\mathrm{ToF}}(\langle E_n \rangle) \ \leq\ t_{\mathrm{ToF},i}\ <\ t_{\mathrm{ToF}}(\langle E_n \rangle - 1\sigma_{E_n})\end{aligned} \qquad (6.25)$$

where $\langle E_n \rangle$ and σ_{E_n} are the results on the mean and width of the assumed Gaussian neutron energy distribution from the ToF-fit to the respective measurement (see section 6.3.1). $t_{\mathrm{ToF}}(E_n)$ is the ToF corresponding to a neutron energy E_n according to equation (6.20). The selection intervals given in equation (6.25) correspond to the two intervals between each of the red vertical lines and the green one shown in figure 6.4(a) as an example for the selection of the proton recoil events.

Both recoil spectra, obtained for the low and high energy selection according to equation (6.25), are fitted with the model described in section 6.4.2. The systematic error on $E_{\mathrm{vis}}^{\max}$ due to the selection (see equation (6.19)) is then derived from the obtained results for the maximum proton recoil energy for both spectra, $(E_{\mathrm{vis}}^{\max})_{\mathrm{highE}}$ and $(E_{\mathrm{vis}}^{\max})_{\mathrm{lowE}}$, respectively, in the following way:

$$\begin{aligned}\text{upper error:} \quad & (\Delta E_{\mathrm{vis}}^{\max})_{\mathrm{sel}}^{+} = (E_{\mathrm{vis}}^{\max})_{\mathrm{highE}} - E_{\mathrm{vis}}^{\max} \\ \text{lower error:} \quad & (\Delta E_{\mathrm{vis}}^{\max})_{\mathrm{sel}}^{-} = E_{\mathrm{vis}}^{\max} - (E_{\mathrm{vis}}^{\max})_{\mathrm{lowE}}\end{aligned} \qquad (6.26)$$

The asymmetry of the resulting upper and lower error due to the selection $(\Delta E_{\mathrm{vis}}^{\max})_{\mathrm{sel}}^{+}$ and $(\Delta E_{\mathrm{vis}}^{\max})_{\mathrm{sel}}^{-}$ depends mainly on the asymmetry of the obtained ^{11}B beam bunches in the respective measurement. As the low energy pulsing (see section 4.1.2) needed to be adjusted manually for each measurement, the bunches were not perfectly symmetric. The nonlinearity of the transformation from the time of flight to the kinetic energy (see equation (6.20)) is already covered by the definition of the selection intervals according to equation (6.19).

- **Error due to energy calibration:** The systematic error due to the energy calibration $(\Delta E_{\mathrm{vis}}^{\max})_{\mathrm{Ecalib}}$ is determined by Gaussian error propagation of the respectively applied calibration function (see equations 5.16 and 5.17), using the values of, errors on and correlations between the parameters obtained from the respective fit result. The relative error due to the linear calibration is in the range of $\sim 1.2 - 1.3\,\%$ in the investigated energy range, while the error for the quadratic calibration ranges from $\sim 4.5\,\%$ at $E_{\mathrm{vis}} \sim 5.5\,\mathrm{MeV}$ to $\sim 1.2\,\%$ at $\sim 2.5\,\mathrm{MeV}$. The behavior for the calibration using the quadratic function can be understood by the relatively large error

on the quadratic term (see figure 5.15 and table B.3), which leads to an increasing uncertainty towards higher energies.

- **Error due to gain correction:** The relative systematic error due to gain variations, after applying the gain correction factors (see section 5.7) to each measurement, was assumed to be $0.5\,\%$, as described in section 5.7.2. To obtain the total systematical error on the reconstructed $E_{\mathrm{vis}}^{\mathrm{max}}$ due to the gain correction, this error is added linearly to the respective relative statistical error, obtained from the determination of each gain correction factor (see tables B.4-B.6) as described in section 5.7.2.

- **Error due to used fit model:** The validity of the used model, based on the complementary error function (see section 6.4.2), was tested with a toy Monte-Carlo simulation. As the effect due to the energy distribution should be already covered by the error due to the selection described above, flat proton recoil spectra were generated with maximum energies between $5\,\mathrm{MeV}$ and $11\,\mathrm{MeV}$. Furthermore, ionization quenching (see section 3.2) was included according to equation (6.1), using a Birks-factor of $kB = 0.01\,\frac{\mathrm{cm}}{\mathrm{MeV}}$. The energy dependent energy loss for the protons was calculated for LAB with an effective chemical formula $C_{18}H_{30}$ and a density of $0.863\,\mathrm{g\,cm^{-3}}$, using data from the PSTAR database [123] (see section 6.5.1). Furthermore, a constant relative energy resolution between $6.2 - 7.1\,\%$, decreasing with rising incident neutron energy, was used, which matches the approximate resolution of the detector in the region around the edge in the measured proton recoil spectra.

  The simulated quenched proton recoil spectra were fitted in the region around the edge, using the model described in section 6.4.2. The fit results for the maximum visible proton recoil energy $E_{\mathrm{vis}}^{\mathrm{max}}$ from the fit were compared with the expected values obtained by calculating the quenched energy for the set maximum proton energy, using the same quenching model as used to simulate the spectra. A discrepancy of $0.6 - 1.2\,\%$ was found for spectra simulated with different maximum proton recoil energies. Based on the observed discrepancy and the rather simple model used to simulate the recoil spectra, an energy independent relative systematic error on $E_{\mathrm{vis}}^{\mathrm{max}}$ of $1\,\%$ due to the used fit model was assumed.

All error contributions described above are input to the quenching fit according to the Birks model described in section 6.5. In appendix C.3 the results on $E_{\mathrm{vis}}^{\mathrm{max}}$ for all measurements with the investigated scintillator samples at the different detector positions are given with the upper and lower systematic errors due to the selection of the recoil events. While the results obtained for linear calibration (see section 5.5.1) are summarized in table C.7, the results for quadratic calibration (see section 5.5.2) are given in table C.9.

In the scope of the pulse shape discrimination performance analysis of the data taken in the three performed beam times (see chapter 7) a non-negligible background due to γ-ray induced events, contributing to the neutron peaks in the ToF-spectra (see figure 6.2), was observed. This background cannot be explained fully by the accidental background, which can be estimated from events before the γ-ray peak and actually accounts only to a small part of the γ-ray background in the neutron peaks (see section 7.2.2 and figure 7.5). Therefore, this background has to be caused by correlated γ-rays, which are scattered in

the surrounding materials or produced by neutron activation. To estimate the influence of this background a pulse shape discrimination (PSD) analysis of the selected recoil events (see section 6.4.1) was performed in a similar way as described for the AmBe calibration data in section 5.4.2. It was found that the influence on the reconstructed maximum proton recoil energy (see section 6.4.2) at all detector positions is on the level of few per mill and can, hence, be neglected. Furthermore, it was not possible to carry out this PSD analysis on the proton recoil events for all investigated scintillator samples, as the PSD performance of some of the scintillators is not good enough. Therefore, the maximum visible proton recoil energy $E_{\text{vis}}^{\text{max}}$ was determined for all measurements as described above to guarantee comparable results.

6.5. Birks-Quenching Fit

After the determination of the maximum deposited recoil energy of the protons $E_{\text{dep},i}^{\text{max}} \approx \langle E_n \rangle_i$ (see section 6.3) and the maximum visible recoil energy $E_{\text{vis},i}^{\text{max}}$ (see section 6.4) from the data taken for each investigated scintillator sample at the different used detector positions i, the Birks-factor kB can be determined by a fit of the Birks quenching model

$$F_{\text{Birks}}(E_{\text{dep}}) = E_{\text{vis}} = \int_0^{E_{\text{dep}}} \frac{A}{1 + kB \frac{\mathrm{d}E}{\mathrm{d}x}(E)} \, \mathrm{d}E \qquad (6.27)$$

to the obtained data points ($\langle E_n \rangle_i$, $E_{\text{vis},i}^{\text{max}}$). Before the fit can be performed, two further inputs to the Birks model are required (see also section 6.1). These are the energy dependent energy loss, which is calculated as described in section 6.5.1, and the parameter A (see section 6.5.2).

6.5.1. Energy Loss

The NIST PSTAR database provides energy dependent mass stopping powers for protons and for various elements and compound materials [123]. The mass stopping power is the density independent representation of the energy loss given by $\frac{1}{\rho}\frac{\mathrm{d}E}{\mathrm{d}x}(E)$ [158] with ρ being the density of the material and $\frac{\mathrm{d}E}{\mathrm{d}x}(E)$ the energy dependent energy loss or stopping power. Unfortunately, mass stopping powers for the scintillators investigated in the scope of this thesis are not provided by the PSTAR database and, therefore, needed to be calculated. A good approximation for the stopping power of compound materials is obtained using Bragg's Law [158]:

$$\frac{1}{\rho}\frac{\mathrm{d}E}{\mathrm{d}x}(E) = \sum_{i=1}^{N_A} \frac{w_i}{\rho_i} \left(\frac{\mathrm{d}E}{\mathrm{d}x}(E) \right)_i \qquad (6.28)$$

where ρ is the density of the compound material, N_A is the number of different elements in the molecules of the compound material, $\frac{1}{\rho_i}\left(\frac{\mathrm{d}E}{\mathrm{d}x}(E)\right)_i$ is the mass stopping power for

scintillator sample	eff. chem. formula	density $(\mathrm{g\,cm^{-3}})$
LAB-X-Y	$C_{18}H_{30}$	0.863
DCTarget	$C_{10}H_{19}$	0.804
DCGC	$C_{100}H_{205}$	0.804
DCMV	$C_{15}H_{28}$	0.804
Borexino	C_9H_{12}	0.880
50LAB-50nPar	$C_{15}H_{28}$	0.805
75LAB-25nPar	$C_{33}H_{58}$	0.830

Table 6.2.: Effective chemical formulas and densities used to calculate the energy dependent stopping powers for the different investigated scintillator samples. The given scintillator abbreviations were introduced in tables 4.2, 4.4 and 4.6.

the ith element in the molecule and ρ_i is the density of element i. The weights w_i are determined by

$$w_i = \frac{a_i\,A_i}{A_\mathrm{m}} \tag{6.29}$$

with a_i being the number of atoms of the ith element in the molecule, A_i being the atomic weight of the ith element and $A_\mathrm{m} = \sum_{i=1}^{N_\mathrm{A}} a_i A_i$.

To calculate the stopping powers for each scintillator according to equation (6.28), the effective chemical formulas and densities given in table 6.2 were used to combine the energy dependent mass stopping powers for hydrogen ($A_\mathrm{H} = 1$) and carbon ($A_\mathrm{C} = 12$), which are provided by the PSTAR database. As the stopping powers are only available for certain energies, linear interpolation is used to calculate the stopping powers in the regions between the provided energies. Figure 6.7 shows the calculated energy dependent stopping power for LAB-based scintillator using an effective chemical formula of $C_{18}H_{30}$ and a density of $0.863\,\mathrm{g/cm^3}$.

6.5.2. Parameter A

As discussed in section 6.1, the parameter A in the representation of the Birks model given in equation (6.27) corresponds to the quotient of the visible energy and the deposited energy in case of no quenching, which means $kB = 0$ (see also figure 3.4). As the detector was calibrated with energy depositions by Compton electrons (see chapter 5), which feature energies high enough that the influence of ionization quenching can be neglected in good approximation, the parameter A should be set to 1. Of course, the uncertainty on this parameter caused by both the energy and gain calibration needs to be considered. This uncertainty is estimated for each measurement, using the result for the maximum visible proton recoil energy $E_\mathrm{vis}^\mathrm{max}$ obtained at the detector position closest to the beam axis (mostly Pos0 or Pos-1, see section 4.2.2). At this position the highest value for $E_\mathrm{vis}^\mathrm{max}$ is obtained,
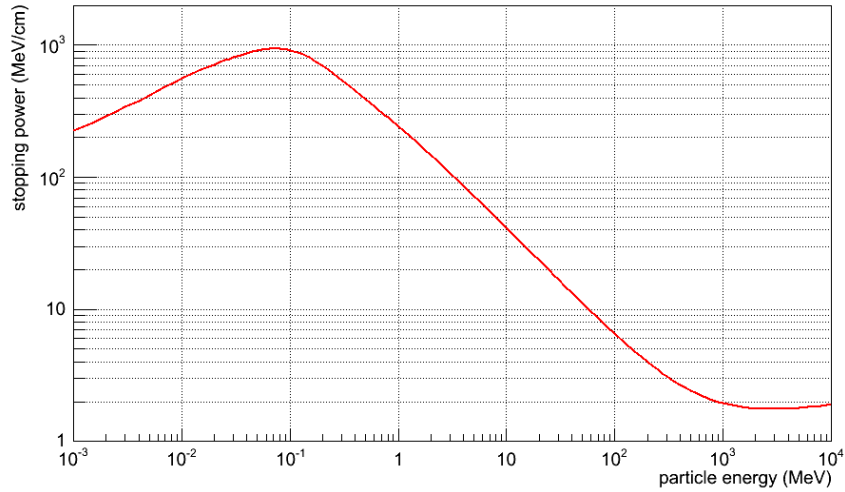
Figure 6.7.: Energy dependent stopping power of protons in linear alkyl benzene (LAB) calculated from data provided by the NIST PSTAR database [123] for an effective chemical formula $C_{18}H_{30}$ and a density of $0.863\,\text{g/cm}^3$ using Bragg's Law (see equation (6.28)).

as the mean energy of the incident neutrons decreases with increasing angle to the beam axis. This way, the most conservative uncertainty on parameter A due to the energy calibration is obtained for each measurement with the respective scintillator sample. The uncertainty due to the energy calibration is determined by Gaussian error propagation of the result from the respectively used calibration fit function (see section 5.5). The relative uncertainty is typically in the order of $\sim 1.3\,\%$, when the linear calibration function is used (see section 5.5.1), and in the order of $\sim 4.5\,\%$, when the quadratic calibration function is applied to the data (see section 5.5.2). Additionally, the systematic uncertainty due to the gain correction of $0.5\,\%$ (see section 5.7) is added in quadrature to the uncertainty due to the energy calibration. The determined uncertainty due to the calibration is used to limit parameter A using a nuisance parameter in the fit of the Birks model to the data, as described in the following section.

6.5.3. Final Quenching Fit

Likelihood-Fit

After the determination of the maximum deposited proton recoil energy $E_{\text{dep},i}^{\text{max}} = \langle E_n, i \rangle = E_{\text{dep}}^i$ (see section 6.3) and the maximum visible recoil energy $E_{\text{vis},i}^{\text{max}} = E_{\text{vis}}^i$ (see section 6.4) from all measurements performed for each scintillator at the different used detector positions i, the desired Birks-factor kB is extracted by a fit of the Birks quenching model $F_{\text{Birks}}(E_{\text{dep}})$ (see equation (6.27)) to the obtained data points (E_{dep}^i, E_{vis}^i). A likelihood fit is carried out using the MINUIT minimization framework [164] and the following pa-

rameterization for the likelihood:

$$-2\ln L(kB, A, \hat{E}_{\text{dep}}^i, \hat{E}_{\text{vis}}^i) = \sum_{i=1}^{N_{\text{pts}}} \left[\frac{(\hat{E}_{\text{vis}}^i - F_{\text{Birks}}(\hat{E}_{\text{dep}}^i, kB, A))^2}{(\Delta E_{\text{vis}}^i)_{\text{stat}}^2} + \frac{(E_{\text{vis}}^i - \hat{E}_{\text{vis}}^i)^2}{(\Delta E_{\text{vis}}^i)_{\text{syst}}^2} \right]$$
$$+ \sum_{i=1}^{N_{\text{pts}}} \left[\frac{(E_{\text{dep}}^i - \hat{E}_{\text{dep}}^i)^2}{(\Delta E_{\text{dep}}^i)_{\text{syst}}^2} \right]$$
$$+ \left(\frac{A - 1}{\Delta A} \right)^2$$

$$(6.30)$$

with N_{Pts} being the number of data points, i.e. the number of used detector positions, in each measurement with the respective scintillator sample. Furthermore, $(\Delta E_{\text{vis}}^i)_{\text{stat}}$ are the statistical uncertainties on the measured values for E_{vis}^i. The total systematic errors on the maximum visible recoil energies $(\Delta E_{\text{vis}}^i)_{\text{syst}}$ and on the maximum deposited recoil energies $(\Delta E_{\text{dep}}^i)_{\text{syst}}$ are calculated from the respective contributing systematic errors (see sections 6.3.2 and 6.4.3) as described below. $F_{\text{Birks}}(\hat{E}_{\text{dep}}^i, kB, A)$ is the expected visible energy for a given deposited energy according to the Birks quenching model given in equation (6.27) and needs to be determined by numerical integration, as the integral in equation (6.27) cannot be solved analytically.

To account for the systematic errors on each of the measured values for E_{vis}^i and E_{dep}^i, the nuisance parameters $\hat{E}_{\text{vis}}^i$ and $\hat{E}_{\text{dep}}^i$ are introduced. These nuisance parameters should describe the variations of the fit parameters kB and A due to the systematic uncertainties on both coordinates of each of the measured data points (E_{dep}^i, E_{vis}^i) [168]. The second term in the first line and the term in the second line of equation (6.30) are so-called pull terms, which are used to couple the nuisance parameters $\hat{E}_{\text{vis}}^i$ and $\hat{E}_{\text{dep}}^i$ to the corresponding data points (E_{dep}^i, E_{vis}^i). Furthermore, a pull term for the parameter A (see equation (6.27)) is introduced, which accounts for the systematic uncertainty ΔA on the expected value of $A = 1$ due to the calibration (see section 6.5.2).

To obtain the total systematic uncertainty on each of the measured maximum visible recoil energies $(\Delta E_{\text{vis}}^i)_{\text{syst}}$ all systematic uncertainties described in section 6.4.3 are combined in the following way:

$$(\Delta E_{\text{vis}}^i)_{\text{syst}}^2 = \left[(\Delta E_{\text{vis}}^i)_{\text{calib}}^2 + (\Delta E_{\text{vis}}^i)_{\text{gain}}^2 + (\Delta E_{\text{vis}}^i)_{\text{erfc}}^2 + (\Delta E_{\text{vis}}^i)_{\text{sel}}^2 \right] \qquad (6.31)$$

with $(\Delta E_{\text{vis}}^i)_{\text{calib}}$, $(\Delta E_{\text{vis}}^i)_{\text{gain}}$ and $(\Delta E_{\text{vis}}^i)_{\text{erfc}}$ the systematic errors on the reconstructed maximum visible recoil energy due to the energy calibration, gain correction and used fit function, respectively, as described in section 6.4.3. To account for the asymmetry of the systematic error due to the selection $(\Delta E_{\text{vis}}^i)_{\text{sel}}$ of the proton recoil events using the time of flight (see section 6.4.3), the corresponding term in equation (6.31) was modified in the following way according to [169]:

$$(\Delta E_{\text{vis}}^i)_{\text{sel}}^2 \longrightarrow (\Delta E_{\text{vis}}^i)_{\text{sel}}^+ \cdot (\Delta E_{\text{vis}}^i)_{\text{sel}}^- + \left[(\Delta E_{\text{vis}}^i)_{\text{sel}}^+ - (\Delta E_{\text{vis}}^i)_{\text{sel}}^- \right] \cdot \left[E_{\text{vis}}^i - \hat{E}_{\text{vis}}^i \right] \qquad (6.32)$$

with $(\Delta E_{\text{vis}}^i)_{\text{sel}}^+$ and $(\Delta E_{\text{vis}}^i)_{\text{sel}}^-$ being the asymmetric upper and lower errors due to the recoil event selection, E_{vis}^i the respective measured value for the maximum visible recoil energy and $\hat{E}_{\text{vis}}^i$ the corresponding nuisance parameter in the fit.

The systematic error on each of the determined maximum deposited proton recoil energies E_{dep}^i (see section 6.3) is determined in the following way:

$$(\Delta E_{\text{dep}}^i)_{\text{syst}}^2 = \left[(\Delta E_{\text{dep}}^i)_{\text{stat}}^2 + (\Delta E_{\text{dep}}^i)_{\text{model}}^2 + (\Delta E_{\text{dep}}^i)_{\text{dist}}^2 \right] \tag{6.33}$$

where $(\Delta E_{\text{dep}}^i)_{\text{model}}$ and $(\Delta E_{\text{dep}}^i)_{\text{dist}}$ are the systematic uncertainties on each of the E_{dep}^i caused by the used model to fit the time of flight spectra and the distance measurement as described in section 6.3.2. $(\Delta E_{\text{dep}}^i)_{\text{stat}}$ are the statistical errors on the measured E_{dep}^i and are treated as systematic uncertainties in the fit.

As an example, the results for the fit to the data points (E_{dep}^i, E_{vis}^i) obtained for the LAB-3-20 sample (September 2013) are shown in figure 6.8 for each the linear and the quadratic calibration function applied to the data (see section 5.5). The difference in the given errors on the Birks-factor kB, which is determined as described below, is caused by the increased systematic error due to the energy calibration using the quadratic function. A summary and a detailed discussion of the results on kB, obtained for the different investigated scintillator samples, are given in section 6.6.

Error Determination

The error on the Birks-factor kB, resulting from the fit, is determined from the profile $(-\ln L)$-function, which is calculated by minimizing the negative logarithmic likelihood function given in equation (6.30), while fixing the parameter kB at the respective value:

$$(-\ln L(kB))_{\text{prof}} = \min_{A, \hat{E}_{\text{dep}}^i, \hat{E}_{\text{vis}}^i} \left[-\ln L(kB, A, \hat{E}_{\text{dep}}^i, \hat{E}_{\text{vis}}^i) \right] \tag{6.34}$$

From the obtained profile likelihood, the confidence interval for a $n\sigma$ confidence level can be determined according to [170] by requiring the following condition for all points inside the confidence interval:

$$\Delta(-\ln L(kB))_{\text{prof}} = (-\ln L(kB))_{\text{prof}} - (-\ln L)_{\text{min}} < \frac{n^2}{2} \tag{6.35}$$

with $(-\ln L)_{\text{min}}$ being the global minimum of the $(-\ln L)$-function. The determination of the error on the Birks-factor kB from the fit is illustrated in figure 6.9 for the fit to the data obtained for the LAB-3-20 sample (September 2013), using the linear calibration function (see section 5.5.1). The corresponding fit result is depicted in figure 6.8(a). Additionally, the two dimensional profile obtained for the parameters A and kB is shown.

The contribution of the statistical error to the error on kB from the fit was estimated by redoing the fit with all systematic errors set to zero and fixed nuisance parameters for the maximum visible proton recoil energies $\hat{E}_{\text{dep}}^i = E_{\text{dep}}^i$ and the parameter A set to 1. The
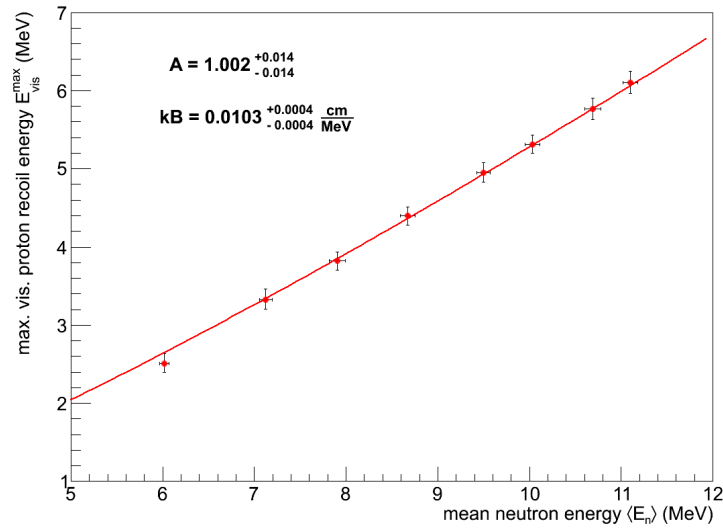
(a) Linear calibration
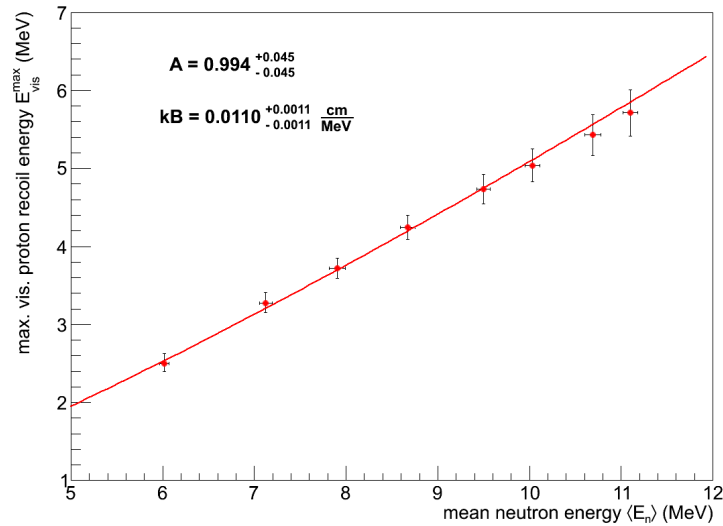
(b) Quadratic calibration

Figure 6.8.: Measured maximum visible proton recoil energy as a function of the determined mean neutron energy (= maximum deposited recoil energy of the protons), as obtained for the LAB-3-20 sample (September 2013). (a) shows the data, when the linear calibration (see section 5.5.1) was used, and (b) refers to the results, which were obtained using the quadratic calibration function (see section 5.5.2). The obtained data points were fitted with the Birks model F_{Birks}, given in equation (6.27), in a likelihood fit using the likelihood given in equation (6.30). The results for the Birks-factor kB and the parameter A are indicated in the respective plot. The shown error bars represent the total errors for each point and were determined by linearly adding the respective statistical and the systematic error, where the systematic error was calculated by quadratically adding the respective systematic contributions.
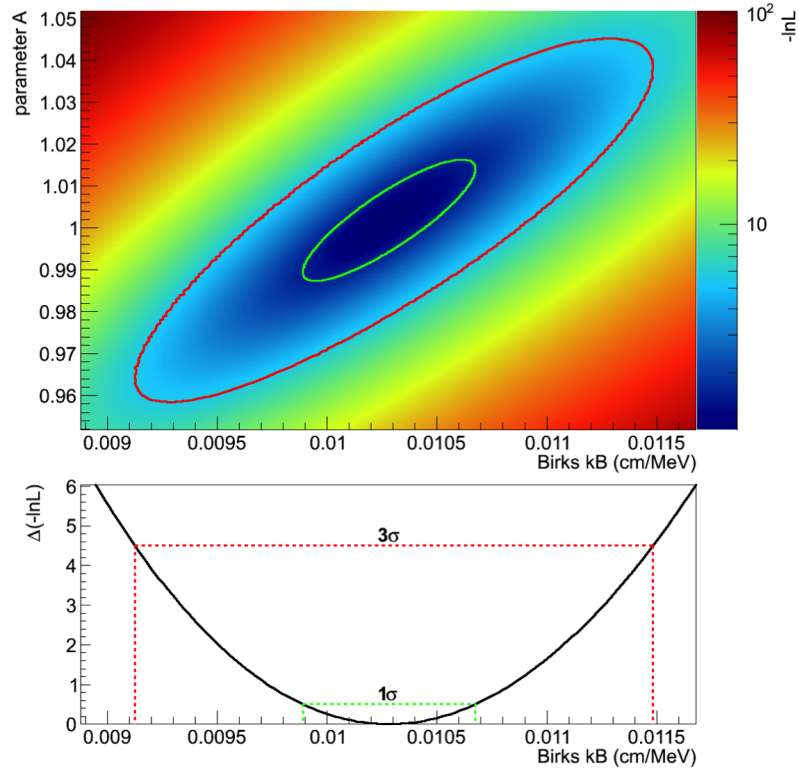
Figure 6.9.: The values for the negative logarithmic likelihood $(-\ln L)$ (see equation (6.30)) as a function of the Birks-factor kB and the parameter A (upper panel), obtained by minimizing over all nuisance parameters. The profile of $(-\ln L)$ was obtained for the fit to the data measured for the LAB-3-20 sample (September 2013), using the linear calibration function (see section 5.5.1). The corresponding fit result is shown in figure 6.8(a). The green and red lines indicate the one dimensional 1σ and 3σ confidence regions, respectively. The graph in the lower panel shows the one dimensional projection of $\Delta(-\ln L) = (-\ln L)_{\mathrm{prof}}(kB) - (-\ln L)_{\mathrm{min}}$ (see equations (6.34) and (6.35)) as a function of the Birks-factor kB. The 1σ and 3σ confidence intervals are indicated by the green and red dashed lines, respectively.

nuisance parameters for the deposited recoil energies $\hat{E}_{\mathrm{vis}}^{i}$ were left free to account for the statistical errors on the measured values of E_{vis}^{i}. The resulting 1σ errors on the parameter for the Birks-factor kB (determined as described above) were found to be more than one order of magnitude smaller than the total error, which means that the error from the fit, including all systematic errors and nuisance parameters, is dominated by the systematic uncertainties.

6.5.4. Systematic Errors on Birks-factor kB

Besides the error from the fit, two additional contributions to the error on the measured Birks-factor kB are taken into account:

- **Error on kB due to calculated stopping powers:** An uncertainty arises from the used stopping powers, which are calculated based on input from the NIST PSTAR database [123] as described in section 6.5.1. An energy independent uncertainty of $\Delta(\frac{\mathrm{d}E}{\mathrm{d}x}) = 3\,\%$ on the calculated stopping powers was assumed, based on the information given in [123]. The assumed uncertainty on the stopping power directly translates to an additional relative uncertainty of $\Delta kB_{\mathrm{d}E/\mathrm{d}x} = 3\,\%$ on the values of kB.

- **Error on kB due to charge determination:** An additional error on the quenching parameter kB arises from the used determination of the pulse charge, which is described in section 4.3. A reflection of the PMT signal, present in the data recorded in the September beam time and caused by a wrongly used load resistance of $1\,\mathrm{M\Omega}$ (instead of $50\,\Omega$) for the PMT signal at the PMT voltage divider, limited the upper integration boundary used to determine the pulse charge to $175\,\mathrm{ns}$ after the maximum of each pulse (see equation (4.2)).

  As described in sections 3.2 and 3.3, an increasing ionization density results in an increased fraction of excited triplet states, which causes an enhanced slow scintillation component. The relative amplitude of the slow scintillation component rises with increasing particle mass or decreasing initial particle energy. In consequence, the charge determination can have an effect on the quenching result, as the fraction of detected scintillation light included in the charge integration varies for electrons and protons. Due to the enhanced slow component in case of protons compared to electrons, the quenching effect appears to be stronger than it actually is.

  To estimate the error due to this effect the full analysis, including energy and gain calibration (see chapter 5), the time of flight analysis (see section 6.3) and the proton recoil analysis (see section 6.4), was performed for the LAB-3-10 sample (February 2014)[4], using a wider charge integration window, ranging up to $300\,\mathrm{ns}$ after the pulse maximum instead of $175\,\mathrm{ns}$. The Birks-factor was then determined by the fit of the Birks quenching model to the obtained data points (E_{dep}^{i} , E_{vis}^{i}) as described in the

---

[4] The sample was selected arbitrary. The only used criterion was that the data of the chosen sample was not recorded in the September 2013 beam time.

previous section. Comparing the results, the value for kB, obtained for the wider charge integration window, is by about $\Delta kB_{\text{charge}}^{\text{lin}} = 1.4\,\%$ lower, when the linear function is used for energy calibration (see section 5.5.1), and by about $\Delta kB_{\text{charge}}^{\text{quad}} = 1.7\,\%$ lower, when the quadratic function is used (see section 5.5.2). Both obtained relative difference, $\Delta kB_{\text{charge}}^{\text{lin}}$ and $\Delta kB_{\text{charge}}^{\text{quad}}$, are used as an additional systematic error on the respective value of kB obtained from the fit of the Birks model to the data.

For the final results on kB, summarized in section 6.6, both additional errors on the measured value for the Birks-factor kB are added in quadrature to the error obtained from the fit (see section 6.5.3). While the error due to the calculated stopping powers $\Delta kB_{\text{d}E/\text{d}x}$ is added to both the upper and the lower error, the error due to the charge determination $\Delta kB_{\text{charge}}^{\text{lin}}$ and $\Delta kB_{\text{charge}}^{\text{quad}}$, respectively, is added only to the lower error on kB, as the used charge determination causes an systematic shift of the determined values for kB to higher values.

6.6. Summary of Results

The results on the quenching parameter kB from the fits of the Birks quenching model to the data, obtained for the scintillator samples investigated in the three beam times in 2013 and 2014, are summarized in table 6.3. The measured values for kB are given for both the linear and the quadratic calibration (see section 5.5) applied to the data. Furthermore, the given total errors include the error resulting from the fit of the Birks model to the data (see section 6.5.3) and the errors described in section 6.5.4.

The results presented in table 6.3 show that the central values for kB obtained, when the quadratic calibration is applied to the data, are all up to more than $10\,\%$ higher compared to the respective results, using the linear calibration. This is caused by the bending of the quadratic function towards higher energies, which can be seen comparing the example calibration functions shown in figures 5.14 and 5.15. Furthermore, the higher errors on kB, obtained when applying the quadratic calibration, are caused by the larger errors resulting from the quadratic fit to the calibration data. Nevertheless, the respective results on kB, using both the linear and quadratic calibration, are all compatible within the given errors.

The investigated scintillator samples (see section 3.4.4 and 4.5) can be divided into two main groups: Firstly, scintillators based on LAB with different admixed concentrations of the first and second wavelength shifters PPO and bisMSB and diluted with different amounts of nonscintillating n-paraffine (see section 3.4 for descriptions of all used scintillator components) and, secondly, scintillators from the currently running or planned experiments Double Chooz, Borexino, LENA and JUNO.

	sample	Results for kB ($\frac{cm}{MeV}$):	
		linear calibration	quadratic calibration
Sept. 2013	DCMV	$0.0127^{+0.0005}_{-0.0006}$	0.0132 ± 0.0009
	LAB-3-20	0.0103 ± 0.0005	0.0110 ± 0.0012
	Borexino	0.0112 ± 0.0005	$0.0120^{+0.0012}_{-0.0011}$
	LAB-5-20	0.0098 ± 0.0005	0.0107 ± 0.0011
	LAB-3-40	0.0103 ± 0.0005	0.0111 ± 0.0011
Feb. 2014	LAB-3-20(2)	0.0098 ± 0.0005	0.0110 ± 0.0011
	DCTarget	0.0122 ± 0.0006	0.0133 ± 0.0012
	LAB-3-10	0.0098 ± 0.0005	0.0110 ± 0.0012
	LAB-3-0	0.0095 ± 0.0005	0.0105 ± 0.0011
	LAB-7-20	0.0095 ± 0.0005	0.0105 ± 0.0011
	LAB-9-20	0.0097 ± 0.0005	0.0106 ± 0.0011
	LAB-3-80	0.0100 ± 0.0005	0.0110 ± 0.0011
May/June 2014	50LAB-50nPar	0.0125 ± 0.0006	0.0134 ± 0.0010
	LAB-1-20	$0.0119^{+0.0005}_{-0.0006}$	0.0125 ± 0.0009
	DCGC	0.0149 ± 0.0007	0.0160 ± 0.0012
	75LAB-25nPar	0.0103 ± 0.0005	0.0114 ± 0.0012
	Borexino(2)	0.0101 ± 0.0006	0.0112 ± 0.0012
	LAB-3-0(2)	0.0098 ± 0.0005	0.0110 ± 0.0012

Table 6.3.: All results for kB, determined from the fit of the Birks model to the data obtained for the different scintillator samples (see section 4.5 for the used abbreviations), which have been investigated in the three conducted beam times. The results are given for both the linear and the quadratic calibration (see section 5.5) applied to the data. The shown errors include the errors from the fit (see section 6.5.3) and the systematic errors due to the calculated stopping powers and the determination of the pulse charge (see section 6.5.4). In general, the obtained total errors feature a slight asymmetry, which vanishes for most of the measurements after rounding to the last significant decimal place. The results for kB obtained, using the quadratic calibration, are all several percent higher than the respective result obtained, when the linear calibration is applied to the data.

6.6.1. Comparison of the Results Obtained for LAB-based Scintillators

The LAB-based scintillator samples can be subdivided into three subgroups: Samples with fixed concentration of bisMSB and varying concentration of PPO, samples with fixed concentration of PPO and varying concentration of bisMSB and samples, which were diluted with different amounts of n-paraffine, while the absolute concentrations of PPO and bisMSB in the diluted mixtures are the same. The results for the different groups of scintillators will be compared and discussed in the following.

Dependency of kB on the Concentration of the First Wavelength Shifter PPO:

In figure 6.10 the results on kB obtained for the LAB-based scintillator samples, featuring different concentrations of the first wavelength shifter PPO between $1\,\mathrm{g/l} - 9\,\mathrm{g/l}$ and a fixed concentration of the second wavelength shifter bisMSB of $20\,\mathrm{mg/l}$, are shown for both used calibration functions (see section 5.5).

The results indicate an increasing kB, i.e. a stronger quenching effect, for PPO concentrations below $\sim 3\,\mathrm{g/l}$. No significant changes in kB are found for PPO concentrations above $3\,\mathrm{g/l}$. The increased quenching effect towards lower PPO concentrations can be explained by the energy transfer from solvent molecules to molecules of the first solute, which happens mainly by a dipole-dipole interaction, also called Förster interaction (see section 3.1.3). This dipole-dipole interaction features a strong dependency of the transfer rate on the distance between the interacting molecules (see equation (3.2)). Hence, primary excitations of solvent molecules, caused by the incident ionizing particle, need to be transported to the closer vicinity of a solute molecule first. This transport of primary excitation energy is mainly carried out by thermal diffusion and non-radiative solvent-solvent transfer, which both increase the risk of non-radiative losses of excitation energy. In consequence, the transfer of primary excitation energy becomes less efficient for decreasing concentration of first solute.

This effect is further increased for high ionization densities in case of heavier particles (here protons), which leads to an increasing density of excited triplet states (see section 3.2). These triplet states need to to be converted to singlet states by reactions like that given in equation (3.1) in order to produce fluorescence photons.

The constant behavior above PPO concentrations of $\sim 3\,\mathrm{g/l}$ can be explained by a saturation effect, when enough molecules of the first solute are available in the closer vicinity inside the critical radius of the dipole-dipole interaction (see equation (3.2)). Just recently measurements by a Chinese group regarding the light yield of LAB-based scintillators with varying concentrations of PPO were presented in [171]. The results show a saturation of the light yield for PPO concentrations above $\sim 4\,\mathrm{g/l}$, which confirms the explanation given above.

(a) Results for linear calibration
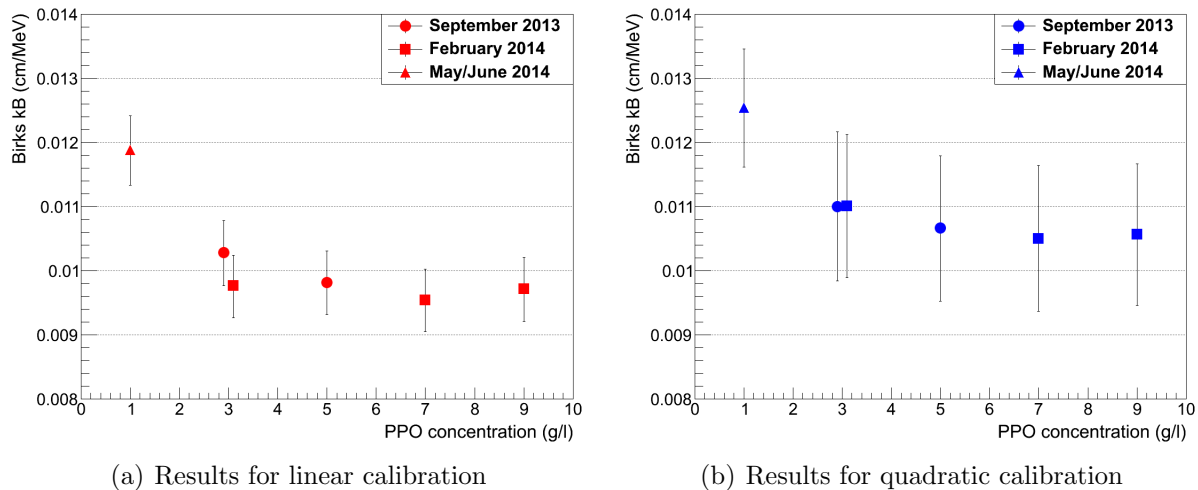
(b) Results for quadratic calibration

Figure 6.10.: Results on the Birks-factor kB as a function of the PPO concentration in the LAB-based scintillator samples. The concentration of the second wavelength shifter bisMSB was fixed to 20 mg/l. (a) shows the results, when the linear calibration is applied to the data (see section 5.5.1), while in (b) the results obtained, using the quadratic calibration (see section 5.5.2), are depicted. The different markers represent measurements performed in the respective beam times. The results for the LAB-3-20 and LAB-3-20(2) sample, obtained in the September 2013 and February 2014 beam time, respectively, were separated artificially by applying small offsets to the true PPO concentration of 3 g/l. For the discussion of the results please refer to the text. The measured values for kB with the respective total errors are given in table 6.3.

Dependency of kB on the Concentration of Second Wavelength Shifter bisMSB:

Figure 6.11 summarizes the results on kB obtained for the LAB-based scintillator samples, featuring different concentrations of the second wavelength shifter bisMSB between $0\,\text{mg/l} - 80\,\text{mg/l}$ and a fixed concentration of the first fluor PPO of $3\,\text{g/l}$.

The results obtained for each the linear (see figure 6.11(a)) and the quadratic calibration (see figure 6.11(a)) applied to the data show no significant dependency of the quenching effect (indicated by the Birks-factor kB) on the concentration of the used second wavelength shifter bisMSB. From this observation, it can be concluded that all processes contributing to the quenching effect take place in interactions between solvent molecules or between molecules of the solvent and the first solute. Furthermore, the results suggest a very efficient transfer of excitation energy from the first to the second wavelength shifter.

The slightly lower value of kB obtained for the LAB-3-0 sample (February 2014) compared to that obtained for the same scintillator sample (LAB-3-0(2)) in the beam time in May/June 2014 may be explained by a decreased performance of the beam pulsing during the measurements at the detector positions Pos1, Pos2, Pos4 and Pos6 (see section 4.2.2).
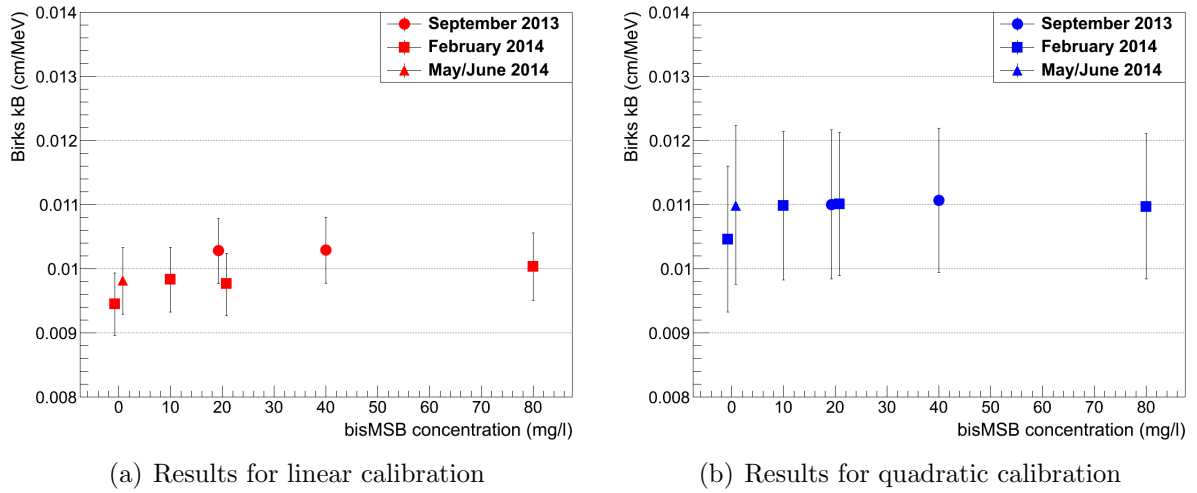
(a) Results for linear calibration

(b) Results for quadratic calibration

Figure 6.11.: Results on the Birks-factor kB as a function of the bisMSB concentration in the LAB-based scintillator samples. The concentration of the primary wavelength shifter PPO was fixed to $3\,\mathrm{g/l}$. (a) shows the results, when the linear calibration is applied to the data (see section 5.5.1), while in (b) the results obtained, using the quadratic calibration (see section 5.5.2), are depicted. The different markers represent measurements performed in the respective beam times. The results for the LAB-3-20 and LAB-3-20(2) sample, measured in the September 2013 and February 2014 beam time, and the results for the LAB-3-0 and LAB-3-0(2) samples, investigated in both 2014 beam times, were separated artificially by applying small offsets to the true bisMSB concentration of $0\,\mathrm{mg/l}$ and $20\,\mathrm{mg/l}$, respectively. For the discussion of the results please refer to the text. The measured values for kB with the respective total errors are given in table 6.3.

Dependency of kB on the Concentration of n-Paraffine:

In figure 6.12 the results on kB obtained for the LAB-based scintillator samples, which were diluted with different concentrations of nonscintillating n-paraffine, are summarized. The absolute concentrations of the wavelength shifters PPO and bisMSB of $3\,\mathrm{g/l}$ and $20\,\mathrm{mg/l}$, respectively, in the diluted liquid were the same in all shown samples.

A clear rise towards increasing concentrations of n-paraffine is observed. While the quenching effect for the 50LAB-50nPar sample, which was diluted with $50\,\mathrm{vol\%}$ of n-paraffine, is considerably increased, only a small increase is observed for the 75LAB-25nPar sample, diluted with $25\,\mathrm{vol\%}$ n-paraffine. Here two effects influence the quenching effect. On the one hand, the presence of nonscintillating molecules in the liquid inhibit collisions of molecules in excited triplet states, which allow for a conversion to singlet states by reactions like that given in equation (3.1). In consequence, the light output for heavier particles, which cause higher ionization densities and, thereby, higher densities of excited triplet states, is further reduced in comparison to electrons. On the other hand, the density is decreased by dilution with n-paraffine, reducing the ionization density due to incident ionizing particles. In consequence, the quenching effect is reduced. While both effects described above seem to roughly balance in case of the 75LAB-25nPar sample, the first effect, which increases

(a) Results for linear calibration

(b) Results for quadratic calibration
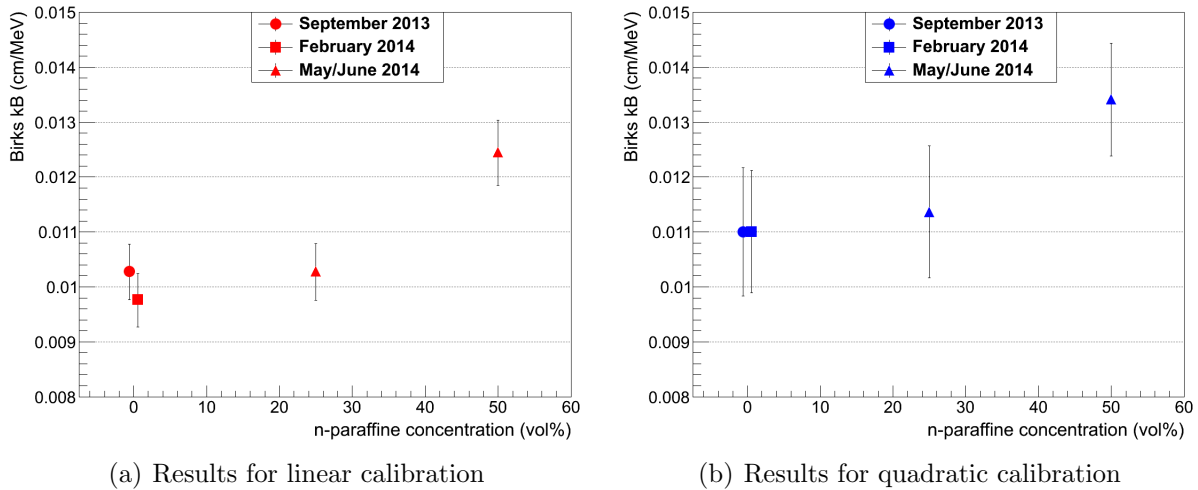
Figure 6.12.: Results on the Birks-factor kB as a function of the concentration of non-scintillating n-paraffine in the LAB-based scintillator samples. The concentrations of PPO and bisMSB were fixed to $3\,\mathrm{g/l}$ and $20\,\mathrm{mg/l}$, respectively. (a) shows the results, when the linear calibration is applied to the data (see section 5.5.1), while in (b) the results obtained, using the quadratic calibration (see section 5.5.2), are depicted. The different markers represent measurements performed in the respective beam times. The results for the LAB-3-20 and LAB-3-20(2) sample, obtained in the September 2013 and February 2014 beam time, respectively, were separated artificially by applying small offsets to the true n-paraffine concentration of $0\,\mathrm{vol\%}$. For the discussion of the results please refer to the text. The measured values for kB with the respective total errors are given in table 6.3.

the quenching, clearly dominates in case of the 50LAB-50nPar sample.

6.6.2. Comparison of the Results Obtained For Scintillators Used in Neutrino Experiments

In table 6.4 and figure 6.13 the results on the Birks-factor kB, obtained for the scintillator samples from the running Double Chooz and Borexino experiments and the scintillator favored for the future LENA and JUNO projects, are summarized.

The Double Chooz Scintillators:

The measured value of kB obtained for the Double Chooz muon veto scintillator (DCMV) is similar to that obtained for the 50LAB-50nPar sample (see table 6.3). This is expected, as both scintillators are very similar (see section 3.4.4).

Comparing the results on kB for the Double Chooz target scintillator (DCTarget) and the DCMV scintillator (see table 3.4 for detailed compositions), no significant difference can be observed. Although the fraction of scintillating compounds (PXE) is only $20\,\mathrm{vol\%}$

| sample	Results for kB ($\frac{cm}{MeV}$):		experiment
	linear calibration	quadratic calibration	
DCMV	$0.0127^{+0.0005}_{-0.0006}$	0.0132 ± 0.0009	Double Chooz
DCTarget	0.0122 ± 0.0006	0.0133 ± 0.0012	
DCGC	0.0149 ± 0.0007	0.0160 ± 0.0012	
Borexino	0.0112 ± 0.0005	$0.0120^{+0.0012}_{-0.0011}$	Borexino
Borexino(2)	0.0101 ± 0.0006	0.0112 ± 0.0012	
LAB-3-20	0.0103 ± 0.0005	0.0110 ± 0.0012	LENA / JUNO
LAB-3-20(2)	0.0098 ± 0.0005	0.0110 ± 0.0011	

Table 6.4.: Summarized results on the Birks-factor kB, obtained for the scintillators used in the running Double Chooz and Borexino experiments and favored for the LENA and JUNO projects. The results were already shown in table 6.3. For detailed compositions of the respective scintillators please refer to sections 3.4.4 and 4.5.

for the DCTarget scintillator and, therefore, significantly smaller compared to the DCMV scintillator, the quenching effect for protons appears to be of equal strength. This may be due to the different solvent, used for the DCTarget scintillator. Furthermore, according to the behavior of the quenching, which was observed for LAB samples with different concentrations of PPO (see figure 6.10), the higher PPO concentration of 7 g/l in the DCTarget scintillator (compared to 2 g/l in the DCMV scintillator) may partly account for the reduced quenching effect. A major impact on the ionization quenching, which may be expected due to the Gd dissolved in the DCTarget scintillator, cannot be observed.

The strongest quenching of the light output due to proton recoils for all investigated scintillator samples is observed for the Double Chooz gamma catcher (DCGC) scintillator (see table 3.4 for detailed composition). This is expected, as this scintillator mainly consists of nonscintillating mineral oils, featuring a small fraction of scintillating PXE of only 4 vol%. As the DCGC scintillator features a PPO concentration of 2 g/l, the increased quenching compared to the DCTarget scintillator may be also explained to some extend by the observed dependency of the quenching effect on the concentration of the first wavelength shifter PPO in LAB-based scintillators (see figure 6.10).

The Favored Scintillator for LENA and JUNO:

The favored scintillator for the proposed LENA detector is LAB with 3 g/l PPO and 20 mg/l bisMSB. JUNO favors a similar scintillator with a slightly lower concentration of the second wavelength shifter bisMSB of 15 mg/l. According to the observed independence of the quenching effect regarding the bisMSB concentration in LAB-based scintillators (see figure 6.11 and discussion in section 6.6.1), the slightly lower concentration of bisMSB
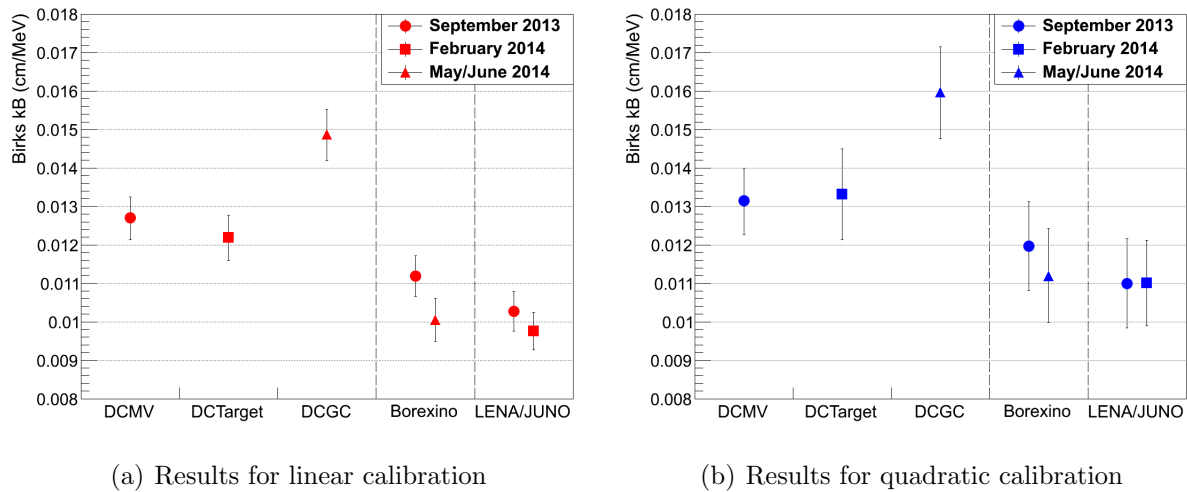
(a) Results for linear calibration

(b) Results for quadratic calibration

Figure 6.13.: Results on the Birks-factor kB, obtained for the scintillators used in the running Double Chooz and Borexino experiments and for the scintillators favored for the future LENA and JUNO projects. (a) shows the results, when the linear calibration is applied to the data (see section 5.5.1), while in (b) the results obtained, using the quadratic calibration (see section 5.5.2), are depicted. The different markers represent measurements performed in the respective beam times. For the discussion of the results please refer to the text. The measured values for kB with the respective total errors are given in tables 6.3 and 6.4.

should have no effect on the respective value of kB. The LAB-3-20 sample was measured in the September 2013 beam time as well as in the February 2014 beam time (LAB-3-20(2)). The obtained results using the respective calibration function (see section 5.5) are compatible within the determined errors, while there is a slight tension between the results obtained with linear calibration. This small discrepancy may be caused by the $1\,\text{M}\Omega$ load resistance, which was wrongly used in the September 2013 beam time and affected the decay time of the PMT signal. A possible systematic effect on the quenching measurement cannot be fully excluded.

The Borexino Scintillator:

The scintillator used in the running Borexino experiment was measured in the September 2013 beam time (Borexino) as well as in the May/June 2014 beam time (Borexino(2)). The results for each of the used calibration functions applied to the data obtained for the Borexino sample (September 2013) show higher values for kB compared to the results obtained from the data taken for the Borexino(2) sample (see tables 6.3 and 6.4). As for the results obtained for the LAB-3-20 and LAB-3-20(2) samples, this could again be caused by the wrongly used $1\,\text{M}\Omega$ load resistance in the September 2013 beam time (see section 4.5.1).

Comparing the measured values of kB for the Borexino scintillator samples to those ob-

tained for the favored LENA scintillator, i.e. LAB-3-20 and LAB-3-20(2), the values determined for the Borexino samples are slightly higher. The difference is expected to be partly due to PC used as solute in case of the Borexino scintillator, which increases the density of the scintillator and, therefore, the energy loss of the protons. Furthermore, the rather small used concentration of PPO of 1.5 g/l may increase the quenching effect, which is observed for the LAB-based scintillators with varying PPO concentrations (see figure 6.10).

6.6.3. Comparison to Results From Other Quenching Measurements

Proton quenching measurements of LAB-based scintillators were also performed for the SNO+ experiment by a group from the Technische Universität Dresden [172]. Protons with an energy of 19 MeV were shot on a solid beryllium target to obtain a white neutron beam with a maximum energy of 17.15 MeV. Proton recoil events induced by neutrons with different energies between $\sim 2 - 16$ MeV were selected by a time of flight analysis to extract the maximum recoil energy from the obtained spectra. The results were fitted with the Birks model in order to extract the quenching parameter kB.

LAB-based scintillators with PPO concentrations of 2 g/l and 3 g/l and bisMSB concentrations of 0 mg/l and 15 mg/l for each of the PPO concentrations were studied. The resulting value for kB obtained for the scintillator with concentrations of 3 g/l of PPO and 15 mg/l of bisMSB is (0.0098 ± 0.0003) cm MeV^{-1}, which is in good agreement with the results for LAB-3-20 of (0.0103 ± 0.0005) cm MeV^{-1}, LAB-3-20(2) of (0.0098 ± 0.0005) cm MeV^{-1} and LAB-3-10 of (0.0098 ± 0.0005) cm MeV^{-1} obtained in the measurements described in this thesis, using the linear calibration function (see table 6.3).

The same applies for the result presented in [172] for the LAB scintillator with a PPO concentration of 3 g/l, using no secondary wavelength shifter, of (0.0094 ± 0.0002) cm MeV^{-1}. In case of using the linear calibration function, the results obtained in this thesis for LAB-3-0 of (0.0095 ± 0.0005) cm MeV^{-1} and LAB-3-0(2) of (0.0098 ± 0.0005) cm MeV^{-1}, measured in the two 2014 beam times (see table 6.3), are also in good agreement.

The major difference of the measurements described in [172] compared to the measurements described in this thesis is the use of a white neutron beam instead of producing monoenergetic neutrons by inverse kinematics (see section 4.1.3). Using a white beam allows for access to a wider energy range of incident neutrons. This difference to the measurement presented in this thesis should account at least for a part of the larger error on the values of kB, obtained as described in sections 6.5.3 and 6.5.4. However, the good agreement between the results, obtained in the both beam based experiments, indicates that both experimental setups give reliable results for the Birks-factor kB.

6.6.4. Relevance of the Proton Quenching Results

In case of the Double Chooz scintillators, the results on the quenching parameter kB for protons, given in table 6.4, are an important input to the detector simulation. The

simulation can be used to study background events due to recoil protons, which are induced by fast neutron produced by cosmic muons in the rock surrounding the detectors (see section 2.1.3).

The results for kB obtained for the Borexino scintillator and the favored scintillator for LENA and JUNO are necessary to estimate the expected event rates of elastic neutrino-proton scattering (see section 2.2.3), which is a major detection channel for neutrinos from a galactic core collapse supernova (see section 1.5). In case of LENA, the event rate in this channel was estimated in [96] (see section 2.2.3). In this estimation a Birks-factor of $kB = 0.01\,\mathrm{cm\,MeV^{-1}}$ was used, which is in agreement with the results obtained in the measurements presented in this thesis (see table 6.3 or 6.4) and the results given in [172]. Additionaly, as for Double Chooz, the measured values for the quenching parameter kB of the Birks model are an important input to the detector simulations.

The results from the quenching studies of the different LAB-based samples, which are summarized and discussed in section 6.6.1, help to consolidate our understanding of the processes in multicomponent organic liquid scintillators. A study of the quenching effect due to protons in organic liquid scintillators, covering this many different scintillator samples based on LAB with different concentrations of first and second wavelength shifters PPO and bisMSB and dilutions with different amounts of nonscintillating mineral oil (here n-paraffine), is unprecedented.

7. Pulse Shape Discrimination Performance Analysis of the Beam Data

As described in section 3.3, the photons emitted by a organic liquid scintillator feature a distinctive distribution in time. This so-called pulse shape varies for different types of ionizing particles and can, therefore, be used to discriminate between events caused by different particles by a so-called pulse shape discrimination (PSD) analysis. This technique is an important tool for background suppression in liquid scintillator detectors.

In liquid scintillator based neutrino experiments fast neutrons pose a major background for the detection of electron antineutrinos by the inverse β-decay (IBD) reaction (see section 2.1.2). Fast neutrons are produced by cosmic muons in the rock surrounding the detector (see section 2.1.3), (α, n)-reactions in the scintillator or neutral current interactions of atmospheric neutrinos on ^{12}C (see section 2.2.4). The combination of the prompt light produced by a proton scattered off by the neutron and the successive capture of the neutron on hydrogen (or gadolinium in case of Double Chooz) mimics the delayed coincidence of the IBD reaction, as described in section 2.1.2. PSD can be used to identify the prompt proton recoil events and is, therefore, a viable tool to study and reduce background due to fast neutrons.

Fast neutrons produced by neutral current interactions of atmospheric neutrinos on ^{12}C in the scintillator pose the major background for the detection of the diffuse supernova neutrino background (DSNB) by next generation neutrino detectors (see sections 1.5.4 and 2.2.4). This background needs to be reduced significantly in order to be sensitive to the low flux of DSNB neutrinos. This can only be achieved by a PSD analysis. Furthermore, both elastic neutrino-proton and elastic neutrino-electron scattering are important detection channels for neutrinos from a galactic supernova (see section 2.2.3). Both channels can only be separated by a PSD analysis.

The time of flight setup at the neutron scattering facility at the Maier-Leibnitz-Laboratorium (see chapter 4) provides an optimal possibility to study the pulse shape discrimination (PSD) performance of scintillating materials with respect to the separation of γ-ray and neutron induced events. Due to the time of flight technique, samples of γ-ray and neutron induced events can be selected. This is a substantial advantage in comparison to experiments using neutron sources, like AmBe or ^{252}Cf, which produce neutrons and γ-rays simultaneously. Therefore, measurements based on such sources suffer from pile-up of neutrons and γ-rays, hitting the detector at the same time (see section 5.4.2 and 5.5).

In the following an analysis of the data recorded in the February and May/June 2014 beam times regarding the PSD performance of the investigated scintillator samples will be presented. First, the used data and the selection of the neutron and γ-ray induced events based on the time of flight measurement will be described in section 7.1. Furthermore, the determination of the pulse shape discrimination performance based on the so-called tail-to-total parameter (see section 7.2.1) is presented in section 7.2. Finally, in section 7.3 the results obtained for the PSD performance of the different investigated scintillator samples are summarized and discussed.

7.1. Data Handling and Event Selection

7.1.1. Used Data Sets and Applied Quality Cuts

As described in section 4.5.1, in the September 2013 beam time a $1\,\mathrm{M\Omega}$ load resistance was used for the PMT signal at the PMT voltage divider instead of $50\,\Omega$. It was observed that the wrongly used $1\,\mathrm{M\Omega}$ load resistance affected the decay time of the recorded pulses, which was found to have a negative impact on the PSD performance (see section 7.3.3). Therefore, only the data, which was recorded in the February and May/June 2014 beam times, was analyzed with regard to the PSD performance to obtain comparable results for the different investigated scintillator samples. For samples, which have been measured in the September 2013 beam time, but not in the February 2014 beam time, additional data was recorded for PSD investigations during the May/June 2014 beam time at a single detector position (see table 4.7).

The analysis described in this chapter was performed with the same data sets, which were used to determine the quenching effect as described in chapter 6. The total statistics recorded for the investigated scintillator samples at the different used detector positions (see section 4.2.2) are summarized in tables C.2 and C.3 in appendix C.1. Additionally, the data recorded for the samples labeled with PSD, which has been recorded for PSD studies only, was used.

The quality cuts applied to the recorded PMT and pulsing signals were identical to those described in section 6.2 for the analysis regarding proton quenching. The cuts applied to the data taken for the samples labeled with PSD were defined in the same way.

Furthermore, the gain correction factors, determined as described in section 5.7, were applied to the respective measurements performed for each scintillator sample at the different detector positions (see appendix B.5). To obtain the visible energy for each recorded event the respective result for the linear energy calibration function (see section 5.5.1), which was determined from data recorded with different γ-ray sources as described in chapter 5, was used.

7.1.2. Event Selection

The time of flight (ToF) measurement, which was performed using the coincidence setup described in section 4.2.3, provides an optimal separation between γ-ray and neutron induced events in the scintillator. This can be seen in the ToF spectrum shown in figure 6.2.

The ToF (with an arbitrary offset) is determined for each event from the reconstructed start times of the PMT and pulsing signals (see section 4.3) according to equation (6.2). Using the results from the fits to the ToF spectra described in section 6.3.1, samples for γ-ray and neutron induced events are selected from the respective peaks in the ToF spectra using the following selection cuts:

$$
\begin{aligned}
\gamma\text{-ray events:} & \quad t_\gamma - \Delta t_\gamma^- \ \leq \ t_{\text{ToF},i} \ < t_\gamma + \Delta t_\gamma^+ \\
\text{neutron events:} & \quad t_n - \Delta t_n^- \ \leq \ t_{\text{ToF},i} \ < t_n + \Delta t_n^+
\end{aligned}
\tag{7.1}
$$

with $t_{\text{ToF},i}$ being the ToF determined for event i according to equation (6.18). t_γ and t_n are the positions of the γ-ray and neutron peaks in the respective ToF spectrum according to equations (6.3) and (6.4). Finally, Δt_γ^+ and Δt_γ^- (Δt_n^+ and Δt_n^-) are the generally asymmetric upper and lower values defining the selection intervals for the γ-ray (neutron) event samples. These boundaries were defined manually for each measurement performed for the respective scintillator sample at the different detector positions (see section 4.2.2) depending on the performance of the pulsing. While the used values for Δt_γ^+ and Δt_γ^- were within 3.5 ns and 6 ns, those used for Δt_n^+ and Δt_n^- were chosen between 4 ns and 6.5 ns. As an example, the vertical lines in figure 7.1 show the selection intervals in case of the LAB-3-20(2) sample (February 2014) at position Pos0 (see table 4.1).

The γ-ray and neutron events, selected according to equation (7.1) from the data recorded for each scintillator sample at the different used detector positions, are combined to one data set for each of the event types. Both obtained data sets are used to determine the PSD performance as described in section 7.2. Using the combined data sets is possible, as the PSD performance only depends on the light output due to an energy deposition and not on the initial energy of the incident particles (here neutrons and γ-ray produced in the H_2-cell).

Figure 7.2 shows averaged pulses for neutron and γ-ray induced events with visible energies between 1.0 MeV and 1.5 MeV, which are based on pulses recorded with the LAB-3-20(2) sample (February 2014) at Pos0. The averaged pulses were calculated by summing up all pulses selected from the respective intervals. Before summation, the pulses were aligned to a common onset. The onset of each pulse was determined by the time, at which the pulse height exceeds five times the width of the constant baseline (see section 4.3). By normalizating to the pulse height the difference in the relative amplitudes of the slow scintillation decay times (see section 3.3) for both event types is highlighted. The difference in the relative amplitude of the slow decay becomes visible at about 20 ns after the maximum, where the amplitude of the averaged pulse for neutrons exceeds that for γ-ray events. This difference can be used in a PSD analysis to distinguish events induced by both particle types.
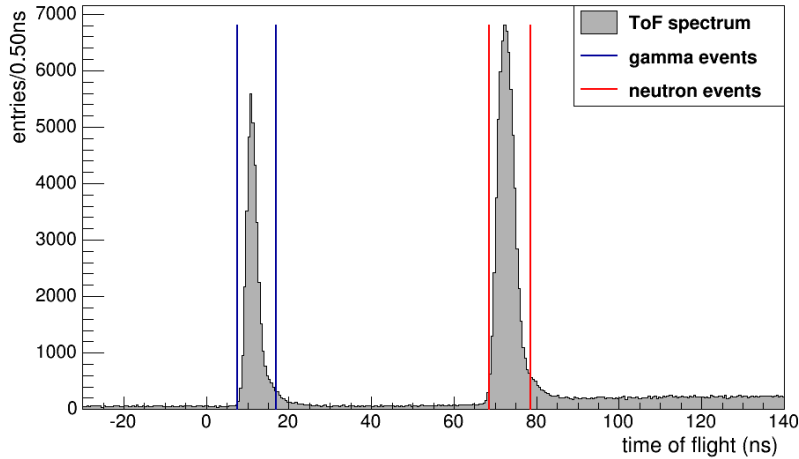
Figure 7.1.: Time of flight spectrum measured with the LAB-3-20(2) scintillator (February 2014) at Pos0. The colored lines illustrate the selection intervals for γ-ray (blue) and neutron (red) induced events. The ToF axis was calibrated using the result for the ToF offset, which is obtained from the fit to the ToF spectrum as described in section 6.3.1.
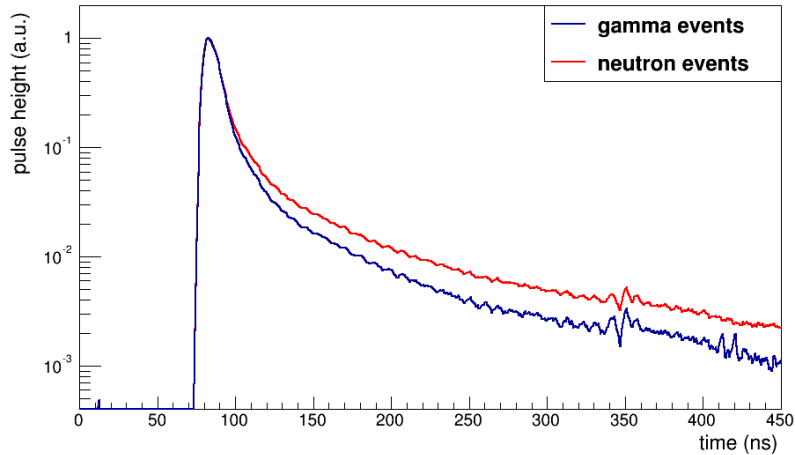
Figure 7.2.: Averaged pulses for γ-ray and neutron induced events with visible energies between $1.0 - 1.5\,\text{MeV}$ for the LAB-3-20(2) sample (February 2014) at Pos0. The averaged pulses were determined by summing up the recorded pulses for γ-ray and neutron induced events, which were selected from the respective intervals shown in figure 7.1. Both pulses were normalized to a pulse height of 1. Before summation, the recorded pulses were aligned with respect to their onset, which was determined by the time each pulse exceeds five times the width of the reconstructed constant baseline (see section 4.3). The oscillating behavior of both pulses is caused by electronic effects, while the feature around $350\,\text{ns}$ is due to a reflection of the PMT signal.

7.2. Determination of the PSD Performance

7.2.1. Tail-to-Total Ratio

The analysis with regard to the PSD performance of the different scintillators, studied in the two beam times performed in 2014, is based on the so-called tail-to-total parameter[1]. The tail-to-total parameter t_2t is the quotient of the baseline corrected integral over the tail region of the pulse and the integral over the total pulse, including the tail region. It is determined for each recorded PMT pulse in the following way:

$$t_2t = \frac{\int_{t_t}^{t_e} \left[p(t) - b \right] \mathrm{d}t}{\int_{t_s}^{t_e} \left[p(t) - b \right] \mathrm{d}t} \tag{7.2}$$

with $p(t)$ being the pulse height of the recorded PMT pulse at time t and b being the constant baseline, reconstructed as described in section 4.3. Furthermore, $t_s = t_{max} - 50\,\mathrm{ns}$ and $t_e = t_{max} + 350\,\mathrm{ns}$ are fixed integration boundaries, where t_{max} is the time corresponding to the pulse maximum. The lower boundary for the tail integral t_t is varied in order to obtain the optimal PSD performance for each scintillator sample (see section 7.2.4). In figure 7.3 the determination of t_2t is illustrated by means of the averaged pulses already shown in figure 7.2.

The t_2t parameter is a measure for the relative amplitude of the tail of each pulse, i.e. the slow component of the scintillation light emission. Therefore, neutron induced events, featuring an enhanced pulse tail, are expected at higher values for t_2t than γ-ray induced events. Figure 7.4 shows the two-dimensional distribution of the tail-to-total parameter t_2t as a function of the visible energy for the LAB-3-20(2) sample (February 2014). Both, the γ-ray and neutron induced events are included in the plot. Two characteristic bands can be seen in figure 7.4: The band at lower values of t_2t around 0.15 corresponds to γ-ray induced proton recoils, while the band at higher values of t_2t is caused by neutron induced proton recoils. Both bands are visibly separated above energies of $\sim 0.7\,\mathrm{MeV}$. This indicates a good PSD performance of the LAB-3-20(2) scintillator. The bending of the band corresponding to the neutron induced events is caused by the energy loss of the recoil protons, which steeply increases with decreasing energy (see figure 6.7). Therefore, the slow decay of the scintillation light emission is increasingly enhanced for decreasing energy of the recoil protons. In contrast to the neutron induced events, the band for the γ-ray induced events shows no obvious bending, as the energy loss of the Compton electrons features no strong dependence on the energy in the shown energy region [123]. Furthermore, the width of both bands increases with decreasing energy, which is caused by the correspondingly decreasing number of detected scintillation photons.

---

[1] The tail-to-total parameter was also used to extract the Compton spectrum from the calibration data recorded with the AmBe-source (see section 5.4.2).
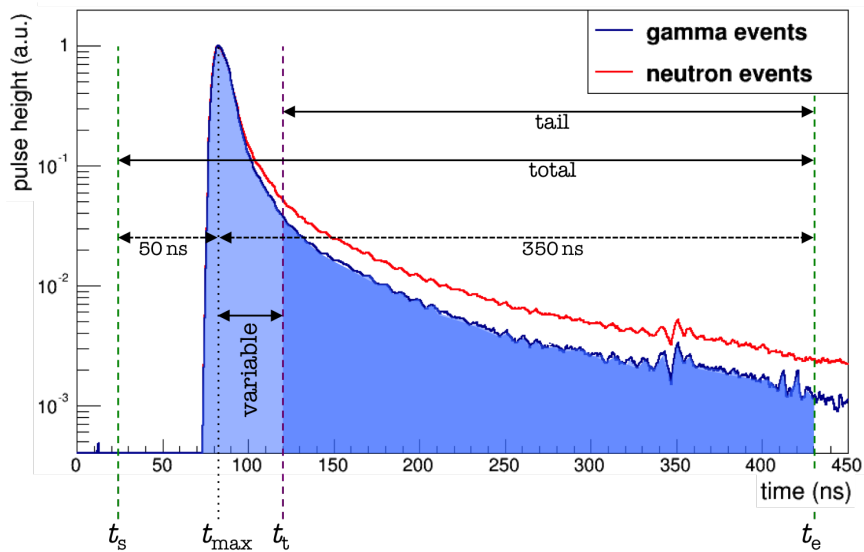
Figure 7.3.: Illustration of the integration regions for the tail-to-total parameter t_2t (see equation 7.2) by means of the average pulses already shown in figure 7.2. While the boundaries for the integral over the total pulse are fixed, the lower boundary for the integral over the tail region is variable in order to optimize the PSD performance as described in section 7.2.4.
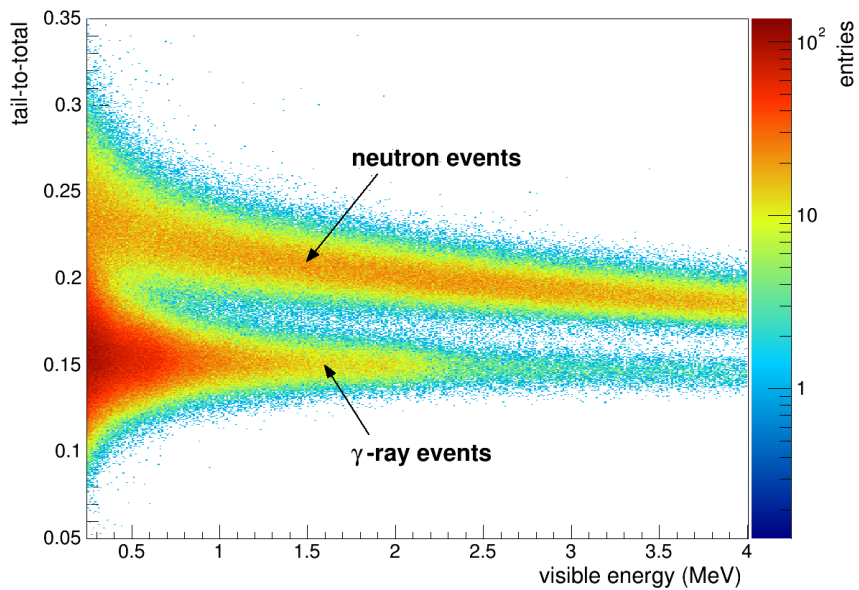
Figure 7.4.: Two-dimensional distribution of the tail-to-total parameter as a function of the visible energy for the LAB-3-20(2) sample (February 2014). The band at lower values of the tail-to-total parameter around 0.15 corresponds to γ-ray induced events, while the band at higher values is caused by neutron induced proton recoils. For further details, please refer to the text.

7.2.2. Fit to the Tail-To-Total Distributions

The PSD performance of the investigated scintillator samples is determined for different intervals in terms of the visible energy. Six energy intervals have been defined between 250 keV and 4 MeV as given in table 7.1. The lower energy threshold of 250 keV was chosen well above the energy thresholds of the setups used in the February and May/June 2014 beam times, respectively (see section 6.2). The upper analysis boundary of 4 MeV was chosen due to limited statistics for γ-ray induced events above that energy (see figure 7.4). The increasing widths of the used energy intervals with rising energy (see table 7.1) were chosen to account for the decreasing statistics and decreasing bending of the band due to neutron induced events with rising energy (see figure 7.4).

For each of the defined energy intervals, distributions of the tail-to-total parameter t_2t are obtained by filling the determined values for t_2t into histograms for each event type. An example for distributions of t_2t, obtained for the LAB-3-20(2) sample (February 2014) for events with visible energies between $1.0 - 1.5$ MeV, is shown in figure 7.5. The distributions obtained for the events selected from the γ-ray peaks (see figure 7.5(a)) and for events selected from the neutron peaks (see figure 7.5(b)) in the different ToF spectra are shown.

The distribution obtained for events selected from the γ-ray peaks (see figure 7.5(a)) features only a small contamination of neutron induced events around $t_2t \approx 0.22$, which is caused by scattered neutrons, produced in the previous beam bunch. However, the distribution of the tail-to-total parameter for the events selected from the neutron peaks (see figure 7.5(b)) shows a significant contamination of events induced by γ-rays around $t_2t \approx 0.15$. Additionally, figure 7.5(b) shows the distribution of accidental background events (see also figure 6.2), which were selected from a time interval before the γ-ray peak in the respective measurement, using the same width for the selection intervals as used for the selection of events from the corresponding neutron peaks. Obviously, the contamination of γ-ray events cannot be explained by the accidental coincidence background. This is observed for all scintillator samples.

interval	energy range
0	$0.25 - 0.5$ MeV
1	$0.5 - 1.0$ MeV
2	$1.0 - 1.5$ MeV
3	$1.5 - 2.0$ MeV
4	$2.0 - 3.0$ MeV
5	$3.0 - 4.0$ MeV

Table 7.1.: Energy intervals used for the determination for the PSD performance of the investigated scintillator samples.

(a) γ-ray peak events
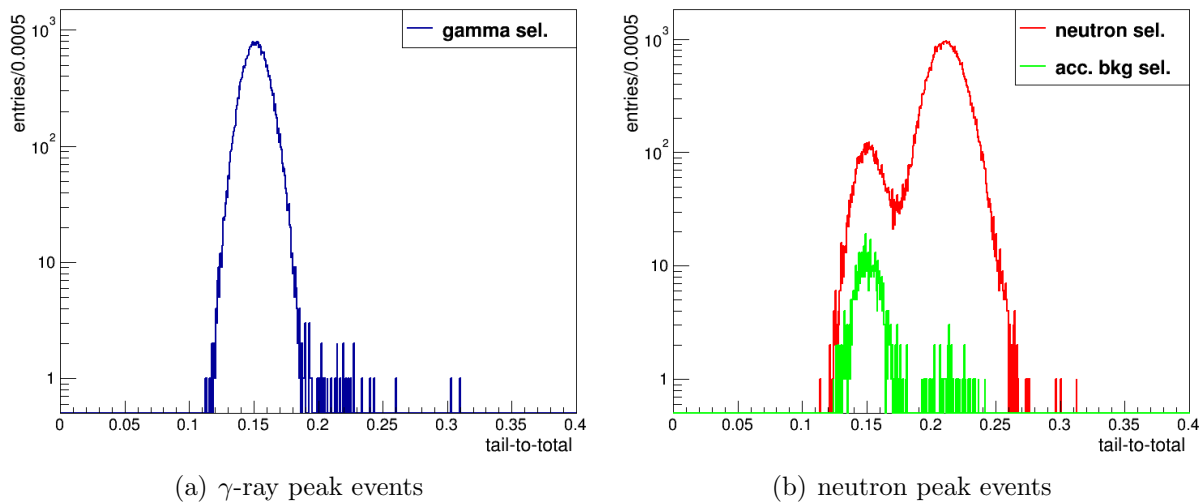
(b) neutron peak events

Figure 7.5.: Distributions of the tail-to-total parameter for events selected from the γ-ray peaks (a) and selected from the neutron peaks (b) of all measurements with the LAB-3-20(2) sample (February 2014). The shown distributions contain events with visible energies between $1.0 - 1.5\,\text{MeV}$. To determine the tail-to-total parameter (see equation (7.2)) for each event the optimized lower boundary of the tail integral (see section 7.2.4) of $t_\text{t} = t_\text{max} + 28.5\,\text{ns}$ was used. The distribution for the events selected from the neutron peaks (red) features a significant contribution of γ-ray events (peak around $t_2 t \approx 0.15$). This contribution cannot be fully explained by the accidental coincidence background (see figure 6.2), which is shown by the green distribution of events in figure (b). The accidental background events were selected from a time interval before the γ-ray peaks with equal widths as used for the selections of the neutron events.

The contamination of γ-ray events in the selected neutron samples range from $\sim 16\,\%$ for visible energies between $0.25 - 0.5\,\text{MeV}$ to $\sim 4\,\%$ for energies of $3 - 4\,\text{MeV}$ and decreases with rising energy. While the accidental coincidence background accounts for $\sim 40\,\%$ of the contamination for energies between $0.25 - 0.5\,\text{MeV}$, less than $\sim 10\,\%$ of the contamination can be explained by accidental background in the energy interval of $3 - 4\,\text{MeV}$.

As the contamination of γ-ray events in the selected neutron event samples cannot be explained by the accidental coincidence background, it has to be correlated to the beam bunches. Therefore, the contamination is caused by γ-rays due to either neutron activation of the surrounding materials or inelastic scattering in the materials in the surroundings of the experimental setup. As the described contamination cannot be removed from the selected neutron sample without using PSD, the PSD performance of the investigated scintillator samples cannot be derived directly from counting the events in the samples selected from each the γ-ray peaks and neutron peaks (see equation (7.1) and figure 7.1). Therefore, the distribution for the tail-to-total parameter, obtained for the combined sample of events selected from both the γ-ray peaks and the neutron peaks, is fitted with a model, which describes the contributions of γ-ray and neutron induced events.

As indicated by the distributions for the tail-to-total parameter shown in figure 7.5, the
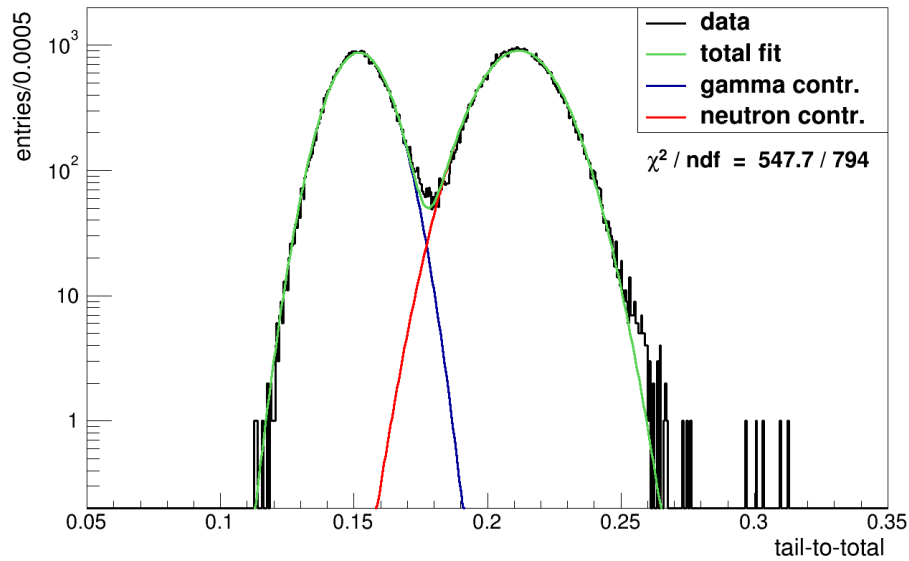
Figure 7.6.: Distribution of the tail-to-total parameter for events selected from both the γ-ray peaks and the neutron peaks of all measurements with the LAB-3-20(2) sample (February 2014) at the different used detector positions (see table 4.5). The shown distribution contains events with visible energies between $1.0 - 1.5$ MeV. To determine the the tail-to-total parameter (see equation (7.2)) for each event, the optimized lower boundary of the tail integral (see section 7.2.4) of $t_t = t_{max} + 28.5$ ns was used. The obtained distribution was fitted with the sum of two Gaussian distributions according to equation (7.3). The fit results for the respective Gaussian distributions, describing the contributions of the γ-ray and neutron induced events, are used to determine the PSD performance as described in section 7.2.3.

contributions of γ-ray and neutron induced events are rather symmetric. Therefore, each distribution for the tail-to-total parameter, obtained for the combined sample of γ-ray and neutron events, is fitted by a sum of two Gaussian distributions in a likelihood fit:

$$f_i(t_2t) = g_{\gamma,i}(t_2t) + g_{n,i}(t_2t) \tag{7.3}$$

with $g_{\gamma,i}(t_2t)$ and $g_{n,i}(t_2t)$ being the Gaussian distributions modeling the γ-ray and the neutron induced events, respectively. Each Gaussian is parameterized by a mean value ($\mu_{\gamma,i}$ and $\mu_{n,i}$), a width ($\sigma_{\gamma,i}$ and $\sigma_{n,i}$) and a normalization parameter ($N_{\gamma,i}$ and $N_{n,i}$). Figure 7.6 shows the fitted distribution of the tail-to-total parameter, obtained for the combined γ-ray and neutron event sample selected from the data recorded with the LAB-3-20(2) scintillator sample in the February 2014 beam time. The shown distribution corresponds to the energy interval of $1.0 - 1.5$ MeV. As indicated by the reduced $\chi^2/\mathrm{ndf} = 547.7 / 794$, the model fits the distribution of the tail-to-total parameter quite well. After the fit, the model, described above, can be used to extract PSD performance parameters as described in the following section.

7.2.3. PSD Performance Parameters

To characterize the PSD performance for each investigated scintillator sample and each of the different used energy intervals (see table 7.1), different parameters are available:

- **Figure of Merit:** To quantify the overlap of the distributions of the tail-to-total parameter due to γ-ray and neutron induced events a figure of merit FoM is used. The FoM is determined for each energy interval i in the following way [173]:

$$\mathrm{FoM}_i = \frac{|\mu_{n,i} - \mu_{\gamma,i}|}{\sqrt{\sigma_{n,i}^2 + \sigma_{\gamma,i}^2}} \tag{7.4}$$

  with $\mu_{\gamma,i}$ and $\mu_{n,i}$ being the fit results for the mean values of the Gaussians describing the contributions of the γ-ray and neutron induced events, respectively (see equation (7.3) and figure 7.6). $\sigma_{\gamma,i}$ and $\sigma_{n,i}$ are the corresponding fit results for the widths of the fitted Gaussian distributions. The FoM parameter describes the statistical separability of the two Gaussian distributions and, therefore, provides a measure for PSD performance. Values for the FoM parameter of at least 1 imply a good PSD performance of the scintillator [173].

  An error on the determined values of the figure of merit FoM_i is obtained from Gaussian error propagation, using the errors on the parameters from the fit to the distribution of the tail-to-total parameter for each energy interval i (see section 7.2.2).

  Figure 7.7 shows the figure of merits for the different energy intervals as determined from the data recorded with the LAB-3-20(2) scintillator (February 2014). A clear increase of the figure of merit with increasing energy can be observed. This is mainly caused by the accordingly increasing number of detected scintillation photons, which leads to decreasing widths of the distributions for the tail-to-total parameter for both the events induced by neutrons and γ-rays. A good PSD performance is already obtained for low energies between $0.25-0.5\,\mathrm{MeV}$, indicated by a FoM of 2.160 ± 0.012.

- **Rejection Efficiency or Remaining Fraction at Fixed Selection Efficiency:** A further measure for the PSD performance is the efficiency in rejecting events of one particle type for a given selection efficiency of events caused by the other particle type. The selection efficiency of neutron induced events is determined for each energy interval i by:

$$\eta_{n,i} = \frac{N_{n,i}^{\mathrm{sel}}}{N_{n,i}^{\mathrm{sel}} + N_{n,i}^{\mathrm{rej}}} \tag{7.5}$$

  where

$$N_{n,i}^{\mathrm{sel}} = \int_{t_2 t_{\mathrm{cut}}}^{\infty} g_{n,i}(t_2 t)\,\mathrm{d}t_2 t \quad \text{and} \quad N_{n,i}^{\mathrm{rej}} = \int_{-\infty}^{t_2 t_{\mathrm{cut}}} g_{n,i}(t_2 t)\,\mathrm{d}t_2 t \tag{7.6}$$

  are the selected and rejected neutron events[2], respectively, determined using the fit

---

[2] The separation of selected and rejected events in equation (7.5) is of importance for the error determination, as the number of selected neutron events is contained in the total number of events, which means that both are correlated.
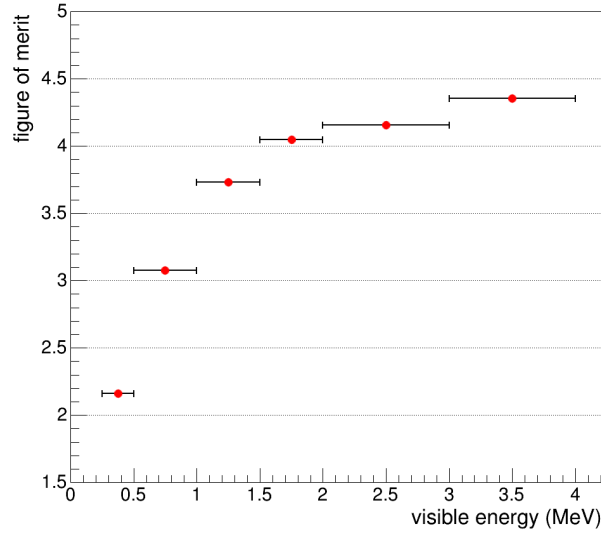
Figure 7.7.: The figure of merit (see equation (7.4)) as a function of the visible energy as obtained for the LAB-3-20(2) sample (February 2014). The horizontal positions of the data points correspond to the central values of the used energy intervals, while the horizontal errors represent to the widths of the energy intervals (see table 7.1). The obtained statistical errors on the figure of merit are too small to be visible.

results for the corresponding Gaussian fit $g_{n,i}(t_2 t)$ (see equation (7.3)). $t_2 t_{\mathrm{cut}}$ is the applied cut value for the tail-to-total parameter. Accordingly, the selection efficiency for γ-ray induced events is determined by:

$$\eta_{\gamma,i} = \frac{N_{\gamma,i}^{\mathrm{sel}}}{N_{\gamma,i}^{\mathrm{sel}} + N_{\gamma,i}^{\mathrm{rej}}} \tag{7.7}$$

with

$$N_{\gamma,i}^{\mathrm{sel}} = \int_{-\infty}^{t_2 t_{\mathrm{cut}}} g_{\gamma,i}(t_2 t)\, \mathrm{d}t_2 t \quad \text{and} \quad N_{\gamma,i}^{\mathrm{rej}} = \int_{t_2 t_{\mathrm{cut}}}^{\infty} g_{\gamma,i}(t_2 t)\, \mathrm{d}t_2 t \ , \tag{7.8}$$

calculated using the fit result of the corresponding Gaussian distribution $g_{\gamma,i}(t_2 t)$, describing the contribution of the γ-ray induced events (see equation (7.3)).

For a given selection efficiency of events caused by one particle type ($\eta_{n,i}$ and $\eta_{\gamma,i}$) the corresponding rejection efficiency for events due to the other particle type ($\eta_{\gamma,i}^{\mathrm{rej}}$ and $\eta_{n,i}^{\mathrm{rej}}$) coincides with the selection efficiency for events of this particle type, i.e. $\eta_{\gamma,i}^{\mathrm{rej}}(t_2 t_{\mathrm{cut}}) = \eta_{\gamma,i}(t_2 t_{\mathrm{cut}})$ and $\eta_{n,i}^{\mathrm{rej}}(t_2 t_{\mathrm{cut}}) = \eta_{n,i}(t_2 t_{\mathrm{cut}})$.

The remaining fraction of events caused by one particle type ($r_{n,i}$ and $r_{\gamma,i}$), when selecting events due to the other particle type with a given efficiency, is determined by

$$r_{n,i} = \frac{N_{n,i}^{\mathrm{rej}}}{N_{n,i}^{\mathrm{sel}} + N_{n,i}^{\mathrm{rej}}} = 1 - \eta_{n,i} \tag{7.9}$$
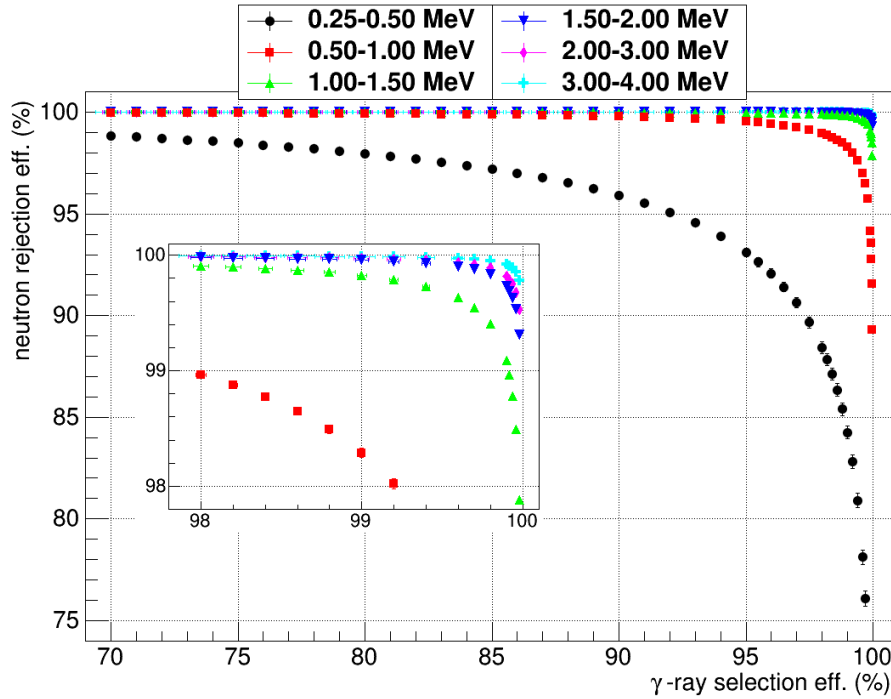
Figure 7.8.: Rejection efficiency for neutron events as a function of the selection efficiency for γ-ray induced events for the LAB-3-20(2) scintillator sample (February 2014). The data points were calculated for fixed γ-ray event selection efficiencies between 70 % and 99.98%, using the results from the fits to the distributions of the tail-to-total parameter, obtained for each energy interval, as described in section 7.2.2. The inset shows a zoom to the selection and rejection efficiency regions above 99 %.

for neutron induced events and by

$$r_{\gamma,i} \ = \ \frac{N_{\gamma,i}^{\text{rej}}}{N_{\gamma,i}^{\text{sel}} + N_{\gamma,i}^{\text{rej}}} \ = \ 1 - \eta_{\gamma,i} \tag{7.10}$$

for γ-ray induced events, using equations (7.6) and (7.8), respectively.

The errors on the parameters for the selection/rejection efficiencies $\eta_{n,i}$ and $\eta_{\gamma,i}$ and the remaining fractions of events $r_{n,i}$ and $r_{\gamma,i}$ are determined by Gaussian error propagation of the errors on the parameters of the respective Gaussian distribution ($g_{\gamma,i}(t_2t)$ and $g_{n,i}(t_2t)$), obtained from the fit to the distribution of the tail-to-total parameter for each energy interval i (see section 7.2.2).

Figure 7.8 shows the rejection efficiencies for neutron induced events (see equation (7.5)), calculated for fixed selection efficiencies for γ-ray events (see equation (7.7)) between 70 % and 99.98%, in case of the LAB-3-20(2) scintillator sample (February 2014). Furthermore, in figure 7.9 the remaining fraction of neutron induced events for a selection efficiency of γ-ray events of 99% (figure 7.9(a)) and the remaining fraction of γ-ray events for a 99 % selection efficiency of neutrons (figure 7.9(b)) are

(a) remaining fraction of neutrons   (b) remaining fraction of γ-rays
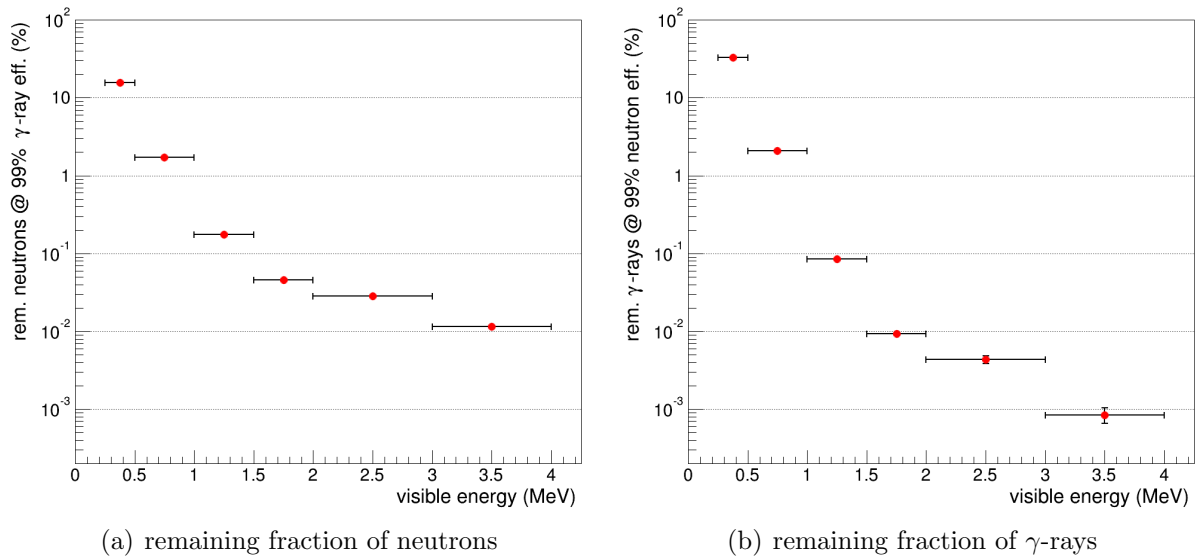
Figure 7.9.: The remaining fraction of neutron events (a) for a selection efficiency of γ-ray events of 99 % and the remaining fraction of γ-ray events (b) for a neutron selection efficiency of 99 % in case of the LAB-3-20(2) scintillator (February 2014). The horizontal positions of the data points correspond to the central values of the used energy intervals, while the horizontal errors represent the widths of the energy intervals (see table 7.1).

shown for the LAB-3-20(2) scintillator sample (February 2014) as a function of the visible energy. The different behavior, when selecting γ-rays and neutrons, respectively, can be understood with the help of figure 7.4. While the fraction of remaining γ-ray events is higher for energies below 1 MeV, the rejection of γ-ray events is about one order of magnitude better for energies above 3 MeV. The behavior for higher energies can be understood by the width of the respective distribution for the tail-to-total parameter. The width for neutron induced events is always slightly higher than for γ-ray events. This leads to a more efficient rejection of neutron events than of γ-ray events. The behavior for energies below 1 MeV can be understood by the energy spectra for both event types in this energy region. The spectrum for the γ-rays rises much more steeply towards lower energies than that for neutron events. Therefore, events from the lower energetic part of each interval, which show a worse PSD performance than events with higher energies due to the reduced light yield, make out a larger fraction of the events in each interval. Thus, the PSD performance obtained for the respective energy interval is artificially reduced.

7.2.4. Optimization of the Performance of the Tail-to-Total Parameter

The performance of the tail-to-total parameter was optimized for each investigated scintillator sample separately. While the boundaries for the integral over the total pulse and

the upper boundary of the integral over the tail of each pulse were fixed, the lower integration boundary for the tail t_t in equation (7.2) was varied in order to obtain the maximum discrimination power.

For each energy interval (see table 7.1), the lower boundary of the tail integral t_t was varied in steps of $0.5\,\mathrm{ns}^3$ between $t_{max} + 12.5\,\mathrm{ns} \leq t_t < t_{max} + 55\,\mathrm{ns}$, where t_{max} is the time corresponding to the maximum of each pulse (see section 4.3). The resulting distributions for the tail-to-total parameter were fitted as described in section 7.2.2. Using the fit result, the figure of merit, which was introduced in equation (7.4), was calculated for each value of t_t. To reduce the complexity of the obtained results, only one value of $\hat{t}_t$ was used for each scintillator sample. It was determined by averaging over the optimal t_t values, found for each energy interval.

In figure 7.10 the optimization of the lower boundary for the tail integration is shown for the analysis of the data recorded with the LAB-3-20(2) scintillator sample (February 2014). In the shown example, the optimized value for the lower boundary of the tail integral was determined to be $\hat{t}_t = t_{max} + 28.5\,\mathrm{ns}$. The shown data indicates that with increasing energy the dependency of the figure of merit (see equation (7.4)) on the start time of the tail integral continuously decreases. This behavior can be explained by the signal to noise ratio in the tail region of each pulse, which improves for increasing visible energy. Furthermore, with increasing energy the optimum tail integration start time, featuring the maximum value of FoM for each energy interval, ends up at later times. This behavior can be explained by the energy loss, which decreases with rising energy (see figure 6.7). Thus, the difference in the relative intensity of the slow scintillation component for γ-ray and neutron induced events decreases with increasing energy. As a consequence, the time, at which the difference in the relative intensity of the slow component becomes significant (see figure 7.2), shifts to later times for increasing visible energy. Nevertheless, the PSD performance increases with rising energy, which is indicated by the higher values for the figure of merit and is caused by the increasing number of detected photons.

---

[3] The used time steps correspond to the sampling rate of the used analog-to-digital converter (ADC) (see section 4.2.3).
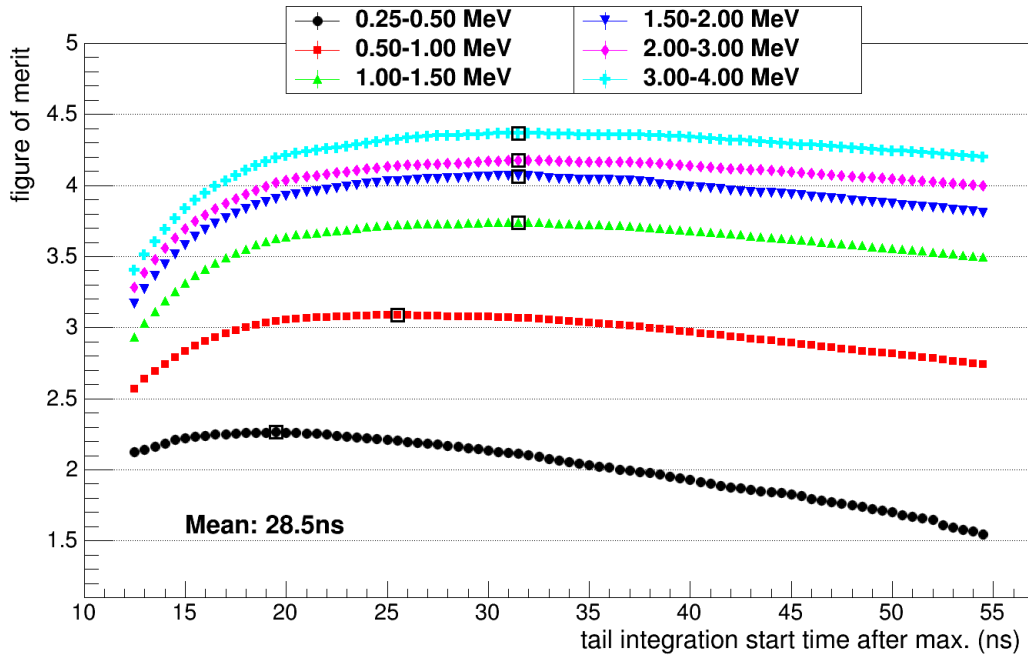
Figure 7.10.: The figure of merit (FoM) (see equation (7.4)) as a function of the lower boundary for the integral over the tail t_t of the pulses (see equation (7.2)), which were recorded with the LAB-3-20(2) sample in the February 2014 beam time. The different colors correspond to the different energy intervals used in the PSD performance analysis (see table 7.1). The data points, featuring the maximum values for the FoM in each energy interval, are highlighted by the black rectangles. The mean value of the tail integral lower boundaries, featuring the maximum FoM in each energy interval, was determined to be $t_{max} + 28.5$ ns, where t_{max} is the time corresponding to the maximum of each recorded pulse (see section 4.3).

7.3. Summary of Results

The results for the figure of merit FoM (see equation (7.4)) for each energy interval are given in table 7.2 for all scintillator samples, which were investigated in the two 2014 beam times. The given errors correspond to the statistical errors, which are derived from the results of the fits to the tail-to-total distributions. Additionally, the lower boundary for the determination of the tail integral t_t (see equation (7.2)) relative to the time corresponding to the maximum of the respective recorded pulse t_max is shown. The used value for $(t_\mathrm{t} - t_\mathrm{max})$ was optimized as described in section 7.2.4. Additionally, in table 7.2 the estimated number of detected photoelectrons (p.e.) at a visible energy of $1\,\mathrm{MeV}$, determined from the energy resolution of the scintillator detector as described in section 5.6, is given for each of the investigated scintillators. To a certain extent, the given photoelectron yields can be used to estimate the PSD performance for the respective scintillator for a detector featuring a different light collection efficiency.

As described in section 7.2.3 the FoM is a measure of the separability of the distributions of the tail-to-total parameter due to γ-ray and neutron induced events, respectively. Values of at least 1 imply a good PSD performance of the scintillator, while the performance improves for rising values. According to the results given in table 7.2, most of the scintillators feature an excellent PSD performance with values for the FoM significantly larger than 1. Only for three scintillators, namely the DCTarget (February 2014), the DCGC (May/June 2014) and the 50LAB-50nPar (May/June 2014), show values for the FoM below 1 for energies of $0.25 - 0.5\,\mathrm{MeV}$. This is mainly caused by the lower light yield of theses scintillators compared to the others.

Furthermore, in table 7.3 the results for the remaining fraction of neutron events for a selection efficiency for γ-ray events of $99\,\%$, determined for each energy interval as described in section 7.2.3, are shown along with the optimized start time of the tail integral and the estimated photoelectron yield at $1\,\mathrm{MeV}$. In table 7.4 the corresponding results for the remaining fraction of γ-ray events for a neutron event selection efficiency of $99\,\%$ are given.

Similar to the discussion of the results obtained from the proton quenching analysis (see chapter 6), the investigated scintillator mixtures (see sections 3.4.4 and 4.5) can be divided into two main groups: Firstly, scintillators based on LAB with different admixed concentrations of the first and second wavelength shifters PPO and bisMSB and diluted with different amounts of nonscintillating n-paraffine and, secondly, the scintillators used in currently running Double Chooz and Borexino experiments and favored for the planned LENA and JUNO experiments. Please refer to section 3.4 for the descriptions of the different scintillator components.

7.3.1. PSD Performance of LAB-based Scintillators

The LAB based scintillators can be further subdivided into three subgroups: Scintillator samples with fixed concentration of bisMSB and varying concentration of PPO, samples

sample	Results for the figure of merit for each energy interval (MeV):						$t_t - t_{max}$ (ns)	p.e. yield at 1 MeV
	0.25 – 0.5	0.5 – 1.0	1.0 – 1.5	1.5 – 2.0	2.0 – 3.0	3.0 – 4.0		
February 2014								
LAB-3-20(2)	2.160(12)	3.078(8)	3.730(10)	4.049(12)	4.157(12)	4.352(19)	28.5	628 ± 40
DCTarget	0.849(7)	2.055(10)	2.801(8)	3.119(9)	3.298(10)	3.539(17)	37.0	402 ± 17
LAB-3-10	2.217(11)	3.183(7)	3.904(9)	4.238(11)	4.336(11)	4.618(18)	30.0	560 ± 136
LAB-3-0	2.093(11)	2.966(7)	3.631(9)	3.933(11)	4.057(11)	4.324(19)	29.0	720 ± 228
LAB-7-20	2.408(9)	3.420(7)	4.135(10)	4.476(12)	4.555(13)	4.75(2)	24.5	637 ± 37
LAB-9-20	2.290(10)	3.276(7)	4.014(9)	4.358(12)	4.462(12)	4.729(19)	28.0	600 ± 33
LAB-3-80	2.238(12)	3.198(8)	3.910(11)	4.249(13)	4.401(14)	4.67(2)	29.0	750 ± 228
May/June 2014								
50LAB-50nPar	0.915(12)	2.448(11)	3.127(11)	3.448(13)	3.684(13)	3.895(19)	32.0	547 ± 30
LAB-1-20	1.048(14)	2.226(12)	2.826(11)	3.057(12)	3.224(13)	3.40(2)	48.0	498 ± 23
DCMV-PSD	1.37(7)	2.504(16)	3.144(18)	3.44(2)	3.64(2)	4.00(4)	38.5	503 ± 24
DCGC	0.574(9)	1.024(9)	1.738(8)	2.005(10)	2.253(15)	2.48(3)	29.5	424 ± 19
LAB-5-20-PSD	2.304(13)	3.340(12)	4.034(16)	4.34(2)	4.40(2)	4.66(3)	25.5	547 ± 27
75LAB-25nPar	1.975(11)	2.959(6)	3.656(8)	4.006(9)	4.162(10)	4.444(16)	31.0	556 ± 30
LAB-3-40-PSD	2.217(13)	3.171(11)	3.829(15)	4.179(18)	4.292(19)	4.55(3)	29.5	664 ± 168
Borexino(2)	3.368(9)	4.404(10)	5.140(14)	5.416(16)	5.331(13)	5.573(18)	22.0	753 ± 214
LAB-3-0(2)	2.058(11)	2.995(8)	3.678(10)	4.005(12)	4.124(12)	4.39(2)	29.5	685 ± 206

Table 7.2.: Results for the figure of merit, determined from the result of the fit to the distribution of the tail-to-total parameter (see section 7.2.2) for each energy interval (see table 7.1) as described in section 7.2.3, for all scintillator samples investigated in the two 2014 beam times (see section 4.5). The numbers in brackets correspond to the statistical errors on the last decimal place(s) (see section 7.2.3). Furthermore, the lower boundaries for the integral over the tail t_t relative to the time corresponding to the maximum of each recorded pulse t_{max}, optimized for each scintillator sample as described in section 7.2.4, are given. To provide a comparability to detectors with different light collection efficiencies, the photoelectron (p.e.) yields for a visible energy of 1 MeV, estimated as described in section 5.6, are provided for each investigated scintillator.

sample	Remaining fraction of neutrons in (%) for 99 % γ-ray selection efficiency for each energy interval (MeV):						$t_t - t_{max}$ (ns)	p.e. yield at 1 MeV
	0.25 − 0.5	0.5 − 1.0	1.0 − 1.5	1.5 − 2.0	2.0 − 3.0	3.0 − 4.0		
February 2014								
LAB-3-20(2)	15.7(3)	1.71(4)	0.175(6)	0.046(2)	0.0285(10)	0.0116(5)	28.5	628 ± 40
DCTarget	60.0(3)	16.7(3)	3.43(7)	1.37(3)	0.779(15)	0.345(9)	37.0	402 ± 17
LAB-3-10	14.0(3)	1.23(3)	0.086(3)	0.0197(9)	0.0124(4)	0.00314(15)	30.0	560 ± 136
LAB-3-0	18.7(4)	2.47(5)	0.261(8)	0.076(3)	0.0441(13)	0.0129(5)	29.0	720 ± 228
LAB-7-20	10.8(2)	0.581(15)	0.0303(13)	0.0059(3)	0.00401(16)	0.00149(8)	24.5	637 ± 37
LAB-9-20	14.1(3)	0.97(2)	0.053(2)	0.0106(5)	0.0064(2)	0.00165(8)	28.0	600 ± 33
LAB-3-80	14.2(3)	1.22(3)	0.084(3)	0.0185(9)	0.0090(4)	0.00237(15)	29.0	750 ± 228
May/June 2014								
50LAB-50nPar	55.6(5)	8.8(2)	1.45(5)	0.499(19)	0.208(7)	0.088(5)	32.0	547 ± 30
LAB-1-20	50.6(6)	12.5(3)	3.33(9)	1.71(6)	1.02(3)	0.572(18)	48.0	498 ± 23
DCMV-PSD	39.8(28)	7.5(3)	1.41(7)	0.52(3)	0.252(13)	0.056(4)	38.5	503 ± 24
DCGC	81.5(4)	57.4(4)	31.4(4)	23.1(3)	14.76(14)	9.20(11)	29.5	424 ± 19
LAB-5-20-PSD	13.5(4)	0.77(3)	0.048(3)	0.0115(10)	0.0086(6)	0.00237(18)	25.5	547 ± 27
75LAB-25nPar	21.3(3)	2.44(4)	0.235(6)	0.0554(19)	0.0277(8)	0.0074(3)	31.0	556 ± 30
LAB-3-40-PSD	15.4(4)	1.32(5)	0.118(6)	0.0247(17)	0.0147(8)	0.0044(3)	29.5	664 ± 168
Borexino(2)	0.67(2)	0.0092(4)	0.000214(17)	0.000047(4)	0.000080(5)	0.000020(2)	22.0	753 ± 214
LAB-3-0(2)	20.2(4)	2.28(5)	0.219(7)	0.055(2)	0.0325(11)	0.0094(4)	29.5	685 ± 206

Table 7.3.: Results for each scintillator sample, investigated in the two 2014 beam times (see section 4.5), on the remaining fraction of neutron events for a selection efficiency of 99 % for γ-ray events, determined from the result of the fit to the distribution of the tail-to-total parameter (see section 7.2.2) for each energy interval (see table 7.1) as described in section 7.2.3. The numbers in brackets correspond to the statistical errors on the last decimal place(s) (see section 7.2.3). Furthermore, the lower boundaries for the integral over the tail t_t relative to the time corresponding to the maximum of each recorded pulse t_{max}, optimized for each scintillator sample as described in section 7.2.4, are given. To provide a comparability to detectors with different light collection efficiencies, the photoelectron (p.e.) yields for a visible energy of 1 MeV, estimated as described in section 5.6, are provided for each investigated scintillator.

sample	Remaining fraction of γ-ray in (%) for 99% neutron selection efficiency for each energy interval (MeV):						$t_t - t_{max}$ (ns)	p.e. yield at 1 MeV
	0.25 − 0.5	0.5 − 1.0	1.0 − 1.5	1.5 − 2.0	2.0 − 3.0	3.0 − 4.0		
February 2014								
LAB-3-20(2)	32.75(14)	2.08(3)	0.086(4)	0.0093(8)	0.0043(5)	0.00084(19)	28.5	628 ± 40
DCTarget	99.574(17)	43.7(2)	5.95(13)	1.61(6)	0.68(4)	0.19(2)	37.0	402 ± 17
LAB-3-10	29.46(13)	1.33(2)	0.0291(14)	0.0023(2)	0.00113(13)	0.00008(2)	30.0	560 ± 136
LAB-3-0	35.62(15)	3.28(4)	0.163(7)	0.0271(19)	0.0119(11)	0.0017(3)	29.0	720 ± 228
LAB-7-20	17.50(11)	0.493(9)	0.0088(5)	0.00063(6)	0.00031(4)	0.000053(15)	24.5	637 ± 37
LAB-9-20	22.60(12)	0.956(15)	0.0189(10)	0.00171(15)	0.00069(9)	0.000055(14)	28.0	600 ± 33
LAB-3-80	27.05(15)	1.30(2)	0.0299(17)	0.0027(3)	0.00076(11)	0.00007(2)	29.0	750 ± 228
May/June 2014								
50LAB-50nPar	99.54(2)	17.16(17)	1.68(6)	0.37(2)	0.102(9)	0.025(4)	32.0	547 ± 30
LAB-1-20	98.75(5)	30.9(2)	5.43(15)	2.19(10)	1.03(7)	0.44(6)	48.0	498 ± 23
DCMV-PSD	91.2(5)	15.0(3)	1.59(11)	0.40(5)	0.14(2)	0.011(4)	38.5	503 ± 24
DCGC	99.15(5)	97.26(14)	61.0(5)	39.3(7)	24.9(8)	14.6(10)	29.5	424 ± 19
LAB-5-20-PSD	22.2(3)	0.71(2)	0.0170(17)	0.0024(4)	0.0015(3)	0.00011(5)	25.5	547 ± 27
75LAB-25nPar	45.90(13)	3.34(4)	0.132(5)	0.0145(9)	0.0048(4)	0.00044(9)	31.0	556 ± 30
LAB-3-40-PSD	27.5(3)	1.45(4)	0.052(4)	0.0067(9)	0.0026(5)	0.00023(8)	29.5	664 ± 168
Borexino(2)	0.574(9)	0.000326(15)	0.000000(*)	0.000000(*)	0.000000(*)	0.000000(*)	22.0	753 ± 214
LAB-3-0(2)	37.51(16)	2.94(4)	0.134(6)	0.0181(14)	0.0082(9)	0.0010(2)	29.5	685 ± 206

Table 7.4.: Results for each scintillator sample, investigated in the two 2014 beam times (see section 4.5), on the remaining fraction of γ-ray events for a selection efficiency of 99% for neutron events, determined for each energy interval (see table 7.1) as described in section 7.2.3. The numbers in brackets correspond to the statistical errors on the last decimal place(s) (see section 7.2.3), where an asterisk indicates an error on the last decimal place smaller than 10^{-3}. Furthermore, the lower boundaries for the integral over the tail t_t relative to the time corresponding to the maximum of each recorded pulse t_{max}, optimized for each scintillator sample as described in section 7.2.4, are given. To provide a comparability to detectors with different light collection efficiencies, the photoelectron (p.e.) yields for a visible energy of 1 MeV, estimated as described in section 5.6, are provided for each investigated scintillator.

with fixed concentration of PPO and varying concentration of bisMSB and scintillators, which were diluted with different amounts of n-paraffine, while the absolute concentrations of PPO and bisMSB in the diluted mixtures are the same. In the following, the results for the different groups of scintillators will be compared and discussed.
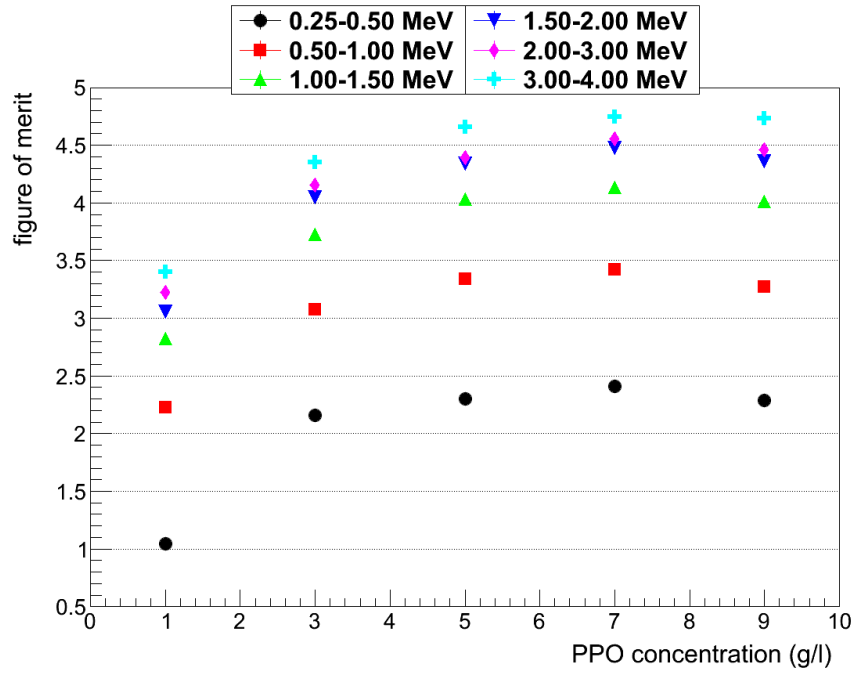
Dependency of the PSD Performance on the Concentration of the First Wavelength Shifter PPO:

In figure 7.11 the results for the figure of merit (see figure 7.11(a)) and the remaining fraction of neutron events for a 99 % selection efficiency for γ-rays (see figure 7.11(b)) are depicted for LAB-based scintillator samples, featuring concentrations of the first wavelength shifter PPO of $1\,\mathrm{g/l} - 9\,\mathrm{g/l}$ and a fixed concentration of the second wavelength shifter bisMSB of $20\,\mathrm{mg/l}$. The results for the different energy intervals (see table 7.1) are depicted in different colors.

The data indicates a clear improvement of the PSD performance with increasing concentration of PPO, while a saturation effect above a concentration of $5\,\mathrm{g/l}$ is observed. This behavior is similar to the behavior observed for the quenching effect (see figure 6.10), which strengthens towards lower PPO concentrations. The decreasing PSD performance can also be explained by the transfer of energy from excited solvent molecules to molecules of the first solute PPO. The efficiency of this energy transfer, which mainly happens via a dipole-dipole interaction, features a strong dependency on the distance between the interacting molecules (see section 3.1.3 and equation (3.2)). In case of a too low concentration of the first solute, the excitation energy needs to be transported to the vicinity of a solute molecule, which mainly takes place by thermal diffusion and non-radiative solvent-solvent transfer and increases the non-radiative losses of excitation energy. Therefore, the light output of the liquid scintillator decreases, which results in a worsening of the PSD performance.

For heavy ionizing particles, here protons scattered off by incident neutrons, the increased energy loss causes an increased density of ionized molecules, which mainly recombine to excited triplet states (see section 3.1.2). To obtain fluorescence photons, these excited triplet states need to be converted to excited singlet states, which is realized by processes like that given in equation (3.1). The resulting losses lead to the effect of ionization quenching (see section 3.2). Therefore, the losses in the scintillation light yield for heavier particles are mainly caused by the losses of photons from the slow scintillation component (see section 3.3). As described above in section 7.2.1 and shown in figure 7.2, the relative intensity of the slow component is the key feature, which makes PSD with organic liquid scintillators possible. Hence, the loss of light in the slow scintillation component due to ionization quenching provides another explanation for the decreasing PSD performance for decreasing PPO concentrations below $5\,\mathrm{g/l}$.

The constant behavior of the PSD performance for PPO concentrations above $5\,\%$ can be explained by the saturating effect of the scintillation light output, when enough PPO molecules are within the critical radius for the dipole-dipole interaction (see equation (3.2)).

(a) figure of merit
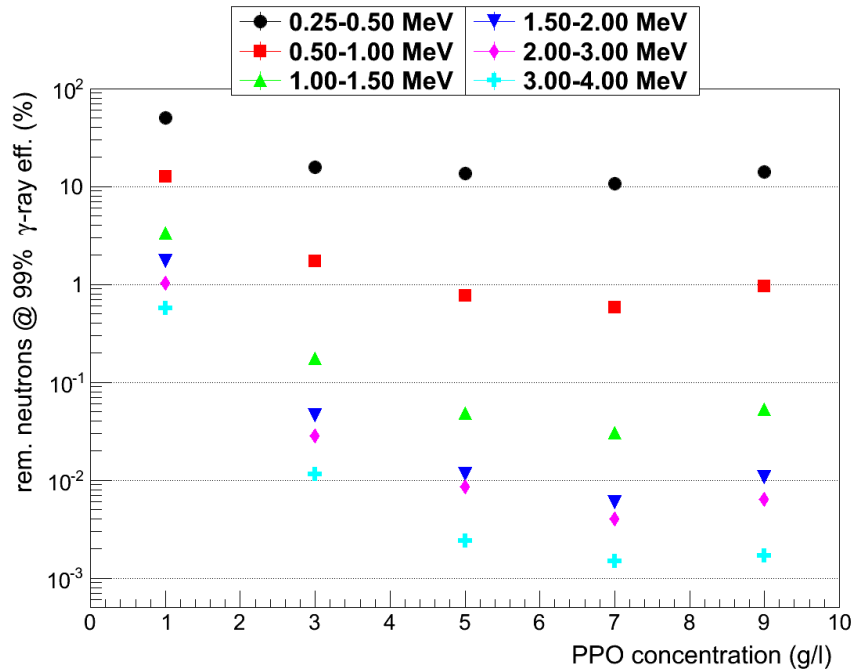
(b) remaining fraction of neutron events

Figure 7.11.: Results on the figure of merit (a) and the remaining fraction of neutron events in case of 99 % selection efficiency for γ-ray events (b) as a function of the concentration of the first wavelength shifter PPO in the LAB based scintillator samples. The concentration of the second fluor bisMSB was fixed to 20 mg/l. The respective values for the figure of merit and the corresponding errors are given in table 7.2. The individual results and errors for the remaining fraction of neutron events are given in table 7.3.

Just recently, measurements regarding the light yield of LAB-based scintillators with varying concentrations of PPO were presented in [171], which show a stagnating light yield for PPO concentrations above $\sim 4\,\mathrm{g/l}$.

Dependency of the PSD Performance on the Concentration of Second Wavelength Shifter bisMSB:

In figure 7.12 the results for the figure of merit (see figure 7.12(a)) and the remaining fraction of neutron events for a $99\,\%$ selection efficiency for γ-rays (see figure 7.12(b)) are depicted for LAB-based scintillator samples, featuring a fixed concentration of the first wavelength shifter PPO of $3\,\mathrm{g/l}$ and varying concentrations of the second wavelength shifter bisMSB between $0\,\mathrm{mg/l} - 80\,\mathrm{mg/l}$.

Similar to the results obtained for the quenching of the light output due to protons (see section 6.6.1 and figure 6.11), no large effect of the concentration of the second wavelength shifter bisMSB on the PSD performance is observed. This observation confirms that the transfer of excitation energy from the first to the second fluor is very efficient and practically independent on the concentration of the second wavelength shifter. Thus, the bisMSB concentration has practically no influence on the scintillation light yield and pulse shape of the scintillator. Recent measurements by a Chinese group, described in [171], show that the light yield of LAB-based scintillators saturates for bisMSB concentrations above $\sim 8\,\mathrm{mg/l}$, while the change in the light output for smaller concentrations is small.

In case of no bisMSB being admixed to the scintillator, a small decrease in the detected scintillation light is expected due to a shift of the emission spectrum from wavelengths peaking around $\sim 420\,\mathrm{nm}$ towards smaller wavelengths around $\sim 365\,\mathrm{nm}$. As the used PMT (see section 4.2.1) is sensitive down to wavelengths of $\sim 280\,\mathrm{nm}$, the effect of the wavelength shift on the detected amount of scintillation light is rather small and, hence, the effect on the results for the PSD performance is small.

For the scintillator, featuring no admixed second fluor bisMSB, data was taken in the February as well as in the June/May 2014 beam time. The variation of the results obtained for the LAB-3-0 and the LAB-3-0(2) samples give a hint for the systematic uncertainty of the determination of the PSD performance as described in the present chapter. The slightly decreased PSD performance obtained from the data taken for the LAB-3-20(2) sample, especially for lower energies, is expected to be explained by the systematics of the analysis.

Dependency of the PSD Performance on the Concentration of n-Paraffine:

In figure 7.13 the results for the figure of merit (see figure 7.13(a)) and the remaining fraction of neutron events for a $99\,\%$ selection efficiency for γ-rays (see figure 7.13(b)) are depicted for LAB-based scintillator samples, which were diluted with different concentrations of nonscintillating n-paraffine between $0\,\mathrm{vol\%} - 50\,\mathrm{vol\%}$. The absolute concentrations of the wavelength shifters PPO and bisMSB in the diluted liquid of $3\,\mathrm{g/l}$ and $20\,\mathrm{mg/l}$,
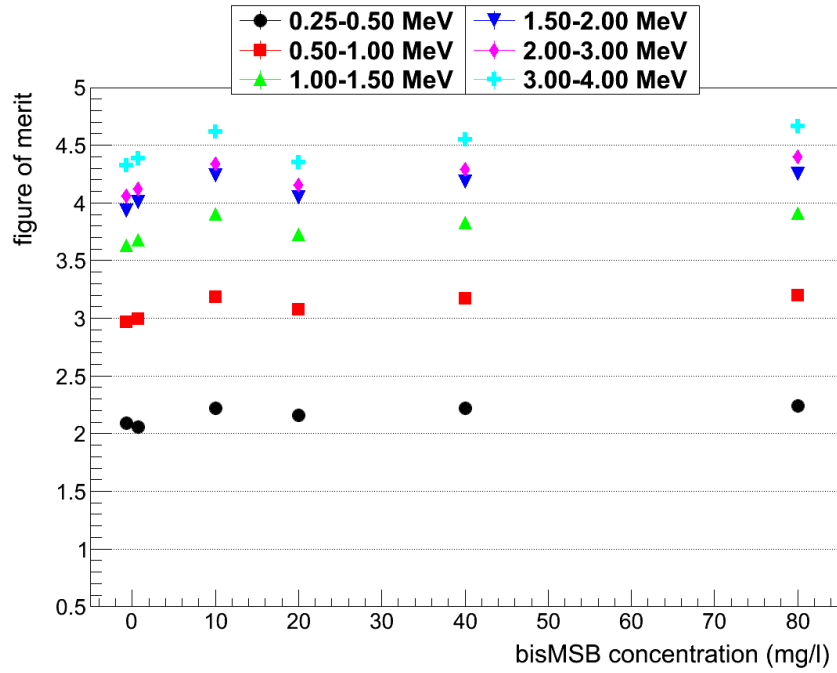
(a) figure of merit
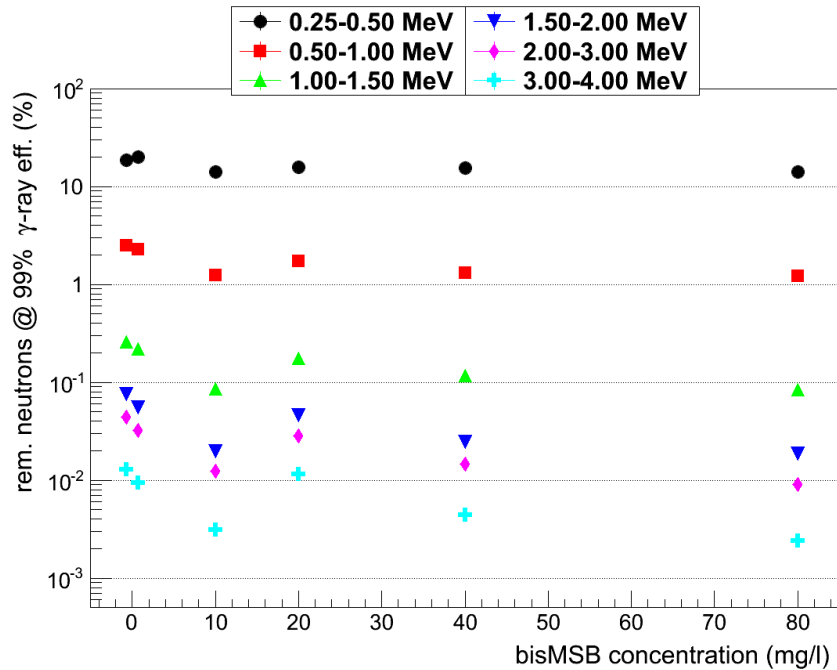
(b) remaining fraction of neutron events

Figure 7.12.: Results on the figure of merit (a) and the remaining fraction of neutron events in case of 99 % selection efficiency for γ-ray events (b) as a function of the concentration of the second wavelength shifter bisMSB in the LAB based scintillator samples. The concentration of the first fluor PPO was fixed to 3 g/l. The respective values for the figure of merit and the corresponding errors are given in table 7.2. The individual results and errors for the remaining fraction of neutron events are given in table 7.3. The results for the LAB-3-0 and LAB-3-0(2) samples were separated artificially by applying offsets to the true bisMSB concentration of 0 mg/l.

respectively, were the same in all shown samples.

The PSD performance clearly decreases with increasing concentration of n-paraffine. As observed for the results on the quenching, described in section 6.6.1 and shown in figure 6.12, the effect for the 50LAB-50nPar sample, which was diluted with $50\,\mathrm{vol}\%$ of n-paraffine, is considerably larger than for the 75LAB-25nPar sample ($25\,\mathrm{vol}\%$ of n-paraffine). As discussed for the quenching results, two effects affect the light output of scintillators, which are diluted with nonscintillating components: Firstly, the presence of diluter molecules inhibit the solvent-solvent energy transfer, which reduces the light yield of the scintillator. Furthermore, the presence of nonscintillating molecules interferes with the conversion of excited triplet states to singlet states. In case of heavy particles, which cause higher ionization densities and, therefore, higher densities of molecules in excited triplet states, the loss in light yield is further increased. As this mainly affects the slow component of the scintillator (see section 3.3), the PSD performance decreases. Secondly, dilution with n-paraffine reduces the density of the scintillator, which results in a decreasing energy loss of the incident ionizing particles. Therefore, the density of excited triplet states is reduced, which reduces the quenching effect. Hence the light output and in consequence the PSD performance of the scintillator improves.

While both effects, described above, seem to balance in case of the 75LAB-25nPar scintillator sample, which results in a similar PSD performance as obtained for the LAB-3-20(2) sample, the first effect dominates for the 50LAB-50nPar sample, which features a considerably reduced PSD performance compared to LAB-3-20(2).

7.3.2. PSD Performance of Scintillators Used in Neutrino Experiments

In figure 7.14 the results obtained for the figure of merit (see figure 7.14(a)) and the remaining fraction of neutron events for a $99\,\%$ selection efficiency for γ-rays (see figure 7.14(b)) are depicted for the scintillators samples from the running Double Chooz and Borexino experiments and for the scintillator favored for the LENA and JUNO projects.

The Borexino Scintillator:

The Borexino scintillator, which consists of pseudocumene (PC) with PPO admixed in a concentration of $1.5\,\mathrm{g/l}$, features by far the best PSD performance of all investigated scintillators. The remaining fractions of neutrons for a selection efficiency for γ-rays of $99\,\%$ for the energy intervals above $1\,\mathrm{MeV}$ (see table 7.3) are too small for the region shown in figure 7.14(b). Already more than $99\,\%$ of the neutron events are rejected at energies between $0.25 - 0.5\,\mathrm{MeV}$. The better PSD performance compared to the investigated LAB-based scintillators can mainly be attributed to the different used solvent, which features a much more pronounced slow decay component for heavier particles [125].

In the Borexino detector a photoelectron (p.e.) yield of $489 \pm 2\,\mathrm{p.e./MeV}$ is achieved, which
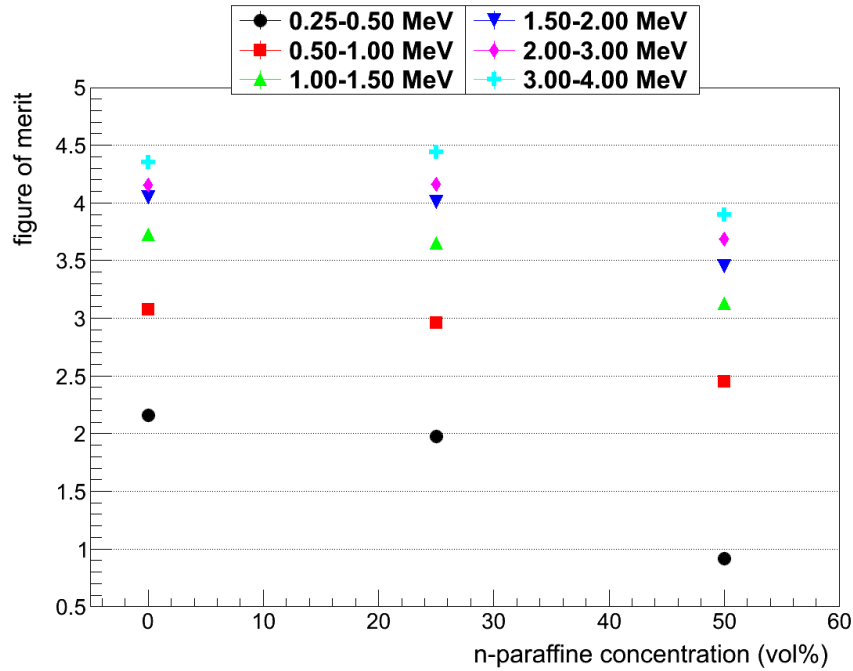
(a) figure of merit

(b) remaining fraction of neutron events

Figure 7.13.: Results on the figure of merit (a) and the remaining fraction of neutron events in case of 99 % selection efficiency for γ-ray events (b) as a function of the concentration of nonscintillating n-paraffine in the LAB based scintillator samples. The absolute concentrations of the first and second wavelength shifters PPO and bisMSP were fixed to $3\,\mathrm{g/l}$ and $20\,\mathrm{mg/l}$, respectively. The respective values for the figure of merit and the corresponding errors are given in table 7.2. The individual results and errors for the remaining fraction of neutron events are given in table 7.3.
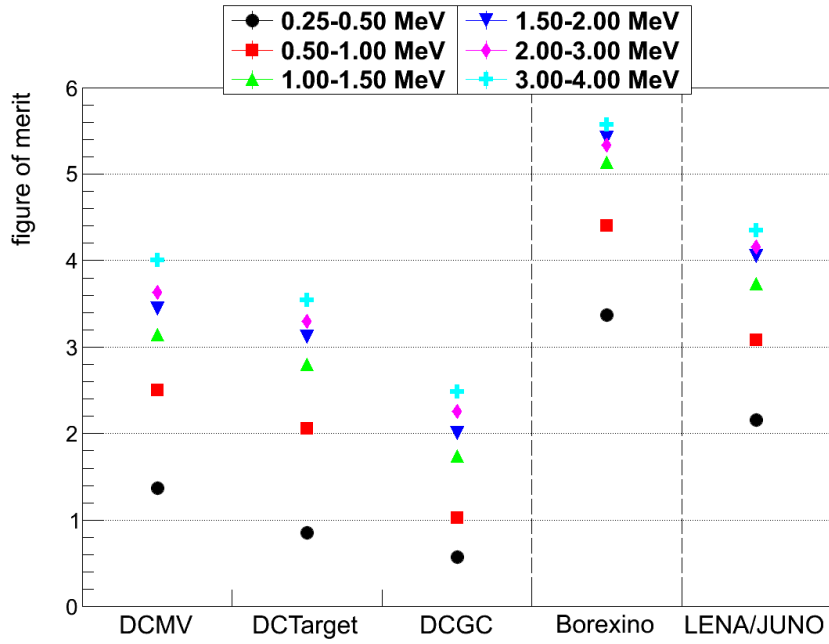
(a) figure of merit
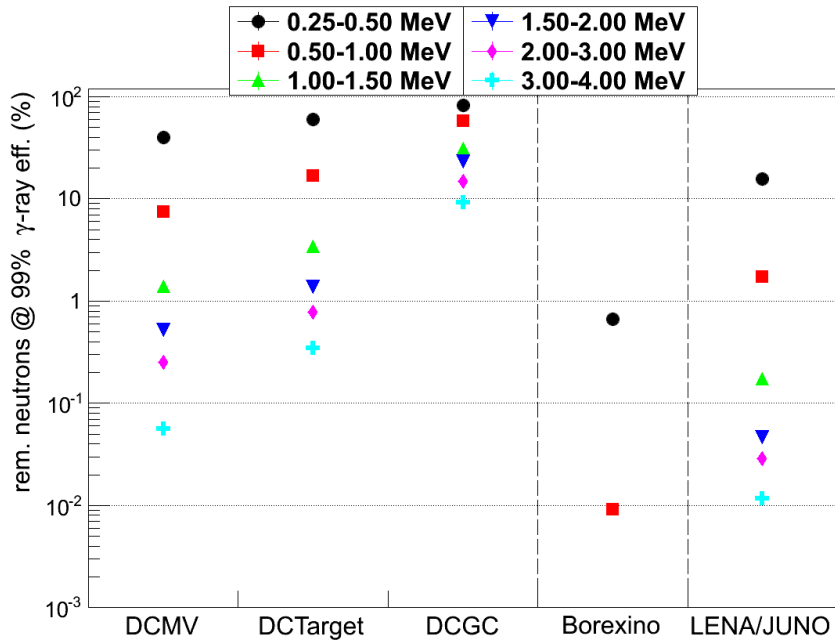
(b) remaining fraction of neutron events

Figure 7.14.: Results on the figure of merit (a) and the remaining fraction of neutron events in case of 99 % selection efficiency for γ-ray events (b) obtained for the scintillators used in the running Double Chooz and Borexino experiment and 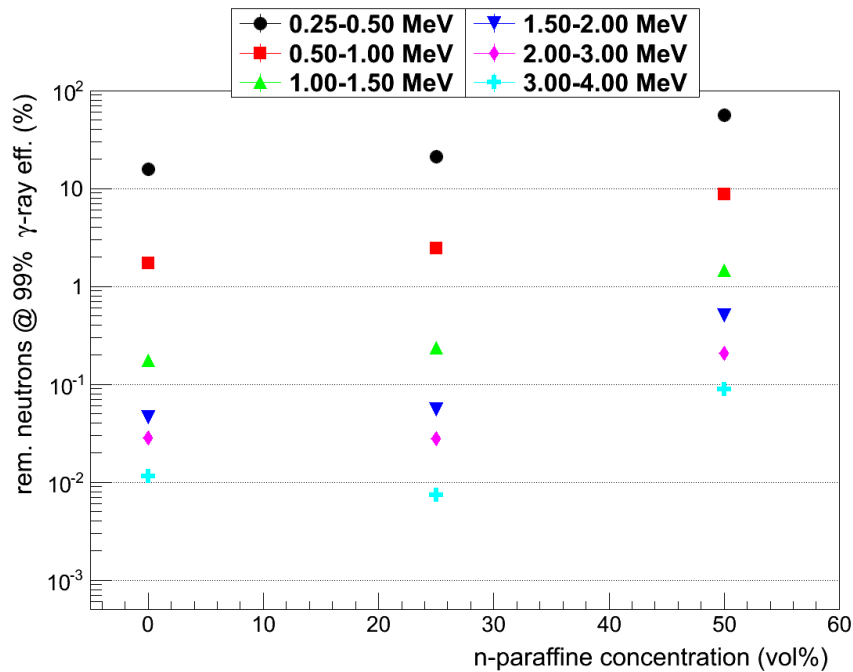for the scintillator favored for the LENA and JUNO projects. The respective values for the figure of merit and the corresponding errors are given in table 7.2. The individual results and errors for the remaining fraction of neutron events are given in table 7.3. The values for the remaining fraction of neutrons obtained for the Borexino scintillator for energies above 1 MeV are to small for the region shown in figure (b).

is about $\sim 65\,\%$ of the central value for the photoelectron yield of 753 ± 214 at $1\,\mathrm{MeV}$, estimated for the detector used in this experiment (see section 5.6). Therefore, the results obtained, for example, for the energy interval between $1.0 - 1.5\,\mathrm{MeV}$ correspond to energies between $\sim 1.5 - 2.3\,\mathrm{MeV}$ in the Borexino detector. Due to scattering of the scintillation photons in the scintillator before detection and a limited spacial reconstruction[4], an additional reduction of the PSD performance in the Borexino detector is expected.

The Double Chooz Scintillators:

The results for the figure of merits and remaining fraction of neutron events at a $99\,\%$ γ-ray selection efficiency obtained for the Double Chooz muon veto scintillator (DCMV-PSD) are similar to those for the 50LAB-50nPar sample (see tables 7.2-7.4), where the results obtained for the DCMV-PSD sample shows a slightly better PSD performance. The compositions of both scintillators (see section 3.4.4) differ mainly in the concentration of PPO, which is $2\,\mathrm{g/l}$ in case of the Double Chooz muon veto scintillator and $3\,\mathrm{g/l}$ in case of the 50LAB-50nPar scintillator. According to this difference, the 50LAB-50nPar sample was expected to show a better PSD performance, due to the higher concentration of PPO (see figure 7.11). The better PSD performance obtained for the DCMV-PSD sample may be explained by a systematic uncertainty, which is suggested by the results obtained for the LAB-3-0 and LAB-3-0(2) samples shown in figure 7.12. Furthermore, the LAB used for the Double Chooz muon veto scintillator originated from a different batch than the LAB, which was used for the different studied LAB-based scintillators. An effect on the PSD performance cannot be excluded.

While the results on the Birks quenching parameter kB obtained for the DCMV and Double Chooz target scintillator (DCTarget) were rather similar (see table 6.4), the results for the PSD performance, shown in figure 7.14, indicate a slightly worse PSD performance of the DCTarget scintillator. This is mainly caused by the fact that the DCTarget scintillator consists mainly of nonscintillating mineral oil (scintillating PXE accounts for only $20\,\mathrm{vol}\%$ of the scintillator (see section 3.4)). As observed for the LAB-based scintillators, which have been diluted with different amounts of nonscintillating n-paraffine (see figure 7.13), the higher concentration of nonscintillating compounds reduces the PSD performance of the scintillator. Additionally, the different solvent has a major influence on the PSD performance [125]. A further cause for the reduced PSD performance is the lower obtained light yield for the DCTarget scintillator compared to the DCMV scintillator, which is indicated by the estimated photoelectron yield, determined as described in section 5.6 and given in table 7.2.

The Double Chooz gamma catcher (DCGC) scintillator features the poorest PSD performance of all investigated scintillators. For energies between $3 - 4\,\mathrm{MeV}$ the fraction of remaining neutron induced events for a $99\,\%$ γ-ray event selection efficiency is still $(9.20 \pm 0.11)\,\%$. As the DCGC scintillator mainly consists of nonscintillating mineral oil

---

[4] The results from the spacial reconstruction is needed in order to correct for the time of flight of the scintillation photons.

and features only $4\,\mathrm{vol}\%$ of scintillating compounds (PXE), the poor PSD performance is expected.

The Double Chooz inner detector, which consists of the neutrino target, the gamma catcher and a nonscintillating transparent buffer (see section 2.1.1), features a photoelectron (p.e.) yield of $\sim 186\,\mathrm{p.e./MeV}$ [42]. In the detector, used in the scope of this thesis, a photoelectron yield of $(402 \pm 17)\,\mathrm{p.e./MeV}$ was achieved for the DCTarget scintillator (see section 5.6). For the DCGC scintillator 424 ± 19 photoelectrons at $1\,\mathrm{MeV}$ were obtained. Both values are compatible within the given uncertainties. They are by a factor ~ 2.2 higher than the photoelectron yield achieved in the Double Chooz detector. Therefore, the PSD performance results obtained for the DCTarget and DCGC samples for example for the energy interval between $1.0 - 1.5\,\mathrm{MeV}$ correspond to energies between $\sim 2.2 - 3.3\,\mathrm{MeV}$ in the Double Chooz detector. In case of the DCTarget scintillator, a good PSD performance for energies above $\sim 1\,\mathrm{MeV}$ should be achievable in Double Chooz. Due to the poorer PSD performance of the DCGC scintillator, which further suffers from the lower photoelectron yield in Double Chooz, the feasibility of applying PSD to events in the Double Chooz gamma catcher seems to be limited. Due to scattering of the scintillation photons in the scintillators and the acrylic vessels before detection and a limited resolution of the spacial reconstruction, an additional reduction of the PSD performance in the Double Chooz detector is expected. Furthermore, the data acquisition time window for the recorded pulses of the Double Chooz detectors is limited to $256\,\mathrm{ns}$ [42], which further reduces the PSD performance due to a smaller possible integration window for the determination of the tail-to-total parameter.

The Favored Scintillator for LENA and JUNO:

The favored scintillator for the proposed LENA detector is LAB with $3\,\mathrm{g/l}$ PPO and $20\,\mathrm{mg/l}$ bisMSB (see section 2.2.1). JUNO favors a similar scintillator with a slightly lower concentration of the second wavelength shifter bisMSB of $15\,\mathrm{mg/l}$ (see section 2.3.1). According to the observed independence of the PSD performance from the bisMSB concentration in LAB-based scintillators (see figure 7.12 and discussion in section 7.3.1), the slightly lower concentration of bisMSB should have no major effect on the PSD performance. The results obtained for the LAB-3-20(2) sample show a good PSD performance in the whole energy region. According to the results shown in figure 7.8, the rejection of neutron or γ-ray induced events at lower energies can efficiently be improved by reducing the selection efficiency for the respective other particle type.

A photoelectron yield of at least $200\,\mathrm{p.e./MeV}$ is envisaged to be achieved in the LENA detector [18], which is about $32\,\%$ of the photoelectron yield of 628 ± 40 at $1\,\mathrm{MeV}$, which was obtained for the LAB-3-20(2) sample with the detector used in the scope of this thesis (see section 4.2.1). Therefore, the results for the PSD performance, obtained for example for the energy interval between $1.0 - 1.5\,\mathrm{MeV}$, correspond to energies of $\sim 3.1 - 4.7\,\mathrm{MeV}$ in the LENA detector. JUNO aims for a photoelectron yield of $1200\,\mathrm{p.e./MeV}$ in order to reach a good enough energy resolution to be sensitive to the mass hierarchy

(see section 2.3). This photoelectron yield would be a factor of ~ 1.9 higher than that obtained for the LAB-3-20(2) sample in the detector used in the scope of this thesis. Hence, the results, obtained for the PSD performance for energies between $1.0 - 1.5\,\mathrm{MeV}$, apply to energies between $0.53 - 0.79\,\mathrm{MeV}$ in the JUNO detector. Due to the enormous sizes of both the LENA and JUNO detector, a worsening of the PSD performance due to scattering of the scintillation photons to some degree is expected. Furthermore, the resolution of the spacial reconstructions, achieved for each detector, has a negative effect on the PSD performance.

7.3.3. Comparison to Results From Earlier Measurements

The results obtained for the LAB-3-20(2) scintillator in the scope of this thesis show a significantly better PSD performance than those obtained by Jürgen Winter, who analyzed the data from a beam time performed in August 2012 [100], using almost the same experimental setup as described in chapter 4. An analysis using a similar tail-to-total parameter resulted in a rejection efficiency of $(98.3 \pm 14.8)\,\%$ for neutron events for a selection efficiency for γ-ray events of $90\,\%$ for events between $1.0 - 1.5\,\mathrm{MeV}$ in LAB with $3\,\mathrm{g/l}$ PPO and $20\,\mathrm{mg/l}$ bisMSB (labeled as LH3 in [100]). The result for the corresponding LAB-3-20(2) sample, investigated in the scope of this thesis, features a $(99.9886 \pm 0.0006)\,\%$ neutron rejection at a γ-ray selection efficiency of $90\,\%$, where the error corresponds to the statistical uncertainty. The origin of the large uncertainties given in [100] is not known, but the errors seem to be overestimated. The large errors can be explained only to a small part by the reduced statistics in the beam time analyzed in [100]. Nevertheless, the difference in the central value can be attributed to a wrongly used $1\,\mathrm{M\Omega}$ load resistance for the PMT signal, which was also used in the September 2013 beam time performed in the scope of this thesis (see section 4.5.1). This load resistance dominated the slow decay of the recorded pulses and, therefore, caused a negative effect on the PSD performance. Furthermore, the upper boundary for both the tail and the total integrals (see equation (7.2)) was limited to $220\,\mathrm{ns}$ after the pulse onset due to a reflection caused by the $1\,\mathrm{M\Omega}$ load resistance. This is significantly smaller than the $350\,\mathrm{ns}$ after the pulse maximum used in this analysis (see equation (7.2)) and also has a negative impact on the PSD performance. Comparing the results for the PSD performance for other equal scintillator mixtures, which have been studied in [100] and in the scope of this thesis, a similar behavior of the obtained values is observed.

Additionally, in [100] a combined PSD analysis, based on the tail-to-total method and the so-called Gatti method, was presented. The Gatti method is based on the comparison of the measured pulses with mean pulses for each type of ionizing particles [126] and typically features a slightly better PSD performance compared to the tail-to-total method. The combined analysis described in [100] gives significantly improved PSD results in comparison to both individual analyses, using only either the tail-to-total parameter or the Gatti method. The neutron rejection efficiency at $90\,\%$ γ-ray selection efficiency was found to be $99.98^{+0.2}_{-0.3}\,\%$, which is much closer to the result of $(99.9886 \pm 0.0006)\,\%$ obtained in the analysis described in this thesis and which is based on only the tail-to-total method.

7.3.4. Outlook

The excellent results for the PSD performance for neutron and γ-ray induced events obtained for the different scintillators samples, which have been studied in the scope of this thesis, show the huge potential of PSD in organic liquid scintillator based neutrino detectors. To determine the feasibility and power of PSD in future experiments like LENA and JUNO the decay times and corresponding amplitudes (see equation 3.11) are needed as an input for the detector simulations. These decay times and corresponding amplitudes can be obtained by a fit to the mean pulses derived from the pulses recorded in the measurements at the MLL as presented in this thesis. In [100] the pulse shapes of the scintillators, investigated in an earlier beam time at the MLL in August 2012, were determined from the recorded pulses. Unfortunately, the results were biased by a wrongly used load resistance of $1\,\mathrm{M\Omega}$, which was also used during the beam time in September 2013 performed in the scope of this thesis.

The sensitivity study for the detection of the diffuse supernova neutrino background (DSNB) with the LENA experiment, summarized in section 2.2.4 and described in [101, 102], is based on the results for the pulse shape of the favored LENA scintillator (LAB with $3\,\mathrm{g/l}$ PPO and $20\,\mathrm{mg/l}$ bisMSB) presented in [100]. The results for the pulse shape obtained in [100] were used in the simulation of the LENA detector, which was used to study the sensitivity for the detection of the DSNB with LENA. Therefore, this study is affected by the bias due to the wrongly used $1\,\mathrm{M\Omega}$ load resistance for the PMT signal. Hence, a similar analysis of the data recorded for the LAB-3-20(2) sample in the February 2014 beam time has to be performed. According to the better PSD performance obtained from the analysis of data recorded for the LAB-3-20(2) sample in February 2014 compared to those obtained for the corresponding scintillator in [100], an improvement of the PSD performance of the LENA detector and, therefore, an increased sensitivity for the detection of the DSNB is expected. The estimation of the sensitivity of JUNO for the detection of the DSNB is based on the study performed for LENA (see section 2.3.2). Therefore, also an improvement of the sensitivity for the detection of the DSNB with JUNO is expected.

The determination of the scintillation pulse shape parameters from mean pulses, derived from the recorded pulses as described in [100], is always affected by electronic features. Especially electronic effects, which are somehow correlated to the onset or the maximum of the measured pulses cause systematic uncertainties on the determined decay times and amplitudes. This can also be seen in figure 7.2, which shows mean pulses for neutron and γ-ray induced events, derived from data recorded for the LAB-3-20(2) sample in the February 2014 beam time. Therefore, a setup, which features a reduced susceptibility to electronic features would be favorable in order to determine the scintillation decay times and corresponding amplitudes. This can be achieved by a coincidence setup with two PMTs, where one PMT is placed close to the scintillator to detect as many scintillation photons as possible, while the second PMT is placed far enough from the scintillator to detect at most one photon in each event[5]. The near PMT provides a start signal (and an

---

[5] Alternatively, neutral grey filters can be used to reduce the scintillation light reaching the second PMT.

energy measurement) and the second PMT a stop signal for each event. Thus, the resulting spectrum for the start time differences of the signals from both PMTs provides a measurement of the scintillation pulse shape. Such experimental setups are, for example, described in [124] and [125]. Furthermore, it would be possible to perform such an experiment in a beam time at the MLL without interfering with the quenching measurements as described in this thesis. Thus, the efficient background reduction by the time of flight technique can be utilized to measure the scintillation pulse shapes for γ-ray and neutron induced events in liquid scintillators.

8. Summary and Outlook

Organic liquid scintillators are a widely-used detection medium in neutrino experiments, like the running Double Chooz and Borexino experiments or the planned 20 kt JUNO and proposed 50 kt LENA detectors. In this work the response of organic liquid scintillators to neutron induced proton recoils was investigated. Two characteristic features of liquid scintillators were addressed: Firstly, the effect of ionization quenching on the light yield for protons was studied. Ionization quenching causes a nonlinear behavior of the light output with respect to the amount of energy deposited by an ionizing particle in the scintillator. The strength of the quenching effect depends on the energy loss, which varies for different kinds of particles at a given energy. Secondly, organic liquid scintillators feature a particle and energy dependent scintillation pulse shape with respect to the emission time of the scintillation photons. The difference in the scintillation pulse shapes can be used for pulse shape discrimination (PSD) in order to identify events due to different types of particles on an event-by-event basis.

In organic liquid scintillator based neutrino experiments, protons scattered off by fast neutrons pose a major background for the detection of electron antineutrinos via the inverse β-decay (IBD). The IBD reaction results in a characteristic delayed coincidence signal, which can perfectly be mimicked by interactions of fast neutrons in the scintillator. Fast neutrons originate from muon spallation in the rocks surrounding the detectors, (α, n)-reactions in the scintillators or neutral current (NC) interactions of atmospheric neutrinos on ^{12}C.

In case of the reactor neutrino experiment Double Chooz, PSD can help to determine the shape and rate of the background due to fast neutrons, which are mainly produced by muon spallation in the rock surrounding the detectors. In next generation large scale neutrino detectors, like JUNO and LENA, fast neutrons due to NC interactions of atmospheric neutrinos on ^{12}C pose the major background for the detection of the so-called diffuse supernova neutrino background (DSNB). The DSNB is the cumulative flux of neutrinos from all core collapse supernovae, which appeared in the causal universe up to now. As the NC background surpasses the signal of electron antineutrinos from the DSNB, the detection of the DSNB is only possible with a good background rejection by PSD [101, 102].

One of the major physics goals of the next generation JUNO and LENA neutrino experiments is the detection of neutrinos from a galactic core collapse supernova (SN) with high statistics. A major detection channel for SN neutrinos of all flavors is elastic neutrino-proton (ν-p) scattering. As neutrino detectors are calibrated for electron-like events, the knowledge of the response of the scintillator to protons, i.e. the quenching effect for protons, is mandatory. It needs to be quantified to reconstruct the energy scale of the recoil

protons correctly. Additionally, the knowledge of the quenching effect is an important input to the detector simulation, which can be used to estimate the expected SN neutrino signal rate in the elastic ν-p scattering channel. Another important channel for the detection of SN neutrinos is elastic neutrino-electron (ν-e) scattering. An excellent PSD performance of the scintillator used in the detector is needed to disentangle the ν-e and ν-p scattering detection channels and to discriminate the ν-p scattering events from background events due to ^{12}C-decays at low energies.

To study the quenching effect for protons and the PSD performance for neutron and γ-ray induced events, a small scale liquid scintillator experiment (~ 120 ml) was performed at the neutron scattering facility at the Maier-Leibnitz-Laboratorium (MLL) in Garching. A pulsed beam of ^{11}B ions was used to produce monoenergetic neutrons by the nuclear reaction p(^{11}B, n)^{11}C . Depending on the scattering angle, neutron energies between ~ 4.7 MeV and ~ 11.2 MeV could be accessed in order to study neutron induced proton recoils. To obtain different incident neutron energies, the detector was placed at up to ten different positions with respect to the beam axis. Using a pulsed beam with a bunch width of $\lesssim 3$ ns (FWHM) allows the determination of the time of flight (ToF) between the particle production and the detection in the scintillator. On the one hand, this provides an efficient separation of events induced by neutrons and γ-rays produced in the beam target. On the other hand, the ToF measurement can be used to determine the kinetic energy of the incident neutrons.

A total of 15 different organic liquid scintillators were investigated in three beam times in September 2013, February 2014 and May/June 2014. The studies included the scintillators used in the currently running neutrino experiments Double Chooz and Borexino as well as the favored scintillators for the planned JUNO and proposed LENA detectors. Additionally, eleven different *linear alkylbenzene* (LAB) based scintillators were investigated: Different concentrations of the primary wavelength shifter *2,5-diphenyloxazole* (PPO) between 1 g/l and 9 g/l and of the secondary fluor *1,4-bis(2-methylstyryl)benzene* (bisMSB) of $0-80$ mg/l were studied. Furthermore, the impact of the dilution with different amounts of transparent nonscintillating *n-paraffine* between $0-50$ vol % was examined. Especially the huge variety of the different LAB-based scintillator mixtures, which were investigated with regard to the response to protons and PSD of γ-ray and neutron induced events, is to our knowledge unprecedented.

An energy calibration of the detector for each investigated scintillator was performed, using calibration sources providing γ-rays with energies ranging from 511 keV to 4.4 MeV. It was found that the recorded Compton spectra are distorted by events, in which the calibration γ-rays scatter multiple times in the scintillator [143]. This complicates the reconstruction of the position of the Compton edge from the measured spectra. Therefore, a reconstruction method was developed, which reliably determines the Compton edge position with a precision of few percent. It uses the data from a Monte Carlo simulation of the detector setup, based on the GEANT4 simulation framework [159, 160]. A reliable determination of the Compton edge position from the measured calibration spectra was found to be a crucial requirement for a reproducible determination of the quenching effect for protons. To

obtain a conversion from the charge of each recorded photomultiplier pulse to the visible energy deposited by the Compton electrons in the scintillator, the data obtained from the Compton edge position reconstruction were fitted with a linear relation. As the result from the reconstructed Compton edge position, obtained for the 4.4 MeV γ-rays from an AmBe-source, features a slight deviation from a linear relation, the data set was additionally fitted using a quadratic function. The observed discrepancy may be explained by pile up events, but is not fully understood. Therefore, the analysis of the data with respect to the quenching effect for protons was performed using the results for each of both calibration functions.

Quenching Effect for Protons

The determination of the strength of the quenching effect for protons in the investigated scintillators is based on the semi-empiric Birks model [117]. It predicts the light output for a given deposited energy in dependence of the energy loss of the particle along its track. The influence of the energy loss, i.e. the strength of the quenching effect, is thereby parameterized by the Birks-factor kB. In order to determine kB for each scintillator, the maximum energy deposited by the recoil protons in the scintillator and the corresponding visible energy (calibrated with Compton electrons) need to be determined from the data recorded for each scintillator at different incident neutron energies.

The maximum deposited energy of neutron induced recoil protons in the scintillator is approximately equal to the energy of the incident neutrons. In order to reconstruct the neutron energy, each measured ToF spectrum was fitted by an empirical model, which describes the contributions from events due to γ-rays and neutrons produced in the beam target as well as backgrounds due to accidental coincidences and scattered neutrons. In the model used a Gaussian shaped energy distribution of the neutrons at each detector position was assumed. Neutron induced proton recoil events were selected from the respective measurement by a cut on the ToF, based on the results from the fit to the ToF spectrum. To obtain the distribution for the visible energy of the proton recoil events, the energy calibration was applied to the data. The maximum visible recoil energy, corresponding to the maximum deposited energy of the protons in the scintillator, was reconstructed by a fit to the proton recoil energy spectrum.

In order to determine the Birks-factor kB for each of the investigated scintillators, the obtained maximum visible proton recoil energy as a function of the incident neutron energy was fitted with the prediction from the Birks model. The predictions agree well with the data.

Table 8.1 summarizes the obtained results on kB for the scintillators used in the running Double Chooz and Borexino experiments and the favored scintillator for the next generation JUNO and LENA experiments. From the results obtained for LAB-based scintillators with a fixed concentration of the secondary wavelength shifter bisMSB of 20 mg/l and varying concentrations of the primary fluor PPO from $1 - 9$ g/l, a clear increase of the quenching effect for protons was observed for decreasing PPO concentrations below ~ 3 g/l. For PPO concentrations above ~ 3 g/l no significant change of the quenching effect with increasing

experiment	Results for kB $\left(\frac{cm}{MeV}\right)$:		scintillator
	linear calibration	quadratic calibration	
Double Chooz	$0.0127^{+0.0005}_{-0.0006}$	0.0132 ± 0.0009	muon veto
	0.0122 ± 0.0006	0.0133 ± 0.0012	target
	0.0149 ± 0.0007	0.0160 ± 0.0012	gamma catcher
Borexino	0.0101 ± 0.0006	0.0112 ± 0.0012	target
LENA / JUNO	0.0098 ± 0.0005	0.0110 ± 0.0011	target

Table 8.1.: Summarized results on the Birks-factor kB for the scintillators used in the running Double Chooz and Borexino experiments and favored for the LENA and JUNO projects.

PPO concentration was found. The observed behavior for different PPO concentrations can be explained by the transfer of excitation energy from LAB to PPO, which seems to saturate at a concentration around $4\,\mathrm{g/l}$ [171]. No significant impact on the quenching effect was found for different bisMSB concentrations of $0-80\,\mathrm{mg/l}$ in LAB-based scintillators with a fixed concentration of PPO of $3\,\mathrm{g/l}$. This observation implies that the processes, contributing to the quenching effect, predominantly take place either in the LAB or in the energy transfer from LAB to PPO. Furthermore, the results for LAB-based scintillators, which were diluted with different amounts of transparent nonscintillating n-paraffine of $0-50\,\mathrm{vol\%}$, while fixing the absolute concentrations of PPO and bisMSB to $3\,\mathrm{g/l}$ and $20\,\mathrm{mg/l}$, respectively, show a clear increase of the quenching effect for increasing dilution with n-paraffine. This can be explained by an inhibited energy transfer from LAB to PPO, caused by the presence of nonscintillating molecules. An absolute interpretation of the results for different concentrations of n-paraffine is not possible, as the density decreases for an increasing amount of admixed n-paraffine. A reduced density results in an accordingly decreased energy loss.

The results for the unprecedented variety of studied LAB-based scintillator mixtures, featuring different concentrations of PPO, bisMSB and nonscintillating n-paraffine, helps to consolidate our understanding of the scintillation processes in multicomponent organic liquid scintillators.

The result for the Birks-factor kB, obtained for different LAB-based scintillator mixtures in this work (using linear calibration), are in good agreement with the results for the respective scintillators from independent measurements performed by a group from Dresden at the Physikalisch-Technische Bundesanstalt [172]. This suggests that both experiments, and particularly the measurement described in this work, give reliable results on the Birks-factor kB for protons.

PSD Performance

The ToF setup at the neutron scattering facility at the MLL provides an excellent environment to study the PSD performance of organic liquid scintillators. Using the ToF information, background reduced datasets of events caused either by γ-rays or neutrons from the beam interactions can be selected. As the pulse shape mainly differs in the relative intensity of the slow decay component of the scintillation light emission, the so-called tail-to-total method was used to parameterize the difference between the pulse shapes for γ-ray and neutron induced events. A wrong load resistance of $1\,\text{M}\Omega$, which was used during the beam time in September 2013, resulted in a negative impact on the PSD performance [100]. Therefore, only the data recorded in the two 2014 beam times was analyzed with respect to the PSD performance. For the scintillators, which were studied during the September 2013 beam time, additional data with regard to PSD performance studies were recorded during the May/June 2014 beam time.

The dataset, recorded for each scintillator sample, was divided into different visible energy intervals between $0.25\,\text{MeV}$ and $4.00\,\text{MeV}$, reconstructed using the respective linear calibration. For each energy interval, different PSD performance parameters have been extracted from the distribution of the tail-to-total parameter. One of the parameters used is the remaining fraction of neutron events for a given selection efficiency for γ-ray events of $99\,\%$. The results for this parameter, obtained for the scintillators used in the currently running Double Chooz and Borexino experiments and for the scintillator favored for the planned JUNO and proposed LENA detectors, are summarized in table 8.2 for visible energies between $1.0 - 1.5\,\text{MeV}$. The Borexino scintillator features by far the best PSD performance of all investigated scintillator samples. The Double Chooz gamma catcher scintillator features the poorest performance, which is mainly caused by the fact that it consists predominantly of mineral oil and only to $4\,\text{vol}\%$ of scintillating *phenyl-o-xylylethane* (PXE).

The investigated LAB-based scintillators generally feature excellent PSD capabilities. However, a decreasing PSD performance was observed for LAB-based scintillators with decreasing PPO concentrations below $\sim 5\,\text{g/l}$ (fixed bisMSB concentration of $20\,\text{mg/l}$). At higher PPO concentrations above $\sim 5\,\text{g/l}$ the PSD performance was found to saturate. This behavior can again be explained by the saturating energy transfer from LAB to PPO around $4\,\text{g/l}$ [171]. The concentration of the secondary wavelength shifter bisMSB was found to have no significant effect on the PSD performance. The results for the LAB-based scintillator samples, which have been diluted with different amounts of nonscintillating n-paraffine, show a decreasing PSD performance with increasing amount of n-paraffine. This can mainly be attributed to the accordingly decreasing light yield.

To compare the PSD performance results for the different scintillators, the photoelectron (p.e.) yield per unit energy was estimated from the calibration data. Additionally, this allows a first order estimation of the PSD performance for large scale neutrino detectors. The p.e. yield was found to be between $\sim 400\,\text{p.e./MeV}$ for the Double Chooz target and gamma catcher scintillators and $\sim 750\,\text{p.e./MeV}$ for the Borexino scintillator. For the different LAB-based scintillators, which have not been diluted with n-paraffine, p.e. yields around $\sim 600\,\text{p.e./MeV}$ were obtained.

experiment	remaining neutrons 1.0 − 1.5 MeV	photoel. yield (p.e. / MeV)	scintillator
Double Chooz	$(1.41 \pm 0.07)\,\%$	503 ± 24	muon veto
	$(3.43 \pm 0.07)\,\%$	402 ± 17	target
	$(31.4 \pm 0.4)\,\%$	424 ± 19	gamma catcher
Borexino	$(0.000214 \pm 0.000017)\,\%$	753 ± 214	target
LENA / JUNO	$(0.175 \pm 0.006)\,\%$	628 ± 40	target

Table 8.2.: Results on the remaining fraction of neutron events for a selection efficiency of $99\,\%$ for γ-ray events for visible energies between $1.0 - 1.5\,\mathrm{MeV}$. For comparability of the results, the estimated photoelectron yields per unit energy are given.

In large scale detectors, effects due to the photon propagation and the limited resolution of the spatial reconstruction have to be taken into account. Both deteriorate the PSD performance. To study the impact of these effects on the feasibility of PSD in future neutrino detectors like LENA and JUNO, the scintillation pulse shape is required as an input to the detector simulation. The pulse shape can be described by the sum of multiple decay times and corresponding amplitudes, which have to be determined experimentally. This can be achieved by fits to the average pulses for each particle type, which can be determined from the individual pulses recorded with the described setup at the MLL [100]. A more precise approach would be a coincidence setup with an additional PMT. Adjusting the additional PMT in such a way that it detects at most one scintillation photon in each event, the probability density function for the scintillation photon emission can be precisely sampled [124, 125]. Such a setup would be less affected by electronic influences compared to the approach of fitting average pulses. Furthermore, it could be operated in a beam time at the MLL without affecting the quenching measurements as described in this work. The combination of both measurements would provide a unique possibility to study several key parameters of organic liquid scintillators simultaneously.

A. Negative-Ion Source at the MLL

The MLL provides a negative-ion injector, which allows for the production of negative ions for a wide range of elements and isotopes [141]. In figure A.1 the working principle of the ion source is illustrated: Caesium is heated and thereby evaporated onto the ionizer and the cone shaped solid source containing ^{11}B. The ionizer is heated to about $1400\,°$C by applying a heating voltage U_{heat} to produce Cs ions. Those are sputtered onto the source, where they may knock out ^{11}B atoms. Passing the Cs layers covering the source the ^{11}B atoms may gather an additional electron from the less electronegative Cs to be extracted and preaccelerated by a positive extraction voltage U_{ext}.

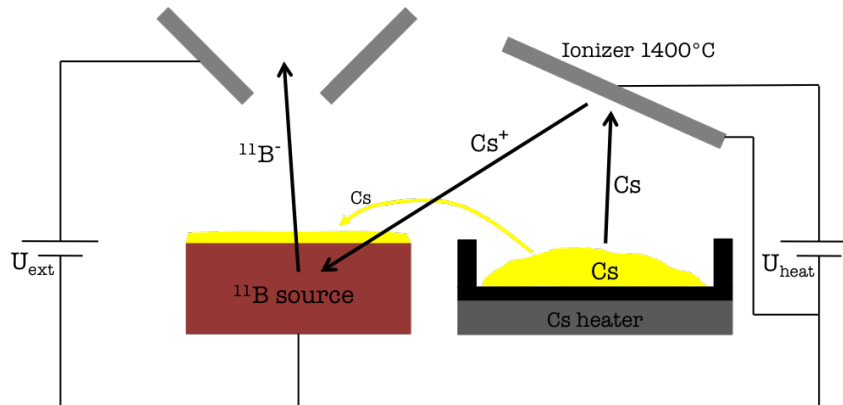**Figure A.1.:** Schematic working principle of the negative-ion source at the MLL [141]. Caesium is heated to ionize evaporated Cs atoms, which are sputtered onto the source, where ^{11}B atoms are knocked out. Those gather an electron from the less electronegative Cs, when crossing evaporated Cs layers covering the source. The negative ^{11}B ions are then extracted by an extraction voltage U_{ext}.

B. Calibration

B.1. Error on Pearson's χ^2

The gain correction analysis described in section 5.7 is based on the comparison of ^{22}Na-spectra measured at each detector position (see section 4.2.2) with a comparison spectrum, for which the corresponding spectrum measured for energy calibration is used. To compare the spectra Pearson's χ^2-test was used (see equation (5.22)), which suffers from statistical fluctuations. Therefore, the figure of merit determined by equation (5.22) has a statistical error, which is determined as described in the following. As equation (5.22) can be written as [174]

$$\chi^2 = \sum_{i=1}^{N_{\text{bins}}} \chi_i^2 \quad \text{with} \quad \chi_i^2 = \frac{(N_{\text{r}}\, n_{\text{c},i} - N_{\text{c}}\, n_{\text{r},i})^2}{N_{\text{r}}\, N_{\text{c}}\, (n_{\text{r},i} + n_{\text{c},i})} \ , \tag{B.1}$$

the error on χ^2 can then be determined by

$$\Delta\chi^2 = \sqrt{\sum_{i=1}^{N_{\text{bins}}} (\Delta\chi_i^2)^2} \ . \tag{B.2}$$

$\Delta\chi_i^2$ can then be determined by

$$\Delta\chi_i^2 = \sqrt{\left(\Delta N_{\text{r}} \frac{\partial \chi_i^2}{\partial N_{\text{r}}}\right)^2 + \left(\Delta N_{\text{c}} \frac{\partial \chi_i^2}{\partial N_{\text{c}}}\right)^2 + \left(\Delta n_{\text{r},i} \frac{\partial \chi_i^2}{\partial n_{\text{r},i}}\right)^2 + \left(\Delta n_{\text{c},i} \frac{\partial \chi_i^2}{\partial n_{\text{c},i}}\right)^2} \ . \tag{B.3}$$

Assuming Poisson distributed bin entries $n_{\text{r},i}$ and $n_{\text{c},i}$ and histogram entries N_{r} and N_{c}, the errors are given by

$$\Delta N_{\text{r}} = \sqrt{N_{\text{r}}} \ , \ \ \Delta N_{\text{c}} = \sqrt{N_{\text{c}}} \ , \ \ \Delta n_{\text{r},i} = \sqrt{n_{\text{r},i}} \ \text{ and } \ \Delta n_{\text{c},i} = \sqrt{n_{\text{c},i}} \ . \tag{B.4}$$

B.2. Taken Calibration Data

The number of events recorded with each of the used γ-ray calibration sources (see table 5.1) for the different investigated scintillator samples are given in table B.1 along with the detector position, at which the energy calibration was performed.

	sample	calib.@	^{22}Na (low)	^{22}Na (high)	^{137}Cs	^{228}Th	AmBe
Sept. 2013	DCMV	Pos0	2×200k	200k	200k	2×200k	3×200k
	LAB-3-20	Pos1	200k	"	"	200k	200k
	Borexino	Pos0	"	"	"	"	"
	LAB-5-20	"	"	"	"	"	"
	LAB-3-40	"	"	"	"	"	"
Feb. 2014	LAB-3-20(2)	Pos0	200k	200k	200k	200k	200k
	DCTarget	"	"	"	"	"	"
	LAB-3-10	"	"	"	"	"	"
	LAB-3-0	"	"	"	"	"	"
	LAB-7-20	"	"	"	"	"	"
	LAB-9-20	"	"	"	"	"	"
	LAB-3-80	"	"	"	"	"	"
May/June 2014	50LAB-50nPar	Pos0	200k	200k	200k	200k	200k + 70k
	LAB-1-20	"	"	"	"	"	300k + 400k
	DCMV-PSD	"	"	"	"	"	300k
	DCGC	"	"	"	"	"	"
	LAB-5-20-PSD	"	"	"	"	"	400k
	75LAB-25nPar	"	"	"	"	"	350k
	LAB-3-40-PSD	Pos1	"	"	"	"	400k
	Borexino(2)	Pos0	"	"	"	"	300k
	LAB-3-0(2)	Pos-1	"	"	"	"	400k

Table B.1.: Taken statistics with the different calibration sources for each investigated scintillator sample. Additionally, the respective detector positions, at which the calibration measurements were performed, are given. Several calibration runs with different sources were taken for the DCMV scintillator, caused by problems with the accelerator in the first days of the September 2013 beam time. The increased statistics for the AmBe-calibrations in the May/June 2014 beam time were taken to compensate for the lowered threshold and more available time. The annotations *low* and *high* given for ^{22}Na correspond to the two different used trigger thresholds. See section 4.5 for scintillator sample nomenclatures.

B.3. Simulated Data

The numbers of events simulated with the GEANT4-based setup described in section 5.3 for each calibration source and the corresponding position of the sources center with respect to the detector front are given in table B.2. The simulated data was used to reconstruct the position of the Compton edge from the measured calibration spectra as described in section 5.4.

source type	position	simulated events	efficiency
^{137}Cs	3.25 cm	10^8	$\sim 2.4\,\%$
^{22}Na	3.25 cm	10^8	$\sim 7.4\,\%$
^{228}Th	3.25 cm	$1.5 \cdot 10^8$	$\sim 5.4\,\%$
AmBe	11.1 cm	10^9	$\sim 0.3\,\%$
	13.6 cm	$1.5 \cdot 10^9$	$\sim 0.2\,\%$

Table B.2.: The number of simulated events for each calibration source at the respective position to the detector. The given efficiencies indicate the approximate fraction of simulated events causing an energy deposition in the scintillator. This efficiency varies slightly for the different simulated scintillator samples given in table 5.2, which is caused by the different densities and hydrogen-to-carbon ratios.

B.4. Results for Energy Calibration with γ-ray Sources

The results from the fits of a linear and a quadratic function (see section 5.5) to the data obtained from the reconstruction of the Compton edges from the measured calibration spectra as described in section 5.4 are given in table B.3 for all investigated scintillator samples (see section 3.4.4 and 4.5).

B.5. Results for the Gain Correction Factors f_{corr}

The gain correction factors f_{corr}, which were determined using the data from ^{22}Na calibration measurements performed for each scintillator (see sections 3.4.4 and 4.5) at each used detector position (see section 4.2.2) as described in section 5.7, are given in tables B.4-B.6.

scintillator sample	linear fit: $E_{vis}(Q) = m \cdot Q + t$		quadratic fit: $E_{vis}(Q) = a \cdot Q^2 + b \cdot Q + c$		
	m $\left(\frac{keV}{mVns}\right)$	t (keV)	a $\left(10^{-6}\frac{keV}{(mVns)^2}\right)$	b $\left(\frac{keV}{mVns}\right)$	c (keV)
Sept. 2013					
DCMV	0.613 ± 0.007	38.6 ± 4.4	-5.3 ± 3.0	0.637 ± 0.016	27.0 ± 8.3
LAB-3-20	0.492 ± 0.007	32.9 ± 6.3	-4.4 ± 2.6	0.513 ± 0.015	19.8 ± 10.6
Borexino	0.676 ± 0.010	31.1 ± 6.3	-10.0 ± 4.8	0.711 ± 0.020	15.3 ± 10.2
LAB-5-20	0.615 ± 0.009	31.6 ± 6.3	-8.2 ± 4.0	0.646 ± 0.019	15.8 ± 10.5
LAB-3-40	0.498 ± 0.007	33.9 ± 6.3	-4.7 ± 2.7	0.520 ± 0.015	20.4 ± 10.5
Feb. 2014					
LAB-3-20(2)	0.687 ± 0.010	39.4 ± 6.2	-16.8 ± 4.2	0.745 ± 0.019	14.1 ± 9.5
DCTarget	0.871 ± 0.013	44.7 ± 6.0	-21.8 ± 7.4	0.929 ± 0.025	25.0 ± 9.7
LAB-3-10	0.662 ± 0.010	38.8 ± 6.1	-11.8 ± 4.4	0.704 ± 0.020	19.9 ± 10.0
LAB-3-0	0.752 ± 0.011	28.3 ± 6.4	-13.8 ± 5.8	0.796 ± 0.023	10.2 ± 10.5
LAB-7-20	0.830 ± 0.012	36.0 ± 6.2	-15.8 ± 7.1	0.874 ± 0.025	19.6 ± 10.1
LAB-9-20	0.925 ± 0.013	35.6 ± 6.2	-18.2 ± 8.9	0.971 ± 0.028	20.4 ± 10.2
LAB-3-80	0.754 ± 0.011	35.8 ± 6.2	-14.0 ± 5.8	0.798 ± 0.022	18.4 ± 10.1
May/June 2014					
50LAB-50nPar	0.846 ± 0.011	40.1 ± 5.8	-15.7 ± 6.2	0.896 ± 0.024	22.2 ± 9.7
LAB-1-20	0.667 ± 0.009	39.7 ± 5.7	-9.2 ± 3.9	0.703 ± 0.019	22.6 ± 9.7
DCMV-PSD	0.691 ± 0.010	39.6 ± 6.1	-10.7 ± 4.9	0.727 ± 0.020	24.0 ± 10.0
DCGC	0.760 ± 0.011	46.7 ± 6.0	-15.2 ± 5.7	0.806 ± 0.022	28.6 ± 9.7
LAB-5-20-PSD	0.833 ± 0.012	36.1 ± 6.2	-16.1 ± 7.1	0.879 ± 0.025	19.4 ± 10.2
75LAB-25nPar	0.683 ± 0.010	32.9 ± 6.3	-11.2 ± 4.7	0.722 ± 0.020	15.4 ± 10.3
LAB-3-40-PSD	0.781 ± 0.011	32.9 ± 6.2	-12.3 ± 6.5	0.819 ± 0.024	18.3 ± 10.4
Borexino(2)	0.893 ± 0.013	26.0 ± 6.4	-17.5 ± 8.1	0.940 ± 0.027	9.5 ± 10.6
LAB-3-0(2)	0.770 ± 0.011	35.7 ± 6.2	-12.2 ± 6.1	0.807 ± 0.023	20.9 ± 10.2

Table B.3.: Results for the energy calibration fits for all investigated scintillator samples in three performed beam times in 2013 and 2014. The calibration data, obtained from the Compton edge position reconstruction (see section 5.4.1) from the measured spectra and the theoretical Compton edge energies (see table 5.1), were fitted with a linear and a quadratic function, respectively (see sections 5.5.1 and 5.5.2). The values for the parameters are given with 1σ errors from the fit.

sample	DCMV	LAB-3-20	Borexino	LAB-5-20	LAB-3-40
ref. spec. @	Pos0	Pos1	Pos0	Pos0	Pos0
Pos-1	-	-	1.0202(6)	-	-
Pos0	1.0215(7)	1.0363(7)	0.9784(6)	0.9868(6)	1.0378(6)
Pos1	1.0369(7)	1	1.0003(6)	0.9980(6)	-
Pos2	1.0364(7)	1.0253(6)	0.9859(6)	0.9909(6)	1.0276(6)
Pos3	1.0307(7)	1.0263(7)	1.0002(6)	0.9990(6)	1.0090(7)
Pos4	1.0361(7)	1.0269(6)	0.9774(6)	0.9874(6)	1.0372(6)
Pos5	1.0289(7)	1.0233(7)	0.9888(6)	0.9892(6)	0.9760(6)
Pos6	1.0259(7)	0.9903(7)	0.9882(6)	0.9901(6)	0.9800(7)
Pos7	1.0350(7)	0.9392(6)	0.9844(6)	0.9888(6)	1.0265(6)
Pos8	-	-	1.0016(6)	-	-

Table B.4.: The gain correction factors obtained as described in section 5.7 for the measurements with the samples investigated in the September 2013 beam time at the different used detector position with respect to the beam axis (see section 4.2.2). The numbers in the brackets correspond to the statistical errors on the last decimal place determined as described in section 5.7.2. Furthermore, the detector positions, at which the reference measurements were performed, are shown. A value of 1 without a given error corresponds to measurements, in which ^{22}Na data for energy calibration was taken right after the respective measurement with the neutron beam superseding an additional measurement with regard to gain correction.

sample	LAB-3-20(2)	DCTarget	LAB-3-10	LAB-3-0	LAB-7-20	LAB-9-20	LAB-3-80
ref. spec. @	Pos0	Pos0	Pos0	Pos0	Pos0	Pos0	Pos0
Pos-1	1.0212(6)	-	-	-	-	-	-
Pos0	1	0.9970(7)	1	-	-	-	-
Pos1	1.0181(6)	0.9902(6)	0.9958(6)	1.0295(6)	1.0237(6)	0.9736(6)	0.9941(6)
Pos2	1.0107(6)	0.9910(7)	0.9973(6)	1.0305(6)	1.0219(6)	1.0012(6)	-
Pos3	1.0118(6)	0.9967(6)	0.9939(6)	1.0314(6)	1.0246(6)	1.0013(6)	0.9989(6)
Pos4	1.0024(6)	0.9990(7)	0.9936(6)	1.0280(6)	1.0203(6)	1.0125(6)	0.9971(6)
Pos5	1.0030(6)	0.9981(6)	0.9862(6)	1.0292(6)	1.0182(6)	1.0086(6)	-
Pos6	0.9977(6)	0.9683(6)	0.9843(6)	1.0285(6)	1.0116(6)	1.0086(6)	0.9910(6)
Pos7	1.0016(6)	0.9360(7)	0.9582(6)	1.0268(6)	1.0111(6)	1.0101(6)	0.9968(6)
Pos8	-	-	-	1.0352(6)	0.9724(6)	1.0135(6)	0.9642(6)

Table B.5.: The gain correction factors obtained as described in section 5.7 for the measurements with the samples investigated in the February 2014 beam time at the different used detector position with respect to the beam axis (see section 4.2.2). The numbers in the brackets correspond to the statistical errors on the last decimal place determined as described in section 5.7.2. Furthermore, the detector positions, at which the reference measurements were performed, are shown. A value of 1 without a given error corresponds to measurements, in which ^{22}Na data for energy calibration was taken right after the respective measurement with the neutron beam superseding an additional measurement with regard to gain correction.

sample	50LAB-50nPar	LAB-1-20	DCGC	75LAB-25nPar	Borexino(2)	LAB-3-0(2)
ref. spec. @	Pos0	Pos0	Pos0	Pos0	Pos0	Pos-1
Pos-1	-	-	1.0098(7)	1.0318(6)	-	0.9983(6)
Pos0	0.9993(6)	1.0244(6)	1.0064(6)	1.0337(6)	1.0382(6)	-
Pos1	0.9986(6)	1.0261(6)	1.0072(6)	1.0333(6)	-	0.9990(6)
Pos2	1.0027(6)	1.0211(6)	1.0034(7)	1.0313(7)	1.0400(6)	0.9956(6)
Pos3	-	1.0213(6)	1.0044(6)	1.0340(6)	-	-
Pos4	1.0098(6)	1.0145(6)	0.9971(7)	1.0296(6)	1.0388(6)	1.0006(6)
Pos5	0.9988(6)	0.9932(6)	0.9980(6)	1.0279(6)	-	-
Pos6	0.9831(6)	0.9843(6)	0.9928(6)	1.0274(6)	1.0364(6)	0.9742(6)
Pos7	0.9858(6)	0.9561(6)	0.9934(6)	1.0333(6)	-	-
Pos8	-	-	-	-	-	-

Table B.6.: The gain correction factors obtained as described in section 5.7 for the measurements with the samples investigated in the May/June 2014 beam time at the different used detector position with respect to the beam axis (see section 4.2.2). The numbers in the brackets correspond to the statistical errors on the last decimal place determined as described in section 5.7.2. Furthermore, the detector positions, at which the reference measurements were performed, are shown.

C. Proton Quenching Analysis

C.1. Taken Beam Data

The amount of data, recorded in each measurement with the respective scintillator sample at the different detector positions, is given in tables C.1-C.3 for each of the three beam times performed in 2013 and 2014. The lower taken statistics in the September 2013 beam time compared to the two later ones was caused mainly by the higher trigger threshold of the coincidence setup (see section 4.2.3) of $\sim 24\,\mathrm{mV}$, which corresponds to an energy of $\sim 200\,\mathrm{keV}$ deposited by an electron. Furthermore, the lower taken statistics was due to a worse performance of the beam and a problem with the discriminator channel used for the pulsing signal. The larger number of taken events in each measurement of the 2014 beam times is caused by using a different discriminator channel for the pulsing signal and reduced thresholds of $\sim 13\,\mathrm{mV}$ ($\sim 130\,\mathrm{keV}$) in the February beam time and of $\sim 8\,\mathrm{mV}$ ($\sim 100\,\mathrm{keV}$) in the May/June beam time. The increased taken statistics towards the end of the May/June 2014 beam time were due to a very good performance of the beam and sufficient time in the end of the beam time.

sample	approx. events taken at each detector position in (10^3 events)									
	Pos-1	Pos0	Pos1	Pos2	Pos3	Pos4	Pos5	Pos6	Pos7	Pos8
DCMV	-	133	111	111	114	111	101 + 55	120	116	-
LAB-3-20	-	131	140	131	130	130	130	130	140	-
Borexino	101	135	132	119	126	122	120	120	118	71
LAB-5-20	-	130	135	130	121	130	121	133	130	-
LAB-3-40	-	131	-	126	99	100* + 104	123	127	123	-

Table C.1.: Statistics taken in each beam measurement with the respective scintillator sample at the different detector positions in the September 2013 beam time. The trigger threshold of the coincidence setup (see section 4.2.3) was $\sim 24\,\mathrm{mV}$, which corresponds to an energy deposition by an electron of $\sim 200\,\mathrm{keV}$. In case of the measurement with the LAB-3-40 sample at Pos4, the pulsing signal was not recorded for the data set marked by the asterisk. The measurement with the DCMV sample at Pos5 was interrupted due to a problem with the beam. See table 4.1 for information on the detector positions and table 4.2 for the scintillator compositions.

sample	approx. events taken at each detector position in (10^3 events)									
	Pos-1	Pos0	Pos1	Pos2	Pos3	Pos4	Pos5	Pos6	Pos7	Pos8
LAB-3-20(2)	123	200	250	291	260	257	250	252	273	-
DCTarget	-	282	284	301	290	288	295	176	180	-
LAB-3-10	-	300	303	317	290	300	277	300	337	-
LAB-3-0	-	259	251	252	300	260	275	305	285	-
LAB-7-20	-	250	265	250	253	252	254	250	307	-
LAB-9-20	-	261	257	262	290	300	300	270	200	-
LAB-3-80	-	266	-	251	257	-	273	280	327	-

Table C.2.: Statistics taken in each beam measurement with the respective scintillator sample at the different detector positions in the February 2014 beam time. The trigger threshold of the coincidence setup (see section 4.2.3) was $\sim 13\,\mathrm{mV}$, which corresponds to an energy deposition by an electron of $\sim 130\,\mathrm{keV}$. See table 4.1 for information on the detector positions and table 4.4 for the scintillator compositions.

sample	approx. events taken at each detector position in (10^3 events)									
	Pos-1	Pos0	Pos1	Pos2	Pos3	Pos4	Pos5	Pos6	Pos7	Pos8
50LAB-50nPar	-	250	241	262	-	276	285	300	364	-
LAB-1-20	-	254	280	300	280	316	251	276	223	-
DCMV-PSD	-	724	-	-	-	-	-	-	-	-
DCGC	450	300	302	306	302	301	322	440	450	-
LAB-5-20-PSD	-	893	-	-	-	-	-	-	-	-
75LAB-25nPar	-	444	475	461	488	503	433	550	401	-
LAB-3-40-PSD	-	-	967	-	-	-	-	-	-	-
Borexino(2)	-	705	-	451	-	465	-	450	-	-
LAB-3-0(2)	450	-	450	451	-	499	-	481	-	-

Table C.3.: Statistics taken in each beam measurement with the respective scintillator sample at the different detector positions in the May/June 2014 beam time. The trigger threshold of the coincidence setup (see section 4.2.3) was $\sim 8\,\mathrm{mV}$, which corresponds to an energy deposition by an electron of $\sim 100\,\mathrm{keV}$. For DCMV-PSD, LAB-5-20-PSD and LAB-3-40-PSD data was taken with high statistics at one position. Those samples have been studied regarding PSD performance only (see chapter 7). See table 4.1 for information on the detector positions and table 4.6 for the scintillator compositions.

C.2. Time of Flight Analysis Results

The results on the mean $\langle E_n \rangle$ and the the width σ_{E_n} of the assumed Gaussian shaped energy distribution of the neutrons, determined by the fit to each measured time of flight spectrum as described in section 6.3), are given in tables C.4 and C.5 for all measurements performed with the investigated scintillator samples (see sections 3.4.4 and 4.5) at the different detector positions (see section 4.2.2). The given errors on the last decimal places correspond to the statistical uncertainties on the respective parameter from the fit.

C.3. Maximum Visible Proton Recoil Energy Analysis Results

In tables C.6-C.9 the results on the maximum visible proton energy $E_{\text{vis}}^{\text{max}}$, determined as described in section 6.4, are given with statistical and systematic errors, respectively, including all measurements with the investigated scintillator samples at the different used detector positions. While tables C.6 and C.7 correspond to the results obtained, when the linear energy calibration function (see section 5.5.1) was applied to the data, tables C.8 and C.9 show the obtained results, using the quadratic calibration function (see section 5.5.2).

Results for $\langle E_n \rangle$ from the fit to the measured ToF-spectrum at each detector position in $\langle$MeV$\rangle$:

Period	sample	Pos-1	Pos0	Pos1	Pos2	Pos3	Pos4	Pos5	Pos6	Pos7	Pos8
Sept. 2013	DCMV	-	10.993(6)	10.566(5)	9.911(5)	9.445(4)	8.582(5)	7.801(5)	7.090(4)	6.003(4)	-
	LAB-3-20	-	11.100(4)	10.690(6)	10.030(5)	9.497(4)	8.671(5)	7.902(5)	7.123(4)	6.016(4)	-
	Borexino	11.046(5)	10.943(4)	10.580(4)	9.946(5)	9.358(5)	8.551(5)	7.764(5)	7.121(5)	6.012(4)	4.712(5)
	LAB-5-20	-	10.955(4)	10.596(4)	9.953(5)	9.404(5)	8.582(5)	7.738(5)	7.109(4)	5.977(4)	-
	LAB-3-40	-	10.979(5)	-	9.929(5)	9.406(11)	8.544(6)	7.797(5)	7.056(5)	5.990(4)	-
Feb. 2014	LAB-3-20(2)	10.997(4)	10.900(4)	10.539(3)	9.901(3)	9.409(3)	8.567(4)	7.750(4)	7.054(4)	5.938(3)	-
	DCTarget	-	10.918(2)	10.534(2)	9.929(2)	9.383(3)	8.565(3)	7.753(3)	7.078(4)	5.981(4)	-
	LAB-3-10	-	10.983(2)	10.584(2)	9.919(2)	9.356(3)	8.553(3)	7.685(3)	7.004(3)	5.927(3)	-
	LAB-3-0	-	10.973(2)	10.619(4)	9.969(4)	9.380(2)	8.582(4)	7.746(3)	7.072(4)	5.961(3)	-
	LAB-7-20	-	10.974(2)	10.582(3)	9.949(3)	9.393(3)	8.584(3)	7.771(3)	7.052(3)	5.959(3)	-
	LAB-9-20	-	10.948(3)	10.588(3)	9.946(3)	9.417(3)	8.585(3)	7.744(3)	7.078(3)	5.964(3)	-
	LAB-3-80	-	10.933(3)	-	9.930(3)	9.384(3)	-	7.707(3)	7.060(3)	5.943(3)	-
	50LAB-50nPar	-	11.006(6)	10.710(5)	10.059(5)	-	8.737(6)	7.875(6)	7.183(6)	6.021(5)	-
	LAB-1-20	-	11.059(4)	10.675(5)	10.004(4)	9.515(5)	8.666(5)	7.928(8)	7.134(9)	6.025(7)	-
May/June 2014	DCMV-PSD	-	-	-	-	-	-	-	-	-	-
	DCGC	11.186(2)	11.122(3)	10.732(3)	10.067(3)	9.501(3)	8.664(4)	7.853(4)	7.149(3)	6.063(3)	-
	LAB-5-20-PSD	-	-	-	-	-	-	-	-	-	-
	75LAB-25nPar	-	11.133(2)	10.753(2)	10.095(2)	9.527(3)	8.718(3)	7.898(3)	7.191(2)	6.053(3)	-
	LAB-3-40-PSD	-	-	-	-	-	-	-	-	-	-
	Borexino(2)	-	11.048(3)	-	10.045(2)	-	8.669(3)	-	7.164(3)	-	-
	LAB-3-0(2)	11.186(2)	-	10.740(2)	10.080(2)	-	8.713(2)	-	7.216(2)	-	-

Table C.4.: The results for $\langle E_n \rangle$ from the fit to the ToF-spectrum (see section 6.3.1), measured for the investigated scintillator samples (see section 3.4.4) at each detector position with respect to the beam axis (see table 4.1). The values in brackets correspond to the statistical errors on the last decimal place as obtained from the fit. The samples labeled with PSD (May/June 2014) were not analyzed with regard to proton quenching. Hence, the fit to the ToF-spectrum was not performed. This data was analyzed with regard to pulse shape discrimination (PSD) performance only (see chapter 7).

Results for σ_{E_n} from the fit to the measured ToF-spectrum at each detector position in (MeV):

	sample	Pos-1	Pos0	Pos1	Pos2	Pos3	Pos4	Pos5	Pos6	Pos7	Pos8
Sept. 2013	DCMV	-	0.319(7)	0.338(6)	0.340(6)	0.305(5)	0.368(5)	0.381(6)	0.379(5)	0.408(5)	-
	LAB-3-20	-	0.233(6)	0.256(10)	0.274(7)	0.285(6)	0.321(6)	0.328(6)	0.381(5)	0.406(4)	-
	Borexino	0.314(5)	0.348(5)	0.357(5)	0.323(5)	0.368(5)	0.388(5)	0.405(5)	0.379(5)	0.425(5)	0.461(6)
	LAB-5-20	-	0.343(5)	0.339(5)	0.317(6)	0.357(6)	0.393(5)	0.408(6)	0.386(5)	0.397(5)	-
	LAB-3-40	-	0.319(6)	-	0.308(7)	0.318(13)	0.377(7)	0.382(6)	0.379(5)	0.409(5)	-
Feb. 2014	LAB-3-20(2)	0.351(4)	0.375(3)	0.342(3)	0.348(3)	0.348(4)	0.380(4)	0.400(4)	0.402(4)	0.417(4)	-
	DCTarget	-	0.385(2)	0.380(2)	0.328(3)	0.380(2)	0.408(3)	0.404(3)	0.411(4)	0.420(4)	-
	LAB-3-10	-	0.337(2)	0.348(2)	0.326(3)	0.358(3)	0.402(3)	0.401(3)	0.403(3)	0.431(3)	-
	LAB-3-0	-	0.367(2)	0.304(6)	0.347(8)	0.371(3)	0.393(7)	0.409(3)	0.421(5)	0.428(3)	-
	LAB-7-20	-	0.323(2)	0.316(3)	0.332(3)	0.340(3)	0.377(3)	0.387(3)	0.409(3)	0.421(3)	-
	LAB-9-20	-	0.362(2)	0.350(3)	0.349(4)	0.329(3)	0.357(3)	0.382(3)	0.388(3)	0.418(3)	-
	LAB-3-80	-	0.361(2)	-	0.341(3)	0.340(3)	-	0.393(3)	0.392(3)	0.427(3)	-
May/June 2014	50LAB-50nPar	-	0.400(8)	0.356(8)	0.362(7)	-	0.523(10)	0.562(10)	0.473(12)	0.382(7)	-
	LAB-1-20	-	0.309(6)	0.287(8)	0.307(6)	0.357(6)	0.422(7)	0.477(13)	0.451(14)	0.379(9)	-
	DCMV-PSD	-	-	-	-	-	-	-	-	-	-
	DCGC	0.293(3)	0.284(5)	0.288(5)	0.290(5)	0.332(5)	0.386(5)	0.392(5)	0.396(3)	0.415(3)	-
	LAB-5-20-PSD	-	-	-	-	-	-	-	-	-	-
	75LAB-25nPar	-	0.285(3)	0.279(3)	0.295(3)	0.336(4)	0.394(3)	0.401(3)	0.403(3)	0.416(3)	-
	LAB-3-40-PSD	-	-	-	-	-	-	-	-	-	-
	Borexino(2)	-	0.343(3)	-	0.323(3)	-	0.403(3)	-	0.404(3)	-	-
	LAB-3-0(2)	0.293(2)	-	0.288(3)	0.299(3)	-	0.381(3)	-	0.389(3)	-	-

Table C.5.: The results for σ_{E_n} from the fit to the ToF-spectrum (see section 6.3.1), measured for the investigated scintillator samples (see section 3.4.4) at each detector position with respect to the beam axis (see table 4.1). The values in brackets correspond to the statistical errors on the last decimal place, as obtained from the fit. The samples labeled with PSD (May/June 2014) were not analyzed with regard to proton quenching. Hence, the fit to the ToF-spectrum was not performed. This data was analyzed with regard to pulse shape discrimination (PSD) performance only (see chapter 7).

	sample	Results for **max. vis. proton rec. energy** with **stat. errors** in (MeV) for **linear calib.**:									
		Pos-1	Pos0	Pos1	Pos2	Pos3	Pos4	Pos5	Pos6	Pos7	Pos8
Sept. 2013	DCMV	-	5.54(2)	5.38(2)	4.92(2)	4.53(2)	3.95(2)	3.48(2)	3.02(1)	2.36(1)	-
	LAB-3-20	-	6.11(3)	5.77(3)	5.32(2)	4.95(2)	4.40(2)	3.82(2)	3.33(2)	2.51(1)	-
	Borexino	6.07(3)	5.92(2)	5.65(2)	5.20(2)	4.77(2)	4.15(2)	3.56(2)	3.14(2)	2.45(1)	1.70(1)
	LAB-5-20	-	6.12(2)	5.93(2)	5.40(2)	5.01(2)	4.35(2)	3.77(2)	3.34(1)	2.59(1)	-
	LAB-3-40	-	5.99(2)	-	5.36(3)	5.00(4)	4.23(3)	3.72(2)	3.20(2)	2.53(1)	-
Feb. 2014	LAB-3-20(2)	6.25(3)	6.17(2)	5.96(2)	5.36(2)	4.96(2)	4.38(2)	3.77(1)	3.30(1)	2.58(1)	-
	DCTarget	-	5.75(1)	5.47(1)	5.06(1)	4.64(1)	4.01(1)	3.48(1)	3.11(1)	2.34(1)	-
	LAB-3-10	-	6.20(2)	5.95(2)	5.36(2)	4.94(2)	4.36(1)	3.69(1)	3.25(1)	2.51(1)	-
	LAB-3-0	-	6.29(2)	6.07(2)	5.48(2)	5.06(1)	4.45(2)	3.81(1)	3.34(1)	2.62(1)	-
	LAB-7-20	-	6.24(2)	6.00(2)	5.47(2)	5.07(1)	4.45(1)	3.81(1)	3.33(1)	2.58(1)	-
	LAB-9-20	-	6.08(1)	5.96(2)	5.41(1)	5.02(1)	4.39(1)	3.79(1)	3.34(1)	2.60(1)	-
	LAB-3-80	-	6.11(2)	-	5.41(1)	4.96(1)	-	3.74(1)	3.26(1)	2.50(1)	-
	50LAB-50nPar	-	5.78(3)	5.54(3)	5.09(2)	-	4.02(2)	3.49(2)	3.03(1)	2.40(1)	-
May/June 2014	DCGC	5.36(1)	5.33(2)	5.10(2)	4.60(2)	4.24(2)	3.68(1)	3.18(1)	2.68(1)	2.14(1)	-
	LAB-1-20	-	5.77(2)	5.53(3)	5.05(2)	4.73(2)	4.06(2)	3.58(2)	3.06(2)	2.32(1)	-
	DCMV-PSD	-	-	-	-	-	-	-	-	-	-
	75LAB-25nPar	-	6.26(2)	6.01(1)	5.45(1)	5.06(2)	4.43(1)	3.82(1)	3.33(1)	2.59(1)	-
	LAB-5-20-PSD	-	-	-	-	-	-	-	-	-	-
	LAB-3-40-PSD	-	-	-	-	-	-	-	-	-	-
	Borexino(2)	-	6.21(2)	-	5.41(1)	4.41(1)	4.41(1)	3.30(1)	3.30(1)	-	-
	LAB-3-0(2)	6.30(1)	-	6.01(1)	5.47(1)	-	4.43(1)	-	3.35(1)	-	-

Table C.6.: Results obtained for the maximum visible proton recoil energy $E_{\mathrm{vis}}^{\max}$ with **statistical errors** (see section 6.4) from the measurements with the investigated scintillator samples (see sections 3.4.4 and 4.5) at the different detector positions with respect to the beam axis (see section 4.2.2). The shown results were obtained for the **linear calibration** (see section 5.5.1) applied to the data. The values in brackets correspond to the statistical errors on the last digits as obtained from the fit to the proton recoil spectrum. The samples labeled with PSD (May/June 2014) were not analyzed with regard to proton quenching. Hence, $E_{\mathrm{vis}}^{\max}$ was not reconstructed from the proton recoil spectra. This data was analyzed with regard to pulse shape discrimination (PSD) performance only (see chapter 7).

Results for max. vis. proton rec. energy with syst. errors* in (MeV) for linear calib.:

Period	sample	Pos-1	Pos0	Pos1	Pos2	Pos3	Pos4	Pos5	Pos6	Pos7	Pos8
Sept. 2013	DCMV	-	$5.54^{+0.06}_{-0.07}$	$5.38^{+0.06}_{-0.05}$	$4.92^{+0.07}_{-0.07}$	$4.53^{+0.06}_{-0.06}$	$3.95^{+0.11}_{-0.10}$	$3.48^{+0.10}_{-0.10}$	$3.02^{+0.09}_{-0.08}$	$2.36^{+0.10}_{-0.07}$	-
	LAB-3-20	-	$6.11^{+0.02}_{-0.02}$	$5.77^{+0.05}_{-0.04}$	$5.32^{+0.00}_{-0.00}$	$4.95^{+0.05}_{-0.05}$	$4.40^{+0.05}_{-0.06}$	$3.82^{+0.06}_{-0.07}$	$3.33^{+0.11}_{-0.09}$	$2.51^{+0.11}_{-0.09}$	-
	Borexino	$6.07^{+0.08}_{-0.06}$	$5.92^{+0.09}_{-0.08}$	$5.65^{+0.08}_{-0.08}$	$5.20^{+0.10}_{-0.11}$	$4.77^{+0.09}_{-0.07}$	$4.15^{+0.11}_{-0.08}$	$3.56^{+0.11}_{-0.09}$	$3.14^{+0.09}_{-0.06}$	$2.45^{+0.10}_{-0.07}$	$1.70^{+0.11}_{-0.07}$
	LAB-5-20	-	$6.12^{+0.12}_{-0.13}$	$5.93^{+0.07}_{-0.07}$	$5.40^{+0.07}_{-0.09}$	$5.01^{+0.09}_{-0.08}$	$4.35^{+0.06}_{-0.04}$	$3.77^{+0.12}_{-0.09}$	$3.34^{+0.10}_{-0.08}$	$2.59^{+0.12}_{-0.10}$	-
	LAB-3-40	-	$5.99^{+0.02}_{-0.02}$	-	$5.36^{+0.01}_{-0.01}$	$5.00^{+0.07}_{-0.04}$	$4.23^{+0.07}_{-0.05}$	$3.72^{+0.06}_{-0.06}$	$3.20^{+0.10}_{-0.07}$	$2.53^{+0.11}_{-0.09}$	-
Feb. 2014	LAB-3-20(2)	$6.25^{+0.06}_{-0.05}$	$6.17^{+0.12}_{-0.13}$	$5.96^{+0.10}_{-0.10}$	$5.36^{+0.10}_{-0.09}$	$4.96^{+0.06}_{-0.06}$	$4.38^{+0.09}_{-0.08}$	$3.77^{+0.08}_{-0.05}$	$3.30^{+0.10}_{-0.07}$	$2.58^{+0.11}_{-0.09}$	-
	DCTarget	-	$5.75^{+0.10}_{-0.09}$	$5.47^{+0.14}_{-0.14}$	$5.06^{+0.10}_{-0.09}$	$4.64^{+0.09}_{-0.08}$	$4.01^{+0.12}_{-0.11}$	$3.48^{+0.13}_{-0.10}$	$3.11^{+0.11}_{-0.07}$	$2.34^{+0.11}_{-0.08}$	-
	LAB-3-10	-	$6.20^{+0.09}_{-0.08}$	$5.95^{+0.07}_{-0.06}$	$5.36^{+0.10}_{-0.09}$	$4.94^{+0.09}_{-0.08}$	$4.36^{+0.12}_{-0.11}$	$3.69^{+0.13}_{-0.11}$	$3.25^{+0.14}_{-0.10}$	$2.51^{+0.13}_{-0.11}$	-
	LAB-3-0	-	$6.29^{+0.12}_{-0.12}$	$6.07^{+0.06}_{-0.06}$	$5.48^{+0.05}_{-0.04}$	$5.06^{+0.13}_{-0.11}$	$4.45^{+0.09}_{-0.08}$	$3.81^{+0.11}_{-0.09}$	$3.34^{+0.12}_{-0.09}$	$2.62^{+0.13}_{-0.11}$	-
	LAB-7-20	-	$6.24^{+0.08}_{-0.08}$	$6.00^{+0.12}_{-0.11}$	$5.47^{+0.07}_{-0.06}$	$5.07^{+0.11}_{-0.08}$	$4.45^{+0.09}_{-0.08}$	$3.81^{+0.14}_{-0.12}$	$3.33^{+0.09}_{-0.06}$	$2.58^{+0.15}_{-0.12}$	-
	LAB-9-20	-	$6.08^{+0.11}_{-0.11}$	$5.96^{+0.07}_{-0.06}$	$5.41^{+0.07}_{-0.07}$	$5.02^{+0.11}_{-0.11}$	$4.39^{+0.10}_{-0.10}$	$3.79^{+0.11}_{-0.10}$	$3.34^{+0.12}_{-0.11}$	$2.60^{+0.12}_{-0.10}$	-
	LAB-3-80	-	$6.11^{+0.11}_{-0.11}$	-	$5.41^{+0.10}_{-0.10}$	$4.96^{+0.09}_{-0.08}$	-	$3.74^{+0.14}_{-0.11}$	$3.26^{+0.13}_{-0.12}$	$2.50^{+0.12}_{-0.09}$	-
May/June 2014	50LAB-50nPar	-	$5.78^{+0.07}_{-0.05}$	$5.54^{+0.02}_{-0.02}$	$5.09^{+0.07}_{-0.06}$	-	$4.02^{+0.08}_{-0.06}$	$3.49^{+0.16}_{-0.14}$	$3.03^{+0.13}_{-0.10}$	$2.40^{+0.12}_{-0.10}$	-
	LAB-1-20	-	$5.77^{+0.05}_{-0.05}$	$5.53^{+0.09}_{-0.09}$	$5.05^{+0.05}_{-0.05}$	$4.73^{+0.11}_{-0.09}$	$4.06^{+0.12}_{-0.09}$	$3.58^{+0.12}_{-0.10}$	$3.06^{+0.09}_{-0.07}$	$2.32^{+0.09}_{-0.06}$	-
	DCMV-PSD	-	-	-	-	-	-	-	-	-	-
	DCGC	$5.36^{+0.05}_{-0.05}$	$5.33^{+0.02}_{-0.01}$	$5.10^{+0.05}_{-0.04}$	$4.60^{+0.06}_{-0.06}$	$4.24^{+0.03}_{-0.03}$	$3.68^{+0.05}_{-0.04}$	$3.18^{+0.06}_{-0.05}$	$2.68^{+0.08}_{-0.08}$	$2.14^{+0.09}_{-0.07}$	-
	LAB-5-20-PSD	-	-	-	-	-	-	-	-	-	-
	75LAB-25nPar	-	$6.26^{+0.06}_{-0.06}$	$6.01^{+0.04}_{-0.04}$	$5.45^{+0.04}_{-0.04}$	$5.06^{+0.08}_{-0.07}$	$4.43^{+0.10}_{-0.08}$	$3.82^{+0.09}_{-0.07}$	$3.33^{+0.11}_{-0.09}$	$2.59^{+0.13}_{-0.11}$	-
	LAB-3-40-PSD	-	-	-	-	-	-	-	-	-	-
	Borexino(2)	-	$6.21^{+0.08}_{-0.08}$	-	$5.41^{+0.06}_{-0.05}$	-	$4.41^{+0.10}_{-0.08}$	-	$3.30^{+0.11}_{-0.09}$	-	-
	LAB-3-0(2)	$6.30^{+0.07}_{-0.06}$	-	$6.01^{+0.06}_{-0.05}$	$5.47^{+0.07}_{-0.07}$	-	$4.43^{+0.07}_{-0.06}$	-	$3.35^{+0.11}_{-0.09}$	-	-

Table C.7.: Results obtained for the maximum visible proton recoil energy $E_{\mathrm{vis}}^{\max}$ with **systematic errors** due to the selection of the recoil events (*) (see section 6.4.3) from the measurements with the investigated scintillator samples (see sections 3.4.4 and 4.5) at the different detector positions with respect to the beam axis (see section 4.2.2). The shown results were obtained for the **linear calibration** (see section 5.5.1) applied to the data. The asymmetric systematic errors were estimated as described in section 6.4.3. The samples labeled with PSD (May/June 2014) were not analyzed with regard to proton quenching. Hence, $E_{\mathrm{vis}}^{\max}$ was not reconstructed from the proton recoil spectra. This data was analyzed with regard to pulse shape discrimination (PSD) performance only (see chapter 7).

Results for **max. vis. proton rec. energy** with **stat. errors** in (MeV) for **quadratic calib.**:

	sample	Pos-1	Pos0	Pos1	Pos2	Pos3	Pos4	Pos5	Pos6	Pos7	Pos8
Sept. 2013	DCMV	-	5.35(1)	5.20(2)	4.79(2)	4.43(2)	3.91(2)	3.46(2)	3.01(1)	2.38(1)	-
	LAB-3-20	-	5.71(2)	5.43(2)	5.04(2)	4.73(2)	4.25(2)	3.72(2)	3.28(1)	2.50(1)	-
	Borexino	5.61(2)	5.49(2)	5.26(2)	4.89(2)	4.54(2)	4.01(2)	3.48(2)	3.10(1)	2.45(1)	1.72(1)
	LAB-5-20	-	5.66(2)	5.49(2)	5.06(2)	4.74(2)	4.18(2)	3.67(2)	3.28(1)	2.58(1)	-
	LAB-3-40	-	5.59(2)	-	5.08(2)	4.76(3)	4.10(2)	3.64(2)	3.16(1)	2.53(1)	-
Feb. 2014	LAB-3-20(2)	5.44(2)	5.39(1)	5.25(1)	4.83(1)	4.55(1)	4.10(1)	3.61(1)	3.20(1)	2.57(1)	-
	DCTarget	-	5.22(1)	5.01(1)	4.70(1)	4.35(1)	3.84(1)	3.38(1)	3.05(1)	2.34(1)	-
	LAB-3-10	-	5.60(1)	5.41(1)	4.96(1)	4.63(1)	4.15(1)	3.58(1)	3.18(1)	2.50(1)	-
	LAB-3-0	-	5.72(1)	5.56(1)	5.10(1)	4.75(1)	4.24(1)	3.70(1)	3.27(1)	2.61(1)	-
	LAB-7-20	-	5.72(1)	5.54(1)	5.11(1)	4.77(1)	4.25(1)	3.70(1)	3.27(1)	2.57(1)	-
	LAB-9-20	-	5.63(1)	5.53(1)	5.08(1)	4.75(1)	4.22(1)	3.69(1)	3.28(1)	2.59(1)	-
	LAB-3-80	-	5.59(1)	-	5.03(1)	4.67(1)	-	3.63(1)	3.20(1)	2.50(1)	-
May/June 2014	50LAB-50nPar	-	5.42(2)	5.22(2)	4.84(2)	-	3.92(2)	3.44(1)	3.00(1)	2.42(1)	-
	LAB-1-20	-	5.43(2)	5.23(2)	4.82(2)	4.54(2)	3.97(2)	3.53(2)	3.04(2)	2.34(1)	-
	DCMV-PSD	-	-	-	-	-	-	-	-	-	-
	DCGC	4.97(1)	4.95(1)	4.76(1)	4.35(1)	4.06(1)	3.57(1)	3.12(1)	2.66(1)	2.15(1)	-
	LAB-5-20-PSD	-	-	-	-	-	-	-	-	-	-
	75LAB-25nPar	-	5.72(1)	5.53(1)	5.08(1)	4.76(1)	4.23(1)	3.71(1)	3.27(1)	2.58(1)	-
	LAB-3-40-PSD	-	-	-	-	-	-	-	-	-	-
	Borexino(2)	-	5.74(1)	-	5.08(1)	-	4.23(1)	-	3.24(1)	-	-
	LAB-3-0(2)	5.83(1)	-	5.60(1)	5.14(1)	-	4.26(1)	-	3.29(1)	-	-

Table C.8.: Results obtained for the maximum visible proton recoil energy $E_{\mathrm{vis}}^{\max}$ with **statistical errors** (see section 6.4) from the measurements with the investigated scintillator samples (see sections 3.4.4 and 4.5) at the different detector positions with respect to the beam axis (see section 4.2.2). The shown results were obtained for the **quadratic calibration** (see section 5.5.2) applied to the data. The values in brackets correspond to the statistical errors on the last digits as obtained from the fit to the recoil spectrum. The samples labeled with PSD (May/June 2014) were not analyzed with regard to proton quenching. Hence, $E_{\mathrm{vis}}^{\max}$ was not reconstructed from the proton recoil spectra. This data was analyzed with regard to pulse shape discrimination (PSD) performance only (see chapter 7).

				Results for max. vis. proton rec. energy with syst. errors* in (MeV) for quadratic calib.:						
sample	Pos-1	Pos0	Pos1	Pos2	Pos3	Pos4	Pos5	Pos6	Pos7	Pos8
Sept. 2013										
DCMV	-	$5.35^{+0.06}_{-0.06}$	$5.20^{+0.05}_{-0.05}$	$4.79^{+0.07}_{-0.06}$	$4.43^{+0.06}_{-0.05}$	$3.91^{+0.10}_{-0.09}$	$3.46^{+0.09}_{-0.09}$	$3.01^{+0.08}_{-0.08}$	$2.38^{+0.10}_{-0.07}$	-
LAB-3-20	-	$5.71^{+0.02}_{-0.01}$	$5.43^{+0.04}_{-0.04}$	$5.04^{+0.01}_{-0.01}$	$4.73^{+0.05}_{-0.04}$	$4.25^{+0.05}_{-0.05}$	$3.72^{+0.06}_{-0.06}$	$3.28^{+0.10}_{-0.09}$	$2.50^{+0.11}_{-0.09}$	-
Borexino	$5.61^{+0.08}_{-0.05}$	$5.49^{+0.07}_{-0.06}$	$5.26^{+0.06}_{-0.06}$	$4.89^{+0.08}_{-0.08}$	$4.54^{+0.08}_{-0.06}$	$4.01^{+0.10}_{-0.08}$	$3.48^{+0.10}_{-0.08}$	$3.10^{+0.09}_{-0.06}$	$2.45^{+0.10}_{-0.07}$	$1.72^{+0.10}_{-0.07}$
LAB-5-20	-	$5.66^{+0.09}_{-0.09}$	$5.49^{+0.05}_{-0.05}$	$5.06^{+0.06}_{-0.07}$	$4.74^{+0.07}_{-0.07}$	$4.18^{+0.06}_{-0.04}$	$3.67^{+0.10}_{-0.08}$	$3.28^{+0.09}_{-0.08}$	$2.58^{+0.11}_{-0.09}$	-
LAB-3-40	-	$5.59^{+0.02}_{-0.02}$	-	$5.08^{+0.02}_{-0.02}$	$4.76^{+0.05}_{-0.03}$	$4.10^{+0.06}_{-0.04}$	$3.64^{+0.06}_{-0.06}$	$3.16^{+0.09}_{-0.07}$	$2.53^{+0.11}_{-0.09}$	-
Feb. 2014										
LAB-3-20(2)	$5.44^{+0.05}_{-0.05}$	$5.39^{+0.08}_{-0.09}$	$5.25^{+0.07}_{-0.07}$	$4.83^{+0.07}_{-0.07}$	$4.55^{+0.05}_{-0.05}$	$4.10^{+0.07}_{-0.07}$	$3.61^{+0.06}_{-0.05}$	$3.20^{+0.08}_{-0.07}$	$2.57^{+0.10}_{-0.08}$	-
DCTarget	-	$5.22^{+0.07}_{-0.07}$	$5.01^{+0.10}_{-0.11}$	$4.70^{+0.08}_{-0.07}$	$4.35^{+0.07}_{-0.07}$	$3.84^{+0.10}_{-0.10}$	$3.38^{+0.11}_{-0.09}$	$3.05^{+0.11}_{-0.08}$	$2.34^{+0.11}_{-0.07}$	-
LAB-3-10	-	$5.60^{+0.07}_{-0.07}$	$5.41^{+0.06}_{-0.05}$	$4.96^{+0.08}_{-0.07}$	$4.63^{+0.07}_{-0.06}$	$4.15^{+0.10}_{-0.09}$	$3.58^{+0.11}_{-0.09}$	$3.18^{+0.12}_{-0.09}$	$2.50^{+0.12}_{-0.10}$	-
LAB-3-0	-	$5.72^{+0.09}_{-0.09}$	$5.56^{+0.05}_{-0.05}$	$5.10^{+0.04}_{-0.03}$	$4.75^{+0.11}_{-0.10}$	$4.24^{+0.08}_{-0.07}$	$3.70^{+0.10}_{-0.08}$	$3.27^{+0.11}_{-0.09}$	$2.61^{+0.12}_{-0.10}$	-
LAB-7-20	-	$5.72^{+0.06}_{-0.06}$	$5.54^{+0.09}_{-0.09}$	$5.11^{+0.05}_{-0.05}$	$4.77^{+0.09}_{-0.07}$	$4.25^{+0.08}_{-0.07}$	$3.70^{+0.12}_{-0.11}$	$3.27^{+0.08}_{-0.06}$	$2.57^{+0.13}_{-0.11}$	-
LAB-9-20	-	$5.63^{+0.08}_{-0.08}$	$5.53^{+0.06}_{-0.05}$	$5.08^{+0.06}_{-0.06}$	$4.75^{+0.10}_{-0.10}$	$4.22^{+0.09}_{-0.08}$	$3.69^{+0.10}_{-0.09}$	$3.28^{+0.11}_{-0.10}$	$2.59^{+0.11}_{-0.10}$	-
LAB-3-80	-	$5.59^{+0.08}_{-0.08}$	-	$5.03^{+0.08}_{-0.08}$	$4.67^{+0.07}_{-0.07}$	-	$3.63^{+0.12}_{-0.10}$	$3.20^{+0.11}_{-0.11}$	$2.50^{+0.11}_{-0.09}$	-
May/June 2014										
50LAB-50nPar	-	$5.42^{+0.06}_{-0.05}$	$5.22^{+0.02}_{-0.02}$	$4.84^{+0.06}_{-0.06}$	-	$3.92^{+0.08}_{-0.05}$	$3.44^{+0.15}_{-0.13}$	$3.00^{+0.12}_{-0.10}$	$2.42^{+0.11}_{-0.10}$	-
LAB-1-20	-	$5.43^{+0.05}_{-0.04}$	$5.23^{+0.07}_{-0.07}$	$4.82^{+0.05}_{-0.04}$	$4.54^{+0.09}_{-0.08}$	$3.97^{+0.11}_{-0.08}$	$3.53^{+0.10}_{-0.09}$	$3.04^{+0.09}_{-0.07}$	$2.34^{+0.09}_{-0.07}$	-
DCMV-PSD	-	-	-	-	-	-	-	-	-	-
DCGC	$4.97^{+0.04}_{-0.04}$	$4.95^{+0.02}_{-0.01}$	$4.76^{+0.04}_{-0.04}$	$4.35^{+0.05}_{-0.05}$	$4.06^{+0.03}_{-0.03}$	$3.57^{+0.05}_{-0.04}$	$3.12^{+0.06}_{-0.05}$	$2.66^{+0.08}_{-0.08}$	$2.15^{+0.09}_{-0.07}$	-
LAB-5-20-PSD	-	-	-	-	-	-	-	-	-	-
75LAB-25nPar	-	$5.72^{+0.05}_{-0.05}$	$5.53^{+0.03}_{-0.03}$	$5.08^{+0.04}_{-0.04}$	$4.76^{+0.07}_{-0.06}$	$4.23^{+0.08}_{-0.07}$	$3.71^{+0.08}_{-0.07}$	$3.27^{+0.10}_{-0.09}$	$2.58^{+0.12}_{-0.11}$	-
LAB-3-40-PSD	-	-	-	-	-	-	-	-	-	-
Borexino(2)	-	$5.74^{+0.06}_{-0.06}$	-	$5.08^{+0.06}_{-0.05}$	-	$4.23^{+0.09}_{-0.07}$	-	$3.24^{+0.10}_{-0.08}$	-	-
LAB-3-0(2)	$5.83^{+0.06}_{-0.05}$	-	$5.60^{+0.05}_{-0.04}$	$5.14^{+0.06}_{-0.06}$	-	$4.26^{+0.06}_{-0.05}$	-	$3.29^{+0.10}_{-0.08}$	-	-

Table C.9.: Results obtained for the maximum visible proton recoil energy $E_{\mathrm{vis}}^{\mathrm{max}}$ with **systematic errors** due to the selection of the recoil events (*) (see section 6.4.3) from the measurements with the investigated scintillator samples (see sections 3.4.4 and 4.5) at the different detector positions with respect to the beam axis (see section 4.2.2). The shown results were obtained for the **quadratic calibration** (see section 5.5.2) applied to the data. The asymmetric systematic errors were estimated as described in section 6.4.3. The samples labeled with PSD (May/June 2014) were not analyzed with regard to proton quenching. Hence, $E_{\mathrm{vis}}^{\mathrm{max}}$ was not reconstructed from the proton recoil spectra. This data was analyzed with regard to pulse shape discrimination (PSD) performance only (see chapter 7).

Bibliography

[1] N. Schmitz, *Neutrinophysik*, Teubner Studienbücher, Stuttgart (1997)

[2] F. Reines and C. L. Cowan, *Detection of the Free Neutrino*, Phys. Rev. **92** (1953), 830.

[3] C. L. Cowan et al., *Detection of the Free Neutrino: a Confirmation*, Science **124** (1956), 103.

[4] R. Davies et al., *Measurement of the Solar Electron Neutrino Flux with the Homestake Chlorine Detector*, Astrophys. J. **496** (1998), 505.

[5] J. N. Abdurashitov et al., *Measurement of the Solar Neutrino Capture Rate by the Russian-American Gallium Solar Neutrino Experiment During One Half of the 22-Year Cycle of Solar Activity*, Zh. Eksp. Teor. Fiz. **122** (2002), 211.

[6] W. Hampel et al., *GALLEX Solar Neutrino Observations: Results for GALLEX IV*, Phys. Lett. B **447** (1999), 127.

[7] M. Altmann et al., *Complete Results for Five Years of GNO Solar Neutrino Observations*, Phys. Lett. B **616** (2005), 174.

[8] Y. Fukuda et al., *Evidence for Oscillation of Atmospheric Neutrinos*, Phys. Rev. Lett. **81** (1998), 1562.

[9] Q. R. Ahmad et al., *Direct Evidence for Neutrino Flavor Transformation from Neutral-Current Interactions in the Sudbury Neutrino Observatory*, Phys. Rev. Lett. **89** (2002), 011301.

[10] K. Eguchi et al., *First Results from KamLAND: Evidence for Reactor Antineutrino Disappearance*, Phys. Rev. Lett. **90** (2003), 021802.

[11] G. Alimonti et al., *The Borexino Detector at the Laboratori Nazionali del Gran Sasso*, Nucl. Instr. and Meth. in Phys. Res. A **600** (2009), 568.

[12] C. Arpesella et al., *First Real Time Detection of ^{7}Be Solar Neutrinos by Borexino*, Phys. Lett. B **658** (2008), 101.

[13] G. Bellini et al., *First Evidence of pep Solar Neutrinos by Direct Detection in Borexino*, Phys. Rev. Lett. **108** (2012), 051302.

[14] G. Bellini, *Neutrinos From the Primary Proton–Proton Fusion Process in the Sun*, Nature **512** (2014), 383.

[15] Y. Abe et al., *Indication of Reactor $\bar{\nu}_e$ Disappearance in the Double Chooz Experiment*, Phys. Rev. Lett. **108** (2012), 131801.

[16] F. P. An et al., *Observation of Electron-Antineutrino Disappearance at Daya Bay*, Phys. Rev. Lett. **108** (2012), 171803.

[17] J. K. Ahn et al., *Observation of Reactor Electron Antineutrinos Disappearance in the RENO Experiment*, Phys. Rev. Lett. **108** (2012), 191802.

[18] M. Wurm et al., *The Next-Generation Liquid-Scintillator Neutrino Observatory LENA*, Astropart. Phys. **35** (2012), 685.

[19] F. An et al., *Neutrino Physics with JUNO*, arXiv:1507.05613 (2015)

[20] K.A. Olive et al. (Particle Data Group), Chin. Phys. C **38** (2014), 090001.

[21] B. Povh et al., *Teilchen und Kerne*, Springer, Berlin Heidelberg, 8th edition (2009)

[22] J. Knopp et al., *Sterile Neutrino Oscillations: The Global Picture*, JHEP **1305** (2013), 050.

[23] S. M. Bilenky et al., *On Oscillations of Neutrinos with Dirac and Majorana Masses*, Phys. Lett. B **94** (1980), 495.

[24] M. Zralek, *From Kaons to Neutrinos: Quantum Mechanics of Particle Oscillations*, Acta Phys. Polon. B **29** (1998), 3925.

[25] S. M. Bilenky, C. Giunti, W. Grimus, *Phenomenology of Neutrino Oscillations*, Prog. Part. Nucl. Phys. **43** (1999), 1.

[26] B. Kayser, *Neutrinos in Particle Physics, Astrophysics and Cosmology*, CRC Press, Boca Raton (2009)

[27] L. Wolfenstein, *Neutrino Oscillations in Matter*, Phys. Rev. D **17** (1978), 2369.

[28] A. Y. Smirnov, *The MSW Effect and Solar Neutrinos*, arXiv:0305106 (2003)

[29] F. Capozzi et al., *Status of Three-Neutrino Oscillation Parameters, Circa 2013*, Phys. Rev. D **89** (2014), 093018.

[30] A. Gando et al., *Reactor On-Off Antineutrino Measurement with KamLAND*, Phys. Rev. D **88** (2013), 033001.

[31] P. Adamson et al., *Measurement of Neutrino and Antineutrino Oscillations Using Beam and Atmospheric Data in MINOS*, Phys. Rev. Lett. **110** (2013), 251801.

[32] K. Abe et al., *Measurement of Neutrino Oscillation Parameters from Muon Neutrino Disappearance with an Off-Axis Beam*, Phys. Rev. Lett. **111** (2013), 211803.

[33] Y. Abe et al., *Reactor $\bar{\nu}_e$ Disappearance in the Double Chooz Experiment*, Phys. Rev. D **86** (2012), 052008.

[34] F. P. An et al., *Spectral Measurement of Electron Antineutrino Oscillation Amplitude and Frequency at Daya Bay*, Phys. Rev. Lett. **112** (2014), 061801.

[35] A. Himmel for the Super-Kamiokande Collaboration, *Recent Atmospheric Neutrino Results from Super-Kamiokande*, AIP Conf. Proc. **1604** (2014), 345.

[36] F. Suekane, *Neutrino Oscillations - A Practical Guide to Basics and Applications*, Springer Japan (2015)

[37] J. Wolf for the KATRIN Collaboration, *The KATRIN Neutrino Mass Experiment*, Nucl. Instrum. Meth. A **623** (2010), 442.

[38] M. Chemarin, *Number of Neutrino Families from LEP1 Measurements*, Nucl. Phys. B (Proc. Suppl.) **85** (2000), 67.

[39] P. Huber et al., *Reactor Neutrino Experiments Compared to Superbeams*, Nucl. Phys. B **665** (2003), 487.

[40] F. P. An et al., *A New Measurement of Antineutrino Oscillation with the Full Detector Configuration at Daya Bay*, arXiv:1505.03456 (2015), submitted to Phys. Rev. Lett.

[41] F. P. An et al., *Improved Measurement of Electron Antineutrino Disappearance at Daya Bay*, Chin. Phys. C **37** (2013), 011001.

[42] Y. Abe et al., *Improved Measurements of the Neutrino Mixing Angle θ_{13} with the Double Chooz Detector*, JHEP **10** (2014), 086. [Erratum ibid. 02 (2015), 074]

[43] Seon-Hee Seo for the RENO Collaboration, *New Results from RENO and the 5 MeV Excess*, AIP Conf. Proc. **1666** (2015), 080002.

[44] W. Zhong for the Daya Bay Collaboration, talk at the ICHEP2014 conference, July 2-9, Valencia (2014)

[45] M. Freund, *Analytic Approximations for Three Neutrino Oscillation Parameters and Probabilities in Matter*, Phys. Rev. D **64** (2001), 053003.

[46] K. Abe et al., *Observation of Electron Neutrino Appearance in a Muon Neutrino Beam*, Phys. Rev. Lett. **112** (2014), 061802.

[47] P. Adamson et al., *Improved Search for Muon-Neutrino to Electron-Neutrino Oscillations in MINOS*, Phys. Rev. Lett. **107** (2011), 181802.

[48] P. Adamson et al., *Electron Neutrino and Antineutrino Appearance in the Full MINOS Data Sample*, Phys. Rev. Lett. **110** (2013), 171801.

[49] X. Qian and P. Vogel, *Neutrino Mass Hierarchy*, PPNP **83** (2015), 1.

[50] S.-B. Kim, *New Results from RENO and Prospects with RENO-50*, arXiv:1412.2199 (2014)

[51] S.K. Agarwalla et al., *The Mass-Hierarchy and CP-Violation Discovery Reach of the LBNO Long-Baseline Neutrino Experiment*, arXiv:1312.6520v3 (2014)

[52] D. Hellgartner, *Advanced Event Reconstruction in LENA and Precision Attenuation-Length Measurements in Liquid Scintillator*, PhD thesis, Technische Universität München (2015)

[53] P. Huber et al., *New Features in the Simulation of Neutrino Oscillation Experiments with GLoBES 3.0: General Long Baseline Experiment Simulator*, Comp. Phys. Comm. **177** (2007), 432.

[54] A. M. Dziewonski and D. L. Anderson, *Preliminary Reference Earth Model*, Physics of The Earth and Planetary Interiors **25** (1981), 297.

[55] C. Adams et al., *The Long-Baseline Neutrino Experiment: Exploring Fundamental Symmetries of the Universe*, arXiv:1307.7335 (2014)

[56] DUNE/LBNF webpage, `http://www.dunescience.org` (acc. 25-Aug-2015)

[57] M. G. Aartsen et al., *Letter of Intent: The Precision IceCube Next Generation Upgrade (PINGU)*, arXiv:1401.2046 (2014)

[58] U. F. Katz, *The ORCA Option for KM3NeT*, PoS (Neutel 2013), 057.

[59] KM3NeT webpage, `http://www.km3net.org` (acc. 25-Aug-2015)

[60] INO webpage, `http://www.ino.tifr.res.in/ino/` (acc. 25-Aug-2015)

[61] K. Abe et al., *A Long Baseline Neutrino Oscillation Experiment Using J-PARC Neutrino Beam and Hyper-Kamiokande*, arXiv:1412.4673 (2015)

[62] G. G. Raffelt, *Neutrinos and the Stars*, arXiv:1201.1637 (2012)

[63] H.-T. Janka et al., *Core-Collapse Supernovae - Reflections and Directions*, Prog. Theor. Exp. Phys. (2012), 01A309.

[64] K. Kotake et al., *Explosion Mechanism, Neutrino Burst, and Gravitational Wave in Core-Collapse Supernovae*, Rept. Prog. Phys. **69** (2006), 971.

[65] T. Fischer et al., *Protoneutron Star Evolution and the Neutrino-Driven Wind in General Relativistic Neutrino Radiation Hydrodynamics Simulations*, Astron. Astrophys. **517** (2010), A80.

[66] G. G. Raffelt, *Stars as Laboratories for Fundamental Physics*, The University of Chicago Press, Chicago (1996)

[67] K. Hirata et al., *Observation of a Neutrino Burst from the Supernova SN1987A*, Phys. Rev. Lett. **58** (1987), 1490.

[68] K. Hirata et al., *Observation in the Kamiokande-II Detector of the Neutrino Burst from Supernova SN1987A*, Phys. Rev. D **38** (1988), 448.

[69] R. M. Bionta et al., *Observation of a Neutrino Burst in Coincidence with Supernova 1987A in the Large Magellanic Cloud*, Phys. Rev. Lett. **58** (1987), 1494.

[70] C. B. Bratton et al., *Angular Distribution of Events from SN1987A*, Phys. Rev. D **37** (1988), 3361.

[71] E. N. Alekseev et al., *Possible Detection of a Neutrino Signal on 23 February 1987 at the Baksan Underground Scintillation Telescope of the Institute of Nuclear Research*, Pisma Zh. Eksp. Teor. Fiz. **45** (1987), 461. [JETP Lett. **45** (1987), 589]

[72] E. N. Alekseev et al., *Detection of the Neutrino Signal from SN 1987A in the LMC Using the INR Baksan Underground Scintillation Telescope*, Phys. Lett. B **205** (1988), 209.

[73] J. F. Beacom, *The Diffuse Supernova Neutrino Background*, Ann. Rev. Nucl. Part. Sci. **60** (2010), 439.

[74] K. Bays et al., *Supernova Relic Neutrino Search at Super-Kamiokande*, Phys. Rev.

D **85** (2012), 052007.

[75] G. Bellini, *Final Results of Borexino Phase-I on Low Energy Solar Neutrino Spectroscopy*, Phys. Rev. D **89** (2014), 112007.

[76] M. Apollonio et al., *Search for Neutrino Oscillations on a Long Base-Line at the Chooz Nuclear Power Station*, Eur. Phys. J. C **27** (2003), 331.

[77] Double Chooz Collaboration, Double Chooz Internal Document, DC-doc-1037-v1 (2009)

[78] L.P. Ekström and R.B. Firestone, *WWW Table of Neutron Capture Gammas*, database version 3/17/04 from URL: `http://ie.lbl.gov/ng.html` (acc. 15-Jun-2015)

[79] Double Chooz Collaboration, Double Chooz Internal Document, DC-doc-1041-v1 (2009)

[80] D. Dietrich et al., *Monte Carlo Aided Design of the Inner Muon Veto Detectors for the Double Chooz Experiment*, JINST **7** (2012), P08012.

[81] J. A. Formaggio and G. P. Zeller, *From eV to EeV: Neutrino Cross Sections Across Energy Scales*, Rev. Mod. Phys. **84** (2012), 1307.

[82] Th. A. Mueller et al., *Improved Predictions of Reactor Antineutrino Spectra*, Phys. Rev. C **83** (2011), 054615.

[83] Y. Abe et al., *First Measurement of θ_{13} From Delayed Neutron Capture on Hydrogen in the Double Chooz Experiment*, Phys. Lett. B **723** (2013), 66.

[84] T. Hagner et al., *Muon-Induced Production of Radioactive Isotopes in Scintillation Detectors*, Astropart. Phys. **14** (2000), 33.

[85] S. Abe et al., *Production of Radioactive Isotopes Through Cosmic Muon Spallation in KamLAND*, Phys. Rev. C **81** (2010), 025807.

[86] The National Nuclear Data Center (NNDC), *Nuclear Physics Database*, Brookhaven National Laboratory, `http://www.nndc.bnl.gov/` (acc. 4-Jun-2015).

[87] Y. Abe et al., *Background-Independent Measurement of θ_{13} in Double Chooz*, Phys. Lett. B **735** (2014), 51.

[88] K. Schreckenbach, et al., *Determination of the Antineutrino Spectrum from ^{235}U Thermal Neutron Fission Products up to* $9.5\,\mathrm{MeV}$, Phys. Lett. B **160** (1985), 325.

[89] F. von Feilitzsch et al., *Experimental Beta-Spectra from ^{239}Pu and ^{235}U Thermal Neutron Fission Products and their Correlated Antineutrino Spectra*, Phys. Lett. B **118** (1982), 162.

[90] A. Hahn et al., *Antineutrino Spectra From ^{241}Pu and ^{239}Pu Thermal Neutron Fission Products*, Phys. Lett. B **218** (1989), 365.

[91] N. Haag et al., *Experimental Determination of the Antineutrino Spectrum of the Fission Products of ^{238}U*, Phys. Rev. Lett. **112** (2014), 122501.

[92] N. Haag, *Experimental Determination of the Antineutrino Spectrum of the Fission Products of* ^{238}U, PhD thesis, Technische Universität München (2013)

[93] Y. Declais et al., *Study of Reactor Anti-Neutrino Interaction with Proton at Bugey Nuclear Power Plant*, Phys. Lett. B **338** (1994), 383.

[94] Y. Abe et al., *Direct Measurement of Backgrounds Using Reactor-Off Data in Double Chooz*, Phys. Rev. D **87** (2013), 011102.

[95] L. Oberauer et al., *Liquid Scintillator Specification Document*, LAGUNA-LBNO internal report (2012)

[96] M. Kaiser, *Supernova Neutrinos in LENA: Towards a Time- and Flavor-Resolved Analysis*, Master thesis, Universität Hamburg (2012)

[97] A. Beck et al., *SNOwGLoBES: SuperNova Observatories with GLoBES: DRAFT* (2013), `http://www.tapir.caltech.edu/~cott/CGWAS2013/snowglobes_1.1.pdf` (acc. 26-Jun-2015)

[98] J. Gava et al., *A Dynamical Collective Calculation of Supernova Neutrino Signals*, Phys. Rev. Lett. **103** (2009), 071101.

[99] R. B. Firestone and L. P. Ekström, *WWW Table of Radioactive Isotopes*, Database Version 2.1 (January 2004) from URL: *http://ie.lbl.gov/toi/* (acc. 4-Jun-2015)

[100] J. Winter, *Detection of Supernova Neutrinos in the Liquid-Scintillator Experiment LENA*, PhD thesis, Technische Universität München (2014)

[101] R. Möllenberg, *Monte Carlo Study of Solar* ^{8}B *Neutrinos and the Diffuse Supernova Neutrino Background in LENA*, PhD thesis, Technische Universität München (2013)

[102] R. Möllenberg et al., *Detecting the Diffuse Supernova Neutrino Background with LENA*, Phys. Rev. D **91** (2015), 032005.

[103] M. Wurm et al., *Search for Modulations of the Solar* ^{7}Be *Flux in the Next-Generation Neutrino Observatory LENA*, Phys. Rev. D. **83** (2011), 032010.

[104] R. Möllenberg et al., *Detecting the Upturn of the Solar* ^{8}B *Neutrino Spectrum with LENA*, Phys. Lett. B **737** (2014), 251.

[105] G. Bellini et al., *Measurement of Geo-Neutrinos from 1353 Days of Borexino*, Phys. Lett. B **722** (2013), 295.

[106] K. A. Hochmuth et al., *Probing the Earth's Interior with a Large-Volume Liquid Scintillator Detector*, Astropart. Phys. **27** (2007), 21.

[107] D. Griffiths, *Introduction to Elementary Particles*, Wiley-VCH, Weinheim (2004)

[108] G. Senjanović, *Proton Decay and Grand Unification*, AIP Conf. Proc. **1200** (2010), 131.

[109] H. Nishino et al., *Search for Proton Decay via* $p \to e^+\pi^0$ *and* $p \to \mu^+\pi^0$ *in a Large Water Cherenkov Detector*, Phys. Rev. Lett. **102** (2009), 141801.

[110] K. Kobayashi et al., *Search for Nucleon Decay via Modes Favored by Supersymmetric*

Grand Unification Models in Super-Kamiokande-I, Phys. Rev. D **72** (2005), 052007.

[111] S. Lorenz et al., *Report on Unified Detector Performance Evaluation*, LAGUNA-LBNO Deliverables (2014)

[112] Y. F. Li et al., *Unambiguous Determination of the Neutrino Mass Hierarchy Using Reactor Neutrinos*, Phys. Rev. D **88** (2013), 013008.

[113] D. Meschede, *Gerthsen Physik*, 23rd edition, Springer Verlag, Berlin (2005)

[114] J. Sawatzki, *Sensitivity Study of the Neutrino Mass Hierarchy Determination in JUNO Using Reactor Antineutrinos*, Master thesis, Technische Universität München (2014)

[115] A. B. Balantekin et al., *Neutrino Mass Hierarchy Determination and Other Physics Potential of Medium-Baseline Reactor Neutrino Oscillation Experiments*, arXiv:1307.7419 (2013)

[116] R. Möllenberg, Technische Universität München, private communication (2014)

[117] J. B. Birks, *The Theory and Practice of Scintillation Counting*, Pergamon Press, First Edition (1964)

[118] A. Jabłoński, *Efficiency of Anti-Stokes Fluorescence in Dyes*, Nature **131** (1933), 839.

[119] J. Franck and E. G. Dymond, *Elementary Processes of Photochemical Reactions*, Trans. Faraday Soc. **21** (1926), 536.

[120] E. Condon, *A Theory of Intensity Distribution in Band Systems*, Phys. Rev. **28** (1926), 1182.

[121] D. L. Horrocks, *Application of Liquid Scinitillation Counting*, Academic Press (1974).

[122] T. Förster, *Transfer Mechanisms of Electronic Excitation*, Discuss. Faraday Soc. **27** (1959), 7.

[123] M. J. Berger et al., *ESTAR, PSTAR, and ASTAR: Computer Programs for Calculating Stopping-Power and Range Tables for Electrons, Protons, and Helium Ions*, version 1.2.3 (2005). `http://physics.nist.gov/Star` (acc. 13-May-2014). National Institute of Standards and Technology, Gaithersburg, MD.

[124] T. Marrodán Undagoitia, *Measurement of Light Emission in Organic Liquid Scintillators and Studies Towards the Search for Proton Decay in the Future Large-Scale Detector LENA*, PhD thesis, Technische Universität München (2008)

[125] P. Lombardi et al., *Decay Time and Pulse Shape Discrimination of Liquid Scintillators Based on Novel Solvents*, Nucl. Instr. and Meth. in Phys. Res. A **701** (2013), 133.

[126] E. Gatti and F. de Martini, *A New Linear Method of Discrimination Between Elementary Particles in Scintillation Counters*, Nuclear Electronics **2** (1962), 265.

[127] I. B. Berlman, *Handbook of Fluorescence Spectra of Aromatic Molecules*, Academic Press, New York and London (1971)

[128] Helm AG, `http://www.helmag.com` (acc. 29-Apr-2015)

[129] Dixie Chemical, `http://www.dixiechemical.com` (acc. 29-Apr-2015)

[130] Eni S.p.A., `http://www.eni.com` (acc. 29-Apr-2015)

[131] C. Aberle et al., *Large Scale Gd-beta-diketonate Based Organic Liquid Scintillator Production for Antineutrino Detection*, JINST **7** (2012), P06008.

[132] C. Kraus for the SNO+ collaboration, *SNO with Liquid Scintillator: SNO+*, Prog. Part. Nucl. Phys. **57** (2006), 150.

[133] PerkinElmer, `http://www.perkinelmer.com` (acc. 29-Apr-2015)

[134] Japan Energy Corporation, `http://www.noe.jx-group.co.jp` (acc. 29-Apr-2015)

[135] Cölner Benzin Rafinerie (CBR), `http://www.cbr-online.de` (acc. 29-Apr-2015)

[136] Shell Deutschland Oil GmbH, `http://www.shell.de` (acc. 29-Apr-2015)

[137] H.-H. Trinh Thi, Technische Universität München, private communication (2015)

[138] J. Meyer, *Realization and Characterization of the Muon Veto Scintillator and the Buffer Liquid of the Double Chooz Experiment*, Diploma thesis, Technische Universität München (2010)

[139] T. Jagemann, *Measurement of the Scintillation Light Quenching for Nuclear Recoils Induced by Neutron Scattering in Detectors for Dark Matter Particles*, PhD thesis, Technische Universität München (2004)

[140] C. Ciemniak, *Setup of a Neutron Scattering Facility for the Measurement of Scintillation Light Quenching Factors of Low-Temperature Detectors Used in the Direct Dark Matter Search Experiments CRESST and EURECA*, PhD thesis, Technische Universität München (2011)

[141] R. Strauß, *Energy-Dependent Quenching Factor Measurements of $CaWO_4$ Crystals at mK Temperatures and Detector Prototypes for Direct Dark Matter Search with CRESST*, PhD thesis, Technische Universität München (2013)

[142] J. Scherzinger, *Quenching Factor Measurements of Liquid Scintillator by Neutron Induced Protons for the Proposed Low Energy Neutrino Astronomy Detector - LENA*, Diploma thesis, Technische Universität München (2011)

[143] L. Prade, *Precise Determination of Quenching Factors and of the Energy Response Function of Liquid Scintillators for Future Neutrino-Astroparticle Physics Experiments*, Diploma thesis, Technische Universität München (2013)

[144] L. Rohrer et al., *The Four Gap Double Drift Buncher at Munich*, Nucl. Instr. and Meth. in Phys. Res. **220** (1984), 161.

[145] M. Drosg, *Novel Monoenergetic Neutron Sources for Energies Between 2.5 and 25.7 MeV*, Nucl. Instr. and Meth. in Phys. Res. A **254** (1987), 466.

[146] S. Chiba et al., *The ${}^1H({}^{11}B,n){}^{11}C$ Reaction as a Practical Low Background Mono Energetic Neutron Source in the 10 MeV Region*, Nucl. Instr. and Meth. in Phys. Res.

A **281** (1989), 581.

[147] ET Enterprises, data sheet for PMT 9822KB,
`http://my.et-enterprises.com/pdf/9822B.pdf` (acc. 6-Jun-2015)

[148] VACUUMSCHMELZE GmbH & Co. KG, `http://www.vacuumschmelze.de` (acc. 6-Jun-2015)

[149] item Industrietechnik GmbH, `http://www.item24.de` (acc. 8-Jun-2015)

[150] LEICA Geosystems, `http://www.leica-geosystems.com` (acc. 8-Jun-2015)

[151] CAEN S.p.A., `http://www.caen.it` (acc. 10-Jun-2015)

[152] CAEN S.p.A., V1729A Technical Information Manual, Rev.3 (2010),
`http://www.caen.it/servlet/checkCaenManualFile?Id=5465` (acc. 10-Jun-2015)

[153] ROOT Analysis Framework Webpage, `http://root.cern.ch/` (acc. 10-Jun-2015)

[154] R. Brun and F. Rademakers, *ROOT — An Object Oriented Data Analysis Framework*, Nucl. Instr. and Meth. in Phys. Res. A **389** (1997), 81.

[155] I. Antcheva et al., *ROOT — A C++ Framework for Petabyte Data Storage, Statistical Analysis and Visualization*, Computer Phys. Com. **180** (2009), 2499.

[156] Sigma Aldrich, `http://www.sigmaaldrich.com` (acc. 14-Jun-2015)

[157] Dräger Safety AG & Co. KGaA, `http://www.draeger.com` (acc. 14-Jun-2015)

[158] W. R. Leo, *Techniques for Nuclear and Particle Physics Experiments*, Springer-Verlag, 2nd Edition (1994)

[159] S. Agostinelli et al., *Geant4 - A Simulation Toolkit*, Nucl. Instr. and Meth. A **506** (2003), 250.

[160] J. Allison et al., *Geant4 Developments and Applications*, IEEE Trans. on Nucl. Sci. **53** (2006), 270.

[161] Geant4 Colloboration, *Geant4: Physics Reference Manual*, Version 10.1 (2014),
`http://geant4.web.cern.ch/geant4/UserDocumentation/UsersGuides/PhysicsReferenceManual/fo/PhysicsReferenceManual.pdf` (acc. 26-Aug-2015)

[162] Geant4 Colloboration, *Geant4: Testing and Validation* (2009), `http://geant4.web.cern.ch/geant4/results/results.shtml` (acc. 26-Aug-2015)

[163] J. Apostolakis et al., *Progress in Hadronic Physics Modelling in Geant4*, J. Phys.: Conf. Ser. **160** (2009), 012073.

[164] Minuit Home Page, `http://seal.web.cern.ch/seal/snapshot/work-packages/mathlibs/minuit/` (acc. 26-Aug-2015)

[165] C. Aberle, *Optimization, Simulation and Analysis of the Scintillation Signals in the Double Chooz Experiment*, PhD thesis, MPIK Heidelberg (2011)

[166] T. S. Ferguson, *A Course in Large Sample Theory*, Chapman and Hall/CRC, 1st edition (1996)

[167] I. N. Bronstein et al., *Taschenbuch der Mathematik*, Harri Deutsch, Frankfurt am Main (2005)

[168] F. James, L. Lyons and Y. Perrin (editors), *Comment on Methods for Setting Confidence Limits*, Workshop on confidence limits, CERN, CERN-Library (2000)

[169] R. Barlow, *Asymmetric Statistical Errors*, arXiv:0406120 (2004)

[170] G. Cowan, *Statistical Data Analysis*, Oxford University Press, Oxford New York (1998)

[171] X.-C. Ye et al., *Preliminary Study of Light Yield Dependence on LAB Liquid Scintillator Composition*, arXiv:1506.00237 (2015), submitted to Chin. Phys. C

[172] B. von Krosigk et al., *Measurement of the Proton Light Response of Various LAB Based Scintillators and its Implication for Supernova Neutrino Detection via Neutrino–Proton Scattering*, Eur. Phys. J. C **73** (2013), 2390.

[173] F. Elisei et al, *Measurements of Liquid Scintillator Properties for the Borexino Detector*, Nucl. Instrum. Methods Phys. Res. A **400** (1997), 53.

[174] S. Hellgartner, *A Calibration Experiment for the AGATA Pulse Shape Analysis*, Diploma thesis, Technische Universität München (2011)

Danksagung